Mass-Selected Model Systems in Catalysis

- from Nanoparticles to Single Atoms

Ph.D. Thesis

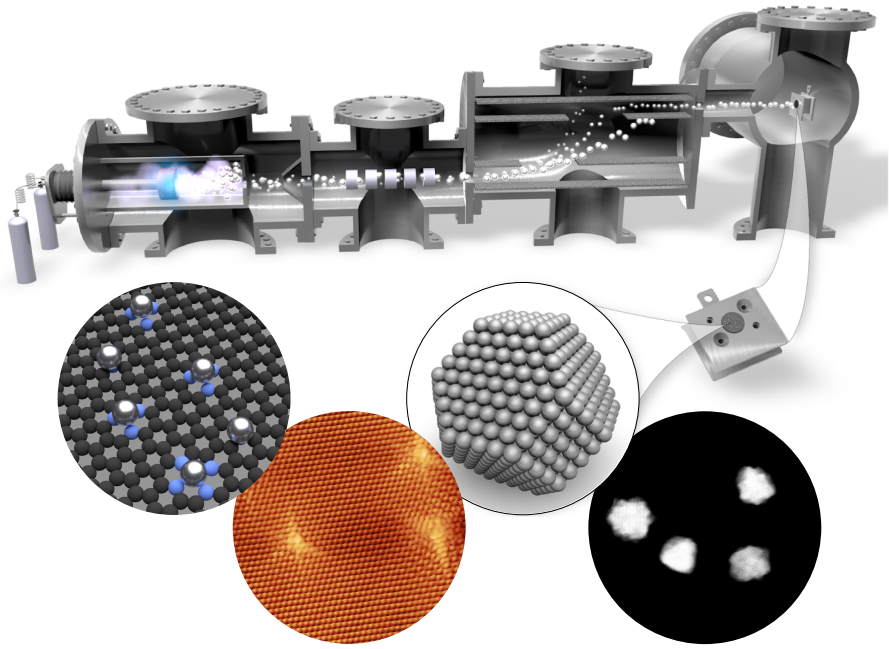

Niklas Mørch Secher

Technical University of Denmark
Department of Physics
Surface Physics and Catalysis (SurfCat)

March 2020

The work described in this thesis was carried out under the supervision of:
Supervisor: Professor Ib Chorkendorff
Co-supervisor: Associate Professor Jakob Kibsgaard

Front page: Thanks to Jakob Kibsgaard for the 3D rendered image of the Nanobeam cluster source

Abstract

A quick glimpse into the literature on heterogeneous catalysis research reveals many different approaches to developing novel catalysts. This Ph.D. thesis describes an approach based on applying mass-selected clusters and nanoparticles in model systems, to gain increased fundamental understanding of relevant catalytic processes. The thesis opens with a brief introduction to the exponentially increasing global energy demand leading to the necessary transition to sustainable energy sources, including chemical energy storage. This is followed by a brief introduction to the fundamentals of catalysis and the experimental techniques applied in this work. The subsequent chapters present studies within different topics in catalysis and will therefore be summarized individually:

Platinum Dissolution During the Oxygen Reduction Reaction: One of the major degradation phenomena in a polymer electrolyte membrane fuel cell is dissolution of the platinum based oxygen reduction reaction (ORR) catalyst. Together with other research groups we studied the dissolution of Pt nanoparticles under ORR conditions using scanning flow cell measurements with online inductively coupled plasma mass spectrometry. Mass-selected Pt nanoparticles from 2-10 nm, combined with simulations and an industrially relevant 2 nm Pt catalyst, showed that the dissolution rate is proportional to the edge-to-edge interparticle distances. Furthermore, the mass-selected Pt nanoparticles were used to show that the standard dissolution testing protocols create a misleading volcano shaped particle size effect.

Benchmarking the Hydrogen Evolution Activity of Platinum: Platinum is an excellent catalyst for the hydrogen evolution reaction (HER), but its natural abundance is far from ideal for the necessary terawatt scale applications. Instead many novel HER catalysts based on earth-abundant materials are being reported with misleading claims of platinum-like activity based on the overpotential at 10 mA/cm^2 geometric current density, η_{10mA/cm^2}. A mass-selected 3.8 nm Pt nanoparticle "benchmark" catalyst is used to show, that this metric is heavily affected by the amount of catalyst material loaded onto the working electrode. Meanwhile, catalyst loading is rarely reported in literature, leading to erroneous comparison. The "benchmark" catalyst displays η_{10mA/cm^2} from 16 mV to 150 mV for catalyst

loadings from 5000 ng/cm^2 to 13 ng/cm^2, measured in a rotating disc electrode setup. The HER activity is reported as $\eta_{10\mathrm{mA/cm^2}}$, mass activity and intrinsic activity, to allow for proper scientific comparison.

Improving the CO Oxidation Performance of Gold: The lack of stability of Au nanoparticles during CO oxidation is adressed by alloying Au with Ti. This study uses a microreactor to investigate the CO oxidation activity and stability of mass-selected AuTi nanoparticles. Preliminary results show that 2.5 nm AuTi nanoparticles on a TiO_x support are superior in mass-activity compared to Au nanoparticles of similar size. Additionally, AuTi nanoparticles on an SiO_x support display activities similar to Au nanoparticles on TiO_x support.

Developing a Model System for Single Atoms and Clusters: This chapter motivates and presents the on-going development of a model system for single atom and cluster catalysts. The model system is based on anchoring the active species with nitrogen defects in a highly oriented pyrolitic graphite (HOPG) support. Preliminary results show, that nitrogen defects of different densities can be created by NH_3 sputtering. XPS and STM characterization indicates that the defect types are similar to those observed in different single atom catalysts reported in literature. Additionally, the ability to measure the electrochemical activity of these model systems is shown.

Resumé

En hurtig gennemgang af den eksisterende litteratur omkring heterogen katalyse afslører flere forskellige tilgange til udviklingen af nye og bedre katalysatorer. Denne Ph.D.-afhandling beskriver en tilgang, der er baseret på at anvende masse-selekteret klynger og nanopartikler i modelsystemer. Disse modelsystemer bruges til at øge den fundamentale forståelse af nogle få udvalgte katalytiske processer. Afhandlingen tager udgangspunkt i en kort gennemgang af det eksponentielt voksende globale energiforbrug, hvilket fører til den nødvendige overgang til bæredygtige energikilder og kemisk energilagring. De efterfølgende kapitler indeholder studier i forskellige emner indenfor katalyse og bliver derfor opsummeret individuelt:

Platin opløsning under reduktionen af ilt: Opløsningen af platin i katalysatoren, er en af de største degraderings-mekanismer i en polymer electrolyt membran brændselscelle. Vi har, sammen med andre forskningsgrupper, studeret opløsningen af platin ved betingelser, magen til dem i en brændselscelle, med teknikken "scanning flow cell with online inductively coupled plasma mass spectrometry". Masse-selekteret Pt nanopartikler med størrelser fra 2-10 nm, kombineret med simuleringer og en industriel relevant 2 nm Pt katalysator, viste at opløsningen af Pt afhænger af kant til kant afstanden mellem partiklerne. Derudover blev de masse-selekteret partikler brugt til at vise at de standardiserede testprotokoller skaber en misvisende vulkanformet størrelseseffekt.

Et "benchmark" brintudviklings studie af platin: Platin er en exceptionel katalysator til at udvikle brint, men dens naturlige fremkomst i naturen er langt fra optimal i forhold til den nødvendige teknologiske skalering til terawatt. I stedet er der mange forskere, der undersøger katalysatorer baseret på grundstoffer med en højere naturlig fremkomst. Desværre, bruger de misvisende data ud fra det overpotentiale der skal til at drive en geometrisk strømdensitet på 10 mA/cm^2, η_{10mA/cm^2} til at argumentere for platinlignende brintudvikling. Her viser vi, ved brug af en "benchmark" Pt katalysator baseret på masse-selekteret 3.8 nm partikler, at mængden af katalysator på elektroden påvirker dette overpotentiale markant. Dette er særlig vigtigt da mængden af katalysator på elektroden sjældent rapporteres i videnskabelige publikationer, hvilket fører til forkerte sammenligninger. "Benchmark" systemet viser η_{10mA/cm^2} mellem 16 mV og 150 mV for Pt mængder fra

5000 ng/cm^2 til 13 ng/cm^2, målt i en roterende disk-electrode. Brintudviklings aktiviteten er rapporteret i $\eta_{10\mathrm{mA/cm^2}}$, masseaktivitet og intrinsisk aktivitet.

Forbedring af CO oxidering med guld: Den manglende stabilitet af Au nanopartikler under oxidering af CO bliver adresseret ved at legere Au med Ti. Dette studier bruger mikroreaktorer til at undersøge CO oxiderings-aktiviteten og stabiliteten af masse-selekteret AuTi nanopartikler. Indledende resultater viser at 2,5 nm AuTi nanopartikler på en TiO_2 support er overlegne i masseaktivitet i forhold til Au nanopartikler af samme størrelse. Derudover viser AuTi nanopartikler på en SiO_x support, en CO oxideringsaktivitet der er sammenlignelig med Au på TiO_x.

Udviklingen af et modelsystem til enkeltatom- og klynge-katalysatorer: Kapitlet beskriver den igangværende udvikling af et modelsystem til katalysatorer bestående af enkelte atomer og små klynger. Modelsystemet består af en forankring af den aktive enhed vha. nitrogendefekter i en "highly oriented pyrolitic graphite" (HOPG) overflade. Indledende resultater viser at man kan skabe nitrogendefekter ved at bombardere overfladen med NH_3. XPS og STM karakterisering indikerer at defekttyperne er magen til dem der er observeret i eksisterende enkeltatoms katalysatorer. Derudover vises muligheden for at måle den elektrokemiske aktivitet af disse modelsystemer.

Preface

This thesis is submitted to fulfil the requirements for obtaining the Ph.D. degree from the Technical University of Denmark. The work presented herein was carried out under the supervision of Prof. Ib Chorkendorff and Assoc. Prof. Jakob Kibsgaard from March 2017 to March 2020 at the Surface Physics and Catalysis (SurfCat) group at the Department of Physics, Technical University of Denmark.

I have sincerely enjoyed working in the highly social and collaborative environment at SurfCat, created by both fellow Ph.D. students, Postdocs and Professors. Specifically, I would like to thank Ib Chorkendorff for exceptional supervision and his ambitious and creative mindset, which has been highly motivating. One rarely leaves his office without an answer or a new idea, which are extremely valuable when the experiments don't agree with you. Next, I would like to thank Jakob Kibsgaard for his open door policy, which I have used frequently for supervision and scientific discussions.

I have collaborated with too many colleagues to mention them all here and have attempted to give due credit in the specific chapters. Of special importance I would like to highlight my lab partner in crime, Jakob Ejler Sørensen. Together we have caused and fixed more problems on the UHV chambers than I can count. The combination of his subtle optimism with my not so subtle optimism and our combined sense of humor has created a great atmosphere in the lab. I would also like to thank Karl Toudahl and Johannes Novak Hansen for our extensive discussions/speculations on single atoms, why they don't behave and a lot of less scientific topics. I would also like to thank all the others at SurfCat for contributing to the highly social, motivating and productive atmosphere.

Finally, I would like to thank my girlfriend Katrine Haaning, for accepting that working with UHV means odd and unpredictable hours. She has been extremely supportive over the last three years, which has been an invaluable help in getting through the challenging periods of the Ph.D. studies.

Niklas Mørch Secher

List of Appended Papers

Paper I: The Dissolution Dilemma for Low Pt Loading Polymer Electrolyte Membrane Fuel Cells
Daniel J. S. Sandbeck*, **Niklas Mørch Secher***, Masanori Inaba, Jonathan Quinson, Jakob Ejler Sørensen, Jakob Kibsgaard, Alessandro Zana, Francesco Bizzotto, Florian D. Speck, Alexandra Dworzak, Carsten Dosche, Mehtap Oezaslan, Ib Chorkendorff, Matthias Arenz, Serhiy Cherevko
Subtmitted to Advanced Energy Materials
*These authors contributed equally.

Paper II: The Particle Size Effect on Platinum Dissolution: Considerations for Accelerated Stability Testing of Fuel Cell Catalysts
Daniel J. S. Sandbeck*, **Niklas Mørch Secher***, Florian D. Speck, Jakob Ejler Sørensen, Jakob Kibsgaard, Ib Chorkendorff, Serhiy Cherevko
In review at ACS Catalysis
*These authors contributed equally.

Contents

List of Figures

List of Tables

List of Abbreviations and Acronyms

AST Accelerated Stability Testing

CatTheory Center for Catalysis Theory

CE Counter Electrode

CV Cyclic Voltammetry

ECSA Electrochemically Active Surface Area

EDL Electrochemical Double Layer

EDS Energy Dispersive X-ray Spectroscopy

ETEM Environmental Transmission Electron Microscopy

GDP Gross Domestic Product

HER Hydrogen Evolution Reaction

HOPG Highly Oriented Pyrolitic Graphite

HOR Hydrogen Oxidation Reaction

ISS Ion Scattering Spectroscopy

MEA Membrane Electrode Assembly

OER Oxygen Evolution Reaction

ORR Oxygen Reduction Reaction

PEMFC Polymer Electrolyte Membrane Fuel Cell

PEM Polymer Electrolyte Membrane

PGM Platinum Group Metal

QMS Quadrupole Mass Spectrometer

RDE Rotating Disk Electrode

RE Reference Electrode

RHE Reversible Hydrogen Electrode

RSF Relative Sensitivity Factor

RTD Resistance Temperature Detector

SAC Single Atom Catalyst

SEM Scanning Electron Microscopy

SFC-ICP-MS Scanning Flow Cell with Online Inductively Coupled Plasma Mass Spectrometry

STEM Scanning Transmission Electron Microscopy

STM Scanning Tunneling Microscopy

TEM Transmission Electron Microscopy

TPD Temperature Programmed Desorption

UHV Ultra-High Vacuum

WE Working Electrode

XPS X-ray Photoelectron Spectroscopy

Chapter 1

Introduction

With this introduction I hope to motivate the field of catalysis through an understanding of the increasing energy demand and its effect on the climate crisis. This is followed by a conceptual description of the key concepts in catalysis research, which will set the stage for the research projects I have partaken in. Finally, I will give a brief overview of the thesis contents.

1.1 The Problem with Exponential Growth

In 2018 the global energy consumption rate reached 18.6 TW and recent reports predict it will increase to more than 30 TW by 2050 [1, 2]. The cause of the increasing energy consumption goes back to the technological advances during the industrial revolution. They sparked a steep increase in the global population, which resulted in an increased energy demand. This was further accelerated in the early 1900's, when Haber and Bosch discovered and industrialized the fixation of nitrogen into ammonia using a catalytic process known as the Haber-Bosch Process. Ammonia is used in fertilizers and the discovery allowed for an increased production of food to sustain an even larger global population. From 1900 to 2019 the global population has increased from 1.6 billion to 7.7 billion [3] resulting in a significant growth in energy consumption as seen in Figure 1.1 [4]. However, the increasing population is not the only cause of the growing energy consumption. From an economic and political standpoint a stable growth for a country's gross domestic product (GDP) is 2-3% each year (5-8% for developing countries)[5]. Studies have shown a linear correlation between a country's energy consumption per capita and the GDP per capita [6]. Thus even as the population growth starts to stagnate, the energy consumption will continue to increase.

1.1.1 A Need for Sustainable Energy

As is evident from Figure 1.1 the vast majority of our energy consumption is supplied by fossil fuel sources, which poses a problem. The burning of fossil fuels emits

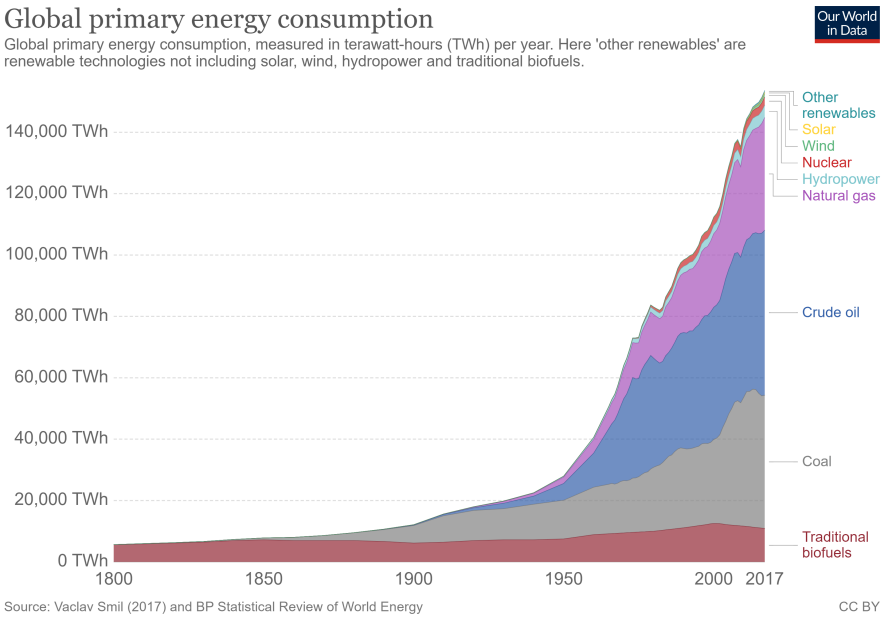

Figure 1.1: The global energy consumption from 1800 to 2017, color coded by energy source. Reprinted from [4]

greenhouse gases, which are the main cause of climate change [7]. I will not go into this topic in further detail, but I will refer the reader to the report of the United Nation's Intergovernmental Panel on Climate Change (IPCC), which concludes with 95% certainty that humans are the main cause of global warming[7]. All the countries in the world except for Nicaragua, Syria and USA have agreed to the 2015 Paris agreement, thereby promising to: "holding the increase in the global average temperature to well below 2 °C above preindustrial levels and pursuing efforts to limit the temperature increase to 1.5 °C above preindustrial levels." [8].

Keeping the temperature increase below 1.5-2 °C requires that future energy sources have a net zero emission of greenhouse gases. These sources are commonly referred to as sustainable energy sources, the most common being: hydropower, nuclear, solar and wind. Hydropower is already a widespread source of energy that comes from building dams to generate electricity and cannot be easily scaled by orders of magnitude. This leaves nuclear, solar and wind to bridge the 11.4 TW gap from now to 2050. This corresponds to 400 GW/year of energy production that needs to be developed. A modern nuclear reactor can generate 1 GW [9], the largest wind turbine in the world generates 10 MW [10] and a solar cell plant can generate around 37 MW per 1 km^2, with the largest plants reaching around 2 GW [11]. For

one of these technologies to fill the gap requires a daily production of: more than 1 nuclear reactor, 110 of the largest wind turbines in the world or 30 km^2 solar cells. There are currently 442 nuclear reactors in the world with an additional 54 under construction, 109 planned and 330 proposed [9]. Considering the capital costs, a minimum 5 year construction time and gap from the number of planned to required reactors, it becomes clear that existing nuclear energy technologies will play a limited role in the future energy supply. While all 3 technologies are far from matured, it is clear that we will need to fill the gap with a combination of the three instead of one single technology.

1.1.2 Chemical Energy Storage

One of the major challenges with implementing sustainable energy is the fact that sustainable energy sources only produce electricity. Meanwhile, electricity only constitutes around 15% of the total energy consumption [2]. Thus there is a need to electrify the infrastructure and industries that can be electrified. However, some industries such as commercial transportation, which consume more than 1.9 TW [2, 12], are not easily electrified and here chemical fuels are more suited. Additionally, solar and wind energy sources are intermittent and the supply occasionally surpasses demand, but often the opposite is the case as seen for two weeks in Denmark in 2015 in Figure 1.2.

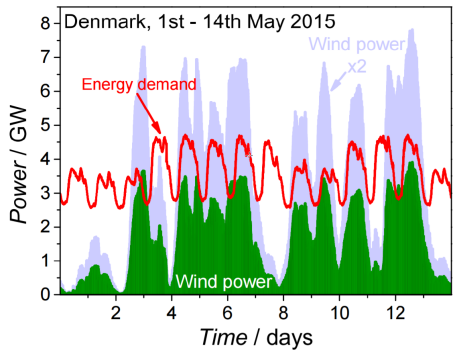

Figure 1.2: Electricity generated by wind turbines (green) in Denmark for a period of two weeks in 2015. The intermittency of the power generation means that production does not follow demand (red). Double the windpower is shown in light blue. Reprinted from [13] with data from EMD International A/S.

It is evident from Figure 1.2 that even if the amount of wind power is doubled, intermittency remains an issue. Considering these challenges it would be advantageous to be able to produce chemical fuels from electricity. Not only to store energy for intermittent sources, but also to produce fuels for transportation or other applications that are not readily electrified. Additionally, excess chemicals can be used

as feedstock in the production of industrial chemicals and plastics [12].

A viable scheme for implementing a sustainable production of chemical fuels into a modern infrastructure was presented by Seh and coworkers[12]. The scheme is shown in Figure 1.3.

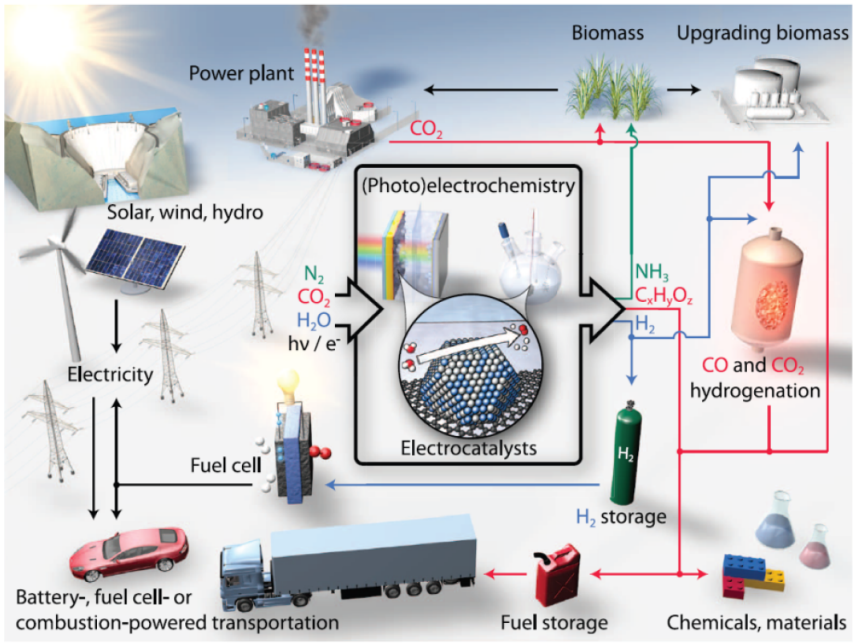

Figure 1.3: Chemical energy storage and fuels production. Reprinted from [12]. With permission from AAAS.

There are a few requirements when selecting chemicals to act as energy carriers in a chemical energy storage scheme [12]. First of all, they have to be in a reduced form to readily react with oxygen from the atmosphere and release the stored energy. Second, they have to be produced from abundantly available reactants so that a large-scale integration into the power grid is economically viable. Finally, the production of the chemical must be through a sufficiently efficient reaction. Two promising strategies for driving the reaction are:

- **Electrochemical reactions:** The chemicals are produced by electrolyzers, which use electricity to drive a reaction between a liquid-phase electrolyte and a gas.

- **Thermochemical reactions:** The chemicals are produced in the gas-phase in large-scale reactors at elevated temperatures and pressures.

The most obvious chemical reaction for energy storage is the production of hydrogen from the electrolysis of water:

$$2\,H_2O \rightarrow 2\,H_2 + O_2 \tag{1.1}$$

This reaction has the major advantage that water is an abundant feedstock, but the hydrogen gas has a low volumetric energy density and must therefore be compressed before being suited for most applications. Alternatively, hydrogen can be used to reduce CO or CO_2 through a thermochemical reaction in a large gas-phase reactor.

Instead of reducing CO_2 in a gas-phase reaction it can be done electrochemically to create hydrocarbons or oxygenates. Even products with carbon-carbon bonds e.g. higher alcohols can be produced. Methanol and ethanol are especially interesting since they can serve as liquid fuels. The reaction can be generalized through the unbalanced reaction:

$$CO_2 + H_2O \rightarrow C_xH_yO_z \tag{1.2}$$

One of the major challenges in CO_2 reduction is the huge spread in possible products such as carbon monoxide, formaldehyde, formate, methane and methanol [12]. Thus tailoring the selectivity of the reaction becomes essential [12].

1.1.3 Releasing the Energy Stored in Chemical Bonds

The most energy efficient way to release the energy stored in a hydrogen bond is by using a fuel cell. Fuel cells provide a way of releasing the energy stored in chemical bonds through a chemical reaction and are therefore essential for an infrastructure utilizing sustainable energy storage in hydrogen. There are a number of different fuel cell types, each with their own advantages. For transportation purposes the most promising type is the polymer electrolyte membrane fuel cell (PEMFC) due to its fast startup time and high power-to-weight ratio [14]. Recent developments in battery technology by Tesla Inc. and others, have shifted the focus of the automotive industry towards battery powered electrical vehicles. However these vehicles are for some purposes limited in range and charging time along with concerns regarding lithium resources [15–17]. PEMFC vehicles alleviate some of these shortcomings of battery vehicles [18], but also provide challenges such as high cost and lifetime limitations. Therefore some car manufacturers are focusing on PEMFC vehicles in parallel to batter powered electrical vehicles [19].

To release the energy stored in the chemical bonds, a PEMFC runs the overall reaction [20]:

$$2\,H_2 + O_2 \rightarrow 2\,H_2O \tag{1.3}$$

The reaction proceeds in two half-cell reactions, the hydrogen oxidation reaction (HOR) in Equation 1.4 and the oxygen reduction reaction (ORR) in Equation 1.5

$$H_2 \rightarrow 2\,H^+ + 2\,e^- \tag{1.4}$$

$$O_2 + 4\,H^+ + 4\,e^- \rightarrow 2\,H_2O \tag{1.5}$$

There is a 1.23 V potential energy difference between the HOR and ORR[20]. A PEMFC uses this potential to drive an electron through an external circuit to power electrical applications such as an electrical car.

Common for all these chemical reactions is that the reaction must be sufficiently energy efficient to be economically feasible. This is achieved by using a catalyst when running the reaction and each reaction needs a custom tailored catalyst. Considering the many different reactions of interest, there are a large number of research branches in catalysis.

1.2 An Introduction to Catalysis

To understand catalytic reactions one must first consider the energetics of a reaction. An example from [20] is shown in Figure 1.4. The spontaneous reaction of reactants A and B to form the product P has one fundamental requirement: the potential energy of the product must be lower than the two reactants. If this is the case then there are two overall pathways, one with and one without a catalyst. Without a catalyst there is a large energy barrier due to breaking existing bonds and forming new ones. While the energy expensive pathway may be statistically possible, it is far too inefficient to be viable. Therefore a catalyst is used to create an alternate low energy pathway with multiple intermediate steps. Here there is still a small energy barrier for each step, but when adding them together it is smaller than the pathway without a catalyst. This is because, when the reactants bond to the surface of a catalyst, the energy landscape of breaking and forming bonds changes. For the catalyst to be reused, the product must finally desorb from the surface so it is available for new reactants. Even if there is a small barrier in energy to desorb, it is still more efficient compared to the energy expensive pathway.

This cycle leads to the definition of a catalyst: A catalyst is an entity that accelerates the rate of a chemical reaction without being consumed itself [20]. There are many different entities that can act as catalysts, but from a broader perspective there are two main classifications: homogeneous and heterogeneous catalysts. A homogeneous catalyst is a catalyst in the same phase as the reactants and products e.g. a liquid in a liquid. A heterogeneous catalyst is in another phase than the reactants and products e.g. a solid that catalyses a liquid or gaseous reaction. In the following I will focus only on heterogeneous catalysts as this is what I have worked on throughout my PhD.

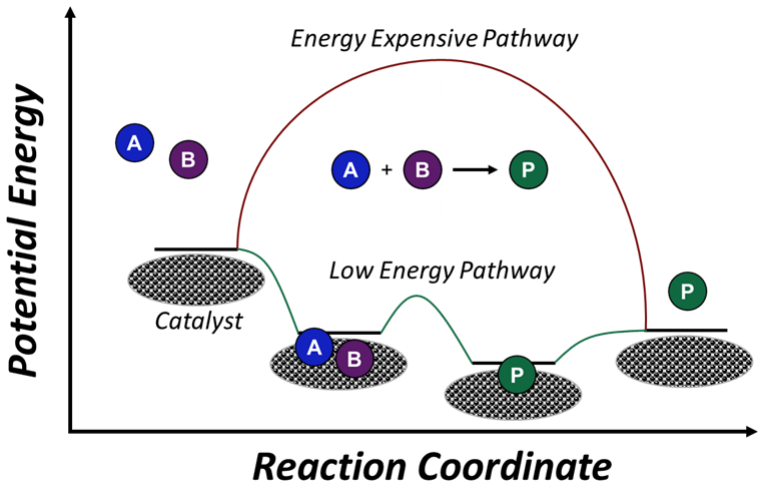

Figure 1.4: Potential energy diagram of a catalytic reaction. A and B react together to form P. This can happen without a catalyst through the energy expensive reaction pathway. Alternatively, A and B can bond to the catalyst surface and react here to form P. P then has to be desorbed from the surface. This low energy pathway allows for increased reaction rates. Figure adapted from [20].

1.2.1 Selecting the Right Catalyst

To understand heterogeneous catalysts consider the CO oxidation reaction in equation 1.6, a thermochemical reaction, which is also the topic of Chapter 5.

$$2\,CO + O_2 \rightarrow 2\,CO_2 \tag{1.6}$$

Imagine that A and B in Figure 1.4 are CO and O_2 reacting to form the product CO_2. While this may seem as an unwanted reaction considering it emits CO_2, it is an extremely relevant chemical reaction that takes place in all car exhausts. CO oxidation can proceed through the Langmuir-Hinshelwood reaction pathway, where CO and O_2 bond to the surface of a metal such as platinum [20]. O_2 will bond strongly to the surface breaking the bond between the two oxygen atoms allowing them to react with CO and form CO_2. This requires just the right binding strength to split the oxygen molecule, but still allow the atoms to react with CO. Likewise CO, which is a very reactive molecule, must not be bound too strongly to allow a reaction with oxygen. This principle is a fundamental guiding principle when designing catalysts, known as the Sabatier Principle [20]. The reactants must bond "just right" with the surface to enhance the reaction rate, which can be visualized by plotting the reaction rate against the binding energy of the intermediates. Since CO oxidation has two different reacting species this becomes a two dimensional (2D) contour plot as seen in Figure 1.5a. These plots are commonly

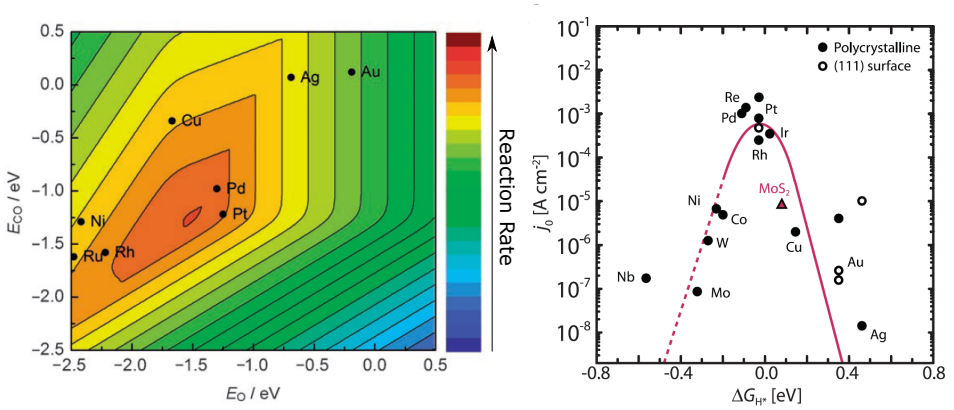

(a) T=600K, P_{O_2}=0.33 bar,P_{CO}=0.67 bar **(b)**

Figure 1.5: a) The calculated reaction rate of CO oxidation on different metal catalysts plotted against the binding energy of CO and O. Figure adapted from [21]. **b)** Volcano plot of HER activity for metals and MoS_2. Reprinted from [12]. With permission from AAAS.

referred to as volcano plots. From the 2D volcano it is evident that under these conditions, Pd and Pt are good CO oxidation catalysts.

Alternatively the Sabatier principle can be understood by examining the electrochemical hydrogen evolution reaction (HER) which is one half-cell reaction in the electrolysis of water and the topic of chapter 4. The reaction can be split into two steps, with two different reaction pathways for the second step [12]:

$$\begin{aligned} &\textbf{First step: } 2\,H^+ + 2* + 2\,e^- \rightarrow 2\,H* \\ &\textbf{Second Step:} \\ &\qquad \text{Tafel} : 2\,H* \rightarrow H_2 \\ &\qquad \text{Heyrovsky} : H* + H^+ + e^- \rightarrow H_2 \end{aligned} \tag{1.7}$$

Here the $*$ denotes a binding site, while $H*$ denotes a hydrogen bound to a binding site. The reaction proceeds by first binding protons to the surface sites in a Volmer step [12]. Then either two bound hydrogen atoms react to form molecular hydrogen through a Tafel step or a bound hydrogen atom reacts with a proton to form molecular hydrogen through a Heyrovsky reaction [12]. The atomic hydrogen must bind to the surface, while still allowing it to react to form molecular hydrogen and desorb. As there is only one intermediate the volcano plot becomes a one dimensional volcano as seen in Figure 1.5b. From the plots in Figure 1.5 it is obvious that Pt is a great catalyst for both CO oxidation and HER, and it is. However, these are two relatively simple reactions and we are not always so lucky

with the binding energy of materials.

1.2.2 Challenges in Catalyst Optimization

One major challenge when designing new catalysts is that the changing of the binding energy towards one intermediate, will change the binding energy of other intermediates bound through the same atom. This is an issue for the ORR which has the O, OH and OOH intermediates all bound through the O atom. As a result the binding energy of individual intermediates cannot be tuned independently, resulting in a linear scaling relation of the binding energies as seen in Figure 1.6. The gibbs free binding energy (ΔG_{OOH}) for OOH scales with ΔG_{OH} along the black line. Consequently the scaling of the binding energies determines how close to the optimum, the binding energy can be tuned. Any deviation from the optimal binding energies, will result in a decrease in the energy efficiency of the reaction. In an electrochemical reaction this effectively means having to apply a larger potential to drive a reaction, thus wasting power. The increase in electrochemical potential compared to the theoretical limiting potential is termed the overpotential and is used to compare the activity of catalysts. In thermal catalysis it translates into using higher temperatures and pressures to accelerate the gas-phase reaction. Again this effectively is a loss in power efficiency for the reaction. Therefore, breaking these scaling relations is one of the major goals of state-of-the-art catalysis research.

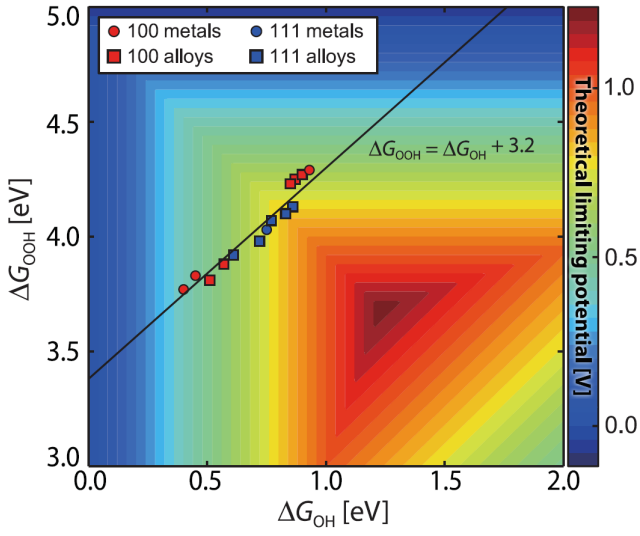

Figure 1.6: Linear scaling relations of the gibbs free energy of OH and OOH binding for the ORR. The scaling relations dictate the achievable reaction potential compared to the theoretical limited potential. Reprinted from [22].

1.3 Catalysis at the Surface

The reacting molecules bond to the surface of catalysts, making the surface properties of the catalysts extremely important. Additionally an increase in surface area results in more active sites available for reactions. Therefore another strategy for increasing the activity of a catalyst has been increasing the available surface area per volume of the catalyst material [12, 23]. Furthermore, since many state-of-the-art catalysts are composed of non-abundant elements, this is also necessary to increase the economic feasibility of catalytic processes. This has lead to the development of smaller and smaller catalyst particles since the surface area to volume ratio for e.g. a sphere with radius r scales as:

$$\frac{A}{V} \propto \frac{1}{r} \tag{1.8}$$

Consequently the smaller the particle, the more of the material is utilized. This has lead to the development of nanoparticle catalysts. Nanoparticles are defined as particles in the size range of 1-100 nm and have many different shapes. Ultimately the most efficient use of material is the dispersion of single atoms, which is also the focus of chapter 6 in this thesis.

1.3.1 Nanoparticle Structure

The structure of a crystalline metal nanoparticle is determined by the balancing of the surface energies of its different crystalline facets. The structure can be derived from the Wulff Construction [20], which assumes that the distance from the center of a particle to a specific facet is proportional to the free surface energy of the facet. Thus facets with low free surface energy will dominate the surface. Furthermore, if the particle is supported on a surface, the structure can be truncated by wetting of the surface, depending on the interface energy [20]. The free surface energy of crystalline facets depends on the presence of any adsorbates. As a consequence, the structure of a nanoparticle depends on the surrounding gas and will differ from vacuum to reaction conditions [20, 24].

For metals, the facets with the lowest free surface energies are mostly the closest-packed facets [20]. The surface of metal nanoparticles is therefore dominated by these facets as seen in Figure 1.7 showing a schematic Wulff construction of a Pt nanoparticle with the (100) and (111) facets having the lowest surface energies. Atoms on the different facets and in the interfaces between facets are coordinated to a different number of neighbouring atoms and are color coded based on their coordination number (black=9, grey=8, blue=7, red=6). The lower coordinated atoms such as steps and kinks have been shown to exhibit stronger binding energies [25], which has been described in the d-band model by the smaller overlap of d-band electrons that play a role in the binding of molecules to the surface [20, 26].

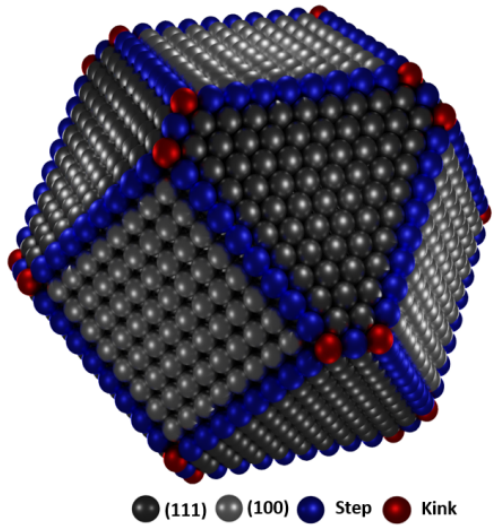

Figure 1.7: Wulff construction of a 3000 atom platinum particle with (111) and (100) facets, steps and kinks. Image courtesy of Karl Toudahl.

Particle Size Effects

As particle size decreases below tens of nanometers, the distribution of the different undercoordinated sites increases. This is a consequence of not having enough atoms to form the low energy facets. Since the various undercoordinated sites have different binding energies, it is possible that the particle size affects the catalytic properties. This is known as a particle size effect and has been demonstrated for nanoparticles for several different reactions e.g. CO oxidation on Au particles [27, 28] and Pt_xY for ORR [29] among others. When the particle size is reduced further below 1-2 nm, the particles reach a size regime where quantum mechanical effects may affect the catalytic properties [30, 31]. Particles of these sizes are commonly referred to as clusters. In this size regime, several observations of size effects have been reported with observations of considerable differences in catalytic activity from adding a single atom [32–34]. Consequently, controlling nanoparticle and cluster size is a vital part of investigations into fundamental catalytic properties.

1.4 Thesis Contents

As described above, the choice of material and particle size strongly affects the catalytic properties of a nanoparticle. Due to the nanometer size range of catalysts, proper characterization is necessary to check the structure of the synthesized catalysts. Additionally, due to the structural complexity of industrial catalysts, nano-scale characterization is difficult. As a result there is a need for well-defined

model systems that can be thoroughly characterized, especially as particle sizes approach single atoms. Thereby, model systems can be used to understand fundamental catalytic trends that can aid in the development of industrial catalysts.

There are different routes to creating model systems for catalysis. Particles of a specific size can be synthesized via colloidal wet chemistry procedures, typically using capping agents. These risk leaving chemical residue from the synthesis, on the surface of the particles. Instead, a more physical approach is the use of a ultra-high vacuum (UHV) based cluster source. A cluster source generates a beam of nanoparticles or clusters that can be filtered based on their mass, resulting in a narrow particle size distribution. This technique is not capable of synthesizing catalysts at a rate relevant for industrial applications, but due to its narrow size control and no risk of chemical residue, it is ideal for creating model systems. The purpose of my PhD has been the development of novel model systems using the Nanobeam cluster source and the adjoining Omicron UHV chamber. The thesis structure is described below:

Chapter 2 describes the experimental equipment and techniques that have been used to produce the results presented in the thesis. The chapter focuses on the synthesis and characterization techniques that I have worked with. Meanwhile techniques for testing catalytic performance are briefly introduced to the degree necessary to understand the results of the following chapters.

Chapter 3 examines the dissolution of Pt nanoparticles under ORR conditions. The work was a collaboration with several research groups, including Daniel Sandbeck and Serhiy Cherevko at the Friedrich-Alexander-University Erlangen-Nürnberg. We investigated how the distance between the catalytic Pt nanoparticles affects the dissolution of Pt by combining results from simulations, a model system and an industrially relevant system. Additionally, using the model system we explored a possible particle size effect. The collaboration resulted in two manuscripts, which have been submitted and are appended in the thesis.

Chapter 4 describes a benchmark study of how the overpotential for HER catalysts is affected by the amount of catalyst that is used, prompted by a recent comment in Nature Energy by Kibsgaard and Chorkendorff [35]. The results are set into perspective of the many studies on earth-abundant HER catalysts claiming platinum-like activity. This work is currently being written into a manuscript for publication.

Chapter 5 describes the development of a AuTi catalyst for CO oxidation. Au nanoparticles are a well known low temperature catalyst for CO oxidation that suffers from instability issues. This study examines the possibility of increasing the stability and activity of Au nanoparticles by self-anchoring using AuTi alloy nanoparticles. The project is still on going, but interesting preliminary results are presented and discussed.

Chapter 6 focuses on developing a model system for single atom and small cluster catalysts anchored by nitrogen coordination on a carbon substrate to be used for electrochemical reactions. The chapter describes the motivation behind choosing this specific model system along with preliminary results. The development is still in the early stages, but as the results will show, significant steps have been taken towards creating the model system.

Chapter 7 provides a brief summary of the main research results from the previous chapters.

All of the studies mentioned above were a collaborative work between myself, colleagues in our group and other groups. I will convey the entirety of the results, but with a focus on the synthesis and characterization parts that I have contributed to. The deposition conditions for producing Pt nanoparticles for the work in Chapter 3 and 4 were already developed in the group when I started. However to obtain homogeneous coverages my colleague Jakob Ejler Sørensen and I developed a rastering technique, which greatly improved the coverage homogeneity. Deposition conditions and procedures for AuTi nanoparticles (Chapter 5) and Pt single atoms and clusters (Chapter 6) were not previously known. I therefore developed these during this work. Additionally, the simulations presented in Chapters 3 and 4 were developed by myself with help from Jakob Ejler Sørensen.

Chapter 2

Experimental Techniques

This chapter describes the working principle and operation procedures of the Nanobeam cluster source and Omicron UHV system, that I have used to produce the model systems reported in this thesis. Apart from operating the equipment I have also been responsible for maintenance and improvements of the cluster source together with Ph.D. student Jakob Ejler Sørensen. Additionally, I will describe the experimental techniques that I have used to characterize the model systems and briefly explain the methods used by my colleagues to test the catalytic performance of the model systems.

2.1 The Ultra-High Vacuum System

The main part of my experimental work has been on the UHV system called "Omicron". Working in UHV is necessary when studying the surface of catalysts since ambient conditions contaminate the surface instantaneously. Additionally, many of the techniques explained in the following only operate in UHV. The setup consists of 3 main parts: the preparation chamber, the analysis chamber and the Nanobeam cluster source as shown in Figure 2.1.

The base pressure in the Omicron system is on the order of 10^{-10} mbar and is maintained by a combination of turbo pumps, ion getter pumps and titanium sublimation pumps. The pressure is monitored by three ion gauges, one in each part of the system. Samples are loaded into the system using a load lock that is connected to the preparation chamber. After pumping down for 1 hour, the load lock can load up to 3 samples into the chamber without compromising the chamber pressure.

Once samples are loaded into the preparation chamber they can be sputtered by ion bombardment with 6.0 purity Argon or 3.8 purity NH_3. Ar is used for cleaning the sample with sputter times of 10-40 minutes, at a sample current of ≈ 1 μA and an ion energy of 1 keV. NH_3 sputtering is used to create nitrogen defects in carbon materials with sputtering times from 10 seconds to 10 minutes, at ion energies of

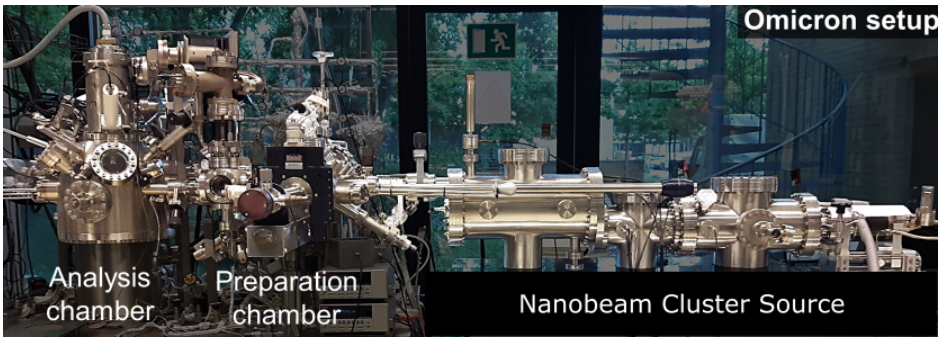

Figure 2.1: The Omicron UHV system consisting of the preparation and analysis chambers connected to the Nanobeam cluster source. The samples are prepared and deposited in the preparation chamber and moved to the analysis chamber for characterization with XPS, ISS and SEM.

150-1000 eV and sample currents of 0.08-2 μA. The main stage in the preparation chamber is also equipped with a pyrolitic boron nitride heater, capable of heating the sample up to 700 °C. Another smaller chamber that is connected to the preparation chamber is a temperature programmed desorption (TPD) chamber, which is still under development. From the preparation chamber, samples can be transferred into the analysis chamber while in UHV.

The analysis chamber is used for sample characterization and is equipped with a Omicron NanoSAM hemispherical analyzer, a SPECS XR50 x-ray lab source, an Omicron ISE 100 ion-gun and an Omicron/Zeiss Gemini scanning electron microscope with in-lens secondary electron detector. This allows for sample characterization using X-ray Photoelectron Spectroscopy (XPS), Ion Scattering Spectroscopy (ISS) and Scanning Electron Microscopy (SEM).

2.1.1 The Nanobeam Cluster Source

A cluster source is an instrument that creates a beam of nanoparticles or clusters that can vary in size from single atoms up to tens of nanometers in diameter. It relies on gas-phase aggregation of smaller species, which was first reported in 1986 by Yatsuya and coworkers [36]. However, there are different methods to supply these small species to the aggregation zone [37]. The Nanobeam cluster source (Nanobeam 2011 from Birmingham Instruments) uses magnetron-sputtering which was reported to be advantageous for many metals and alloys compared to thermal evaporation [38, 39]. After particle growth a lateral time-of-flight mass filter is used to obtain a narrow particle mass distribution, similar to the setup first reported by Palmer and co-workers [40]. A schematic of the working principle is shown in Figure 2.2. The following subsections describe the details of the Nanobeam cluster source along with many of the operational procedures developed in this work.

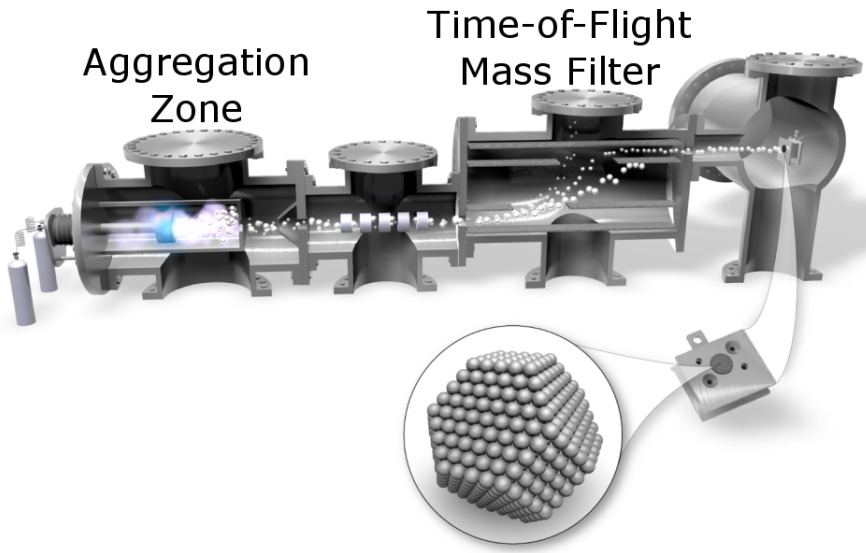

Figure 2.2: The Nanobeam cluster source uses magnetron sputtering to sputter atoms off a target. The atoms aggregate into clusters and nanoparticles, which are accelerated and focused into the lateral time-of-flight mass filter, that filters the particles based on the mass to charge ratio. Particles of the desired mass are subsequently deposited on a substrate. Image courtesy of Jakob Kibsgaard.

Magnetron Sputtering and Gas-phase Aggregation

The synthesis of nanoparticles from gas-phase aggregation requires a feed of atoms or clusters of atoms of the desired material to form larger particles. Magnetron sputtering is an efficient method to sputter atoms off of a disk of material, that can function as building blocks. A schematic of the magnetron sputtering concept is shown in Figure 2.3.

Magnetron sputtering begins by applying a bias ($\approx$ 250 V) to the target, which for all the work in this thesis is a metal. Ar is lead into the chamber through a flow controller at 10-100 SCCM around the target. When a current passes through the gas, a glow discharge is ignited. This creates a region close (<1 mm) to the target called the cathode fall [37]. Here a strong electric field accelerates the ionized Ar^+ ions onto the target. This serves two purposes: it creates electrons that help to maintain the plasma discharge and it knocks atoms of the target material into the vacuum. Additionally, a circular array of magnets positioned behind the target creates a magnetic field through the target. The magnetic field confines the electrons to the area, where the field lines are parallel to the surface [37]. The Ar^+ primarily impinge the target in this area, creating a band of intense sputtering on the target commonly called a racetrack. The sputtering of atoms in the racetrack

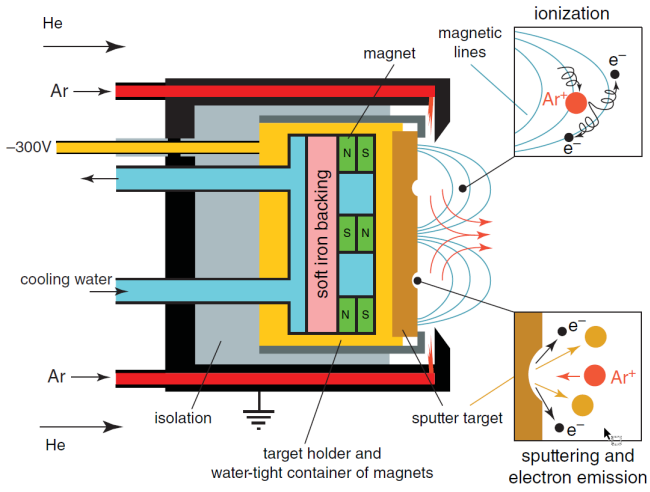

Figure 2.3: Magnetron sputtering utilizes an array of magnets behind the biased target to confine a plasma of electrons close to the target. This accelerates Ar^+ ions towards the target, which removes atoms of the material and generates additional electrons to sustain the plasma. Reprinted from [37].

serves as the feed of building blocks for the gas-phase aggregation.

The gas-phase aggregation occurs in the aggregation zone, where the magnetron sputtering target is located as in Figure 2.2. The aggregation zone is pumped through an exit aperture by a turbo pump in the surrounding chamber and can be cooled to -196 °C using a flow of liquid nitrogen through the surrounding shroud. To increase aggregation into nanoparticles, He is flowed into the aggregation zone. This serves two purposes: He increases heat transfer from the cooled chamber walls to the atoms and clusters and He atoms serve as nucleation centers for the metal atoms. The aggregation process begins with the formation of a metal dimer, but due to the conservation of energy and momentum a single collision between two metal atoms cannot create a dimer. Therefore dimers are created in a three-body collision with the participation of a noble gas atom [39]:

$$M + M + Ar/He \rightarrow M_2 + Ar/He \tag{2.1}$$

After the dimer formation the particles can grow through the addition of single atoms or cluster-cluster aggregation [37, 39]. Previous work on the Nanobeam cluster source shows signs of both mechanisms. The dominating mechanism likely depends on the material and the conditions in the aggregation zone.

Due to its low mass, He does not contribute significantly to the sputtering process. Therefore the He flow allows for separate control of the sputtering and aggregation

process. The pressure in the aggregation zone during operation is in the range of 0.01-1 mbar and can be tuned by the adjustable circular exit aperture. Meanwhile the pressure in the surrounding chamber is around 10^{-4} mbar, creating a gas flow that carries the particles out of the aggregation zone before undergoing a supersonic expansion. At supersonic velocities, the particles no longer aggregate and the outer boundaries for the mass distribution are set. A number of the particles exiting the aggregation zone are electrically charged, primarily with 1 elementary charge. Previous studies have shown that the ratio of neutral, positive and negative particles is evenly distributed at 1/3 each [39], but our experience on the Nanobeam cluster source indicates that nanoparticles >2 nm are negatively charged, while single atoms and clusters up to 10 atoms are positively charged. The range between 2 nm and 10 atoms is difficult to produce with the current setup of the Nanobeam cluster source.

Lateral Time-of-Flight Mass Filtering

The charged particles exiting the aggregation zone can be focused and accelerated by using electrostatic lenses. Before entering the mass filter they are accelerated by a potential of 500 eV and focused into a narrow beam by a series of ion optic lenses. When a particle with charge q and mass m enters an electric field E it will experience an acceleration:

$$a = \frac{qE}{m} \tag{2.2}$$

Since particles of the same mass to charge ratio ($\frac{m}{q}$) experience the same acceleration, it is possible to filter the particles in the lateral time-of-flight mass filter seen in figure 2.4.

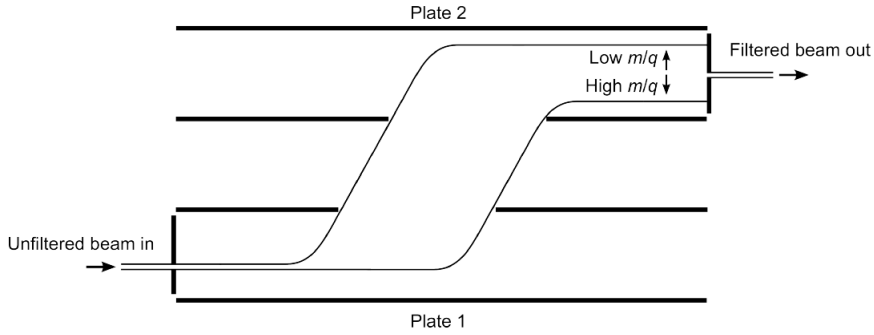

Figure 2.4: The lateral time-of-flight mass filter applies a short pulse to plate 1 displacing the unfiltered beam laterally followed by a pulse on plate 2. This results in a vertical distribution of particles based on $\frac{m}{q}$. The particles are subsequently filtered by an exit aperture.

This type of time-of-flight mass filter was first described by Issendorf and Palmer in 1999 [41]. As seen in Figure 2.4, an unfiltered beam of charged particle enters through an entrance aperture and a short high-voltage pulse is applied to plate 1. The particles experience a vertical acceleration which varies based on their $\frac{m}{q}$. Shortly after, another similar pulse is applied to plate 2, which decelerates the particles vertically and returns them to their original horizontal trajectory. However they are now displaced laterally based on their $\frac{m}{q}$. Subsequently, the particles can be filtered by applying a narrow exit aperture. The filter and entire system of ion optic lenses can be run at both positive or negative potential to select either positive or negative particles.

As mentioned above, most of the charged particles carry one elementary charge, resulting in a filtering that is effectively based on the particle mass. However there are some particles that are double charged. Particles of $\frac{2m}{2q}$ will be filtered similarly to $\frac{m}{q}$ and therefore it is possible to get particles through the filter with double the desired mass. This is unavoidable and something that must be addressed when tuning the cluster source before depositions.

The high voltage pulses are applied consecutively at a high frequency, with the pulse duration determining the selected mass. Thus by scanning the pulse duration, a mass scan can be performed. The mass filter on the Nanobeam is able to filter masses from 30 amu - 20 million amu. The mass resolution of the filter can be tuned from $\frac{m}{\Delta m}$ = 20-100 by changing the size of exit aperture. It was set to 20 under normal operating conditions to maximize the beam current and enable faster deposition times.

Deposition Current and Bias

The filtered beam of mass-selected nanoparticles exits the clustersource into the preparation chamber. The final lens is an einzel lens, which serves to focus the beam into a spot. Approximately 2 cm from the einzel lens sits a metal plate known as the aperture flag. The aperture flag is isolated from ground through an electrometer, which measures the current between the flag and ground. When the charged particles impinge the flag they are neutralized, generating a neutralization current measured by the electrometer. The current is a measurement of the flux of particles onto the flag and by integrating the current over time we are able to calculate the amount of particles that have landed on it. It is therefore also referred to as the deposition current and is used to optimize the deposition conditions before depositions. Below a solid part of the flag there are three circular apertures with 1, 4.5 and 9 mm diameter respectively. When depositing particles, the sample substrate is placed behind one of the apertures to have a well-defined deposition area and the current is measured on the sample instead of the flag. Knowing both the deposition area and the total number of deposited particles, it is possible to very accurately calculate the coverage of particles on the substrate.

Since the particles exiting the cluster source are at a beam potential of 500 eV they are quickly slowed down, when approaching the flag. This causes an increase in the beam spot size that can be minimized by applying a bias to the flag and sample. The bias has the same polarity as the lenses (opposite polarity of the particles) and ranges from 1.5 to 48 V. In practice this is achieved by placing a battery or a number of batteries in series between the flag/sample and the electrometer. Batteries are used because they can maintain a stable and noise-free potential at the deposition currents typically achieved (5 pA- 1 μA). The amplitude of the bias is not entirely determined by its ability to attract the charged particles, but also by its influence on the particle impact on the substrate. If the particles have sufficiently large kinetic energies they can be annealed, shatter or be implanted into the substrate upon impact [42, 43]. This regime is known as "hard landing". Meanwhile if the kinetic energy per atom is below the cohesive energy of the particles they are said to be "soft landed" [44]. The transition from hard to soft landing is not widely agreed upon, but we regard landing energies below 1 eV/atom to be in the soft landing regime. Throughout this work a 48 V bias has been used for the deposition of nanoparticles, which for all nanoparticle sizes is well within the soft landing regime, while for single atoms and small clusters a 1.5-18 V bias was used.

Deposition Procedure

Before beginning a deposition, the conditions in the aggregation zone and the lens settings have to be tuned. The conditions include a number of parameters:

- **He Flow:** Increasing He flow generally shifts the mass distribution to lighter masses.
- **Ar Flow:** Increasing Ar flow increases the sputtering rate, shifting the mass distribution to heavier masses depending on the He flow relative to the Ar.
- **Pressure:** is influenced by the Ar/He flow and independently tuned by the adjustable exit aperture of the aggregation zone. If all other conditions are held constant, increasing the pressure shifts the mass distribution towards heavier masses.
- **Temperature:** The temperature can either be room temperature or -196 °C as there currently is no way to stabilize the temperature between these values. To produce nanoparticles and clusters, the cluster source must be cooled, while single atoms can be produced at room temperature.
- **Magnetron Power:** Increasing magnetron power increases sputtering rate, its effect depends entirely on the combination of Ar/He flow.
- **Lens Potentials:** are generally easier to tune since the effects are instantaneous compared to the effects of the other tuning parameters which take time to stabilize. Tuning the lenses leads to increased deposition currents and can shift the mass distribution slightly, due to the fact that it increases the

transmission of specific masses. The lenses are a vital part of the tuning and incorrect lens potentials can reduce the current by many orders of magnitude.

The deposition conditions are tuned by measuring the deposition current on the flag while scanning the transmitted mass of the mass filter. This mass scan results in a mass profile as seen in Figure 2.5 showing the current as a function of particle mass. Each parameter is tuned individually by observing the change in the current. While general trends as described above are observed, tuning is a brute force method that is not always reproducible due to the geometrical changes of the racetrack. Therefore, previously successful settings are used as initial conditions and then tuned to increase the current for the desired mass. The temperature measurement is placed close to the liquid nitrogen shroud, which can give an incorrect temperature readout since it will be the first part to cool down. This causes drift in the mass profile throughout a deposition as seen in Figure 2.5a. Since the mass profile cannot be monitored during deposition, a mass scan is performed after deposition to check for a mass profile drift. To avoid such a drift we recently adopted a procedure of cooling the cluster source for 2-3 hours before depositing samples. As seen in Figure 2.5b the procedure significantly reduced the mass profile drift.

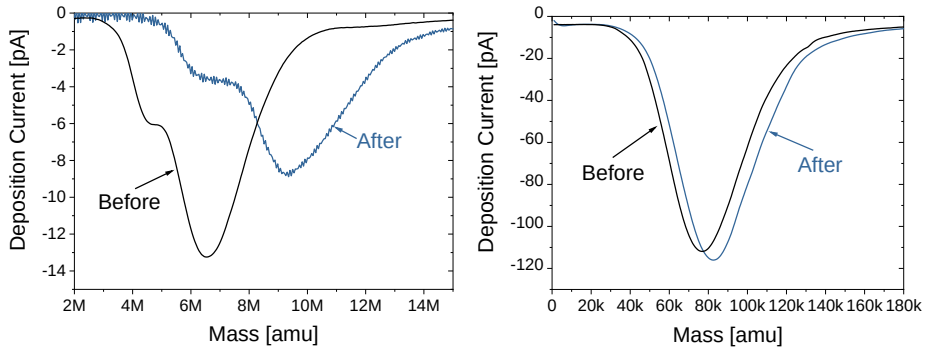

Figure 2.5: Mass scans before and after deposition: **a)** Deposition has been started as soon as the cluster source is cooled. **b)** The cluster source has been cooled for 2 hours before starting the deposition.

The goal of tuning the conditions is not only to increase the deposition current, but also to minimize the relative intensity of the double mass particles to reduce the amount of double mass particles that are deposited. Generally we aim for an order of magnitude difference between the single and double mass currents, but in practice this can be difficult and occasionally we must accept only a factor of 2 or 5 between the two.

Once a satisfactory mass profile has been acquired, the beam is blanked and the

current measurement is switched to the sample, while it is positioned behind the aperture. The beam is unblanked and the sample current is logged until the desired coverage has been achieved. The coverage is calculated concurrently using a script on the control computer. Once the deposition is finished, a post deposition mass scan is performed on the flag. The coverage is calculated by finding the number of deposited particles and multiplying by the cross-sectional area of a single spherical particle with the selected mass. Thus a total projected area covered by the particles is obtained. Coverage can subsequently be calculated by dividing the total projected area by the total deposition area which is determined by the aperture.

Ensuring Sample Homogeneity

While the final lens of the cluster source serves to focus the beam into a spot, we discovered that when depositing high coverages, non homogeneous particle distributions were obtained. This is evident in the SEM image in Figure 2.6a, which shows part of a glassy carbon disc (5 mm in diameter)that has a 20% coverage of 6 nm Pt nanoparticles. There is a very sharp cut off from the bright area, where Pt particles have been deposited and the dark area, where there are no particles. Additionally the spot only covers a very small area compared to the entire glassy carbon disc.

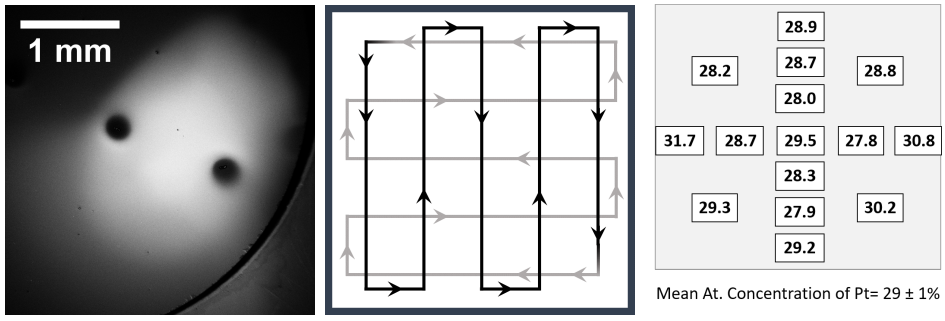

Figure 2.6: a) SEM image of the surface of a glassy carbon disc with 20% coverage of 6 nm Pt nanoparticles. **b)** Raster pattern used for creating a homogeneous distribution of particles. **c)** Atomic concentration of Pt in different spots determined by quantitative XPS analysis of a 70% coverage of 6 nm Pt particles. The particles were deposited on a 1×1 cm glassy carbon plate with the rastering pattern shown in **b**.

Together with my colleague Jakob Ejler Sørensen, I developed a method for rastering the sample in front of the beam to spread out the particles in a homogeneous distribution. In practice this was achieved by installing two computer controlled motors on the manipulators, which move the stage the sample sits in during deposition. The sample can thus be rastered in the plane perpendicular to the beam trajectory. A more elegant solution would be to raster the beam, but due to ge-

ometrical restrictions, this is not feasible. To check the effect of the rastering, a sample with 70% coverage of 6 nm Pt particles was deposited on a flat 1×1 cm glassy carbon plate. The plate was rastered with the meander pattern in Figure 2.6b moving a total of 9 mm in each direction. The raster pattern was repeated until the desired coverage had been obtained. XPS was used to characterize the sample homogeneity, by measuring different spots on the glassy carbon substrate and performing quantitative analysis of the platinum concentration. Figure 2.6c shows that a very homogeneous coverage was obtained from the rastering with an average Pt concentration of 29% ± 1%.

Rastering the sample imposes a new problem; the particles are now also landed outside the sample area onto the stage. This is because the sample is rastered, but the aperture is not. Not all of the measured charge lands on the sample and therefore the coverage calculation is incorrect. This is solved by approximating the spot size and shape of the beam from the SEM image and simulating a deposition with this beam profile and raster pattern. From this the actual deposition area can be found and thus the coverage.

2.2 X-ray Photoelectron Spectroscopy

X-ray Photoelectron Spectroscopy (XPS) is a UHV technique used to determine the chemical composition and oxidation states of the surface of a material. It relies on using X-rays to generate photoelectrons from the surface and counting the number of photoelectrons at different kinetic energies. The kinetic energy E_{kin} depends on the X-ray energy hν, the electron binding energy E_{bin} and the analyzer work function ϕ [20]:

$$E_{kin} = h\nu - E_{bin} - \phi \tag{2.3}$$

ϕ is a system specific value and is included in the operation software or can be determined using a specific standard. hν is set by the x-ray radiation, which can either be a lab source or a synchrotron source. Thus the binding energies of the emitted photoelectrons can be determined.

Each element emits photoelectrons with a characteristic set of binding energies creating a fingerprint of the atoms on the surface. Determining the chemical composition of the surface is therefore possible [20]. This requires a monochromatic x-ray source for a constant value of hν. If a synchrotron is not available, X-ray radiation is generated from a lab source consisting of a metal anode, which is bombarded with high energy electrons (10-15 kV, 20 mA) from a heated filament. The high energy electrons bombarding the surface may remove electrons from the 1s binding state of the metal. The empty state is filled by the relaxation of electrons in the $2p_{1/2}$ or $2p_{3/2}$ energy levels, resulting in the emission of X-rays with an energy corresponding to the electron energy loss. These specific transitions are denoted $K_{\alpha 1,2}$. Our lab source has two different anodes, one coated with Mg and

one coated with Al resulting in radiation with an energy of 1253.6 eV (0.7 eV full width half maximum (FWHM)) and 1486.3 eV (1 eV FWHM) respectively [20]. However there are other energy transitions available and the complete emission spectra is not trivial [45]. The probability of these transitions is lower, for instance Mg has a second line at 8.5 eV higher than Mg Kα with 9.1% of its intensity. This results in X-ray satellites in the XPS spectrum if a monochromator is not used [45].

The kinetic energy of the photoelectrons is measured with a hemispherical energy analyzer. It consists of two concentric hemispheres, slightly displaced and with a potential difference across that deflects incoming electrons into a circular path. Incoming electrons of different energies follow trajectories with different radii and scanning the potential allows different electron energies to pass through an exit slit. Alternatively a grid at the analyzer entrance slows electrons to the specific pass energy set by the analyzer potential resulting in a constant energy resolution for the entire spectrum of kinetic energies. This is called constant pass/analyzer energy mode and is the standard for operation. After passing the exit slit the electrons are detected by a secondary electron multiplier. The Omicron system is equipped with a multichannel detector with 7 electron multipliers, which can be used to scan at slightly different energies, giving a larger signal-to-noise ratio compared to a single channel detector.

Despite the X-rays penetrating deep into the sample material, XPS is a surface sensitive technique due to the mean free path of the photoelectrons which generate the signal. Figure 2.7 shows the mean free path of electrons of different kinetic energies in different materials from a number of different experiments [20].

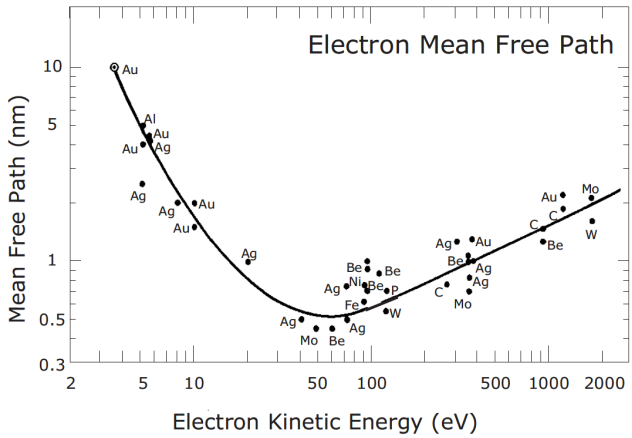

Figure 2.7: The mean free path of electrons at different kinetic energies in different materials. Reprinted from [20].

The detected photoelectrons have energies in the range 20-1400 eV, equivalent to

mean free paths on the order of 1 nm or ≈ 5 monolayers. Thus the photoelectrons contributing to distinct peaks originate close to the surface. XPS can also be used for identification of chemical states since they affect the binding energies of an atom. These can shift up to several eV, typically towards higher binding energies with increasing oxidation state [20].

The photo emission of an electron can also be followed by the relaxation of an electron at a higher energy resulting in the emission of a third electron - an Auger electron. The energy of Auger electrons is independent of the incoming X-ray energy thus easily identifiable by varying the X-ray energy. Such three-electron processes are sufficiently likely that they contribute with peaks in the the XPS spectrum [20].

Quantifying Surface Composition using XPS

The intensity of XPS peaks is proportional to the number of atoms in the sample contributing to the peak. Therefore the surface composition can be quantified by integrating peak areas for the different elements in the sample. However, the yield of photoelectrons depends on the element and electron orbital thus the peak areas must be scaled with a relative sensitivity factor (RSF) , obtained from standards or databases [45]. The RSF may also be instrument dependent, in which case they are supplied by the manufacturer. The ratio between two concentrations in the sample is given by:

$$\frac{c_1}{c_2} = \frac{A_1/RSF_1}{A_2/RSF_2} \tag{2.4}$$

where c_i is the elemental concentration, A_i is the element peak area and RSF_i is the relative sensitivity factor for the specific electron transition.

To obtain accurate peak areas it is often necessary to use peak fitting, since peaks may overlap and the background contribution must be subtracted. Peaks are fitted using a convolution of a Gaussian function, which captures the broadening from the electron detection and X-ray line shape and a Lorenzian function which captures the life-time broadening of the photoelectron emission process [46]. The background originates from inelastic scattering of the photoelectrons when they leave the sample. This gives a tail at lower kinetic energies which is best modelled by the Shirley background. This has been determined empirically and is not a model derived from physical principles [47].

Due to equipment malfunction on the Omicron UHV system, the XPS presented in this thesis was also performed on two other instruments. The XPS spectra presented in Chapter 3 were acquired on a PHI Quantera II scanning X-ray microprobe. The XPS spectra presented in Chapter 5 were acquired on the ThermoFisher Thetaprobe. Table 2.1 shows the settings for each system, all spectra were obtained using an Al K_α source.

Table 2.1: XPS settings for spectra presented in this thesis. Survey scans were used to obtain information on the different elements in the sample, while detailed scans were used to resolve specific peaks for quantitative analysis.

Instrument	Scan Type	Spot [μm]	Stepsize [eV]	Voltage [kV]	Pass Energy [eV]
Omicron	Survey	2000	1	12.5	100
Omicron	Detailed	2000	0.1	12.5	50
ThetaProbe	Survey	400	1	15	200
ThetaProbe	Detailed	400	0.1	15	200
PHI Quantera II	Survey	100	1	15	280

2.3 Ion Scattering Spectroscopy

Ion Scattering Spectroscopy (ISS) also known as Low Energy Ion Scattering (LEIS) is another UHV technique used to determine the surface composition of a sample. The technique is based on binary elastic collisions of noble gas ions on surface atoms. It is an extremely surface sensitive technique and in principle quantifiable, however this requires an extensive set of standards and has not been performed in this work. Instead ISS has been used as a tool to detect contamination, deposited particles and dispersion with a very high sensitivity as low as 0.1% of a monolayer.

The noble gas atoms are ionized and accelerated towards the surface of the sample using a sputter gun. When the noble gas ions impinge the surface they undergo binary elastic collisions with the surface atoms of the sample [20]. The reflected ions can be detected using a bipolar energy analyzer such as the hemispherical analyzer on the Omicron chamber. During the collision with the surface, 99% of the noble gas ions are neutralized, thus very few of the incoming ions actually contribute to the signal detected in the analyzer [20]. Typical incoming ion energies used for ISS are in the range of 1-8 keV using He^+, Ne^+, Ar^+ or Kr^+. In this thesis all ISS measurements were performed using 1 keV He^+ ions, 1 eV steps size and a scattering angle of 146.7° between the incoming ion beam and the analyzer. Additionally, the ion beam was rastered in a 1×1 mm area to probe a representative area on the surface. Assuming only binary elastic collisions, the relation between the incoming ion mass M_i and energy E_i, the surface atom mass M_s and the reflected ion energy E_r can be derived from classical mechanics:

$$E_r = \left(\frac{\cos\theta + \sqrt{(M_s/M_i)^2 - \sin^2\theta}}{1 + M_s/M_i} \right) \times E_i \tag{2.5}$$

where θ is the scattering angle and is instrument specific as it depends on the instrument geometry. Meanwhile M_i and E_i are controlled by the user so M_s can be determined. However the binary collision model is not completely accurate and some inelastic processes may occur during the collision leading to a peak shift to-

wards lower energies compared to the values calculated from equation 2.5.

Heavier noble gases like Ar^+ and Kr^+ will cause significant damage to the surface affecting the surface structure and possibly composition. Instead He^+ is used to provide a "non-destructive" characterization technique that can be performed at different stages of sample synthesis without affecting the synthesis procedure. Due to the low mass of He, the energy resolution of ISS at higher masses becomes very poor considering equation 2.5. As a consequence, distinguishing elements such as Au and Pt is not possible. This is a compromise I have chosen to accept since XPS can be used to distinguish between elements of similar mass.

The extreme surface sensitivity of ISS is in part due to the large neutralization probability since most atoms passing through the first atomic layer will be neutralized so even if they are scattered back to detector from a subsurface layer, they are not detected [20]. Additionally the scattering cross sections are large so not many atoms pass through the first atomic layer. It is however possible to have some contributions from the subsurface from ions that are neutralized. These pass through the surface, are scattered by a subsurface layer and reionized when leaving the surface. This process cannot be described by classical physics and there are no models accurately describing it [20].

2.4 Electron Microscopy

The term electron microscopy covers a number of different imaging techniques including Scanning Electron Microscopy (SEM) , Transmission Electron Microscopy (TEM) and Scanning Transmission Electron Microscopy (STEM) . Common for each of these techniques is that they are used to visualize structures on the nanoscale with resolutions down to 0.8 Å. Achieving resolutions on this scale is possible due to using electrons as the probe instead of visible photons. The wavelength of visible photons is too large to resolve structures smaller than approximately 300 nm according to the Rayleigh Criterion [48]. Instead the wavelength of electrons can be tuned by accelerating them to higher energies to such a degree that the electron wavelength is no longer the factor limiting the resolution (using the De Broglie equation a 100 keV electron has a wavelength of 0.004 pm ignoring relativistic effects)[48].

When electrons interact with a material they can create a large number of secondary signals as seen in Figure 2.8. Each of these signals give information on different properties of the sample e.g. chemical, elemental or structural information and can be detected in the different types of electron microscopy [48].

A common feature for the electron microscopy techniques is the ability to use the emitted characteristic x-rays to determine the elements in the sample. This

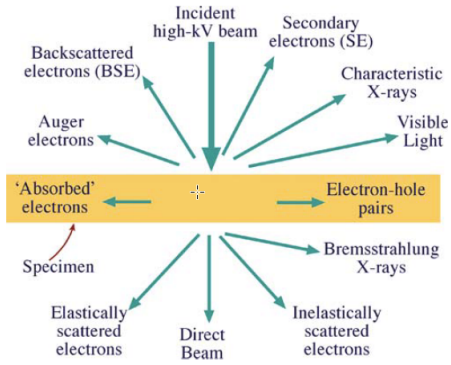

Figure 2.8: High energy electrons interacting with a sample material creates different secondary signals that can give different types of information. Adapted from [48]

technique is known as energy dispersive x-ray spectroscopy (EDS) . It is especially useful in SEM and STEM since here local elemental information can be obtained, allowing for mapping of the atomic elements in the sample [48].

2.4.1 Scanning Electron Microscopy

In scanning electron microscopy a converging electron beam of 5-30 keV electrons is scanned over the sample in a rastering motion. The secondary and/or backscattered electrons are detected using detectors placed to the side of and above the sample respectively. SEM can be used to image nanoparticles by detecting the secondary electrons, which provide topographical information due to their low mean free path. A consequence of their typical energies < 50 eV [48]. Nanoparticles will emit more secondary electrons than their support and therefore appear bright on a darker background. SEM imaging was performed on the FEI QuantaFEG with an Everhart-Thornley detector to detect secondary electrons, this leads to a maximum resolution of 2 nm [49].

2.4.2 Transmission Electron Microscopy

In transmission electron microscopy a broad parallel beam of high energy electrons passes through a thin electron transparent sample. All TEM imaging was performed with a primary electron energy of 300 keV. The direct transmitted beam is detected by an electron detector and several different types of contrast are created. First there is amplitude contrast, which includes mass-thickness and diffraction contrast. Mass-thickness contrast arises from incoherent elastically scattered electrons being scattered to angles that are not included in the image generation [48]. It provides information on the mass and thickness of the sample since these parameters strongly influence the scattering cross section of incoherent elastically

scattered electrons. Diffraction contrast is generated from electrons that are Bragg diffracted by a crystalline sample to such high angles that they are not included in the image generation [48]. Another type of contrast mainly used for high resolution imaging is phase contrast, which arises from the interference between coherent elastically scattered electrons and the unscattered electrons transmitted through the sample [48]. Phase-contrast can provide atomic resolution of lattice planes if the microscope aberrations are reduced significantly. TEM imaging was performed on the FEI Titan E-cell 80-300 ST TEM with a post objective lens spherical aberration corrector from CEOS company which has a maximum resolution of 0.8 Å. The TEM images in this thesis are bright field images meaning that heavy/thick parts of the sample will appear darker. If the images display phase contrast, the dark or bright parts cannot be directly correlated to atoms, but instead the sample structure is represented by the periodicity of the contrast. TEM imaging was performed at DTU and Haldor Topsøe A/S.

Since the structure of nanoparticles depends on the surrounding gas [20, 24], properly characterizing the structure of nanoparticles under reaction conditions requires in-situ imaging. In-situ TEM can be performed in an enviromental TEM (ETEM) , where differential pumping allows for a gas pressure of several mbars around the sample [50]. Additionally, by using micro electro-mechanical systems (MEMS) based TEM chips like the DENS Wildfire chip allows for heating the sample with minimal drift compared to traditional bulk heating holders [51].

2.4.3 Scanning Transmission Electron Microscopy

Scanning transmission electron microscopy using a high angle annular dark field (HAADF)detector is a combination of SEM and TEM. A narrow collimated beam of electrons converge into a small probe at the sample. The probe is rastered across the sample and the corresponding intensity of incoherent elastically scattered electrons scattered to angles > 50 mrad is measured by the HAADF detector [48]. Detecting these electrons generates a Z-contrast that can be tuned by changing the camera length of the detector. STEM imaging was performed with a FEI Titan Analytical 80-300 ST TEM equipped with a pre objective lens spherical aberration corrector and using a primary electron energy of 300 keV. Under optimal imaging conditions this allows for a resolution of 0.8 Å [49], sufficient for achieving atomic resolution of nanoparticles and even single atoms. Due to Z-contrast, heavier elements will appear brighter on STEM HAADF images.

Avoiding Beam Induced Effects

Interaction of the high energy electrons with the sample provides contrast for imaging, but can also lead to beam induced alterations of the sample. One commonly observed effect in all types of electron microscopy is carbon growth from the cracking of hydrocarbons. Additionally in TEM and STEM the electron beam can induce changes in particle structures [52] and affect the imaging resolution in dif-

ferent gases in ETEM [50, 53]. Therefore care should always be taken to avoid beam induced effects in electron microscopy. In practice this was done by using the minimal beam current and dose rate necessary to achieve sufficient signal-to-noise ratios and by checking reference areas that were not previously illuminated by the beam [50, 53].

Other Microscopy Techniques

Apart from the electron microscopy techniques, another type of microscopy that is useful for visualizing structures with atomic resolution is Scanning Tunneling Microscopy (STM) . An STM rasters a sharp W or Pt/Ir tip less than 1 nm above a conducting sample. A bias voltage is applied between the tip and sample that due to quantum mechanics, allows electrons to tunnel from one to the other [20]. The current is sent to the feedback loop in the computer which controls the piezoelectric tubes that move the tip. Since the tunneling current depends exponentially on the gap distance, the smallest changes in distance can be detected. An STM can be run in two modes, constant current, where the tip moves to maintain a constant current while scanning across the sample or constant height in which case the tip is kept at a constant height and the variations in current are measured. In practice this maps out the density of states around the Fermi level[20]. This results in images with atomic resolution of extremely flat samples, however if the surface is rough then the achievable resolution drops significantly.

2.5 Measuring Catalytic Performance

Testing the catalytic performance of the model catalysts deposited with the cluster source is non-trivial due to the loadings (10-1000 ng) that can be achieved with the cluster source. Since electrochemical catalysis consists of the transfer of electrons, this can be measured accurately down to very low loadings. However, contaminants and mass-transfer effects become increasingly detrimental to catalyst performance at these loadings. Thermochemical catalysis testing of low loadings is also challenging due to the large reactor volumes, which make the small amount of reaction products impossible to distinguish from the background. However if the reactor volume is reduced then the reaction products may amount to a detectable concentration. This is the working principle of the microreactor developed in our group [54], which can be used to measure thermochemical catalysis activity from cluster source samples.

Throughout the thesis I will use the term catalytic performance to cover both catalytic activity and catalyst stability as these both are important factors for the application of a catalyst. I have not performed any catalytic performance testing, but have been a part of planning experiments and treating data from the different measurements in close collaboration with my colleagues. I will briefly present the basics of the different testing methods below.

2.5.1 Electrochemical Activity Testing

Electrochemical reactions are redox reactions involving the transfer of electrons between a liquid electrolyte and a solid electrode. A redox reaction can be split into two half-cell reactions: the reduction reaction, which happens at the cathode and the oxidation reaction, that takes place at the anode. By applying a potential between the two electrodes it is possible to shift the reaction equilibrium. Decoupling the two half cell reactions requires the introduction of a third electrode, a reference electrode (RE) as seen in Figure 2.9.

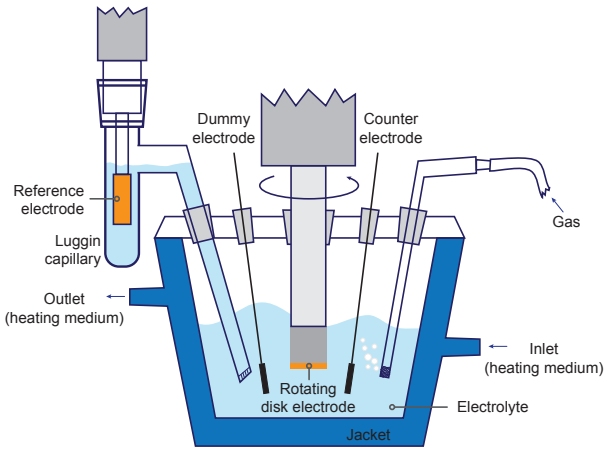

Figure 2.9: Sketch of a three electrode cell used for electrochemical testing of model catalysts. Image courtesy of Taus Holtug.

The catalyst material is deposited on the working electrode (WE) , which is mounted in a rotating disk electrode (RDE) . This is where the half cell reaction of interest occurs. The other occurs at the counter electrode (CE) , while the reference electrode is in electrical contact with both the working and counter electrodes. The potential of the WE is measured against the known potential of the RE, while the current is measured between the working and counter electrodes. Thus the current generated by the electrochemical reaction can be measured against the potential that is used to drive it. The RDE setup is used to increase the convection of electrolyte to the WE, since the mass transport rate can be rate limiting for the reaction. When initially inserting the WE, the potential is not controlled since there is no contact through the electrolyte to the RE. The potential the WE experiences initially is in this case the open circuit voltage which depends on the setup parameters and can be harmful to the catalyst. Therefore a dummy electrode that is connected to the WE is inserted first. This establishes the potential of the WE that is then inserted under potential control.

The standard electrochemical testing procedure is cyclic voltammetry (CV) where the potential of the WE is scanned from the lower potential limit to the upper potential limit and back while the resulting current is measured. This is repeated multiple times to monitor the short term catalyst stability. All potentials in the thesis are reported in terms of the reversible hydrogen electrode (RHE).

2.5.2 Thermochemical Testing

Thermochemical catalysis measurements were performed in the microreactor, where gas is flowed in using flow-controllers through channels 1 and 2 as seen in the sketch in Figure 2.10. These channels join to one and mix the gas in the meander pattern before entering channel 3. Here part of the gas (<10 %) flows through a capillary to the reactor volume (indicated by the arrow), the rest flows out through the channel exit. This channel serves as a gas reservoir that feeds gas to the reactor volume and the outlet is used to set the pressure in the reservoir using a pressure controller. Thus the flow rate through the reactor volume cannot be changed by changing the flow rate of the incoming gasses, but instead the flow rate depends on the temperature and pressure. Additionally this limits backflow of gas from the reactor volume. After passing through the reactor volume, the gas exits through a small capillary in channel 4 and is lead to a quadrupole mass spectrometer. The capillary ensures that the pressure is reduced sufficiently from the 0.1-2 bar in the reactor. The reactor has a volume of 236 nL meaning that even the small loadings deposited in the cluster source can produce a significant partial pressure of products to be detected. The reactor volume is heated using resistive heating contacts on the backside of the reactor. The reactor volume temperature is measured using both a resistance temperature detector (RTD) and a thermocouple. The microreactor has been developed over the last 10 years and additional information can be found in: [55–57]

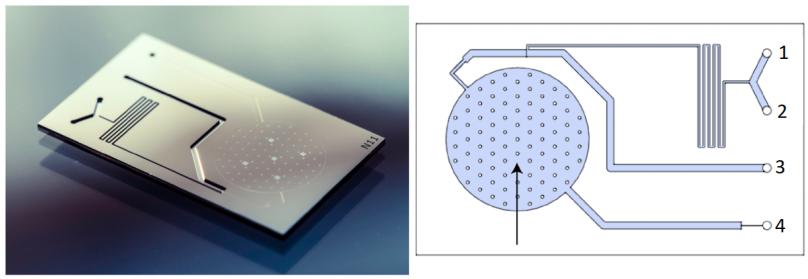

Figure 2.10: Picture and sketch of the microreactor developed in our group. The arrow points to the reactor volume where the catalyst material is deposited.

2.5.3 Scanning Flow Cell

Catalyst stability is often tested by running reactions for longer periods of time in both electrochemical and thermal catalysis measurements. However, during an electrochemical stability measurement it is not possible to distinguish between catalyst dissolution and other degradation mechanisms since they all result in a decrease in current over time. One way to distinguish between the two is using a dedicated setup to measure dissolution. This was done in collaboration with colleagues at Helmholtz-Institute Erlangen-Nürnberg for Renewable Energy, Forschungszentrum Jülich which are now located at the Friedrich-Alexander-University Erlangen Nürnberg. They have developed a scanning flow cell with online inductively coupled plasma mass spectrometry (SFC-ICP-MS) [58–60].

Measuring dissolution in a standard three electrode cell requires removal of small electrolyte volumes at different stages of the experiment and then subsequent ICP-MS measurements. This procedure is simplified by the SFC-ICP-MS setup seen in Figure 2.11 which is placed on top of the desired WE. Electrolyte flows through the CE to the WE where the mass-selected particles are deposited. The connection to the WE is sealed with a silicone ring to determine the WE area(1 mm diameter). After reacting at the WE the electrolyte flows to the ICP-MS where the amount of dissolved catalyst can be measured extremely accurately (< 0.1 parts per billion). In this way it is possible to measure even the slightest dissolution while performing electrochemical measurements.

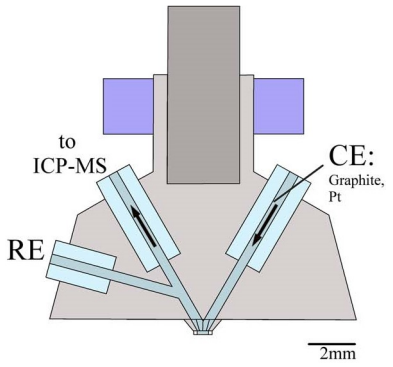

Figure 2.11: Schematic of the SFC-ICP-MS used for dissolution testing. Adapted from [60].

Chapter 3

Platinum Dissolution During the Oxygen Reduction Reaction

One of the challenges in polymer electrolye membrane fuel cells (PEMFC) is the stability of the platinum alloy catalyst that accelerates the oxygen reduction reaction (ORR). The major cause of degradation is the dissolution of the catalyst material in the acidic electrolyte due to the large range of potentials experienced during start/stop and operation. This chapter describes a collaborative work, which examines how varying the edge-to-edge interparticle distance affects dissolution for two Pt catalysts. One is a model system of mass-selected 1.5M amu (≈6 nm) Pt nanoparticles on a flat glassy carbon support, which is termed the 2D samples due to a relatively flat structure. The other is an industrially relevant catalyst of 2 nm Pt nanoparticles on a Vulcan carbon support, which is termed the 3D samples. The dissolution is measured using the SFC-ICP-MS setup described in Chapter 2. The Pt densities in the two catalysts are compared through the mean edge-to-edge interparticle distance. Additionally, the 2D samples are used to understand the effect of nanoparticle size on the Pt dissolution.

This work is the result of two collaborations, the first with colleagues at Forschungszentrum Jülich, Friedrich-Alexander-Universität Erlangen-Nürnberg, University of Copenhagen, Toyota Central R&D labs, University of Bern, Carl von Ossietzky University of Oldenburg and the Technical University of Braunschweig. This resulted in the submission of a manuscript titled "The Dissolution Dilemma for low Pt Loading Polymer Electrolyte Membrane Fuel Cells", which is currently submitted to Advanced Energy Materials. The second collaboration with co-workers at Forschungszentrum Jülich/Friedrich-Alexander-Universität Erlangen-Nürnberg, which resulted in the manuscript titled "The Particle Size Effect on Platinum Dissolution: Considerations for Accelerated Stability Testing of Fuel Cell Catalysts".

This manuscript is currently in review at ACS Catalysis. This chapter is based on these manuscripts.

I will focus on describing the work that I have contributed to and briefly describe the parts that I have not, further details can be found in the appended papers. I have been responsible for synthesizing the 2D samples using the Nanobeam cluster source and characterizing them with ISS. I visited Erlangen to help determine the XPS measurement procedure and have carried out all the data treatment of the XPS spectra on 2D samples. Additionally I have performed SEM and STEM measurements and data treatment and developed the simulation of the interparticle distances for the 2D model system. Daniel Sandbeck wrote the introduction and SFC-ICP-MS results parts of the manuscripts, while I contributed with the synthesis, characterization and simulation results for the 2D samples and together we revised the manuscripts.

3.1 Fuel Cell Catalysis

While the hydrogen oxidation reaction (HOR) in a PEMFC proceeds rapidly, the ORR is slow and requires a suitable catalyst to reduce the overpotential [12], which will lower the potential generated in a fuel cell. Currently the state-of-the-art catalysts for the ORR are Pt-transition metal alloys that have achieved higher activities than pure Pt [12, 29, 61–64]. These are typically loaded on to a high surface area carbon support, creating what is known as the catalyst layer. The total amount of catalyst, is known as the catalyst loading. Pt catalysts on carbon (Pt/C) have already been employed in PEMFC vehicles like the Toyota Mirai [19]. However the high price of noble metals constitutes a significant part of the fuel cell price when the production of fuel cells is scaled up to industrial levels [65–67]. Additionally, Pt is a very scarce material so scaling up requires a significant amount of the global Pt production, limiting the number of vehicles that can be produced with the current PEMFC Pt usage [68]. Thus there is a need for reducing the Pt loading in the PEMFCs.

3.1.1 Challenges in Reducing Platinum Usage

There have been several approaches to reducing the Pt loading in PEMFCs. First, the development of more active catalysts such as the Pt-alloy catalysts [12, 29, 61–64] and shape controlled nanoparticles [23, 69]. Increasing catalyst activity leads to lower catalyst loadings and is therefore the focus of considerable amounts of catalysis research. Meanwhile, dispersing the catalyst as nanoparticles and structuring them for increased activity increases catalyst utilization. Another approach has been to reduce the thickness of the catalyst layer. Unfortunately, this is detrimental to catalyst activity at high current densities in membrane electrode assemblies (MEA) [67, 68]. However, activity is not the only relevant catalytic property to consider when attempting to lower catalyst loadings. Stability is also important as

it affects the lifetime of PEMFCs and understanding the stability and degradation phenomena in the existing state-of-the-art catalysts can help with the development of future catalysts [70]. The degradation of Pt based catalysts in PEMFCs is a combination of several effects including carbon corrosion, Ostwald ripening, particle coalescence, particle detachment and dissolution[71]. Of these, Pt dissolution is the primary degradation mechanism and therefore we have focused on studying this issue.

Interparticle Distance Effects

Previous studies using online dissolution measurements with a SFC-ICP-MS showed that reducing the thickness of the catalyst layer lead to a higher specific dissolution normalized to the electrochemically active surface area (ECSA) [72, 73]. This was argued to be caused by a shift in the Nernst potential for dissolution due to the reduced diffusion length, determined by the catalyst layer thickness. The Nernst potential is shifted because it depends on the concentrations of catalyst ions on the support surface and in the surrounding electrolyte. When the concentration in the surrounding electrolyte drops due to diffusion, the dissolution increases. Thus without further development of the catalyst layer material, reducing the catalyst layer thickness is not a viable way to decrease catalyst loadings. Instead a new approach consists of decreasing the catalyst density in the catalyst layer [74, 75]. This has been reported to decrease ORR activity, but the effect on the degradation mechanisms remain unknown[76, 77]. Therefore we have studied how Pt dissolution depends on the Pt density for constant catalyst layer thickness. We have used two different catalysts: a 2D model system and a 3D industrially relevant catalyst. The 2D samples allow for increased comparison of characterization results with simulations of interparticle distances, meanwhile the 3D catalyst can be compared to the catalysts used in real PEMFCs. The two systems are compared through the mean edge-to-edge interparticle distance parameter, which is used as a descriptor for the catalyst density. Pt nanoparticles were used instead of Pt-alloy catalysts for increased simplicity in the dissolution process. Additionally, having an understanding of the dissolution of pure Pt may be advantageous if new Pt-based alloys are found to posses even higher catalytic activities in the future.

Particle Size Effects

Decreasing the size of the catalyst particles to a few nanometers increases the utilization of the expensive non-abundant materials, ultimately increasing the mass activity (mA/mg_{Pt}). Additionally, the increased dispersion of the catalyst material helps to alleviate issues of O_2 mass transport losses under high power PEMFC operation [67, 78]. When decreasing particle sizes to less than 10 nm, the exact size of the nanoparticle can affect its activity and stability. Unfortunately, previous studies on particle size effects are full of discrepancies. While some studies show a maximum mass activity for particles of 2-5 nm, others show a continuous decrease

in mass activity for increasing particle size[62, 79–84]. The presence of a maxima has been attributed to a minimum adsorption strength of oxygenated species on terrace sites at a particular particle size [79–82]. Further studies on the specific activity (mA/cm_{Pt}) and thus intrinsic activity have shown increased activity for increasing particle sizes approaching bulk Pt [62, 81, 82, 84], while other show no trends within their margin of error [85, 86]. The trend is associated with decreased poisoning by oxygenated species due to decreased oxophilicity for larger particles. Despite the trend of intrinsic activity indicating that larger particles are more active, the mass activity is the cost dominating factor and therefore nanoparticles are necessary to meet PEMFC demands. Previous reports on particle size effects are also ambiguous with regards to stability. Some report decreasing stability for decreasing particle sizes [62, 82, 85], while others report that there is no size dependency [86, 87]. Common for these reports is a significant spread in their size distributions depending on particle size, which is common for procedures that utilize thermal annealing to increase particle size. Furthermore a study using ex-situ ICP-MS showed that the particle size effect of dissolution depended on the applied potential during the testing protocol [88].

Due to the lack of firm conclusions on the particle size effect of Pt dissolution we have studied this using the 2D samples. The Nanobeam cluster source can create particles with a very narrow size distribution, which is ideal for this type of study. To avoid effects of interparticle distance on the observed dissolution, the mean interparticle distance was kept constant across the different particle sizes.

3.2 Simulation of Interparticle Distance

It is obvious that the density of catalyst in the catalyst layer and interparticle distance are related, however the conversion from one to the other is not trivial. Since we wish to study the effect of the interparticle distance on dissolution it is necessary to obtain an estimated distance from the density. When particles are deposited with a cluster source they land in random positions on the substrate surface [75]. Therefore, it's possible to simulate the particle positions for different particle sizes and coverages. From these simulations the interparticle distances for all particles can be found. Therefore I developed a simulation to obtain an estimate of the interparticle distance for the samples prepared with the Nanobeam cluster source. Since the positions are random, the particles do not have the same interparticle distance to their nearest neighbour, but instead there is a distribution of interparticle distances to the nearest neighbour. The most suitable parameter to describe the distribution is the mean interparticle distance to the nearest neighbour.

The simulation begins with determining the size of the simulated area from the number of simulated particles N, the radius of the particles r_p and the coverage C.

$$A = \frac{N\pi r_p^2}{C/100} \tag{3.1}$$

Next, two lists of positions, one for the x-position and one for the y-position are generated randomly. The length of the lists is set by the number of particles N. The positions are random in a range decided by the square root of the simulated area in nanometers, multiplied by 10 to obtain an accuracy of 1 Å:

$$x = \begin{bmatrix} x_1 = Random(0 : \sqrt{A} \cdot 10) \\ x_2 = Random(0 : \sqrt{A} \cdot 10) \\ \vdots \\ x_N = Random(0 : \sqrt{A} \cdot 10) \end{bmatrix} y = \begin{bmatrix} y_1 = Random(0 : \sqrt{A} \cdot 10) \\ y_2 = Random(0 : \sqrt{A} \cdot 10) \\ \vdots \\ y_N = Random(0 : \sqrt{A} \cdot 10) \end{bmatrix} \tag{3.2}$$

Then the center to center distance to the nearest neighbour is found for each particle. Divided by 10 to convert back to nanometers and the particle size is subtracted from the center to center distance to obtain the edge-to-edge interparticle distance. To avoid boundary effects I have not found the interparticle distances for particles within a certain distance from the edge, however they are included for the interparticle distance calculation for particles further away from the edge. The average of the nearest neighbour interparticle distances is the mean interparticle distance of the simulation. For each sample I have simulated 2000 particles 5 times to obtain a standard deviation of the mean interparticle distance. The distribution of interparticle distances for 2000 particles in a sample with 6 nm particles and 1% coverage is shown in Figure 3.1. All values below 0 are caused by particles overlapping to different degrees and are therefore set to 0.

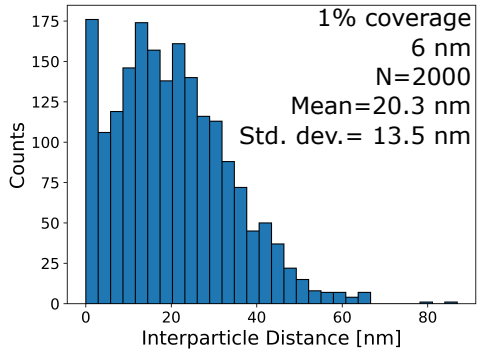

Figure 3.1: The simulated distribution of interparticle distances for 2000 6 nm particles at a coverage of 1 %. The mean interparticle distance is 20.3 nm with a standard deviation of 13.5 nm.

The alternative to simulating the interparticle distance, is assuming that the particles are evenly spaced and dividing a certain area A by the number of particles in that area N. This gives the area per particle that can be translated into a

distance between particles and subtracting the particle size d_p then results in the interparticle distance:

$$d = \sqrt{\frac{A}{N}} - d_p \tag{3.3}$$

This is the state of lowest entropy for a system and will not occur in practice. Therefore this approach consistently overshoots the interparticle distance, but for some systems where the simulations are not feasible, this is the best approach.

3.3 2D Mass-Selected Sample Preparation

The well-defined 2D samples are called 2D because they are flat compared to the industrially relevant 3D catalytic systems, however it is not to be compared with the properties of two-dimensional materials. The 2D samples consist of mass-selected Pt particles on a 1×1 cm glassy carbon plate. The samples were prepared in the Omicron UHV system using the Nanobeam cluster source. First, the glassy carbon plates were sputtered for 10 minutes with 1 keV Ar^+ ions at a sample current of about 1 μA. This cleans off any adventitious carbon that comes from the sample being in air before entering the UHV system. After cleaning, the surface was characterized by ISS to check that there were no contaminants. Next, the Pt nanoparticles were deposited with the desired masses corresponding to equivalent particle sizes of (2-10 nm) and coverage (1-70 % of a monolayer) using a sample bias of 48 V, well within the soft-landing regime. The samples were rastered during deposition to cover the entire glassy carbon plate with a homogeneous coverage. This was done using the meander raster pattern shown in Figure 2.6b with the side length of the pattern being 9 mm. The samples were again characterized with ISS before being removed from the UHV chamber and placed in a sealable container for shipment to Erlangen. In Erlangen they were first characterized with XPS before performing the dissolution measurements. Two different sets of samples were prepared, one set for the interparticle distance study and one set for the particle size effect study.

Interpartical Distance Samples

The interparticle distance samples were all prepared by depositing 1.5M amu Pt nanoparticles with an equivalent particle diameter of 6 nm. This particle size was chosen to allow for SEM imaging of the particles on the glassy carbon plates to validate the simulations of interparticle distances. The samples were prepared using similar deposition conditions to minimize the difference in particle shapes from sample to sample. To prepare a spread of interparticle distances, 9 samples with different coverages were made as shown in Table 3.1. The spread in coverages resulted in interparticle distances from 20.7 to 0.1 nm.

Table 3.1: Coverage and simulated interparticle distances for the samples prepared for the interparticle distance study with 6 nm Pt particles. The deposition conditions were approximately 10 W magnetron power, Ar flow: 35 ml/min, He flow: 15 ml/min and 0.09 mbar in the aggregation zone.

Coverage [% of a monolayer]	1	2	5	10	20	30	50	60	70
Simulated Mean Interparticle Distance [nm]	20.7 ±0.3	13.0 ±0.2	6.4 ±0.1	3.1 ±0.1	1.3 ±0.1	0.6 ±0.1	0.2 ±0.1	0.1 ±0.1	0.1 ±0.1

Particle Size Effect Samples

For the particle size effect study, the samples were prepared with varying coverages and particle sizes to maintain a constant mean interparticle distance across the different samples. The coverages were determined from the interparticle distance simulations using the particle sizes and a desired interparticle distance of 6 nm. The particle mass, size, coverage and interparticle distance are shown in Table 3.2. Since the particle sizes vary from sample to sample, the deposition conditions were different for each sample.

Table 3.2: Particle mass, size, coverage, simulated mean interparticle distance and standard deviation of interparticle distance distributions for the samples prepared for the particle size effect study.

Particle Mass [amu]	65k	185k	430k	1.5M	2.3M	3.45M	6.7M
Equivalent Particle Diameter [nm]	2	3	4	6	7	8	10
Coverage [% of a monolayer]	1.2	2.1	3.2	5	6.1	6.9	8.6
Simulated Mean Interparticle Distance [nm]	6.5 ± 0.1	6.3 ±0.2	6.1 ±0.1	6.3 ±0.1	6.2 ±0.1	6.1 ±0.1	6.2 ±0.1
Standard Deviation of Distribution [nm]	4.4	4.7	4.8	5.7	5.8	6.2	6.8

As Table 3.2 shows, the mean interparticle distance can be kept constant for different particle sizes by tuning the coverage. However, the standard deviation of distributions increases slightly with increasing particle size due to an increasing tail at larger interparticle distances.

3.3.1 3D Sample Preparation

The Pt/Vulcan 3D samples were prepared using the toolbox approach previously reported by Arenz and co-workers [89]. First a suspension of colloidal 2 nm Pt nanoparticles are prepared via an ethylene glycol route. Next, the nanoparticles are immobilized on a vulcan carbon (Vulcan XC72R) support. The loading of Pt on Vulcan carbon was varied by varying the ratio of Pt to carbon in the immobilization step. The loading was determined by digestion of aqua regia and UV-Vis measurements. The mean interparticle distance for the 3D samples was calculated assuming an evenly spaced distribution (Equation 3.3) of particles since simulations of interparticle distances for this type of material is unfeasible. The catalyst powders were used to prepare inks using a previously reported method with slight modifications [90] to enable proper dropcasting onto the GC plates. The Pt/Vulcan catalyst was mixed appropriately with the KOH and isopropanol to obtain 10 μg carbon per cm^2 after dropcasting to maintain a constant catalyst layer thickness. For more details on the 3D sample synthesis and dropcasting, see the appended paper [91].

3.4 Characterization

The simulation of interparticle distances assumes a homogeneous coverage across the entire sample. Thus for the simulations to be comparable to the 2D samples and for multiple measurements on the same plate, the entire 1×1 cm glassy carbon plate must have a homogeneous coverage. This sparked the development of sample rastering. I travelled to Erlangen to set up an XPS measurement procedure with multiple spots on the sample to check the homogeneity of the coverage. A representative overview is given in Figure 2.6c. Rastering the sample lead to a homogeneous coverage with a relative standard deviation of about 3%. The rastering technique introduces an uncertainty in the absolute coverage as previously described. Therefore the coverages of the 6nm Pt interparticle distance samples were quantified using the Pt 4f XPS peak (example in Figure 3.5inset). Figure 3.2 shows that the atomic concentration scales linearly with coverage up until 20-30 % coverage, confirming the relative coverages of the samples. Above 30% coverage the signal intensity deviates from linearity due to increasing overlap of particles.

The absolute coverages were checked by acquiring SEM images of the lowest coverages (1,2,5 %) of the interparticle distance samples, shown in Figure 3.3. The particles in each image were counted on 3 images of each coverage and resulted in coverages of 0.98±0.05%, 1.84±0.05% and 4.1±0.1% respectively. This is close to the target coverages given the small sample size compared to the entire glassy carbon plate. Similar analysis was not viable for higher coverages, since particle overlaps start to become increasingly frequent and the SEM cannot resolve particles too close to one another.

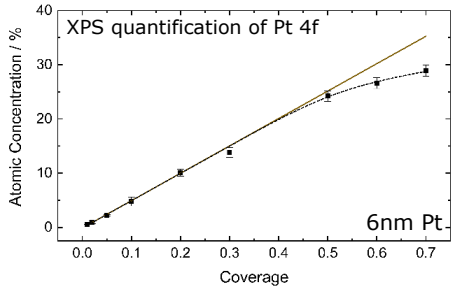

Figure 3.2: The atomic concentration of Pt for the samples used to study the interparticle distance effect on dissolution. The yellow line is a linear fit to the atomic concentrations for coverages up to 20% of a monolayer. The dashed black line is a guide to the eye. Reprinted from [91].

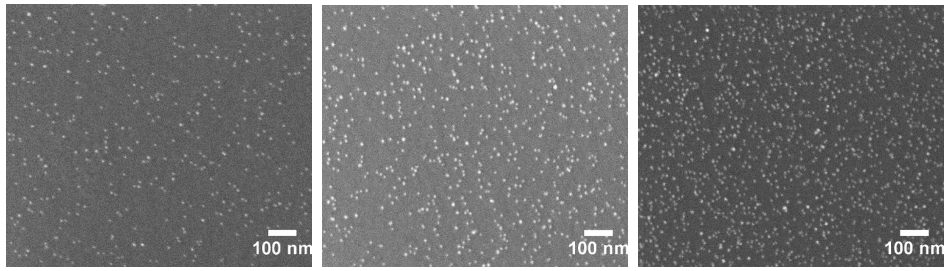

(a) 1% **(b)** 2% **(c)** 5%

Figure 3.3: SEM images of the 2D samples of 6 nm Pt particles on glassy carbon plates with **a)** 1%, **b)** 2% and **c)** 5% coverage. Adapted from [91].

I marked the center of each particle in the SEM images to obtain a list of particle positions similar to that generated in the simulation. The particle positions were treated in a similar fashion to obtain interparticle distances from the SEM images to validate the simulations. The comparison, shown in Figure 3.4 clearly shows that the simulations give a mean interparticle distance close to the measured value. Additionally, it is evident that the evenly spaced calculation is much less accurate. XPS revealed that the samples were clean with no significant contamination present on the surface. Figure 3.5 shows a representative spectrum of a sample with 70% coverage of 6 nm Pt particles on a glassy carbon plate, which only displayed peaks of O, Pt and C.

The particle size was confirmed by depositing 1.5M amu Pt particles on a 3 mm Cu TEM grid with lacey carbon (Agar Scientific). The coverage was kept at 2% of a monolayer to avoid overlapping particles. I acquired STEM images of the Pt particles and treated them with thresholding in the ImageJ software. The "Ana-

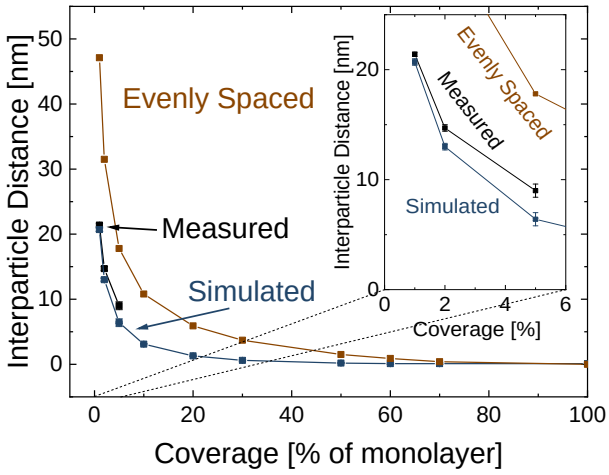

Figure 3.4: Measured, Simulated and Evenly Spaced interparticle distances plotted vs. coverage for the 6 nm Pt particles used for the interparticle distance study. Adapted from [91].

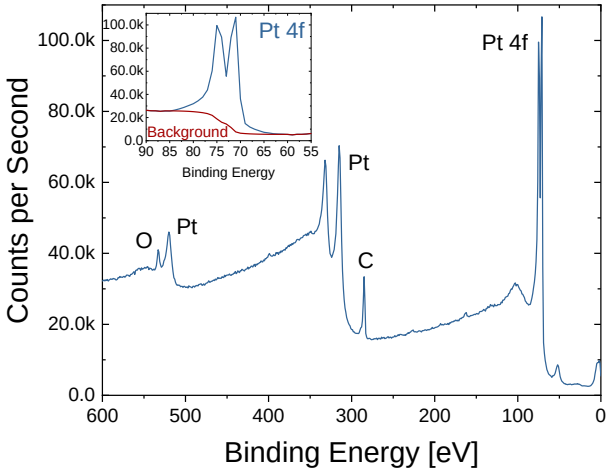

Figure 3.5: XPS spectum for a 70% coverage of 6 nm Pt particles on a glassy carbon plate. The inset shows the Pt 4f peak and Shirley background used for quantitative XPS analysis. Adapted from [91].

lyze Particles" function was used to find the projected area of each particle, which was converted to a particle diameter assuming spherical particles. A representative STEM image and the particle size distribution histogram are shown in Figure 3.6. The STEM images shows the white Pt particles on the dark C background. There

are two distributions in the particle size histogram in Figure 3.6c. One for the single mass particles at 6.5 nm and one for the double charged double mass particles at 8.4 nm. Nonetheless since there are far less double mass particles, this distribution can be disregarded and the particles are found to have a mean diameter of 6.5 ± 0.4 nm. The particles have a variety of shapes, which means that the spherical particle shape assumption is not completely accurate. This leads to a discrepancy between the equivalent particle size of 1.5M amu Pt particles and the measured 6.5 nm Pt particles. The width of the size distribution is also affected by the different shapes observed in the STEM images.

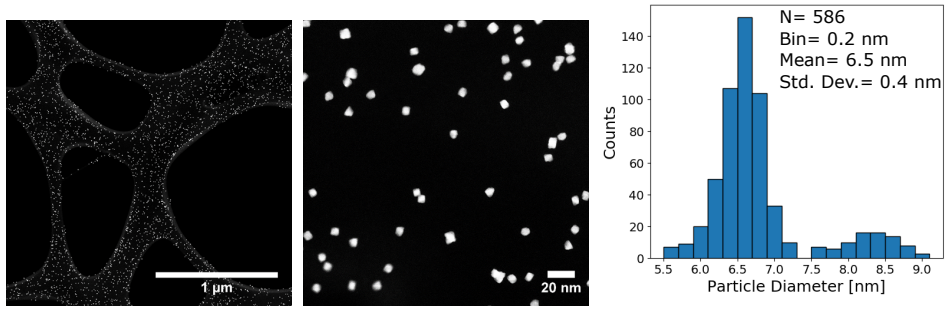

(a) **(b)** **(c)**

Figure 3.6: a) An overview STEM image of the Pt particles on the lacey C grid. **b)** Representative close-up STEM image of 6 nm Pt particles. **c)** Particle size distribution for 586 Pt nanoparticles measured using the ImageJ software. Adapted from [91].

For the particle size effect study, the particles varied in size and therefore I deposited particles of the same masses on Cu lacey C TEM grids and acquired 10 STEM images of each size for a total of at least 100 measurable particles. All the images were acquired with a pixel size of 0.1 nm. The size distributions for the seven different sizes are shown in Figure 3.7a.

The particle sizes are in agreement with the equivalent particle size for all except the 6.7M amu/10 nm particles, which are shown in Figure 3.7b. Here the particle size is considerably larger and the structure is different from the other sizes with small variations in contrast visible on some of the particles. The increase in size compared to the expected size is likely due to a flattening of the particles to lie on the C support, since no narrow particles are observed. Alternatively, as the mass of the particles must be 6.7M amu, the density of Pt in these particles is different. This particle size is on the upper limit of what can be deposited with the cluster source and it may be the agglomeration of multiple smaller particles. Notice that each of the samples contain two size distributions as was the case in Figure 3.6c. Again the double mass particles have been disregarded and the mean and standard deviation values shown in Figure 3.7a are for the single mass particles only.

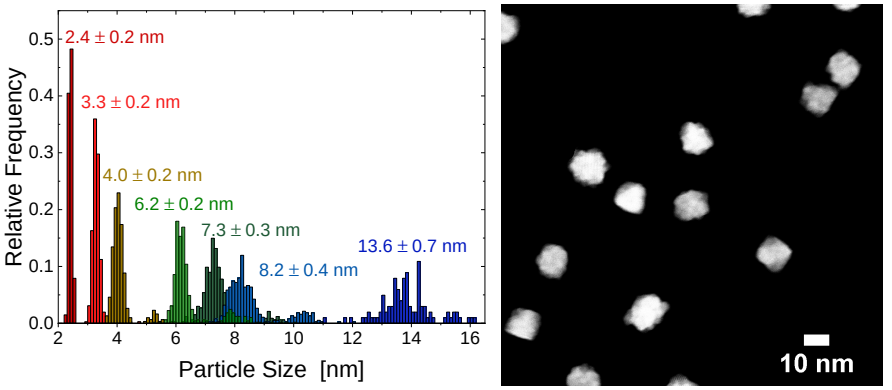

Figure 3.7: a) Size distributions for the seven different sizes of Pt particles used in the particle size effect study. **b)** Close-up STEM image of 6.7M amu Pt particles with an equivalent particle size of 10 nm. Adapted from [92].

3.5 Dissolution Measurements

The dissolution measurements were carried out by Daniel Sandbeck using the SFC-ICP-MS system in Erlangen. Platinum dissolution is an effect of oxidation and reduction at potentials between 0.6 - 1.5 V_{RHE} [93–97]. When scanning anodically during a relatively slow CV, Pt begins to become oxidized leading to an anodic dissolution peak due to the place-exchange mechanism. As the oxide layer continues to form the dissolution decreases due to passivation of the Pt surface. When scanning cathodically, the oxide is reduced leading to a much larger cathodic dissolution peak, which depends on the amount of oxide formed during the anodic scan. However, significant dissolution is only observed if the potential is scanned below 1.0 V_{RHE} due to limited reduction of the oxide above this potential. Therefore the commonly applied protocols of 0.6-1.0 V_{RHE} and 1.0-1.5 V_{RHE}, which are meant to simulate load and start/stop conditions respectively[62, 67, 82, 85–87], will not cause substantial Pt dissolution [98]. Since spikes in the start/stop procedure of a fuel cell are expected to reach potentials below 1.0 V_{RHE}, these protocols are not ideal. To address this issue the group of Cherevko developed a "combined cycle" accelerated stability testing (AST) protocol that scans from 0.6-1.5 V_{RHE} [98]. This was established to cause significant Pt dissolution with minimal carbon corrosion. In these studies the samples are subject to a slow CV (0.05-1.5 V_{RHE}, 10 mV/s) followed by the AST of 1000 cycles (0.6-1.5 V_{RHE}, 500 mv/s) and finally another slow CV. This allows for monitoring the development of the anodic/cathodic dissolution peaks along with the Pt dissolution during the AST cycles. A sketch of the protocol is shown in Figure 3.8a.

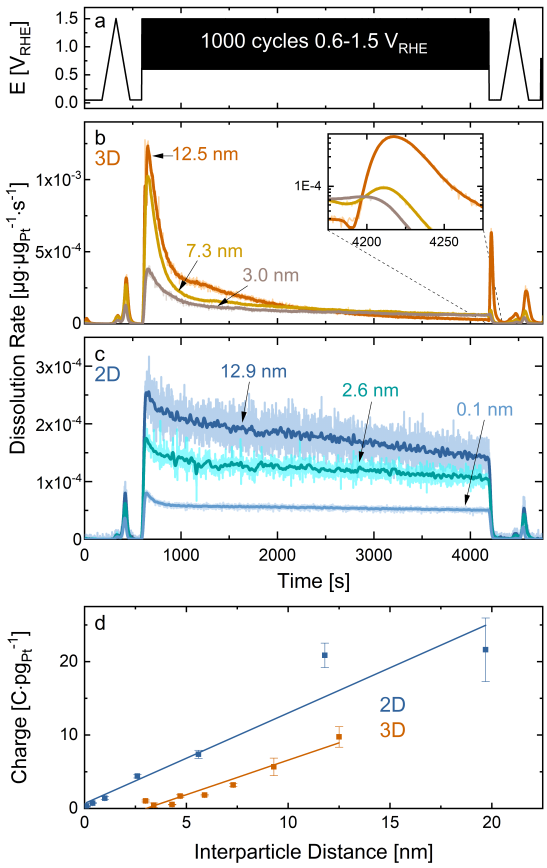

Figure 3.8: a) AST protocol of 1000 CVs (0.6-1.5 V_{RHE}, 500 mV/s). **b)** Dissolution rate profiles for the 3D samples and **c)** 2D samples for three different interparticle distances. **d)** The mass-normalized charge for reducing the oxidized particles during the 0.05 V_{RHE} reductive hold after the AST. The errorbars are the standard deviation from more than 3 different measurements. Reprinted from [91].

3.5.1 Dissolution versus Interparticle Distance

Figures 3.8b and c show the mass-normalized dissolution rate profiles resulting from the AST protocol. The dissolution rate in both systems scales with the interparticle distance, but there is a distinct difference in the dissolution rate profile. The 3D samples display a sharp peak in the beginning of the AST, especially for the two largest interparticle distances. Meanwhile the 2D samples display a more gradual decrease in dissolution for all interparticle distances. Additionally, the 3D samples display a peak at the end of the AST (Figure 3.8b inset), when the reductive hold of 0.05 V_{RHE} is applied before the slow CV. The amplitude of this

peak increases with interparticle distance and is only present for the 3 largest interparticle distances. This peak is not observed on any of the 2D samples with 6.5 nm Pt particles in contrast to the 2 nm particles of the 3D samples. Figure 3.8d shows the mass-normalized reductive charge spent on reducing the samples during the reductive hold of 0.05 V_{RHE} after AST. Though the 2D samples do not display a dissolution peak they do display a reduction charge that scales linearly with interparticle distance, similar to the 3D samples. It appears the 0.6 V_{RHE} lower potential limit of the AST is not cathodic enough to fully reduce the particles during the AST cycles, leading to a partial passivation by PtO_x. The peak observed in the insert for the 3D samples is likely due to the Gibbs-Thomson effect [99] for smaller particles leading to increased particle passivation.

The intercept of the 3D samples in the mass-normalized reductive charge (Figure 3.8d) is shifted due to the overestimation of the interparticle distance for the 3D samples. Additionally, the presence of inaccessible pores in the Pt/Vulcan support leads to an overestimation of the surface area, which also increases the estimated interparticle distance. This emphasizes the strength of well-defined model systems such as the 2D samples, where the fit of the mass-normalized reductive charge intercepts the origin.

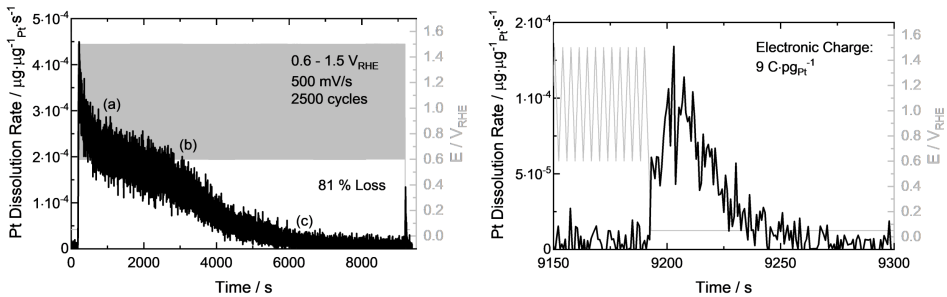

Figure 3.9: a) Mass-normalized dissolution rate profile for the extended AST protocol. Three distinct changes in slope are observed at points (a), (b) and (c). **b)** Magnification of the cathodic reduction peak after applying the 0.05 V_{RHE} reductive hold after the AST cycling. Adapted from [91].

Further understanding of the passivation phenomenon was obtained by expanding the AST protocol to 2500 cycles for the 1% coverage (20.7 nm interparticle distance) 2D sample, seen in Figure 3.9a. The dissolution rate displays 3 distinct changes in rate, which are speculated to be due to (a) surface defects being dissolved initially, at (b) the particles have begun to shrink due to dissolution and thus are more easily passivated by the PtO_x formation. At point (c) passivation completely inhibits dissolution with an overall loss of 81% of the material. The integrated charge of the cathodic reduction peak in Figure 3.9b is identical to the reduction charge after 1000 cycles, indicating that the particles are fully passivated.

The slow CVs before and after AST in Figure 3.10a show the interparticle distance effect without the influence of the passivating PtO_x. The CVs have a lower potential limit of 0.05 V_{RHE} and thus all the formed oxide will be fully reduced during the cathodic scan. Figure 3.10b shows a significant decrease in mass-normalized dissolution rate after the AST protocol with separate anodic and cathodic dissolution peaks. Additionally, a trend in the mass-normalized dissolved quantity is observed for both the 3D and 2D samples in Figure 3.10c. Both systems display a proportionality between the interparticle distance and anodic/cathodic dissolution, both before and after AST.

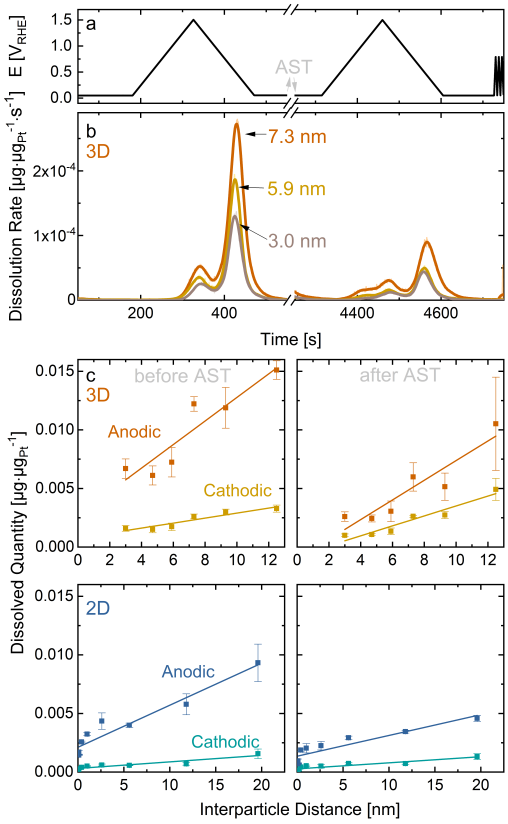

Figure 3.10: a) The two CVs (0.05-1.5 V_{RHE}, 10 mV/s) before and after the AST testing. **b)** Mass-normalized dissolution rate profiles for the 3D samples with 3 different interparticle distances. **c)** Mass-normalized dissolved quantities during anodic/cathodic scans before and after the AST protocol for the 3D samples (top) and 2D samples (bottom). The errorbars are the standard deviations from more than 3 measurements. Adapted from [91].

The passivation effect of PtO_x was studied further for the 3D samples using XPS, EXAFS and XANES, due to the observation of increased passivation effects compared to the 2D samples. Additionally, the flat structure and low absolute loadings of the 2D samples makes the signal to noise ratio insufficient in such measurements. The XPS spectra in Figure 3.11a show increased Pt(II) and Pt(IV) oxidation states relative to the metallic Pt(0) states for larger interparticle distances, indicating increased particle oxidation. Additionally, the EXAFS measurements in Figure 3.11c show a slightly increased coordination of Pt to O (from 2.4±0.9 to 3.1±1.6) for increasing interparticle distances. This indicates an increased oxophilicity for the Pt nanoparticles with larger interparticle distances. These changes in oxidation states are in agreement with the white line shift of the Pt L_{III} edge in the XANES data in Figure 3.11b.

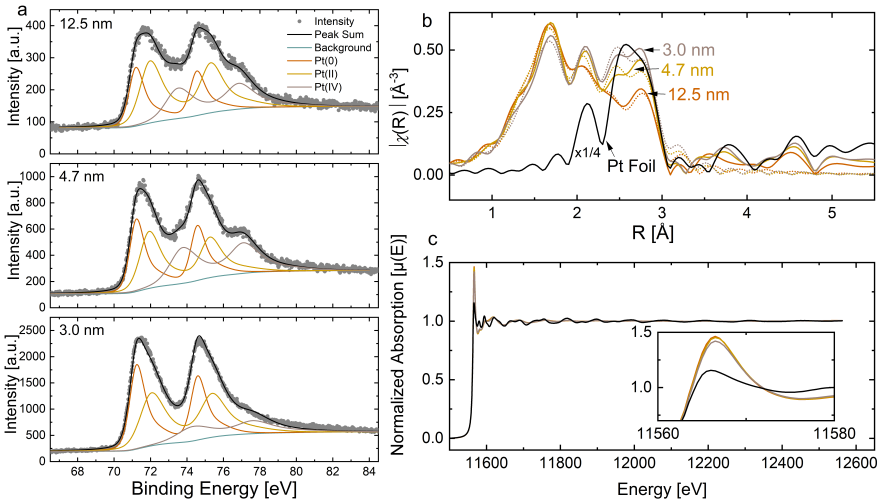

Figure 3.11: a) XPS spectra of the Pt 4f peak, **b)** Fourier transformed magnitudes of k^2-weighted EXAFS spectra and fits(dotted) and **c)** Pt L_{III} XANES spectra, for the 12.5, 4.7 and 3.0 nm interparticle distance 3D samples. Pt foil was used as a reference for the EXAFS and XANES measurements. Adapted from [91].

3.5.2 Understanding the Interparticle Distance Effect

There are three fundamental mechanisms that can be used to explain the proportionality between the dissolution rate/dissolved quantities and the interparticle distance:

1. **A shift in the Nernst equilibrium potential** for electrochemical dissolution caused by a build up of dissolved Pt-ions in the electrolyte around the Pt nanoparticles. There will be a larger concentration of dissolved Pt-ions for shorter interparticle distances [73].

2. **Redeposition of Pt-ions** on nearby Pt nanoparticles is more likely for shorter interparticle distances since more Pt nanoparticles will be within the diffusion length of Pt-ions in the electrolyte.

3. **Overlap of the Electrochemical Double Layer (EDL):** As the interparticle distance decreases there is an increase in the overlap of the EDL around the particles. This changes the oxophilicity of the particles, ultimately shifting the oxidation potential to more positive potentials. Thus during the electrochemical protocols applied here, the particles with shorter interparticle distances are less oxidized and consequently display decreased dissolution [74–76, 100].

While mechanisms 1 and 2 have previously been observed to affect dissolution in studies with constant interparticle distance and varied catalyst layer thickness [67], mechanism 3 has not previously been observed in dissolution studies. In this study it has been evident through the observed partial passivation of the particles' surface by PtO_x during the AST (Figure 3.8), which clearly increased for larger interparticle distances. It was further indicated by the sharp decrease in the initial dissolution peaks of the 3D samples and the cathodic dissolution peak observed when applying the 0.05 V_{RHE} reductive hold after AST. Both of these effects, decreased for smaller interparticle distances. The overlap of the EDL has also previously been credited for increases in ORR activity for short interparticle distances in several catalytic systems [75–77]. This was proposed to be due to reduced poisioning by oxygenated species. The increased oxophilicity for longer interparticle distances observed in XPS, EXAFS and XANES measurements also display an effect of the overlapping EDL. However, while it is evident that there is an effect of the EDL overlap, the physical mechanism of this effect can only be speculated through theoretical considerations at this point [75, 100].

The linear shape of the 2D dissolution rate profiles during AST compared to the 3D samples (Figure 3.8b and c) can be understood from the differences in particle size. According to the Gibbs-Thomson equation[71, 99], the oxidation potential of the 6.5 nm particles in the 2D samples is more positive than for the 1.9 nm particles in the 3D samples. Thus the particles in the 2D samples will be less oxidized. However, the mass-normalized reduction charge in Figure 3.8d follows similar slopes for both systems. This is likely due to particle shrinking during dissolution leading to a larger interparticle distance and consequently, increased passivation by mechanism 3. This was also exemplified by the extended ADT displayed in Figure 3.9a where the passivation dominates after sufficient dissolution. This caused identical reduction charges after 1000 and 2500 cycles of AST.

It is important to note that this study only examines the effect of interparticle distance on dissolution in an extremely ideal system compared to an actual PEMFC setup. Real devices have increased degrees of complexity such as the presence of an ionomer [67, 68]. However, these fundamental studies can increase the understanding of dissolution phenomena such as the Pt "depletion band" observed near

the membrane in full cell membrane electrode assemblies [101]. Here there is a decreased amount of Pt due to dissolution, which was alleviated by increasing the initial Pt density in this layer [101]. This is in agreement with the results of our study. Additionally, the effect of interparticle distance on the other degradation mechanisms, mentioned previously, should be studied as intuitively one would expect phenomena such as particle agglomeration and Ostwald ripening to be affected by reduced interparticle distances.

Ultimately the results of our study can aid in the engineering of future PEMFCs for optimal performance and lifetime. Considering the goal to reduce the overall Pt usage in PEMFCs, our study indicates that this should be achieved by thinner catalyst layers with a higher density of Pt. This may introduce new challenges and the effect of short interparticle distances and thin catalyst layers must therefore be tested in full cell membrane electrode assemblies.

3.5.3 Dissolution versus Particle Size

The differences between the 6.5 nm particles in the 2D samples and the 2 nm particles in the 3D samples show there is an effect of particle size on dissolution. However, these systems have more differences than just particle size so it is difficult to draw any conclusions on the particle size effect. The effect is instead elucidated in the particle size effect study by using different particle sizes in the 2D samples. As mentioned previously the mean interparticle distance is kept constant across all samples to avoid the interparticle distance effects discussed above. The AST protocol from the interparticle distance study was reused here.

The mass-normalized dissolution rate for the 2 nm particles, in Figure 3.12b, displays a sharp peak followed by a sharp drop to baseline values. The peak is due to the high surface area per volume of this particle size. Consequently, the peak height decreases for larger particles up to a size of 6 nm, where only a gradual decrease in dissolution rate is observed. Additionally, the dissolution rate stays well above the baseline for the entirety of the AST. The 7, 8 and 10 nm particles behave similarly to the 6 nm particles, but with a clear decrease in dissolution rate for increasing particle sizes as seen in Figure 3.12b$^{|}$. The 2, 3 and 4 nm particles display a dissolution peak, when the reductive hold is applied after the AST (Figure 3.12b$^{||}$).

The size specific dissolution rate profiles can be explained by the Gibbs-Thomson effect: increasing oxophilicity for decreasing particle size [99]. Since the lower potential limit of 0.6 V_{RHE} is not sufficient to fully reduce the 2, 3 and 4 nm particles, the particles are quickly passivated by PtO_x leading to the sharp drop in dissolution rate and ultimately a complete passivation. This is confirmed by the cathodic dissolution peak during the reductive hold in Figure Figure 3.12b$^{||}$, which increases for smaller particles from 4 to 2 nm. The effect of the size dependent passivation is clear in Figure 3.12c. The particle size effect resembles a volcano, which arises from the trade off of ECSA per volume and passivation.

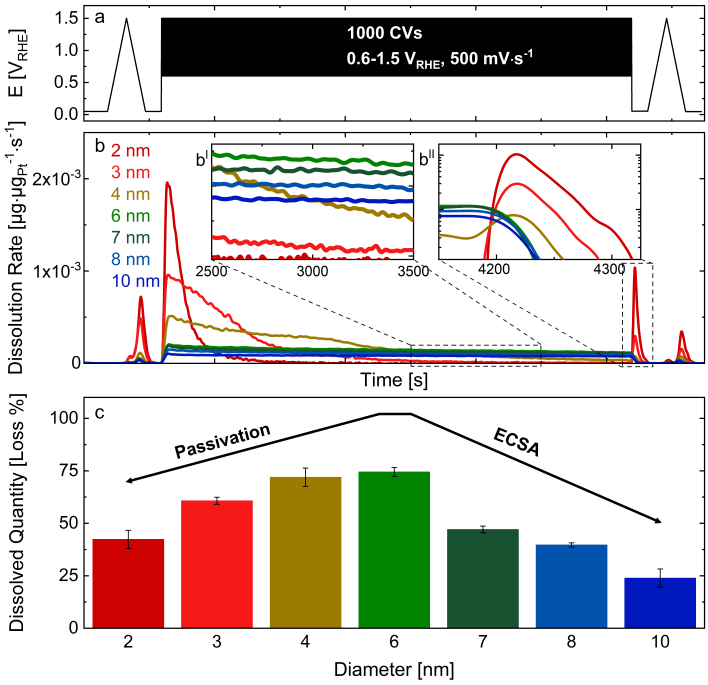

Figure 3.12: a) AST protocol used for dissolution measurements. **b)** Mass-normalized dissolution rate for varying particle sizes. $\mathbf{b}^{\mathrm{I}}$ shows the midway dissolution and $\mathbf{b}^{\mathrm{II}}$ shows the cathodic dissolution peak during the 0.05 V_{RHE} reductive hold after AST. **c)** Mass-normalized quantified dissolved Pt loss during AST. Reprinted from [92].

A decrease in dissolution for larger particles is expected due to the reduced ECSA per volume [62, 81, 82] and is observed for the 6, 7, 8 and 10 nm particles. Meanwhile for particles smaller than 6 nm, the effect of ECSA per volume is convoluted with the increasing passivation for decreasing particle size. This leads to a decrease in dissolution for particles below 6 nm. This behaviour is strongly dependent on the applied AST protocol parameters such as the potential limits, number of cycles and scan rate. If the lower potential limit is reduced below 0.6 V_{RHE} or the scan rate is decreased, then the smallest particles may be reduced. Additionally, increasing or decreasing the number of cycles in the AST will affect the relative importance of the initial transients in the dissolution rate.

The formation of the passivating PtO_x layer can be followed throughout the AST by monitoring the accumulated charge in a CV in the AST. Figure 3.13 shows the normalized accumulated oxidation/reduction charge in 5 different cycles of the AST for each particle size. Note that the dissolution currents only contributes with 0.1-

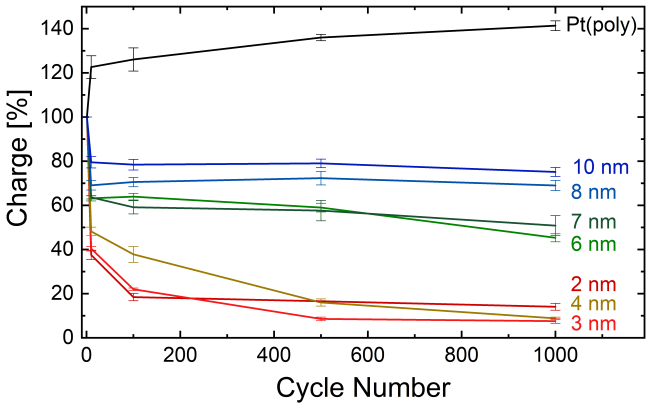

Figure 3.13: Total charge during a CV, normalized to the first CV of the AST cycle, for the 1st, 10th, 100th, 500th and 1000th cycle of the AST. Reprinted from [92].

0.5% of the total current and thus the accumulated charge is due to oxidation and reduction of the Pt nanoparticles (carbon is passivated immediately under these conditions). All nanoparticle samples display a sharp drop in charge in the first 10 cycles due to the oxidation of minor surface contaminants. The charge decreases faster for smaller particles indicating that they are quickly passivated since they are no longer reduced and oxidized in each cycle. The charge for the 2 nm particles drops rapidly to a certain level that is maintained throughout the AST. The drop for the 3 and 4 nm particles is slightly slower, but eventually they reach the same level as the 2 nm particles. This may be due to considerable particle shrinking as a consequence of the significant dissolved quantities ($\approx 60 - 75\%$ Figure 3.12c) for these two samples. Meanwhile the 6 and 7 nm particles only display a slight decrease in charge throughout the AST and the 8 and 10 nm particles maintain their charge per cycle throughout. This indicates minimal passivation for the 6, 7, 8 and 10 nm particles. These changes in oxophilicity as a function of particle size can typically be seen in the shift in oxidation and reduction peaks of the CVs to more positive potentials. However, these can not be observed for these samples due to the low loading, which was necessary to maintain a constant interparticle distance.

The CVs before and after AST (Figure 3.14a) have a slower scan rate and lower potential limit of 0.05 V_{RHE} and they therefore fully reduce the passivating oxides in the cathodic scans. A significantly lower mass-normalized dissolution rate is observed for larger particles in these CVs, shown in Figure 3.14b. This effect can be attributed to decreasing ECSA per volume as discussed above and leads to a similar trend in the mass-normalized dissolved quantities shown in Figure 3.14c. Additionally, the peak of the cathodic dissolution (Figure 3.14b) is shifted to lower potentials, which is evidence of the increased oxophilicity of smaller particles.

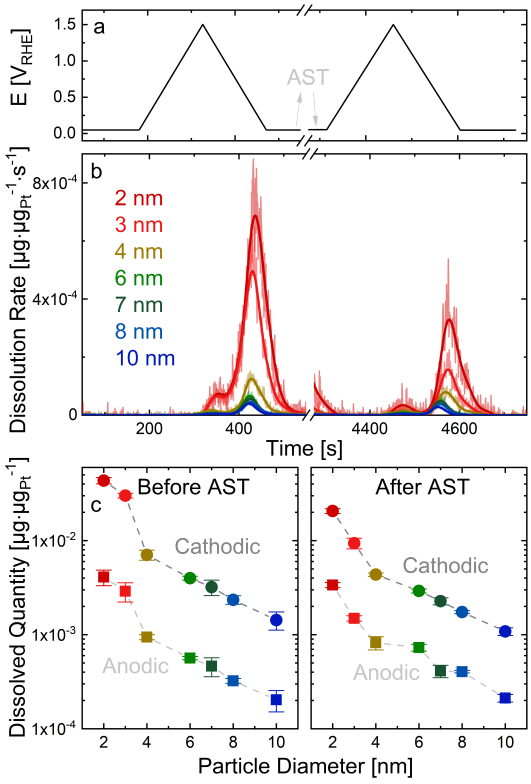

Figure 3.14: a) CVs before and after the AST protocol. **b)** Mass-normalized dissolution rate for varying particle sizes. **c)** Mass-normalized quantified dissolution Pt loss during the CVs. Reprinted from [92].

3.5.4 Importance of the Particle Size Effect

The results of studying the particle size effect show the importance of the applied AST protocol. Due to a shift to lower potentials in the reduction potential for smaller particles, the lower potential limit of the applied AST poses an issue. The 0.6 V_{RHE} lower potential limit is not sufficient to reduce the smallest particles, which causes a volcano shaped particle size effect on the dissolved quantities (Figure 3.12b). However this is a consequence of the lower potential limit and not a physical particle size effect as evidenced by the trends in the dissolved quantities in the CVs before and after the AST protocol (Figure 3.14c). This highlights the importance of considering the potential limits, scan rates and cycle lengths of the AST protocols for each individual sample to avoid discovering false trends in dissolution studies. This in turn complicates comparisons across different research groups and we therefore recommend careful consideration, when comparing samples of different particle size and testing protocol. Additionally, samples with broad distribution

of size and interparticle distance can display a variety of degradation phenomena, which makes it challenging to draw fundamental conclusions. This is often the case due to the thermal annealing treatments, which are used to increase particle size through agglomeration, consequently also altering the interparticle distance. These results therefore emphasize the need for well-defined model systems when studying fundamental dissolution phenomena, which may contribute to improving the experimental techniques in PEMFC research.

Finally, by using a lower potential limit of 0.3 V_{RHE} all particle sizes should be fully reduced, avoiding protocol induced size effects. We therefore suggest an AST protocol of 0.3-1.5 $_{RHE}$ at 500 mV/s for standardized dissolution testing to cause extensize Pt dissolution on a short time scale. While we have only examined the effect of particle size on dissolution, it is likely to affect the other degradation phenomena such as particle agglomeration, detachment and Ostwald ripening. Separate studies should therefore be carried out to uncover these effects.

3.6 Conclusion

In conclusion, we have used simulations and a well-defined 2D model catalyst in combination with an industrially relevant 3D catalyst to uncover the trends in Pt dissolution under ORR conditions for varying interparticle distances. A clear increase in dissolution was observed for longer interparticle distances both during AST protocols and slower CVs. The trend was explained by three fundamental mechanisms:

- **A shift in the Nernst potential** for electrochemical dissolution due to increasing concentrations of Pt-ions in the electrolyte for shorter interparticle distances.
- **Pt redeposition**, which is increased for shorter interparticle distances due to an increased number of Pt particles in the diffusion length of the dissolved Pt-ions.
- **Electrochemical Double Layer overlap** causing a shift in the oxophilicity of particles in vicinity of each other, leading to less passivation by PtO_x for shorter interparticle distances.

Furthermore the 2D model system was used to study particle size effects by samples of varying particle size, but constant mean interparticle distance. The study showed the importance of considering the lower potential limit of the applied AST protocol since particles smaller than 6 nm were not fully reduced using the standard AST. Additionally, a new AST protocol was suggested to enable further comparison of different samples across different research groups. Ultimately, the results highlight the advantages of using well-defined model systems in combination with simulations to increase the understanding of fundamental phenomena and improve experimental techniques.

Chapter 4

Benchmarking the Hydrogen Evolution Activity of Platinum

Platinum catalysts have long been known to display state-of-the-art hydrogen evolution reaction (HER) activity. However, as discussed in the previous chapter, platinum is a less than ideal material for potential scale up technologies due to its scarcity [102]. Therefore substantial research efforts have focused on finding novel earth-abundant catalysts for HER [103]. Unfortunately, proper comparison of novel materials is difficult due to differences in activity standards [35].

This chapter describes the study of a "benchmark" Pt nanoparticle system with different HER activity metrics. A high degree of control over nanoparticle size, amount of Pt and electrochemical surface area makes the HER measurements ideal as a literature comparison for discoveries of novel HER catalysts. My contribution to this work consists of sample synthesis and ISS characterization, together with Ph.D. student Karl Toudahl. Additionally, I developed a simulation for describing how the CO-strip charge scales with loading due to particle overlap. CO-strip and HER measurements were performed by Johannes Novak Hansen. Therefore, I will describe the synthesis, characterization and simulations parts of this work in detail and only briefly present the electrochemical HER results.

This work is currently being written into a manuscript with a few measurements remaining, such as STEM particle size analysis and HER activity measurements for a commercial Pt system. In parallel, we are awaiting theoretical calculations from the Center for Catalysis Theory (CatTheory) group at DTU Physics to support the observations.

4.1 HER Catalysis

The electrolysis of water in acidic media is a promising route to generating hydrogen from renewable electricity [12]. In acid, water electrolysis can be split into the two half-cell reactions HER and the oxygen evolution reaction (OER) :

$$2\,H_2O \rightarrow O_2 + 4\,H^+ + 4\,e^- \quad \text{Oxygen Evolution Reaction} \tag{4.1}$$

$$2\,H^+ + 2\,e^- \rightarrow H_2 \quad \text{Hydrogen Evolution Reaction} \tag{4.2}$$

Of the two half-cell reactions, OER is the most complex and comes with a large overpotential, even for state-of-the-art iridium based catalysts [12]. In contrast, HER is a far simpler reaction and Pt is an excellent catalyst, displaying a low overpotential compared to the thermodynamic limiting potential of 0 V_{RHE}, even at low loadings [104].

As discussed in Chapter 1, for an energy storage technology to meaningfully contribute to the global energy production, it must scale to the TW level [1, 105]. With polymer electrolyte membrane (PEM) electrolyzers based on a Pt catalyst, producing 1 TW equivalent of H_2 requires approximately 100 tonnes of Pt [106]. Compared to the annual global production of Pt, 100 tonnes is about 60%. Since Pt has many other applications, spending the majority of the global production on HER is not desirable [102, 105]. More than a decade ago this led to research into earth-abundant catalysts for acidic HER. Based on DFT-calculations and experiments, nanoparticles of MoS_2 were found to be a promising alternative to Pt [107–109]. Since then, different sulfides, selenides [110], phosphides [111] and carbides [112] have shown promising HER activities [103]. However, the stability of these earth-abundant alternatives is still being investigated [112, 113].

4.1.1 HER Activity Metrics

HER activity is measured as the HER current that is produced by a certain electrochemical potential. To allow for comparison across different setups, different activity metrics are used. The simplest is the geometric current density [mA/cm^2], which is calculated by dividing the measured HER current with the geometric area of the electrode. This is a technologically relevant metric as the size of the electrode is set by the PEM electrolyzer and thus increasing the geometric current density increases the amount of H_2 that can be evolved by the electrolyzer. Another common metric is the mass activity [$A/mg_{catalyst}$], which is calculated by dividing the HER current with the mass of catalyst on the electrode, not including the catalyst support. This is an economically relevant metric as a substantial part of the electrolyzer cost may come from the expensive catalyst material, when PEM electrolyzer technology is scaled to industrial levels [65–67, 105]. Finally, the most absolute measure of catalyst activity is the intrinsic activity, known as the turnover frequency (TOF) [$\#H_2\ site^{-1}\ s^{-1}$]. This is the scientifically relevant measure of activity since it depends on the binding energies and geometries of the active sites

of the catalyst. Calculating the TOF is done by converting the current to # H_2 evolved per second and then dividing by the number of active sites on the electrode. However, the geometric current density, mass activity or TOF themselves are not enough to evaluate HER activity as the current can be increased by increasing the electrochemical potential, which effectively reduces the energy efficiency of the reaction [114]. Thus the overpotential compared to 0 V_{RHE}, at which the activity is attained, is of importance. In HER literature, the overpotential which drives a geometric current density of 10 mA/cm^2, known as η_{10mA/cm^2} is a common metric[35]. This is inspired by the current density in a photoelectrochemical water splitting cell, but in a PEM electrolyzer the current density is typically 1-2 A/cm^2. Thus the relevance of the η_{10mA/cm^2} metric for PEM electrolysis is limited.

4.1.2 Development of Novel HER Catalysts

The process of developing novel catalysts can be approached from two different perspectives[12]. Increasing the intrinsic activity of a catalyst or increasing the number of available sites on the surface. Separate, these two approaches are important and necessary steps in creating technological advances, but together they can lead to even larger progress. The research in replacing Pt with earth-abundant catalysts for HER in acid, has been focused on increasing the number of available sites on the electrode [35]. This has been achieved through increasing the amount of catalyst, known as catalyst loading, on the electrode. When claiming activity comparable or superior to Pt, many use the η_{10mA/cm^2} metric, which does not take into account the catalyst loading. To make matters worse, many do not report the catalyst loading at all, making comparisons of mass activity and intrinsic activity impossible. Considering a higher loading results in more active sites, the geometric current density of 10 mA/cm^2 can be reached at a lower TOF and a lower η, simply by increasing the loading [115]. Thus many of the HER activity comparisons between novel catalysts and state-of-the-art Pt catalysts are misleading, as pointed out by Kibsgaard and Chorkendorff [35].

While comparing η_{10mA/cm^2} is sensible from a technological perspecitve, it becomes more complex when considering the Techno-economics. Increasing the earth-abundant catalyst loading by orders of magnitude may be the cheapest approach to obtaining a competitive η_{10mA/cm^2}, given the earth-abundant material is sufficiently cheaper than Pt. This motivates a new metric of HER activity: HER current per dollar catalyst (A/$) [35]. Calculating the A/$ for catalysts may be subject to substantial change as future developments in material demands can significantly increase the price of materials such as Pt [105]. From prices at the time of writing, a FeP catalyst with η_{10mA/cm^2}=50 mV produces 10600 A/$ [116]. Meanwhile a Pt catalyst with η_{10mA/cm^2}=40 mV produces 3200 A/$ [117]. A similar calculation for Mo_3S_{13} with η_{10mA/cm^2}=200 mV produces 153 A/$ [118]. Thus considering the catalyst activity in A/$, FeP is a promising alternative to Pt, while Mo_3S_{13} is not. However, the comparison is not entirely valid because the catalysts are compared at different η_{10mA/cm^2}, which is influenced by the loading. Specifi-

cally, reducing the η_{10mA/cm^2} of FeP and Mo_3S_{13} from 50 mV and 200 mV to the 40 mV, of Pt will require an increased loading, increasing the cost. This example highlights the importance of reporting catalyst loading along with the activity metrics, when comparing HER activity. In practice, the loadings of earth-abundant catalysts are so high that they can become more expensive than the Pt counterpart.

With regards to developing novel catalysts with higher intrinsic activity, proper identification of the state-of-the-art HER catalyst is difficult. A number of reports on novel HER catalysts claim record breaking platinum-like activity. However, it is difficult to compare the intrinsic activity of existing literature due to the TOF not being reported. This likely stems from difficulties with properly measuring the number of active sites, which is non-trivial for many catalysts [35]. Especially novel catalysts with increasingly complex structures. Consequently, the question of whether or not non-precious catalysts can achieve platinum-like intrinsic activity remains unanswered [35, 113].

4.1.3 A Standard for Comparison

In addition to improper comparisons due to different catalyst loadings, many groups compare the HER activity to homemade measurements of a commercially available Pt/C catalyst [35]. These are often far from state-of-the-art giving an unfair comparison. Other common flaws include a lack of RHE scale calibrations and using Pt as the counter electrode [35]. The RHE scale can be calibrated with a platinum electrode to measure the reversible HER potential in a specific setup. Use of a Pt counter electrode can lead to dissolved Pt from the counter electrode redepositing on the working electrode. Due to its high HER activity, even minute amounts of Pt will substantially increase the HER activity [104]. To alleviate these different causes of erroneous comparisons and to show how the η_{10mA/cm^2} depends on catalyst loading, we have studied the effect of Pt loading on the η_{10mA/cm^2}. By measuring the HER activity of a range of narrowly controlled Pt nanoparticle loadings and sizes, with an Ir counter electrode, we have created a "benchmark" system. The system serves as an example of the effect of loading on the η_{10mA/cm^2}. Furthermore, it allows for a literature comparison for groups studying novel HER catalysts with varying loadings. To ensure proper scientific comparison, the activity is reported in both η_{10mA/cm^2} and TOF.

4.2 Nanoparticle Deposition

Platinum nanoparticles were deposited with the Nanobeam cluster source on glassy carbon discs (diameter=5 mm, height=4 mm, Sigradur G) for RDE measurements. The glassy carbon discs were sputtered for 10 min with 1 keV Ar^+ and a sputter current of 1 μA, to ensure a clean surface before deposition. Pt particles of mass 370k amu corresponding to an equivalent particle size of 3.8 nm, were deposited with loadings from 10 ng/cm^2 to 5000 ng/cm^2. The samples were rastered with

a 1×1 mm square raster pattern ensuring that all the charges, measured in the deposition current, land on the glassy carbon disc. This allows for an accurate determination of the particle loading, while for higher loadings it will lead to a high degree of particle overlap. Therefore three samples; 500 ng/cm^2, 1000 ng/cm^2 and 5000 ng/cm^2, were deposited with a large 5×5 mm meander raster pattern similar to Figure 2.6b. The effect of Pt particle size was studied by depositing 500 ng/cm^2 of 148k amu/2.8 nm, 748k amu/4.8 nm, 1300k amu/5.8 nm with the small raster pattern. A full overview over the Pt particles and loadings is given in Table 4.1.

Table 4.1: Sample overview with particle mass, size, loading and local coverage.

Particle Mass [amu]	Equivalent Particle Size [nm]	Target Loading [ng/cm^2]	Local Coverage [% of monolayer]
370k	3.8 nm	10	0.6
370k	3.8 nm	20	1.0
370k	3.8 nm	50	2.7
370k	3.8 nm	100	5.5
370k	3.8 nm	200	10.9
370k	3.8 nm	500	27.3
370k	3.8 nm	1000	55.1
370k	3.8 nm	5000	275.1
370k	3.8 nm	500 (large raster)	10.4
370k	3.8 nm	1000 (large raster)	18.4
370k	3.8 nm	5000 (large raster)	92.4
148k	2.8 nm	500	37.3
748k	4.8 nm	500	21.8
1300k	5.8 nm	500	17.8

The deposition area for the small raster pattern samples was determined from the SEM image of the 5000 ng/cm^2 loading shown in Figure 4.1a. The area with Pt nanoparticles appears bright on the dark glassy carbon disc. For the small raster pattern the deposition area is clearly confined within the glassy carbon disc. The area was measured to 6.6 mm^2 and used to calculate the coverage in the deposition area, in Table 4.1. The loadings in ng/cm^2 were calculated from the area of the entire glassy carbon disc since the entire disc is used for RDE measurements. The deposition area of the large raster pattern is not confined within the glassy carbon disc, as seen in Figure 4.1b. Therefore the deposition area was estimated from simulations of the large raster pattern, as described in Chapter 2. From the simulation, the deposition area for the large raster pattern was determined to be 31.3 mm^2. All samples were deposited with identical lens conditions, as the beam profile of the nanoparticle beam is affected by the lenses. This ensures that the deposition area, observed in Figure 4.1, is maintained across all samples.

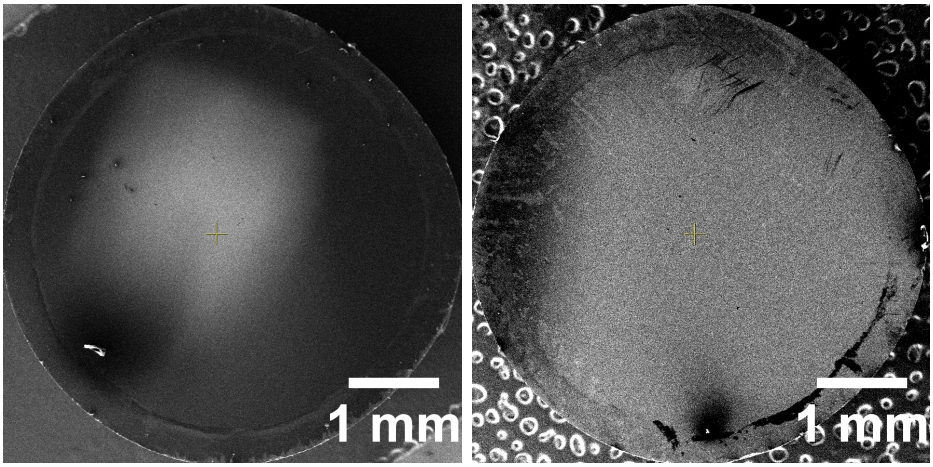

(a) (b)

Figure 4.1: SEM images of glassy carbon discs with 5000 ng/cm^2 of 370k amu Pt nanoparticles. Rastered with **a)** the 1×1 mm square raster pattern and **b)** the 5×5 mm meander raster pattern.

4.3 Characterization

ISS spectra were acquired before deposition to check for a clean surface and after deposition to check that the particles were deposited. Figure 4.2 shows the ISS spectra of the 370k amu Pt nanoparticles, deposited with a small raster pattern. The intensity of the Pt peak scales with the loading. The inset shows a clean glassy carbon disc before deposition with the presence of O, which is commonly found in glassy carbon and Ar from the sputter cleaning procedure. No Pt or contaminations were detected before deposition.

4.3.1 Surface Area Measurements and Simulation

Due to the expected overlap of Pt nanoparticles at high loadings, a CO strip was performed to determine the electrochemical surface area (ECSA). CO stripping is performed in the rotating disk electrode (RDE) setup and consists of holding the working electrode (WE) at +50 mV_{RHE} in the H_2SO_4 electrolyte for 15 minutes. CO is bubbled into the elecrolyte for the first 2 minutes, adsorbing it to the surface. Subsequently, the electrolyte is purged with Ar for 13 minutes. Next, the potential is sweeped anodically to 1.0 V_{RHE} (10 mV/s, 200 rpm) resulting in a distinct CO oxidation/desorption peak. The number of desorbed CO molecules can be measured by integrating the charge of the CO desorption peak. From standard measurements on polycrystalline Pt surfaces in literature, a standard value of 420 $\mu C/cm^2_{Pt}$ can be used to calculate the Pt surface area. The CO-strip charge

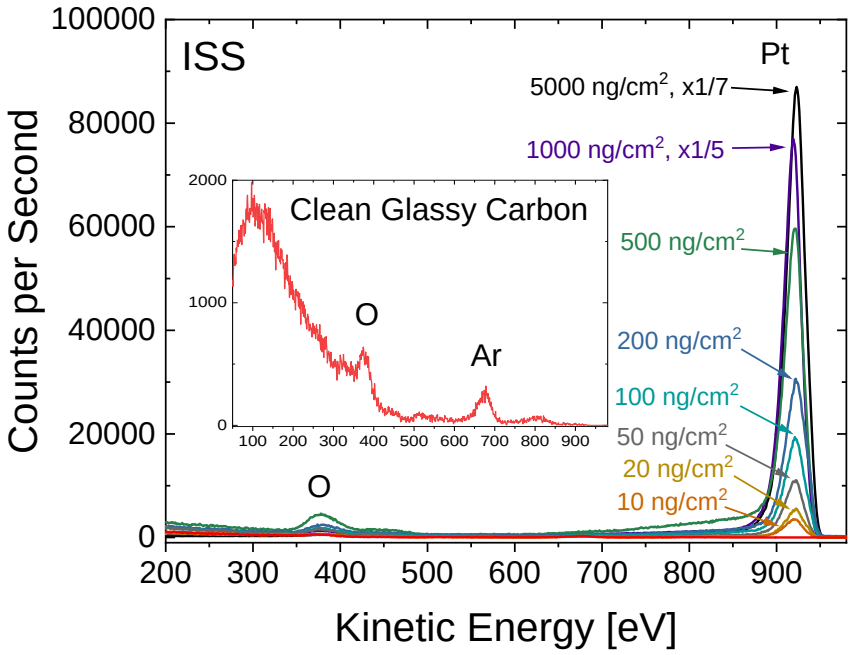

Figure 4.2: ISS spectra for the 370k amu Pt nanoparticles with different loadings on the glassy carbon disc. All deposited with the 1 x 1 mm square raster pattern. The inset shows an ISS spectrum of a clean glassy carbon disc after 10 min 1 keV Ar^+ sputtering.

measured on the Pt nanoparticle samples is shown in Figure 4.3 along with a linear fit to the loadings from 10-500 ng/cm^2. Evidently, the ECSA scales linearly with loadings lower than 500 ng/cm^2. At higher loadings the CO-strip charge deviates from linearity.

The non-linear scaling of the CO-strip charge can be explained by a simple model that was used to simulate the CO-strip charge for these loadings. The model describes the overlap of particles landing on other particles, when deposited from a cluster source, assuming that the particles are sticky hard spheres. The simulation generates a (x, y, z) set of N random particle positions within an area A determined by the coverage. Next, it loops through each particle position. When it finds an overlap with another particle it increases the z value of the overlapping particle. The z value is increased until the particles are in grazing contact with minimal overlap.

The simulation process is shown in the schematic in Figure 4.4. Step 1 shows 3 particles overlapping, the simulation moves two of them up so they are in grazing contact with the first as seen in Step 2. As the loop reaches one of the two particles,

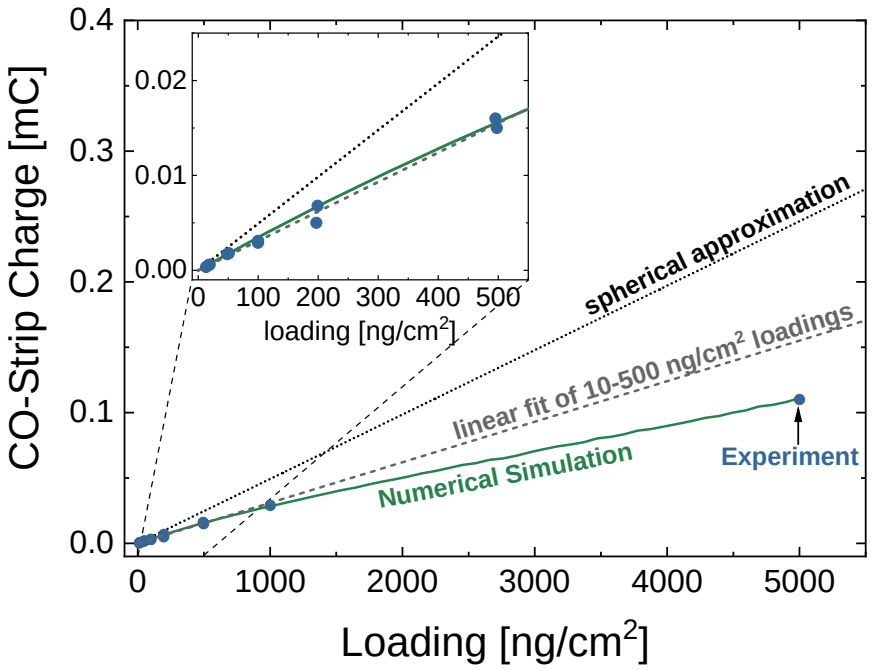

Figure 4.3: CO-strip charge for all small raster pattern samples (blue circles) along with a numerical simulation (green) of the charge. Additionally, the plot shows a linear fit to the lower loadings (10-500 ng/cm^2, gray dashed) and an estimate based on a spherical particle approximation (black dotted).

the other is moved up so the two of them are in grazing contact. This loop is repeated until there are no more overlapping particles. Throughout the loops the particles are never moved in the (x,y) directions. The resulting structure in Step 3 corresponds to 3 Pt particles landing on the glassy carbon support, the top most landing last, assuming the particles do not sinter into larger particles. Finally the simulation counts the number of particle-particle contacts and particles lying on the support surface. Particles on the surface of the support have a reduced surface area available for electrochemical reactions. Additionally, particles in contact with each other will lose a certain surface area. These two surface area losses are not necessarily identical and cannot be estimated. Therefore the two values are found by fitting the simulation to the measured CO-strip charge. A spherical free standing 3.8 nm Pt particle has a surface area of 44 nm^2. The loss from the support surface is found by fitting the loadings from 10-100 ng/cm^2, where minimal particle overlap is expected. The area loss was found to be 12 nm^2. Meanwhile the value of the particle-particle contact loss was found from fitting the entire range of loadings. This was determined to be 8.4 nm^2. The exact values, while interesting, cannot

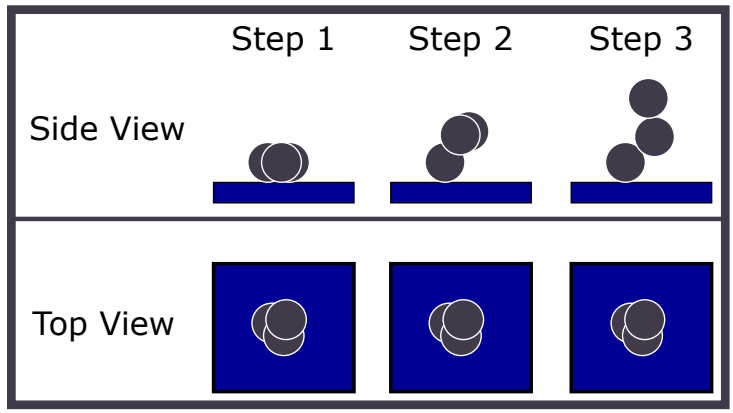

Figure 4.4: Schematic of the simulation process. Step 1: 3 overlapping particles have been landed on the glassy carbon support. Step 2: The simulation moves two of the particles up so they are in grazing contact with the one below. Step 3: One of the particles overlapping in Step 2 is moved up again, remaining in grazing contact with the other. Throughout the steps the particles are only moved upwards as seen from the top view. Finally the simulation can count the number of particles in contact with each other and the number of particles on the glassy carbon support.

validate the model. Instead the model is validated by its ability to describe the scaling behaviour of the CO-strip charge vs. Pt loading, at both low and high loadings. Despite 2.75 monolayers of coverage for 5000 ng/cm^2, the surface area is only reduced by 29% indicating minimal particle agglomeration.

4.4 HER Benchmark Measurements

The HER activity of the Pt nanoparticles was tested in a three electrode RDE setup in 0.5 M sulfuric acid (H_2SO_4). The Hg|$HgSO_4$ reference electrode (RE) was placed in a Luggin capillary and an iridium wire was used as counter electrode. A platinum wire was used as dummy electrode to calibrate the RHE scale of the reference electrode. The HER activity was measured by CVs scanned at 50 mV/s and a rotation speed of 1600 rpm with continuous H_2 purging. All CVs were compensated for Ohmic drop, measured by impedance spectroscopy. The lower potential limits for the CVs were chosen to ensure that all samples reached a geometric current density of 10 mA/cm^2.

4.4.1 Platinum Loading versus Overpotential

Figure 4.5 shows the polarization curves for a select set of loadings from 13-5000 ng/cm^2. The polarization curves are extracted from the cathodic sweep of the CVs. It is evident that as the loading increases, the slope of the geometric current density

j_{geo} increases. Thus, for higher loadings, j_{geo} reaches 10 mA/cm^2 at potentials closer to the thermodynamic limiting HER potential of 0 V_{RHE}. The inset shows the difference between the anodic and cathodic sweeps that increases for higher loadings. This is due to an increased double layer capacitance [114], consistent with an increased ECSA due to a higher loading of Pt. The anodic/cathodic sweeps are centered around j_{geo}= 0 at 0 V_{RHE}, confirming the calibration of the RE to the RHE scale.

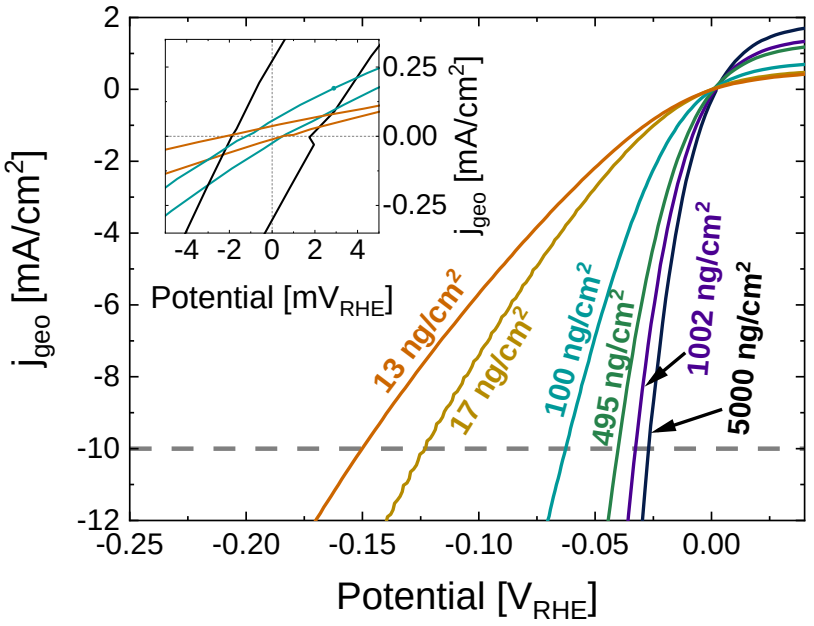

Figure 4.5: Polarization curves for selected loadings from 13-5000 ng/cm^2. **Inset** shows the region of the CVs around 0 V_{RHE} for 13, 100 and 5000 ng/cm^2 samples. The gray dashed line indicates the 10 mA/cm^2 threshold for the overpotential η_{10mA/cm^2}.

The mass activity j_{mass} vs. η_{10mA/cm^2} is extracted from the polarization curves and summarized in Figure 4.6. The overpotential η_{10mA/cm^2} decreases from η_{10mA/cm^2} = 150 mV for 13 ng/cm^2 loading to η_{10mA/cm^2} = 27 mV for 5000 ng/cm^2 loading. As expected, Pt loading has a significant effect on η_{10mA/cm^2}. The inset shows j_{mass} vs. η_{10mA/cm^2} for the different particle sizes at 500 ng/cm^2 loading. Evidently, particle size does not affect the η_{10mA/cm^2} significantly, considering the similar distance between two identical 3.8 nm samples. The 500-5000 ng/cm^2 samples deposited with a large raster pattern display lower η_{10mA/cm^2} than the equivalent loadings deposited with the small raster pattern. Due to the decreased accuracy of the loading it is possible that the loading is slightly lower or higher than estimated. However, the difference in η_{10mA/cm^2} between the two raster patterns is significant,

corresponding to the difference between 200 ng/cm^2 and 500 ng/cm^2. This indicates that particle overlap affects the HER activity for Pt loadings $\geq$ 500 ng/cm^2 deposited with the small raster pattern.

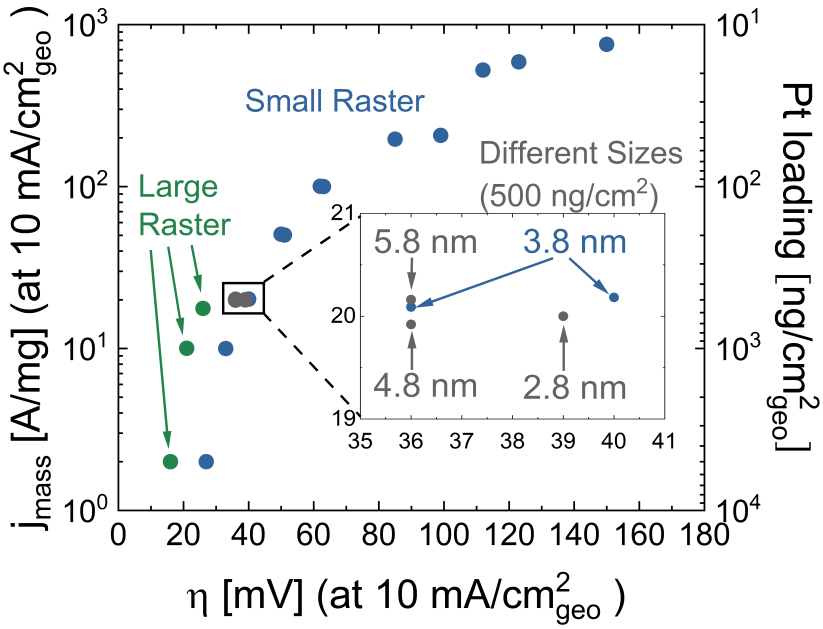

Figure 4.6: HER mass activity j_{mass} and Pt loading vs. η_{10mA/cm^2} for both the large raster pattern (green) and small raster pattern (blue). The inset shows a close-up of the 500 ng/cm^2 samples of different particle sizes.

4.4.2 Intrinsic Activity

From the measurements of the ECSA by CO-stripping and the HER current, the TOF can be determined. Figure 4.7 shows the TOF vs. potential for each loading from 13-5000 ng/cm^2. The TOF at a given potential is higher for smaller loadings. Specifically, there is more than an order of magnitude difference in TOF from 5000 ng/cm^2 to 13 ng/cm^2 at low potentials as shown in the inset. It appears Pt nanoparticles with a larger spacing evolve more H_2 per site per second at a given overpotential. This indicates that the HER activity is mass transport limited, even close to the thermodynamic HER potential of 0 V_{RHE}.

Similar to Figure 4.6, the TOF at 10 mA/cm^2 can be plotted against η_{10mA/cm^2} as in Figure 4.8. The difference in TOF for the 4 different particle sizes is a consequence of the decrease in surface area for larger particles. Since η is measured at 10 mA/cm^2, samples with a smaller surface area must display a higher TOF.

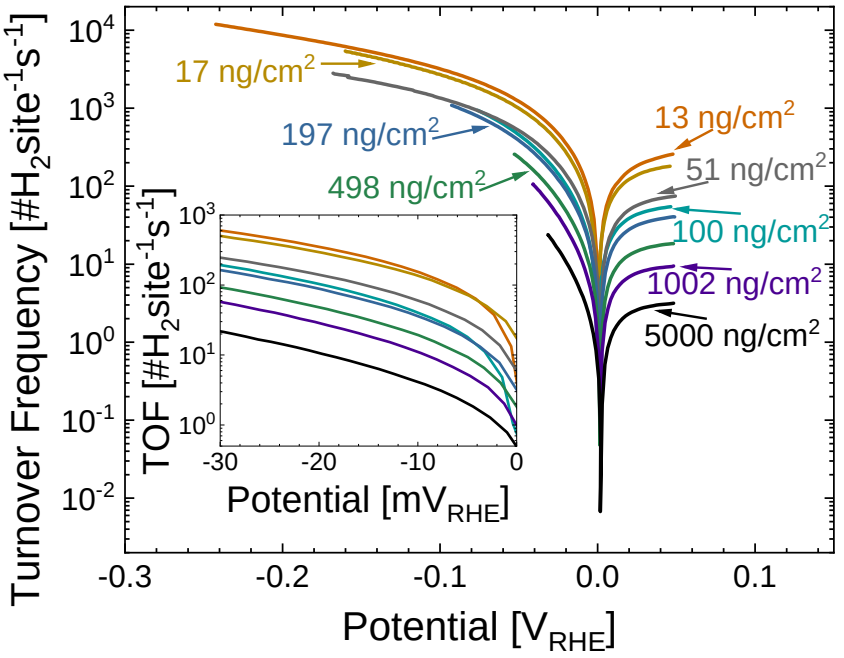

Figure 4.7: Intrinsic HER activity/TOF vs. V_{RHE} for loadings from 13-5000 ng/cm^2. **Inset** shows a close-up of the region from -30 mV_{RHE} - 0 mV_{RHE}.

This is also the cause of the decrease in TOF for lower overpotentials. Since higher loadings require a lower activity per site to reach the 10 mA/cm^2 threshold. Meanwhile, there is a significant difference between the large and small raster pattern samples, despite having normalized to the number of sites. The samples with large raster patterns display TOFs similar to the small raster pattern samples, but at a lower overpotential. Specifically, the 1000 ng/cm^2 large raster sample has a larger TOF than the 5000 ng/cm^2 small raster sample. This cannot be explained by particle overlap, but instead indicates a mass transport limitation. Since the particles deposited with the large raster pattern are spaced further apart, they are not as limited by the mass transport rate. This is in agreement with the observations in Figure 4.7, where a similar observation was made based on different loadings.

4.5 Discussion

Since the Pt nanoparticles were produced by deposition with the Nanobeam cluster source, their mass is known. From previous studies such as Chapter 3 the particle size is expected to be close to equivalent particle size. However, further confirma-

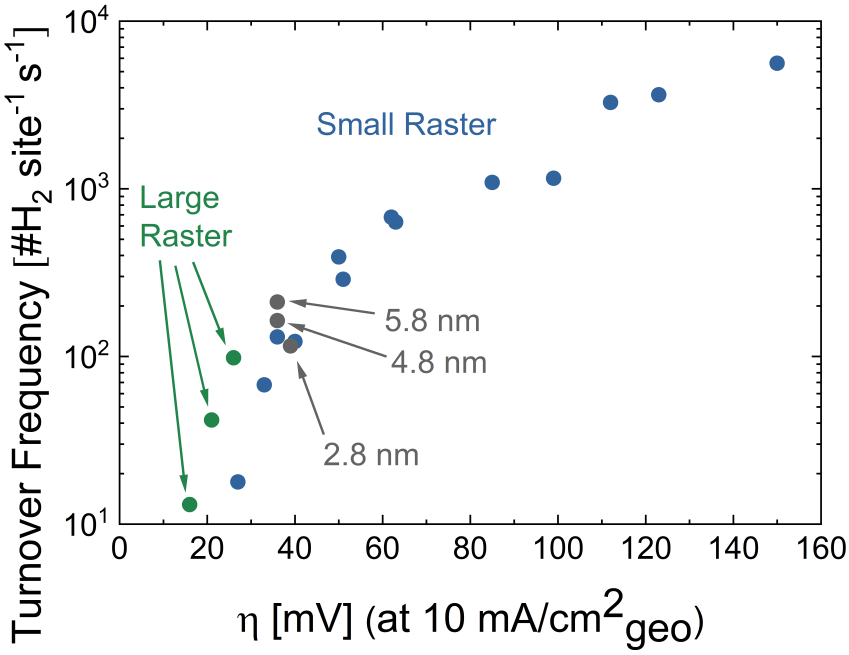

Figure 4.8: Intrinsic HER activity/TOF measured at a geometric current density of 10 mA/cm^2 plotted against the corresponding $\eta_{10\mathrm{mA/cm^2}}$. Small raster pattern (blue), large raster pattern (green), different particle sizes (gray).

tion will be obtained from STEM particle size analysis in the near future. Due to the use of a small raster pattern, the Pt loading is known. Additionally, the ECSA is determined by CO-stripping and the dependence on the loading is understood through a simple simulation. Ultimately, the fine control over the particle size, loading and ECSA, as well as the use of an Ir counter electrode, makes the system a well-defined Pt "benchmark" system. Note that the evolved H_2 was not measured using a mass spectrometer or similar as is recommended for earth-abundant catalysts [103], due to Pt being a well known HER catalyst.

The Pt "benchmark" system displays several indications of mass transport limitations affecting the HER activity. The difference in TOF at a given η in Figure 4.7 indicates mass transport limitations for all loadings. This is further indicated for the highest loadings deposited with the small and large raster patterns in Figure 4.8. Since the large raster samples display lower η for similar TOFs. Mass transport limitations in RDE measurements of the HER activity of Pt is an issue that has previously been reported[115, 119, 120]. The specifics of the mass transport limitations are not well known, but are likely due to a limited transport of protons to the catalyst surface. Alternatively, the limitation could be the transport of

molecular H_2 away from the catalyst surface. Ultimately, the difference between the two raster patterns cannot help in determining the type of mass transport limitations. Therefore, we are currently awaiting the results of theoretical simulations attempting to model this in detail. Consequently, the Pt "benchmark" system does not display the lowest possible $\eta_{10\mathrm{mA/cm^2}}$ for these j_{mass} and TOF. Instead the system serves as a lower bound for the expected HER activity from Pt nanoparticles measured in a RDE setup. Alternative measurements schemes such as floating electrodes may achieve higher mass/intrinsic activities [121]. This approach was chosen to prioritize the accuracy of the reported loadings.

The observed effect of Pt loading on the $\eta_{10\mathrm{mA/cm^2}}$ metric shows the importance of reporting catalyst loadings along with $\eta_{10\mathrm{mA/cm^2}}$ to allow for scientific comparisons [35]. Due to the range of loadings and HER activity metrics this system can serve as a Pt/C comparison for reports on novel earth-abundant catalysts for HER [103]. However, such comparisons must be performed properly depending on the purpose of the scientific study [12, 35]:

- To develop a novel catalyst with Techno-economically relevant performance for comparison to other materials, then the HER activity should be reported in A/$. This metric is a convolution of the cost of the material, catalyst structure and intrinsic activity. A suitable figure for comparison is $\eta_{x\mathrm{A/\$}}$, where x is set to a representative literature value.
- To show an increased HER current by a larger number of active sites per volume by novel structuring, the activity could be compared by $\eta_{10\mathrm{A/mg}}$.
- To develop a novel catalyst with a record breaking intrinsic activity, then the HER activity should be reported in TOF and could be compared by the metric of $\eta_{100\mathrm{H_2 site^{-1} s^{-1}}}$.

The exact value of x, 10 A/mg or 100 H_2 site^{-1} s^{-1} is not important as long as it is reported, but to ease comparisons a widely agreed upon standard value would be preferable. Finally, the metric of $\eta_{10\mathrm{mA/cm^2}}$ should not be used for comparisons of HER catalysts for PEM electrolysis since it has limited relevance and is heavily affected by the catalyst loading.

4.6 Conclusion

In conclusion, we have created a model system of mass-filtered Pt nanoparticles on a glassy carbon support using the Nanobeam cluster source. The Pt loading and coverage was narrowly controlled and the ECSA was experimentally determined, resulting in a well-defined Pt "benchmark" system. Due to the large range of Pt loadings from 13-5000 ng/cm^2 and the different HER activity metrics the system can serve as a literature comparison for future studies on novel HER catalysts.Due to mass transport limitations, the "benchmark" system provides a lower bound for

the HER activity measured in an RDE.

The system shows that increasing the Pt loading decreases the $\eta_{10\mathrm{mA/cm^2}}$. The HER activity ranges from $\eta_{10\mathrm{mA/cm^2}}$=150 mV for a Pt loading of 13 ng/cm^2 to $\eta_{10\mathrm{mA/cm^2}}$=16 mV for a loading of 5000 ng/cm^2 with the large raster pattern. In the same potential range, turnover frequencies range from 13 to 5,600 [$\#\mathrm{H_2\,site^{-1}\,s^{-1}}$]. The results emphasize the importance of always specifying the catalyst loading when reporting novel catalysts. Especially, earth-abundant catalysts, where catalyst loadings often exceed that of Pt by orders of magnitude [35]. Given the effect of loading and the limited relevance of the $\eta_{10\mathrm{mA/cm^2}}$ metric for PEM electrolyzers - mass activity and turnover frequency are more suitable metrics for this research field.

Chapter 5

Improving the CO Oxidation Performance of Gold

Current state-of-the-art low temperature CO oxidation catalysts are based on platinum group metals (PGM) that are active for CO oxidation above 150 °C [122]. Meanwhile, Au nanoparticles display high CO oxidation activity at much lower temperatures, but they suffer from stability issues [27, 123]. This chapter presents an ongoing study on Au/Ti alloys to increase the stability of Au nanoparticles for CO oxidation.

AuTi nanoparticles with sizes from 2.5 to 5.5 nm were deposited with the Nanobeam cluster source on SiO_x and thin film TiO_x in microreactors. The depositions along with XPS and ISS characterization was done by masters student Jens Ringsholm and myself. The CO oxidation performance was tested with the microreactor system by masters student Olivia Sloth and Ph.D. student Alexander Krabbe. ISS characterization after activity testing was performed on the Omicron system by Ph.D. student Karl Toudahl and myself. I would like to thank them all for a good collaboration. Finally, I used STEM imaging to characterize the particle structures and sizes. This study is still ongoing and the results presented here are therefore preliminary.

5.1 Low Temperature CO Oxidation Catalysis

Low temperature CO oxidation takes place in the catalytic converters in automotive exhausts to reduce the emission of toxic molecules from the internal combustion engine [122]. The converter consists of a highly porous "honeycomb" structure coated in a catalyst that can convert toxic molecules such as CO, NO_x and other pollutants into less harmful alternatives [124]. Approximately 4 grams of PGM per vehicle is used to catalyze the reactions [122] and due to the scarcity of PGM

materials, this comes with a high cost. An additional challenge with the PGM catalysts is their low activity at room temperature. These catalysts do not display a sufficient activity towards CO oxidation until reaching temperatures of around 200 °C [125]. Thus the toxic molecules are not oxidized until the catalytic converter reaches the operating temperature. Consequently, the majority of the pollution from the internal combustion engine is emitted within the first 5 minutes of use [125]. Considering the current trends moving towards sustainable vehicles such as battery powered electric vehicles, CO oxidation may not appear to be the most relevant focus of future research. However, the transition to sustainable transportation is slow and according to some forecasts, more than half of the vehicles on the roads will still be running on fossil fuels in 2050 [126].

5.1.1 Alternatives to Platinum Group Metal Catalysts

A suitable alternative to PGM catalysts in catalytic converters would either have to be cheaper or have lower operating temperatures to compete with PGM catalysts. One alternative that has been shown both experimentally [27, 28, 123, 127] and theoretically [21] to be superior to Pt at low temperatures is gold. Au nanoparticles have been shown to catalyse CO oxidation at temperatures as low as -70 °C [123] and could be used instead of PGM to reduce the initial CO emission.

The initial discovery of Au being active for CO oxidation was surprising given that Au was considered inert. However, when the particle size is reduced to less than 8 nm, the particles become active [123]. The effect of nanoparticle size has been further studied with two groups finding a sharp optimum in the turnover frequency (TOF) for a particle size of 3-3.5 nm [127, 128] seen in Figure 5.1. However, both these studies suffer from a broad size distribution with overlapping standard deviations, causing uncertainty about the exact position of the optimum. The cause of the particle size effect is not agreed upon. Haruta and co-workers speculate that it is due to the perimeter length of the Au-TiO_2 interface, which is increased for smaller particles [28, 128]. Meanwhile, Goodman and co-workers argue that the increased ratio of undercoordinated sites is the reason for higher TOF for smaller particles. This is in agreement with theoretical studies that ascribed the size effect to the CO binding energy [129] and the number of undercoordinated sites on the surface of the Au nanoparticles [130]. To explain the decrease in TOF for smaller particles, Goodman et al. have performed extensive studies which show, that as the Au particle size decreases below 3 nm, the particles develop an electronic bandgap that decreases the activity [131, 132].

Similar to particle size, the choice of support was also shown to have an impact on the CO oxidation activity of Au nanoparticles. Au nanoparticles are active on reducible oxide supports such as Co_3O_4, α-Fe_2O_3 and TiO_2, while on non reducible supports such as SiO_2 they display poor activity [27, 28, 123, 132]. This has been ascribed to the strong metal-support interaction of Ti that alters the electronic state of the Au, making it more active [133–136]. The metal-support interaction

was studied for mass-selected Au clusters < 20 atoms, which showed that the CO binding energy of a single Au atom decreases when bound in an oxygen vacancy in a defected TiO_2 surface [137]. Additionally, larger clusters such as Au_8 displayed an activation for CO oxidation when bound in oxygen vacancies of the MgO support [33, 138, 139]. Thus the defect state of the oxide support appears to influence the CO oxidation activity.

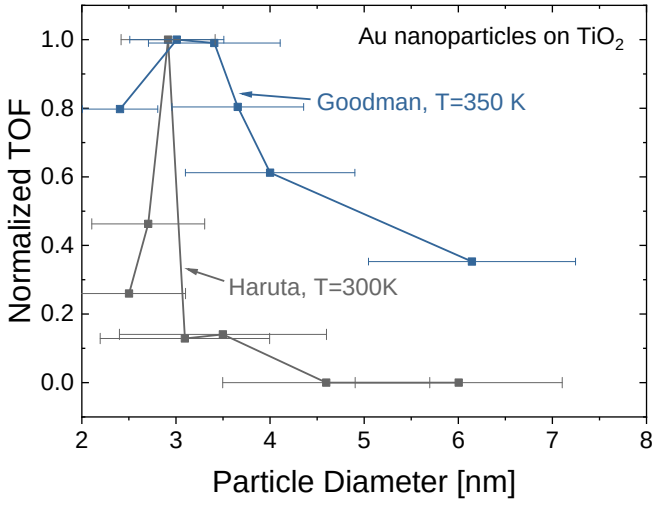

Figure 5.1: Normalized TOF vs. particle diameter for Au nanoparticles on TiO_2 support with values from literature [127, 128].

5.1.2 The Stability Issues of Au

One of the major drawbacks of CO oxidation with Au nanoparticles on TiO_x is their lack of stability. Au nanoparticles have shown degradation due to sintering through Ostwald Ripening [127, 140], which consists of the migration of individual atoms from smaller particles to larger particles. Therefore research efforts have been focused on reducing sintering through different strategies such as reducing the TiO_x support to create defect sites [141], which bind the Au atoms stronger [137]. Another approach was doping a Mo single crystal with Ti to create nucleation sites for Au atoms [134]. Alternatively, applying an appropriate pre-treatment by annealing in hydrogen atmosphere has been shown to strengthen the strong metal-support interaction betwen Au and Ti, stabilizing the Au particles [142]. Recently our group, together with collaborators, reported an alternative approach based on alloying Au with Ti [143]. AuTi nanoparticles were deposited with a cluster source onto a SiO_x support and displayed reduced electron beam induced sintering compared to pure Au nanoparticles.

Inspired by the increased stability under the electron beam, the CO oxidation activity and stability of AuTi nanoparticles was tested by deposition on TiO_x and SiO_x thin films in a microreactor. The particle size was varied to examine the previously reported size effect and in an attempt to achieve the optimal AuTi nanoparticle size considering the structural differences compared to a Au nanoparticle [132]. Additionally, we tested Au nanoparticles on the two supports to have a comparable reference for the AuTi particles. Looking beyond the scope of CO oxidation, this study has a conceptual nature in its attempt to show that unstable particles can be self-anchoring through alloying with a stabilizing element. This has relevance for a wide range of reactions because nanoparticle sintering is a common problem in the field of catalysis [20].

5.2 AuTi Model System

As CO oxidation is a gas-phase reaction, the catalytic performance was tested with the microreactor system. The microreactor has a SiO_x surface in the reactor volume, which was used as a support for the AuTi and Au nanoparticles produced in this study. In addition to the SiO_x support, a 100 nm thin film of TiO_x was deposited on the reactor volume to compare the performance of the catalysts on both the SiO_x and TiO_x support. The TiO_x films were deposited by Alexander Krabbe using the magnetron sputter chambers available at SurfCat.

The AuTi nanoparticles were deposited using a Au/Ti 50/50 at% alloy target (Courtesy of Richard Palmer) in the Nanobeam cluster source. In addition to the Au/Ti target, a pure Au target (AJA, 99.99% purity) was used to deposit Au nanoparticles. All particles were deposited with a bias of 48 V, which is in the soft-landing regime. A coverage of 5 % of a monolayer was used for all samples to obtain measurable activity vs. temperature ramps before reaching full conversion. The particles were deposited using the meander raster pattern shown in Figure 2.6b with a side length of 9 mm, ensuring that all the particles land within the reactor volume and are homogeneously dispersed. Before depositing particles, the microreactors were sputtered for 40 minutes with 1 keV Ar^+ and a sample current of 1 μA to clean the surface of any adventitious carbon. AuTi nanoparticles were also deposited on lacey carbon Cu TEM grids to image the particles with STEM.

An overview of the sample types is seen in Table 5.1. The equivalent particle size for the AuTi particles, was calculated from the density of a 50/50 at% AuTi alloy [144] since this is the composition of the target and the composition of the particles was initially unknown. To refer to specific samples I will name them by Size Particle Type/Support, so 2.5 nm Au/SiO_x for 2.5 nm Au nanoparticles on the SiO_x support.

Table 5.1: Overview of the different types of samples made for the AuTi study on the two different supports showing particle mass and equivalent particle size calculated assuming spherical particles with a bulk density of Au:19.3 g/cm^3 and AuTi:11.9 g/cm^3.

Particles	Support	Mass [amu]	Equivalent Particle Size [nm]
Au	SiO_x	100k	2.5
Au	TiO_x	100k	2.5
AuTi	TiO_x	70k	2.7
AuTi	SiO_x	70k	2.7
AuTi	SiO_x	160k	3.5
AuTi	SiO_x	350k	4.5
AuTi	SiO_x	620k	5.5

5.2.1 AuTi Composition

Even though the AuTi target has a 50/50 Au/Ti at% composition, the particles do not necessarily grow to the same composition. Therefore the ratio of Au/Ti was checked with XPS on 2.7 nm AuTi/SiO_x on the Thetaprobe XPS instrument. A representative XPS spectrum is shown in Figure 5.2 with the inserts showing the detailed scans of the Au 4f and Ti 2p regions used for quantification.

The XPS survey spectrum shows the presence of O, Ti, Si, Au and no detectable contaminants. A small N peak was visible in some spectra, which is possibly an impurity from the clean room processes used to fabricate the microreactors and the C peak is from transferring through air before performing XPS. Six different 2.5 nm AuTi/SiO_x samples were quantified resulting in an average Au/Ti atomic composition of $30/70 \pm 1.8$ %. The Au/Ti composition appears highly reproducible for the same size. However, previous work on alloy nanoparticles produced from the Nanobeam cluster source has shown that varying particle sizes display different alloy compositions. XPS measurements of the remaining particle sizes from Table 5.1 are yet to be performed. The Ti $2p_{3/2}$ peak position at 458.5 eV Ti 2p peaks indicates that Ti is oxidized, while the Au $4f_{7/2}$ peak at 84 eV corresponds to metallic Au [45].

5.2.2 AuTi Structure and Size

A representative set of ISS spectra for 2.5 nm AuTi/SiO_x and AuTi/TiO_x are shown in Figure 5.3a and b (grey), respectively. The spectra display peaks corresponding to O, Si, Ti and Au with no detectable contaminations present. Furthermore, they show that the amount of Au on the surface varies considerably for 2.5 nm AuTi on both types of support,despite a constant Au/Ti ratio determined from XPS. Representative ISS spectra of the 2.5 nm Au/SiO_x and Au/TiO_x samples are shown in Figure 5.3(gold). The spectra show that the Au particles are

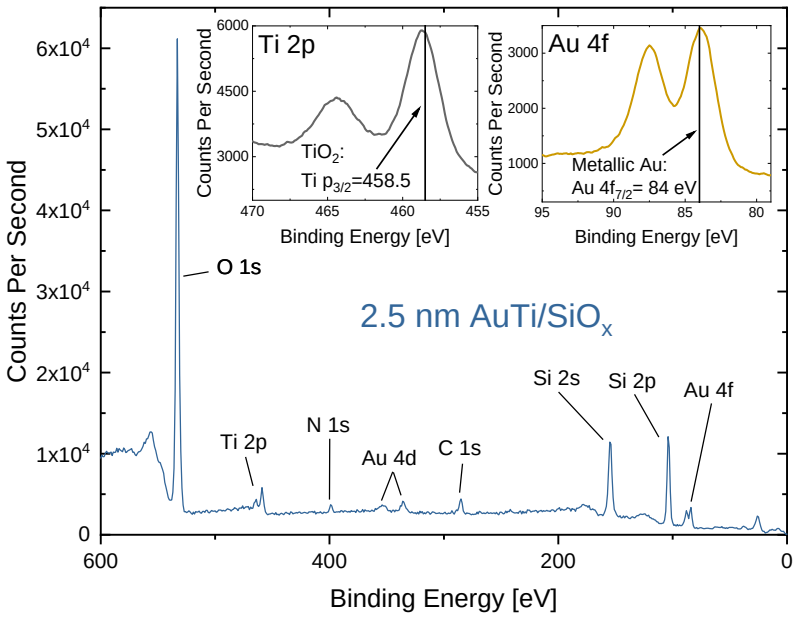

Figure 5.2: Region of survey XPS spectrum of 2.5 nm AuTi/SiO_x displaying peaks from O, Ti, Si, Au, C and N. **Insets:** detailed scans of the Ti 2p and Au 4f peaks for quantification of the Au/Ti ratio. The binding energy of the spectrum was calibrated to the adventitious carbon peak at 284.8 eV.

on the surface of the supports and display significantly higher Au intensities than AuTi, which is expected since the particles are pure Au.

The structure of the AuTi nanoparticles was examined using STEM images acquired with a pixel size of 0.1 nm. The particles appear to have a shell of a lighter element and a core of a heavier element as seen from the dark shell and bright core in Figure 5.4a. Additionally, an EDS line scan (Figure 5.4c) indicates that Ti originates from a larger area than Au. This indicates that the nanoparticles are not a homogeneous alloy of Au and Ti, but instead phase-separated Au and Ti. The active element of the particles is Au, therefore the relevant particle size is the Au core size. Using the "Threshold" and "Analyze Particles" functions in the ImageJ software the size of the Au cores was determined from the STEM images. The Au cores for the 2.5, 3.5, 4.5 and 5.5 nm particles are 1.7, 3.0, 3.4 and 4.0 nm in diameter respectively. These sizes should be used when comparing the CO oxidation activity of the AuTi particles to pure Au particles.

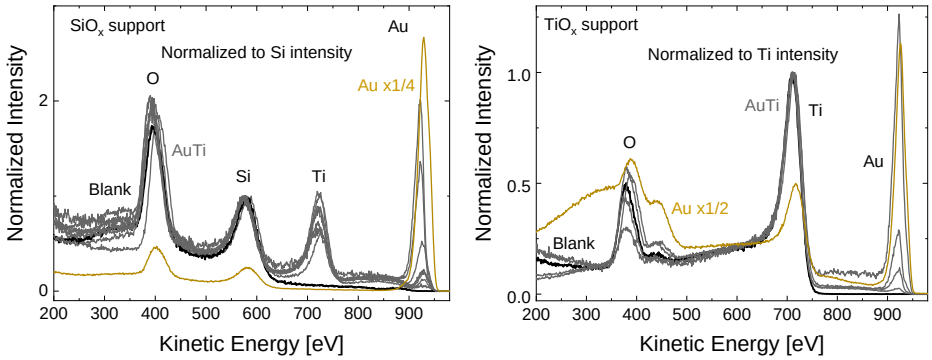

Figure 5.3: ISS spectra of microreactors without particles (black), Au 2.5 nm particles (gold) and AuTi 2.5 nm particles (grey) on **a)** SiO_x support and **b)** TiO_x support. The spectra are normalized to the intensity of the a) Si and b) Ti peaks.

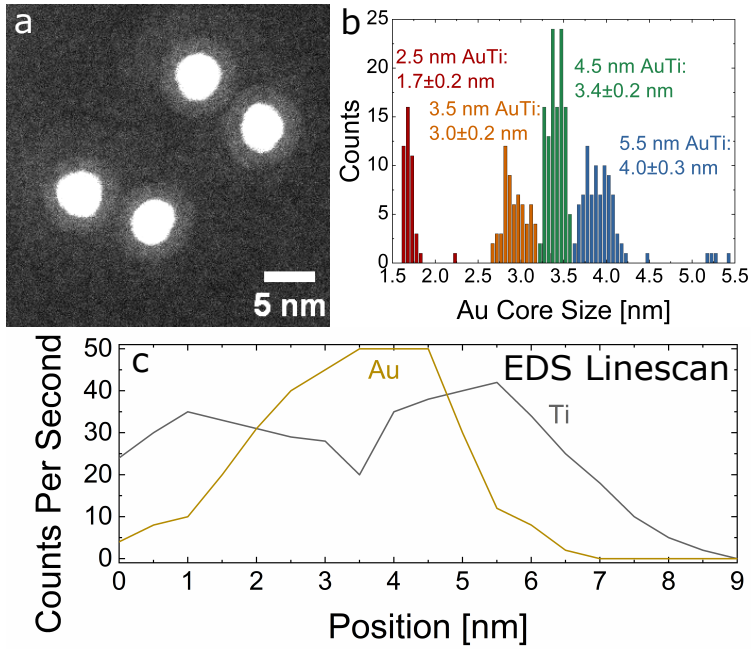

Figure 5.4: a) STEM image of the 4.5 nm AuTi nanoparticles on a lacey carbon support. The brightness was enhanced to show the dark shell. **b)** Au core size distributions for the 2.5, 3.5, 4.5 and 5.5 nm AuTi particles. **c)** EDS linescan across a 5.5 nm AuTi nanoparticle showing the Au and Ti profiles.

5.2.3 Discussion of AuTi Structure

Considering the phase separation of Au and Ti seen in Figure 5.4 and the presence of Au on the surface determined by ISS in Figure 5.3, it appears that the structure resembles a Au or Au/Ti core with a surrounding Ti nest/shell. The variation in Au on the surface indicates that the Ti creeps up onto the Au core in various degrees, possibly due to the strong metal-support interaction of Ti [133, 142]. Similar structures were seen by Tang and co-workers, but with considerably less Ti present [142]. They reported that the degree of Ti coverage depends on factors such as annealing temperature and gas atmosphere and ultimately showed that increasing the strong metal-support interaction increases the stability of Au nanoparticles. Mass-selected CoAu particles have been reported to show a CoAu core with a partial CoO_x shell, indicating this structure is probable from gas aggregation cluster sources with Au alloy targets [145]. The phase separation seen in the STEM image in 5.4 was observed on a carbon support, however TEM images (Appendix A) of 2.5 nm AuTi particles on a SiN film show an identical stucture. Thus it is probable that the particle structure is not an effect of the carbon support, but we are currently looking at confirming this with further STEM studies.

5.3 CO Oxidation Activity of AuTi

The microreactor measurements and data treatment was performed by Masters students Olivia Sloth and Jens Ringsholm, and Ph.D. student Alexander Krabbe. The standard testing procedure is shown in Figure 5.5. First the microreactor and adjoining tubing is flushed with Ar gas and evacuated, twice. Next the 1:1:1 gas composition of Ar:CO:O_2 is flowed through the reactor for 30 minutes to fill the reactor volume and ensure a stable flow. The temperature is ramped to 250 °C with 4 °C/min and held at 250 °C for 1 hour. Finally the temperature is ramped back down to room temperature with a ramp of 4 °C/min. This was repeated 2-3 times to check for short term stability. The gas from the outlet of the microreactor is flowed to a quadrupole mass spectrometer (QMS) to quantify the different gases in the outlet.

The CO oxidation activity is measured from the intensity of the CO_2 signal in the QMS that has been calibrated to an absolute flow [pmol/s] by Alexander Krabbe. Since the absolute levels in the QMS vary throughout the measurement, the CO_2 signal is normalized by the Ar signal, which is inert in the reaction. The normalized signal is termed the calibrated CO_2 signal. Thus for full conversion of CO to CO_2 the calibrated signal should go to 1. This is observed for all samples except 2.5 nm AuTi/SiO_x, which we speculate is due to an error in the CO mass flow controller for this measurement. The catalytic activity is compared at 75 °C, which was evaluated to be far from full conversion, to measure the reaction kinetics instead of the thermodynamic equilibrium [20]. Due to issues with the resistance temperature detector (RTD) in the microreactors, the temperature is measured with a thermocouple on the top of the microreactor. This gives a temperature

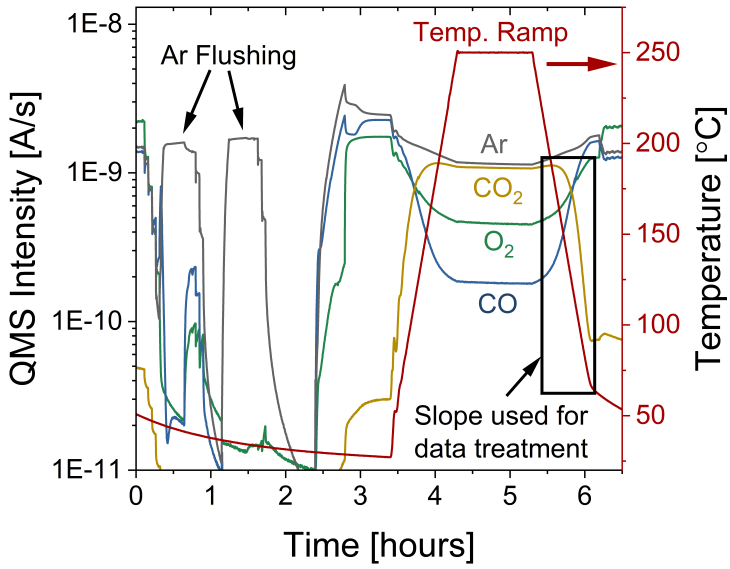

Figure 5.5: Example of raw data for a CO oxidation measurement in the microreactor. Argon flushing is performed twice before heating to 250 °C for 1 hour and then ramping back down. As the temperature increases and CO oxidation begins, the CO and O_2 signals drop and the CO_2 signal increases. The black box indicates the CO_2 signal slope that is used for the data treatment shown in the following.

reading that is estimated to be 25 °C lower than the actual temperature in this range, thus the temperature scale should only be used for internal comparison. Finally, to avoid any influence from possible activation phenomena the CO_2 vs. temperature data shown below is from the ramp down in temperature after 250 °C in the testing procedure.

5.3.1 Contamination Issues

Ar^+ sputtered and pristine microreactors were tested for CO oxidation to obtain a background measurement to compare with the Au and AuTi nanoparticles. Some of the pristine SiO_x microreactors displayed an activity with an onset around 130 °C reaching full conversion around 150 °C as seen in Figure 5.6. The ISS spectrum at high masses of a pristine SiO_x microreactor is shown in blue in the inset displaying a peak corresponding to 100-120 amu. Meanwhile pristine TiO_x reactors displayed almost no activity with a slight onset around 225 °C and never reaching full conversion. A SiO_x microreactor was sputtered with 1 keV Ar^+ for 40 minutes - similar to the treatment before depositing Au/AuTi nanoparticles. ISS after sputtering, shown in green in the inset of Figure 5.6, displays small peaks corresponding to masses around 100-120 amu and 190-200 amu. These peaks have several orders of magnitude lower intensity than the Si and O peaks not shown in this inset. The sputtered SiO_x displayed little CO oxidation activity with a slight onset around 150 °C, never reaching full conversion.

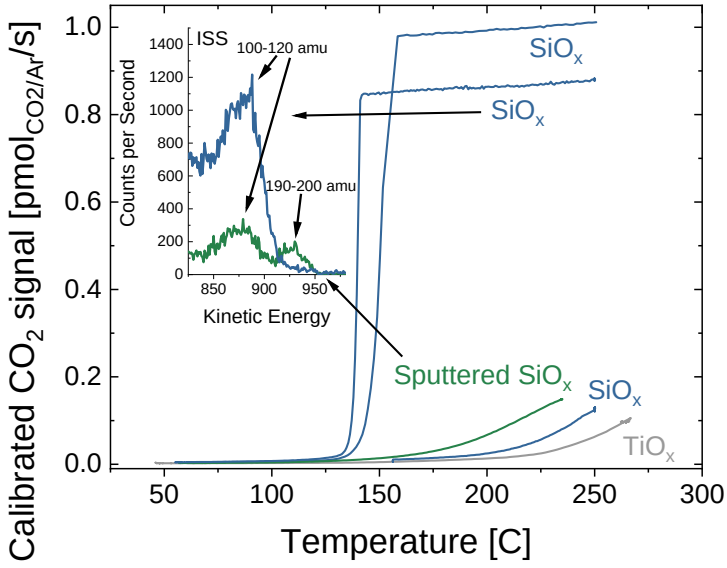

Figure 5.6: Calibrated CO_2 signal vs. temperature for a number of pristine SiO_x microreactors and a pristine TiO_x microreactor along with a SiO_x microreactor sputtered 40 minutes with 1 keV Ar^+. **Inset:** A region of the ISS spectrum for the pristine and sputtered SiO_x microreactor showing contaminants from 100-120 amu and 190-200 amu.

For further analysis of the contaminants, Olivia Sloth placed a droplet of Aqua Regia on the reactor volume of a pristine SiO_x microreactor and subsequently analyzed it with ICP-MS, which showed traces of Pd and Pt. Pd and Pt are well known CO oxidation catalysts with a mass of 106 and 195 amu, corresponding to

the ISS peaks in the inset. It appears that Ar sputtering has removed significant amounts of the contamination leading to a greatly reduced activity. Since all the microreactors are sputtered with these conditions before depositing, the activity originating from these contaminations is not expected to affect the Au and AuTi activity measurements. Nonetheless, it must be kept in mind when analyzing the CO oxidation measurements if activity onsets are observed at these temperatures.

5.3.2 Reproducibility Issues

Figure 5.7 shows the calibrated CO oxidation activity of 4 different 2.5 nm AuTi/SiO_x reactors. The 4 reactors display varying activities with only 1 active reactor that goes to full conversion. It appears there is an issue with reproducing the activity of the 2.5 nm AuTi/SiO_x nanoparticles across multiple samples. The Au region of the ISS spectra measured immediately after deposition for the 4 reactors is shown in the inset in Figure 5.7. The ISS spectra show no correlation between the CO oxidation activity and the Au ISS intensity measured immediately after deposition.

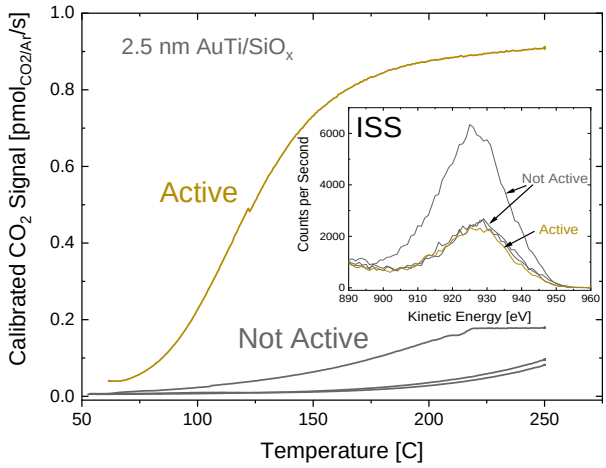

Figure 5.7: Calibrated CO_2 signal vs. temperature for four 2.5 nm AuTi/SiO_x reactors with different CO oxidation activities. **Inset:** ISS Au peaks acquired immediately after depositing the nanoparticles.

After the microreactor measurements, an active and an inactive 4.5 nm AuTi/SiO_x reactor, similar in behaviour to the 2.5 nm AuTi/SiO_x in Figure 5.7, was cut open. ISS sputter profiles were performed on the two reactors by multiple iterations of ISS and Ar^+ sputtering. The two ISS sputter profiles were normalized to the intensity of the Si ISS peak and are shown in Figure 5.8. The active reactor in Figure 5.8a displays an Au peak immediately after activity testing and the peak is increased by sputtering with He^+ and Ar^+ until 40 minutes accumulated Ar^+ sputtering. Meanwhile, the inactive reactor in Figure 5.8b displays no Au peak immediately

after activity testing, but a small peak after an accumulated 10-20 minutes of Ar^+ sputtering. The intensity of the largest Au peak in the two reactors is vastly different from 25k counts for the active reactor to 500 counts for the inactive reactor. The results in Figure 5.8 show that the CO oxidation activity is correlated to the amount of Au on the surface after activity testing. The intensity of Ti on the surface varied minimally.

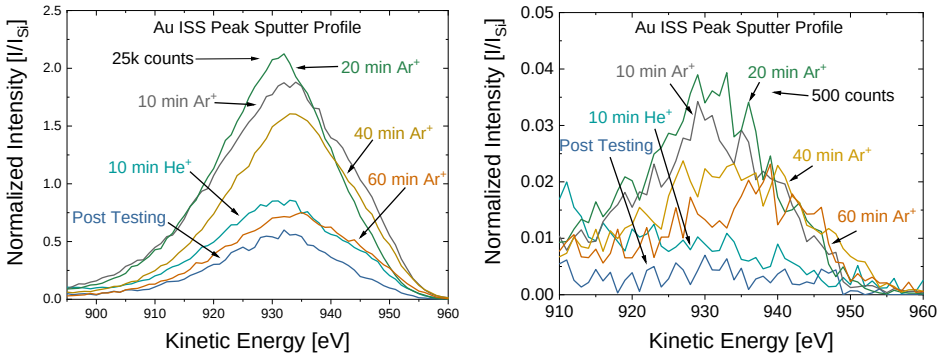

(a) Active 4.5 nm AuTi/SiO_x **(b)** Inactive 4.5 nm AuTi/SiO_x

Figure 5.8: ISS sputter profile spectra of an active and an inactive 4.5 nm AuTi/SiO_x reactor. Sputtering was performed with He^+ and Ar^+.

The deposition conditions for the four 2.5 nm AuTi/SiO_x reactors are almost identical as shown in Table 5.2. Considering the identical deposition conditions and compositions determined from XPS it is unexpected that they display varying Au ISS peak intensities and CO oxidation activity. This is an issue we are still trying to resolve. Though the activity cannot be consistently reproduced, several AuTi/SiO_x systems display activity indicating the observed activities are from the AuTi particles.

Table 5.2: Deposition conditions for the 2.5 nm AuTi/SiO_x microreactors shown in Figure 5.7.

Activity	Active	None	None	None
Ar flow [ml/min]	34	33	33	33
He flow [ml/min]	82	82	82	82
Magnetron Power [W]	21	21	21	21
Aggregation Zone Pressure [mbar]	0.13	0.13	0.13	0.13
Substrate Bias [V]	48	48	48	48

5.3.3 CO Oxidation Activity

Figure 5.9 shows the Au mass normalized CO_2 signal vs. temperature for the different microreactors that were tested. The signal for the Au particles is normalized by the total Au mass calculated from the deposition current and the particle mass. The Au mass in the AuTi particles is estimated from the Au core size distribution and assuming spherical particles with a bulk Au density of 19.3 g/cm^3. The ideal measure for catalytic activity is the TOF. However, this requires knowledge of the exact number of sites. This could potentially be estimated, but I feel that our knowledge of the AuTi structure is too uncertain for such an estimation to be other than speculation. Therefore the mass activities are used, which are interesting from an economic standpoint as discussed previously. Only one reactor of each type displayed CO oxidation activity, except for 2.5 nm Au/TiO_x where two reactors displayed similar activities. The mass-activities are shown in Figure 5.9. Examining Figure 5.9 it is immediately apparent that 3.5 nm AuTi/SiO_x and 2.5 nm Au/SiO_x are not active for CO oxidation. This was expected for the 2.5 nm Au/SiO_x sample [123]. Additionally it is clear that 2.5 nm AuTi/TiO_x by far is the most active with a much lower onset temperature than the other reactors. Meanwhile at 75 °C 5.5 nm, 4.5 nm, 2.5 nm AuTi/SiO_x and 2.5 nm Au/TiO_x display comparable CO oxidation activities. 5.5 nm AuTi/SiO_x displays the highest activity followed by 4.5 nm AuTi/SiO_x and 2.5 nm Au/TiOx, which are similar in activity considering the uncertainty in temperature. The 2.5 nm AuTi/SiO_x sample displays the lowest activity.

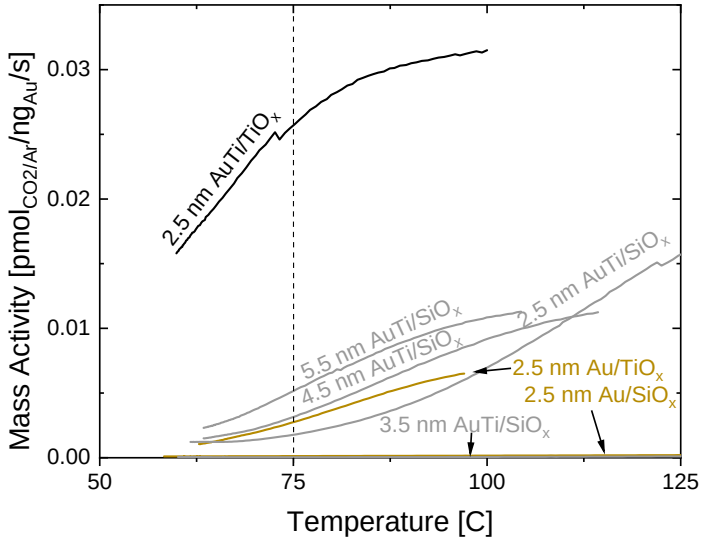

Figure 5.9: Mass normalized calibrated CO_2 signal vs. temperature for the Au/SiO_x, Au/TiO_x, AuTi/SiO_x and AuTi/TiO_x reactors. The vertical dotted line indicates the 75 °C temperature, where the mass activity is compared.

Considering that Au is known to be active on TiO_x supports, the activity of 2.5 nm $AuTi/TiO_x$ is not surprising. However, it is surprising that it displays significantly higher CO oxidation mass activity than 2.5 nm Au/TiO_x considering both active sites are Au. The CO oxidation activity of $AuTi/SiO_x$ nanoparticles is a novel discovery that to my knowledge has not been shown before. Finally, the lack of activity for the 3.5 nm $AuTi/SiO_x$ sample is probably due to the reproducibility issues since both smaller and larger particles are active.

5.4 Discussion of the CO Oxidation Activity

Considering the early onset of CO oxidation on Au and AuTi nanoparticles, the contaminations do not appear to influence the CO oxidation measurements. The size dependent results presented here show that 4.5 nm and 5.5 nm $AuTi/SiO_x$ are more active than 2.5 nm Au/TiO_x. However, their Au core is 3.4 and 4.0 nm respectively and the Au particles are 2.5 nm, thus considering the reported size effects [28, 141], more Au particle sizes must be tested. Otherwise the comparison is influenced by a convolution of particle size effects and structural effects. By comparing only the $AuTi/SiO_x$ particles it becomes evident that within the size range we examined, the 5.5 nm particles with a 4 nm Au core are the most active. Compared to literature this is 0.5-1.0 nm larger than the optimum, but the particle size effect has been argued to depend on the structure of the metal-support interface [28, 132]. Therefore it is possible that the optimal particle size may be shifted for particles with a different interface structure such as the AuTi nanoparticles. Testing of larger particle sizes is on-going to find the optimum size for the AuTi particles. Furthermore, since these results are based on one reactor per size, repeated tests of these sizes are necessary. This is yet to be done due to the issues with reproducibility.

From the variations in the Au ISS peak of the as-deposited AuTi particles and the lack of reproducible CO oxidation activities for similar reactors, it is clear that the particles are not completely identical for samples with particles of the same size. This is unexpected considering the consistent particle compositions and deposition conditions. Additionally, there does not appear to be a correlation between the amount of Au on the surface of the as-deposited particles and the CO oxidation activity. Instead the activity is correlated to the amount of Au on the surface after testing the activity. The sputter profile shows that Au is covered by Ti in the inactive samples, which can be explained by the strong metal-support interaction [142]. The mass-selected CoAu particles displayed changes in the CoO_x shell at elevated temperature [145]. Perhaps the same is occurring for some of the AuTi particles, resulting in a passivating TiO_x shell. Additionally, the Au ISS peak intensity is considerably lower in the sputter profile on the inactive sample, indicating that the particles may have agglomerated or sintered into larger particles. However, if this was the case, we would still expect to see a Au ISS peak that was significantly larger than 500 cts. Reducing the amount of Ti in the particles may help to ensure

that all samples are active. This is possible by switching to a metal target with a different alloy composition such as 80% Au/ 20% Ti or by using new cluster source designs with a multiple magnetron setup to tune the composition from two separate targets. This has been shown to produce core shell structured $AuTiO_x$ particles [146] and such a cluster source has recently been installed at SurfCat. Multiple magnetron cluster sources also allow for controlling the composition, which could prove interesting for AuTi particles for CO oxidation [147]. Alternatively, pre-treatment of the catalyst may be able to increase the activity and stability as has been shown to be crucial for Au nanoparticles on TiO_2 in other systems [28, 142].

The purpose of this study was to examine if AuTi nanoparticles were a more stable alternative to Au nanoparticles. So far we have seen indications that AuTi particles on both SiO_x and TiO_x supports can match and exceed Au in CO oxidation mass activity. However, the instability of Au nanoparticles on TiO_x due to Ostwald ripening is the most prominent issue. The AuTi nanoparticles on a SiO_x support have previously been reported to display increased stability against sintering under an electron beam [143]. However this was under much lower temperatures and pressures, than the particles experience during CO oxidation testing. Therefore the stability of these particles must be investigated in the microreactor system and compared to the stability of Au/TiO_x.

5.5 Conclusion

In conclusion we have used the Nanobeam cluster source to produce mass-selected Au and AuTi nanoparticles on SiO_x and TiO_x supports in microreactors. Using ISS, XPS and STEM EDS, the 2.5 nm AuTi particles were determined to have a 30/70 Au/Ti composition with a structure that resembles a Au core nested in Ti.

Of the novel catalysts tested here, the 2.5 nm $AuTi/TiO_x$ sample was by far the most active with regards to mass activity and onset temperature. Of the $AuTi/SiO_x$ systems, the 5.5 nm, 4.5 nm and 2.5 nm particles displayed CO oxidation activities. The two largest particle sizes were competitive to the Au particles on TiO_x, while a full comparison requires further testing of various nanoparticle sizes. A caveat to these results is a reproducibility issue that remains to be solved before a complete test of particle sizes can be used to draw firm conclusions on their relative activity and stability performance. The lack of reproducibility was attributed to variations in the amount of surface Au after testing the CO oxidation activity. Finally, before the $AuTi/SiO_x$ and $AuTi/TiO_x$ systems can be considered as an alternative to the well known Au/TiO_x system, a thorough study of the particle stabilities must be performed.

5.5.1 Outlook

As mentioned this is an ongoing study so many experiments are already planned, but remain to be completed. I will give a brief overview of the plans here. First, the reproducibility of AuTi/TiO_x will be examined as this appears to be superior to the AuTi/SiO_x system. Next, the effect of particle sizes must be studied for the AuTi/TiO_x and Au/TiO_x systems for proper comparison of particle sizes. Ultimately, reproducing activities on the AuTi/SiO_x system may require changing the deposition procedure to reduce the Ti content in the nanoparticles. Either by use of another alloy target or another cluster source.

The exact structure of the AuTi nanoparticles is interesting considering the proposed structural effects for Au nanoparticles on a Ti support [132]. Since CO oxidation is a gas-phase reaction it is ideal for studying in-situ. Using an ETEM it is possible to study gas-phase reactions in-situ at atmospheric pressures and temperatures up to 1000 °C [148, 149]. CO oxidation on Pt has been studied in ETEM by others revealing interesting structural and oxidation effects [150, 151]. Therefore, we plan to perform in-situ studies of CO oxidation of AuTi nanoparticles to obtain knowledge on the sintering process and perhaps the role of Ti. I have performed a preliminary study that is included in Appendix A, since only limited conclusions can be drawn from the images without similar studies on Au particles for comparison.

Chapter 6

Developing a Model System for Single Atoms and Small Clusters

Breaking the scaling relations of adsorbate binding energies to a catalyst surface is the focus of many research groups attempting to make major advancements to the field of catalysis. In practice, this is achieved through finding new scaling relations that scale closer to the optimal binding energies. One such route is the development of single atom catalysts , which has been inspired by the high activity and selectivity of homogeneous catalysts that are often structured around a single metal atom [152]. Additionally, SACs allow for complete utilization of non-abundant catalyst materials since all atoms are on the surface and can act as active sites, increasing the cost efficiency of the catalyst.

This chapter describes the on-going development of a model system for single atoms and small clusters for electrochemical reactions and the results presented here are therefore preliminary. The development includes producing the model system along with identifying and tuning suitable characterization- and electrochemical testing techniques. Similar to the other chapters, this is a collaboration between a number of people at SurfCat. I started this project at the beginning of my Ph.D. studies and have been developing the model system and the necessary techniques for producing and characterizing the system. In the first 6 months electrochemical testing was performed by former Ph.D. student Claudie Roy and since by Ph.D. student Johannes Novak Hansen. Recently Karl Toudahl has joined the project as a Ph.D. student working alongside me on the cluster source. Finally, STM imaging has been performed by Ph.D. student Miriam Galbiati and Postdoc Arlette Ngankeu. I would like to thank them all for their contributions to this work.

6.1 Catalysis with Clusters - Approaching the Single Atom Limit

Homogeneous catalysts, often structured around a single metal atom center, are highly active and selective, but unstable and catalyst/product separation is difficult [152, 153]. On the other hand, heterogeneous catalysts are stable and the catalyst and product are easily separated, but they display lower catalytic activity and relatively poor selectivity. One of the new frontiers in catalysis research is the development of single atom catalysts (SAC)(alternatively termed single site catalysts (SSC)) [152–154]. SACs are viewed as a bridge across the gap between homogeneous and heterogeneous catalysts [152–154] by stabilizing atomically dispersed reactive metal atoms on a solid support. They are proposed to display high selectivity due to site uniformity, whereas nanoparticles have a distribution of site types due to their crystalline structure [153, 155]. From an economic standpoint, dispersing the non-abundant metals as single atoms is the ultimate utilization of the materials leading to a high cost-efficiency. Considering the structural properties that affect catalytic performance, SACs have several interesting aspects. First of all they are extremely undercoordinated with regards to neighbouring metal atoms which may lead to reactivity that differs from nanoparticles of the same material. Additionally, due to their sub-nanometer size, their d-band energy levels are quantized and novel quantum size effects may arise [30, 31, 44]. Finally, strong metal support interaction is proposed to affect the catalytic performance [155], the extent of this effect is currently unknown.

Despite the recent surge in interest for SACs, they are not a new discovery with the earliest experimental reports more than 20 years ago [32, 33, 156, 157]. However, the development of SACs has been hindered by the high surface energy of the single atoms, which leads to considerable aggregation even at low loadings [153, 155]. This prompted the development of different anchoring strategies that stabilize the single atoms even under reaction conditions [152–155, 158, 159]. Most of the reported SACs are synthesized through wet chemistry approaches and generally speaking there are three different anchoring strategies [153]: defect engineering in oxide supports, spatial confinement in metal-organic frameworks and coordination of single atoms by other elements in carbon defects. Due to the large number of different SAC structures and synthesis procedures, I will limit myself to describing the structure that inspired our model system design - namely anchoring through nitrogen coordination in a carbon matrix.

6.1.1 Anchoring Single Atoms by Nitrogen Coordination

One of the most common anchoring strategies is coordination of a transition metal single atom with nitrogen atoms or defects (N-defects) in a carbon matrix [152, 153, 155, 158, 159]. There are two commons synthesis routes for these structures.

First, pyrolysis of metal salt precursors and N containing precursors along with a sacrificial metal organic framework support [152, 160, 161]. Exchanging the metal salt precursor for another metal allows this technique to generate well dispersed sites for a range of different metals [162, 163]. The second approach is annealing graphene and a metal precursor in a NH_3 atmosphere at $\approx$ 900 °C[164–166]. Using EXAFS measurements and fitting, Zitolo and co-workers identified Fe single atoms to be anchored by coordination to 4 N-defects in the carbon surface [167]. Additionally, they showed a high uniformity of the sites. The coordination of a single Fe atom to 4 N atoms in a carbon matrix is similar to the structure of the "Heme" subgroup of the organic compounds known as porphyrins [168]. Therefore the anchoring of a single metal atom to 4 N-defects is known as a porhpyrin like structure in SAC literature. The porphyrin like structure has been observed by several research groups using EXAFS fitting and appears to be common for anchoring single atoms with N in a carbon matrix [166, 169]. A porphyrin like site was imaged by Zelenay and co-workers using aberration corrected STEM of Fe single atoms on few layer thick graphene sheets [169]. Meanwhile, other groups have shown pyrolysis can also produce SACs that are stabilized by different N-coordinations such as 1 N atom and 2 carbon atoms (1N2C) [170], 1N3C [171], 2N2C or 3N [172, 173].

6.1.2 Small Clusters

In between the conventional nanoparticle catalysts and the single atomic limit there exists a range of cluster sizes that are also of high interest [174]. Clusters with 2, 3, 4 atoms and so on are expected to display quantum size effects, offer unique site geometries and a tunable number of available sites within proximity of one another. These cluster sizes become even more interesting if they can be created with a mix of atomic elements such as hetero-dimers consisting of two different atoms [175, 176]. The combination of two different transition metal sites next to each other creates the possibility of breaking the scaling relations by offering two different binding energies. Currently there are very few reports of few atom clusters synthezised via wet chemistry methods, due to an increased complexity of the synthesis procedure compared to SACs [177–180]. However, with a cluster source, these cluster sizes can be uniformly selected by mass filtering [43, 181–183]. Catalysis with clusters has therefore been the subject of several studies with mass-selected cluster source systems from the groups of S. Anderson [184–186], U. Heiz [33, 34, 139, 187, 188] and S. Vajda [177, 189, 190]. Most of these catalysts were applied for thermal catalysis reactions instead of electrochemical reactions.

6.1.3 A Need for a Tunable Model System

We decided upon a model system with single atoms and clusters anchored by coordination with nitrogen atoms (N-coordination) in a carbon matrix. These structures are reported with increasing frequency in literature, especially for reactions such as

HER [170, 171], CO_2 reduction [172, 191–193] and ORR [169, 175, 194–197]. Given the novelty of these structures, there exists a lack of fundamental knowledge on binding energies and structural effects, such as the effect of the number of N atoms in the N-coordination. and due to the limitations of current synthesis strategies we believe that a model system could provide novel insight.

The N-coordinated SACs created by the wet chemistry synthesis are suitable for characterization with a variety of techniques including XPS, TEM, STEM, EXAFS and STM. Additionally, these structures allow for electrochemical catalysis tests. However, the synthesis methods require a careful tuning of the precursors to avoid simultaneously producing clusters and nanoparticles that can impact the catalytic performance[152, 153]. In addition, the precursors risk leaving residue that may affect the performance either positively or negatively. Furthermore, the density and type of anchoring sites cannot be directly controlled and relies on the support properties [153]. Consequently the effects of site structure and coverage cannot be examined. Finally and perhaps most importantly, these synthesis procedures are only known to work for atomically dispersed catalysts with very few reports of dimers or small clusters [176, 178, 180]. Using a mass-selected cluster source such as the Nanobeam cluster source, dimers and small clusters can be selected uniquely based on their mass, which is a major advantage of this synthesis method.

Model Requirements

An optimal model system must circumvent the issues mentioned above leading to a set of requirements:

- A uniform structure that can be thoroughly characterized with available microscopy and spectroscopy techniques.
- A controllable density of N-defects to act as anchoring sites in a carbon lattice.
- A contaminant free synthesis procedure that creates uniformly dispersed single atoms and clusters.
- A sample geometry suitable for electrochemical testing.
- Ideally the synthesis of the metal single atoms and clusters is possible for different transition metals.

6.2 A Graphite Based Model System

The following sections describe the development of the model system, but before diving into the specifics, I will explain the starting point of this project. When I started in March 2017 a former colleague Anders Bodin had recently explored the possibilities of producing single atoms and clusters of platinum up to about 10 atoms. Using the Nanobeam cluster source he showed that it was possible to

deposit single atoms and that the TOF mass filter can easily resolve the different cluster sizes in a mass scan. He tried depositing single atoms on a lacey carbon TEM grid and saw that the single atoms were dispersed in both single atoms and clusters [198]. This is where I began the project with the purpose of developing a model system for single atoms and small clusters using the Nanobeam cluster source.

Detailed characterization of these systems is a main part of the development work. The STM we had available malfunctioned early on and 6 months ago we started a collaboration with Luca Camilli and Miriam Galbiati at DTU Physics who perform STM measurements. They have since moved to the University of Rome and we have started a new collaboration with Jill Miwa at the University of Århus. Postdoc Arlette Ngankeu has performed STM measurements in Århus.

6.2.1 Choice of Substrate

Given the aforementioned requirements the substrate must have sufficient robustness and a geometry that allows for electrochemical testing, while also being suitable for detailed characterization. Inspired by reports of introducing nitrogen defects with N_2^+ sputtering by Nakamura et al. [199, 200], we decided upon a graphene sheet with N-defects made by sputtering with NH_3 and single atoms and clusters deposited with the Nanobeam cluster source. A schematic of the proposed model system is shown in Figure 6.1, which depicts a graphene sheet with single metal atoms anchored to different N-coordinations. Ideally, one of these structures is created uniformly instead of having different N-coordinations. This structure can be characterized with available techniques including ISS, XPS, STM, TEM, STEM and EXAFS.

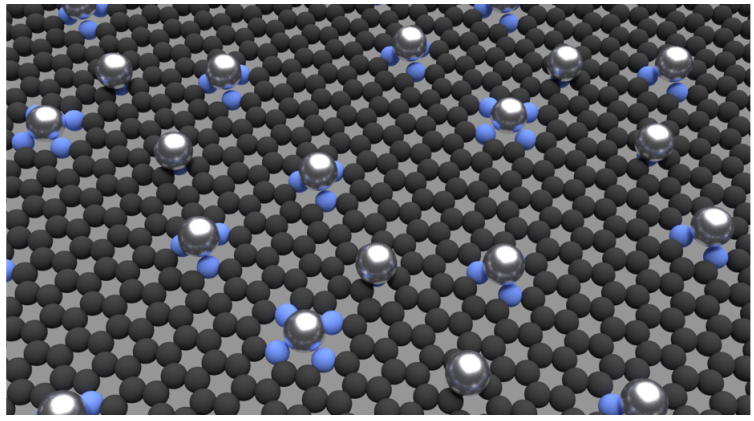

Figure 6.1: Sketch of the proposed model system with different types of N atoms (blue) sitting in defects in a graphene sheet (black) with Pt atoms (grey) anchored on top.

Upon looking into the availability of graphene it became clear that there was no ideal graphene substrate. Graphene is grown on single crystals of Cu, Ir or Ru, but these crystals are either unstable under electrochemical conditions or catalytically active making them unsuited as supports. Graphene has also been grown on electrochemically inert Au(111) single crystal surfaces, but this process is still an ongoing research and developing graphene growth techniques is beyond the scope of this work. Regardless, the development of a model system using only one or a few single crystal substrates would be too time consuming. Therefore we settled on a highly oriented pyrolitic graphite (HOPG) substrate. This shares the structural properties of graphene and is commercially available. HOPG can be characterized with STM, while graphene TEM grids allow for TEM and STEM characterization of analogous structures. Meanwhile ISS and XPS can be used to check the dispersion and chemical state of the structures respectively. Finally, HOPG has a structural robustness that means it potentially can be used for electrochemical measurements in a rotating disk electrode (RDE).

6.2.2 Creating Nitrogen Defects

The creation of nitrogen defects with NH_3 sputtering can be tuned through three parameters, the sputter time, ion energy and gas pressure in the ion gun. The gas pressure is kept constant at 1×10^{-6} mbar to allow for optimal ionization of the gas. Thus only two parameters can be tuned, the sputtering time, which controls the total number of impacts on the surface and the ion energy, which controls the energy transferred to the surface per impacting ion. Therefore, creating N-defects with NH_3 sputtering potentially has the advantage of being able to control the density of defects in the carbon matrix. However the type of defects that are created is unknown and is likely to depend on ion energy [199]. Figure 6.2 shows a detailed XPS spectrum of the N 1s peak from a HOPG plate (1×1×0.3 cm) that was sputtered for 10 minutes with 1 keV NH_3.

Quantification of the N 1s and C 1s XPS peaks revealed a N content of 18 %, which corresponds to more than 1 N per carbon ring. Fitting of the N 1s peak showed the presence of 4 different types of N-defects, pyridinic-N (398.5 eV), pyrollic-N (399.9 eV), graphitic-N (401.1eV) and oxide-N (403.2 eV)[199]. These were previously observed by N_2^+ sputtering [199], in SACs with porphyrin like sites [167] and other N-coordination structures [171, 172]. The pyridinic-, pyrollic- and graphitic-N structures are shown in Figure 6.3 along with Pt_1 in a porhphyrin like site. The quantification shows that the most prevalent defects are the pyridinic-N and pyrrolic-N, which consist of a N atom replacing a C atom in a hexagon/pentagon in the graphene lattice respectively [199]. Both are only bound to two C atoms requiring an extra carbon defect next to the N atom. An oxide-N is similar to the pyridinic-N, but with an O atom bound to the N. Thus these three defects are to be expected in a more defected surface compared to the graphitic-N, which is a direct substitution of a N atom for a C atom [201]. The low ratio of oxide-N is likely due to the absence of O in the UHV chamber. Considering the distribution

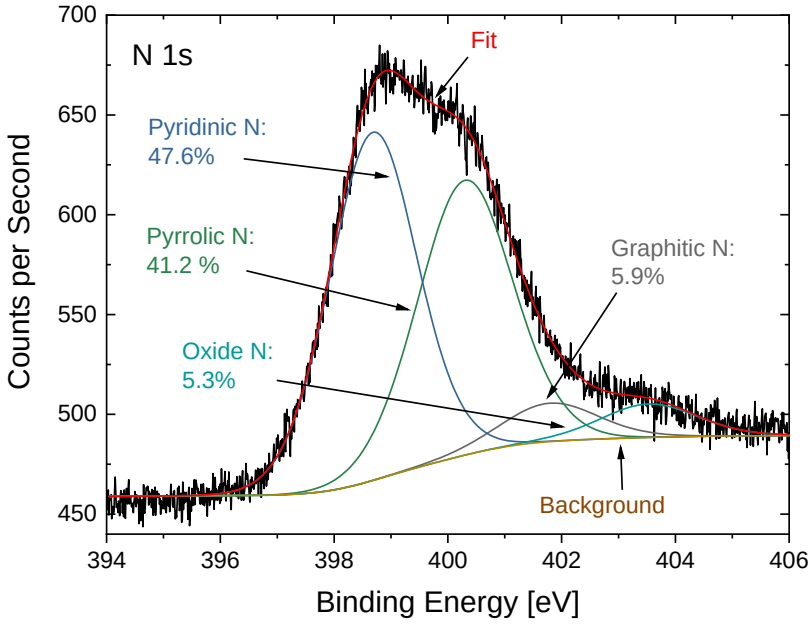

Figure 6.2: Detailed XPS spectrum of the N 1s peak of a HOPG plate sputtered 10 min with 1 keV NH_3 with fits for the pyridinic-N, pyrrolic-N, oxide-N and graphitic-N 1s peaks. Binding energy was calibrated to the graphitic C 1s peak at 284 eV.

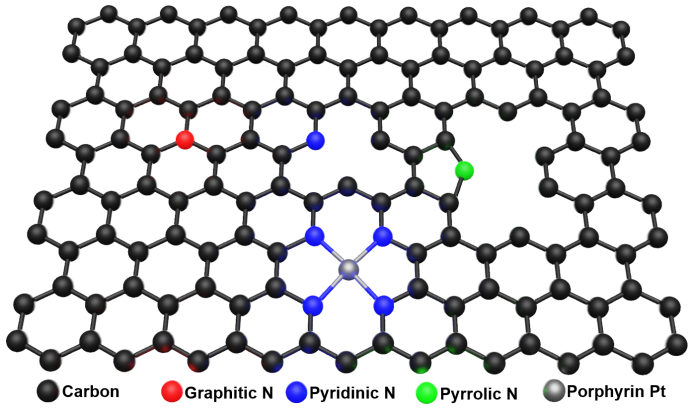

Figure 6.3: Schematic of a graphene layer with pyridinic-N, pyrollic-N and graphitic-N defects. Pt_1 is shown anchored in a porphyrin like site. The porphyrin like site consists of 4 pyridinic-N defects surrounding the metal atom. Oxide-N is a pyridinic-N with an O atom on top. Image courtesy of Karl Toudahl.

of defects and the high N content it would appear that sputtering for 30 minutes with 1 keV NH_3 creates a highly defected surface.

6.2.3 Depositing Single Atoms and Clusters

Single atoms and clusters can be deposited using the Nanobeam cluster source, but the current is highly dependent on the sample bias. Mass scans from Pt_1 up to Pt_4 are shown in Figure 6.4. For Pt_1 a sufficient current is achieved with a sample bias of 1.5 V, which is close to soft-landing (soft-landing for a single atom is not well-defined considering the atom cannot split into smaller entities). For Pt_2 and larger clusters a larger bias is necessary to achieve currents that enable deposition of 1-10 % of a monolayer in a reasonable deposition time e.g. a work day. For Pt_2 a current of 0.14 nA was achieved with a 9 V bias and for Pt_3 a current of 0.2 nA was achieved with a bias of 18 V. The resulting deposition times for 1% of a monolayer are 1 hour/30 minutes respectively. The required bias for Pt_2 and Pt_3 are equivalent to 4.5 and 6 eV/atom, which is higher than the 1 eV/atom soft-landing limit so particle fragmentation is possible.

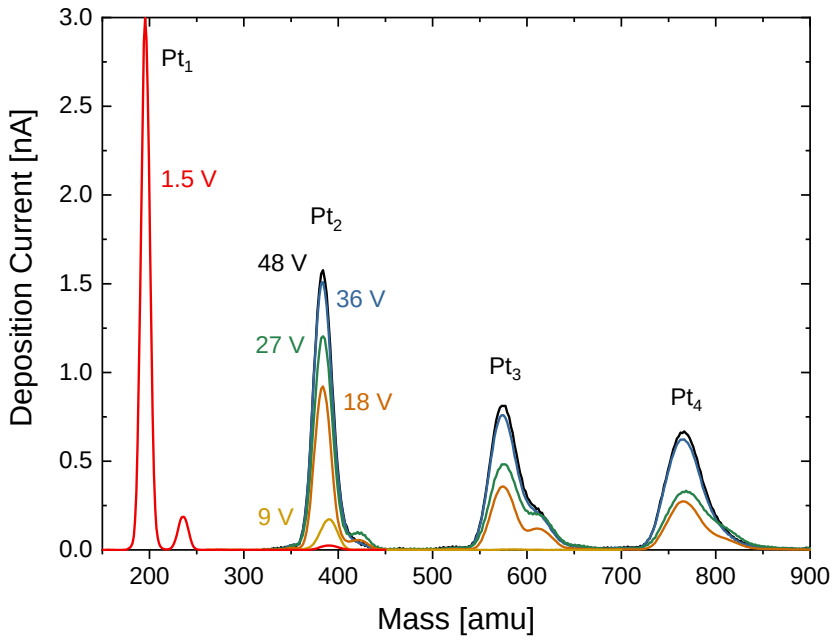

Figure 6.4: Mass scans for Pt_1, Pt_2, Pt_3 and Pt_4 for different sample biases from 1.5 V to 48 V. Each cluster size shows a smaller peak at 40 amu above the peak position due to Ar binding to some of the clusters in the aggregation zone.

In addition to the sample bias, several other deposition conditions have to be

changed between the different cluster sizes. Single atoms and dimers can be produced without any He flow, while larger particles require a low He and high Ar flow. The exact conditions for Pt_1/1.5 V, Pt_2/9 V and Pt_3/18 V are shown in Table 6.1. Mass scans with bias above 18 V are acquired with conditions similar to the 18 V mass scan. The effect of the landing energies above 1 eV/atom must be investigated when characterization of the cluster structure has been developed.

Table 6.1: Deposition conditions for Pt_1, Pt_2 and Pt_3.

Cluster Size [atoms]	Magnetron Power [W]	He Flow [ml/min]	Ar Flow [ml/min]	Aggregation Zone Pressure [mbar]	Bias [V]
1	45	0	9	0.02	1.5
2	31	0	4	0.01	9
3	16	6	96	0.13	18

6.3 Developing the Model System

The development of the model system was supported by TEM, STEM and STM characterization. Grids consisting of a monolayer graphene sheet spread across a quantifoil grid were used for STEM imaging. We tried a variety of ETEM heat treatments in both O_2 and H_2 and found that the optimal conditions were heating to 500 °C in vacuum. However, as Figure 6.5a shows there was still a significant residue of amorphous carbon around the atomically resolved graphene and overall none of the cleaning procedures improved the graphene surface sufficiently. The clean area in Figure 6.5a was the largest that was observed and therefore we looked into other suppliers, but this was the only commercially available monolayer graphene grid. Together with Johannes Novak Hansen, I tried to replicate a procedure for lifting graphene onto Cu TEM grids without success [202]. Ultimately we decided it was outside the scope of our work and continued using these graphene grids for TEM/STEM characterization.

HOPG plates of 7×7×1 mm were cleaved to expose the clean HOPG surface before STM imaging. Cleaving is a cleaning procedure where a piece of tape is used to removed several of the topmost layers of the HOPG exposing a very clean surface. This is the starting point for all treatments of the HOPG plates. Figure 6.5b shows an STM image of a freshly cleaved HOPG plate, which displays a pristine atomic structure. Unless otherwise stated in the image caption, the STM images are acquired at room temperature.

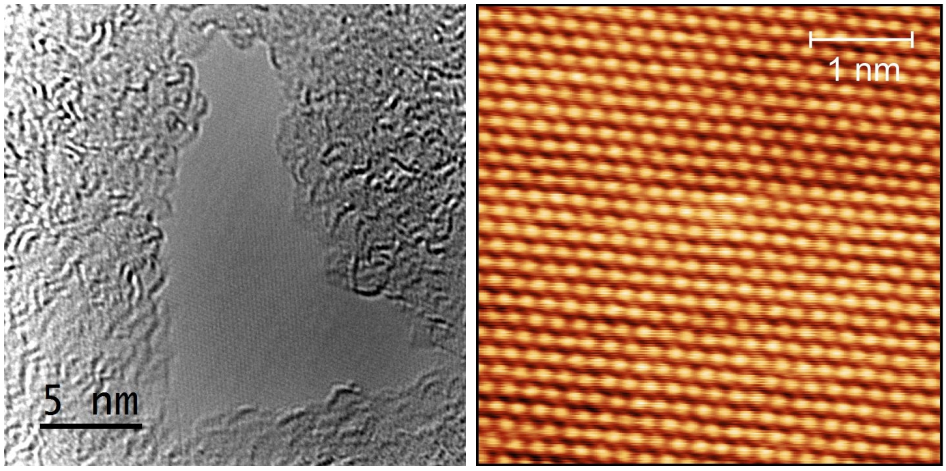

(a) **(b)** I= 0.8 nA, U= 0.1 V

Figure 6.5: a) TEM image of the monolayer graphene TEM grid at room temperature in vacuum after heating to 500 °C for 2 hours in vacuum in the ETEM. **b)** STM image of freshly cleaved HOPG plate by Miriam Galbiati.

6.3.1 Sputtering Conditions

The effect of NH_3 sputtering for anchoring Pt_1 was examined by STEM and STM. A graphene grid was annealed for 2 hours at 500 °C in UHV before being sputtered for 30 min with 1 keV NH_3 and finally depositing 1% Pt_1. A STEM image of the grid is shown in Figure 6.6a with bright spots smaller than 1 nm in diameter. This was one of the only remaining graphene sheets on the grids and it was not completely intact, indicating that the sputtering treatment destroys the graphene monolayers. Given the size of these spots they are likely the Pt_1 dispersed on the graphene support. Figure 6.6b shows a STM image of a HOPG stub that was subject to the same sputtering treatment and single atom deposition before being annealed at 500 °C for 2 hours in UHV. The STM image shows a rough surface with no ordered structure.

Since the STM image in Figure 6.6b was recently acquired and the STEM image in Figure 6.6a shows atomically dispersed Pt_1 on the graphene support, these conditions were initially used for electrochemical testing. However, for the purpose of having a well-defined structure that can be characterized with STM, milder sputtering conditions are necessary. Therefore the NH_3 sputtering conditions were reduced to 20 seconds at 150 eV. An STM image of these sputtering conditions is shown in Figure 6.7a. The image shows bright features on the atomically resolved HOPG surface that are approximately 1 nm in diameter and vary in shape. Figure 6.7b shows a graphene grid that was sputtered with these milder conditions before having 1% coverage of Pt_1 deposited. The grid was annealed at 500 °C for 1 hour

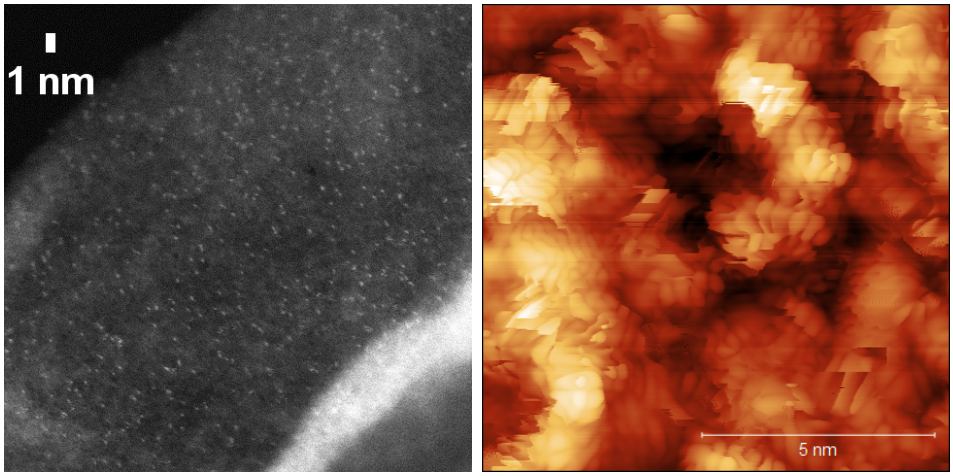

(a) **(b)** I= 0.3 nA, U= -1.0 V, T= 4 K

Figure 6.6: a) STEM image of a graphene grid and **b)** STM image of HOPG plate, both sputtered with 1 keV NH_3 for 30 minutes with 1% Pt_1. The graphene grid was annealed at 500 °C for 2 hours before sputtering and the HOPG plate was annealed for 2 hours at 500 °C in UHV before STM imaging. STM image by Miriam Galbiati.

in the microscope and cooled to room temperature before the image was acquired. The STEM image shows bright nanoparticles and clusters much larger than single atoms while also displaying some spots as small as single atoms. Note that most of the bright spots are on a lighter background of amorphous carbon contamination, while only a few bright spots are on the dark monolayer graphene areas. From this image, it appears that the milder sputtering conditions are not sufficient to anchor single atoms on the TEM grid. This may be due to the amorphous carbon contamination blocking the graphene and thus not creating N-defects or the mild sputtering conditions not providing a sufficient number of N-defects to anchor the Pt_1. From Figure 6.7a the N-defect density is calculated to 0.13% compared to the C atoms.

While the 10 min, 1 keV NH_3 sputtering conditions are not ideal for STM imaging, the resulting structure may be suitable for electrochemical measurements based on the STEM image in Figure 6.6a. It appears that the ideal imaging conditions for STEM and STM may not be identical. Thus further development of the characterization procedures is necessary for these techniques to provide complementary imaging of analogous structures.

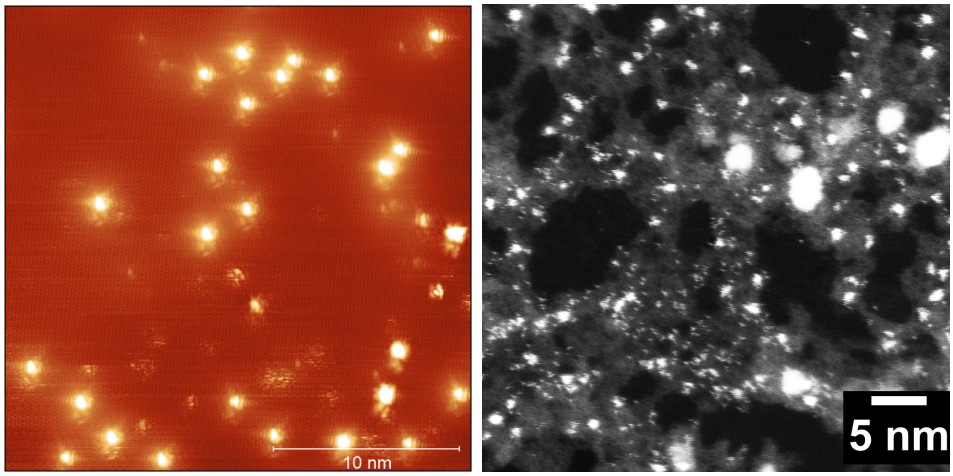

(a) I= 0.5 nA, U= 0.8 V, T= 4 K **(b)**

Figure 6.7: a) STM image of HOPG plate, sputtered for 20 seconds with 150 eV NH_3 and annealed for 2 hours at 500 °C in UHV. STM image by Miriam Galbiati. **b)** STEM image of graphene TEM grid with similar sputtering and 1% Pt_1 deposited. Annealed at 500 °C for 1 hour in the TEM.

6.3.2 Identifying Nitrogen Defects

The different types of N-defects are not immediately apparent from the STM image in Figure 6.7a. Figure 6.8 shows a close up of two different features seen in Figure 6.7a. The feature in Figure 6.8a is star shaped and resembles the structure of the simulated STM image of a pyridinic-N defect as shown in the inset [199]. The feature in Figure 6.8b is triangular and resembles the simulated STM image of a graphitic-N defect shown in the inset. From comparison of the simulated and measured STM images it appears that both graphitic-N and pyridinic-N defects are created by the NH_3 sputtering followed by annealing at 500 °C for 2 hours. It is likely that other defects are also present, but due to a lack of simulated STM images it is not possible to identify them. XPS measurements of these samples have not been performed yet.

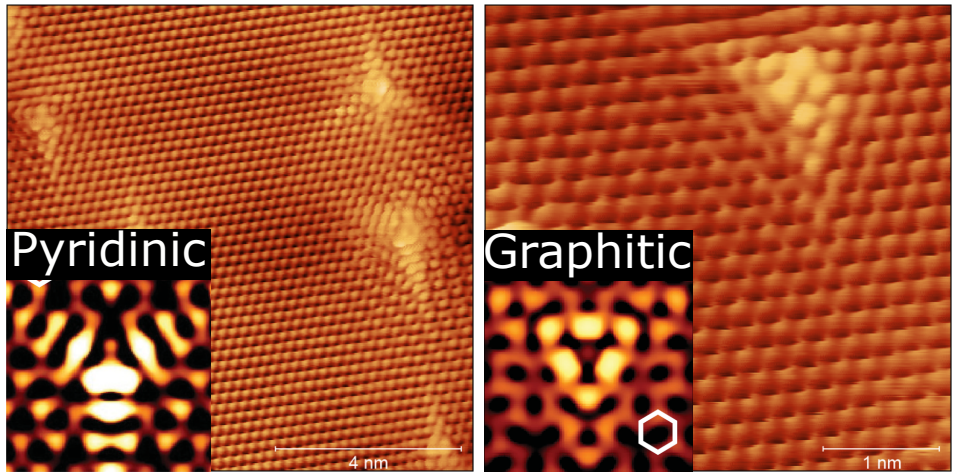

(a) I= 0.8 nA, U= 0.8 V, T= 4 K **(b)** I= 0.8 nA, U= 0.6 V, T= 4 K

Figure 6.8: Atomically resolved STM images of **a)** a pyridinic-nitrogen defect and **b)** a graphitic-nitrogen defect in an HOPG plate. The plate was sputtered for 20 seconds with 150 eV NH_3 and annealed at 500 °C in UHV for 2 hours. The insets show simulated STM images of **inset a)** a pyridinic-nitrogen defect at +1.0 V bias and **inset b)** a graphitic-nitrogen defect at +0.5 V bias adapted from [199]. STM images by Miriam Galbiati.

Defect Formation

In an attempt to further understand the process of creating N-defects, two different annealing steps were performed on the same sample. Figure 6.9a shows an HOPG sputtered with mild sputtering conditions and 1% Pt_1 annealed at 150 °C for 10 minutes. The image shows many bright round features, several nanometers in diameter on the HOPG surface, with a magnified image of a defect in the inset. Figure 6.9b shows the same sample after annealing at 700 °C for 120 minutes. The bright features appear smaller than before and with a star shape, while some of the features are brighter than the others. The round feature in Figure 6.9a inset is similar to reported observations of domes with Ar^+ sitting in the subsurface, indicating that NH_3 is implanted under the surface of the HOPG [203]. From the difference in defect appearance between the two images, it appears that annealing at higher temperatures transforms the "dome" features into the pyridinic-N and graphitic-N defects observed in Figure 6.8. This is conceptually similar to annealing graphene in a NH_3 atmosphere as there is NH_3 in proximity of the surface at elevated temperatures. However, with NH_3 sputtering it may be possible to tune the density of NH_3 "domes" thus tuning the resulting defect density. We are currently awaiting STM images of samples sputtered for 60 s and 120 s to confirm this possibility.

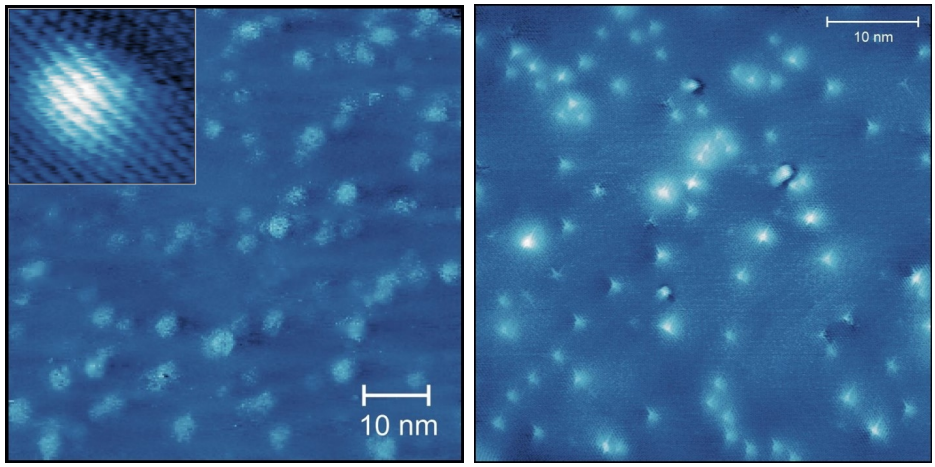

(a) I= 0.8 nA, U= 0.8 V **(b)** I= 0.8 nA, U= 0.6 V

Figure 6.9: STM images of HOPG plates that were sputtered with 150 eV NH_3 for 20 seconds before 1% Pt_1 was deposited. The HOPG plates were annealed at **a)** 150 °C for 10 min and **b)** 700 °C for 2 hours. **inset a)** shows a magnified image of one of the features in **a)**. STM images by Arlette Ngankeu.

6.3.3 Identifying Anchored Single Atoms

To understand how the Pt_1 on NH_3 sputtered HOPG is affected by the annealing procedure at 500 °C, ISS spectra were acquired before and after annealing the samples in UHV. The spectra, seen in Figure 6.10a, show that the Pt peak increases in intensity after the annealing procedure, indicating an increase in Pt dispersion. Thus it appears that Pt agglomeration should not be expected and that anchoring on the N-defects is possible. Figure 6.10b shows an STM image of one of the very bright defects in Figure 6.9b. The defect does not resemble the pyridnic-N or graphitic-N defects but instead has a star shape with a very bright area (inside the black circle). This could be a single atom or several atoms on a N-defect, but further confirmation requires simulations of this geometry, which are currently being performed by collaborators at CatTheory, DTU.

6.4 Measuring the Electrochemical Performance of Single Atoms and Clusters

Measuring the electrochemical performance of single atoms and clusters on NH_3 sputtered HOPG requires mounting HOPG in an RDE setup to reduce mass transport limitations. However, mounting the HOPG in an RDE also poses an issues due to the geometry of a HOPG plate. The RDE tip requires a disc of 5 mm in diameter and 4 mm tall, but the HOPG plates are 10×10×3 mm. This was solved

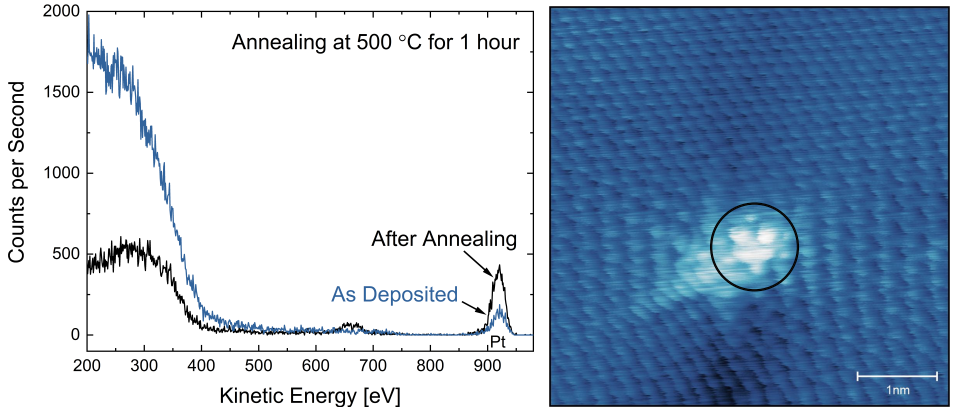

Figure 6.10: a)ISS spectra of HOPG plates that were sputtered with 150 eV NH_3 for 20 s before depositing 1% Pt_1. One spectrum before (blue) and after (black) annealing at 500 °C for 1 hour. **b)** STM image of a nitrogen defect in HOPG sputtered for 20 s with 150 eV NH_3 and 1% Pt_1 coverage annealed at 700 °C. The black circle surrounds a brighter feature that could be one or several atoms. STM image by Arlette Ngankeu.

by grinding the plates into discs that were 5 mm in diameter and 3 mm tall. A copper spacer was placed behind the HOPG disc to fill the remaining 1 mm in height in order to fit properly into the RDE tip. After many attempts at obtaining stable cyclic voltammograms (CV) for ORR with blank HOPG and NH_3 sputtered HOPG, the HOPG stubs split into several pieces due to the weak van der Waals binding between the graphite layers. Additionally, the use of a Cu spacer contaminated the HOPG stubs with Cu so this approach was discontinued. Possible structural alterations in the HOPG surface due to the rough physical treatment of grinding were also a serious concern.

Instead a new RDE tip design was developed by Johannes Novak Hansen that enables using the entire HOPG plate in an RDE tip. The design consists of a round holder larger than the HOPG plate, where the plate is mounted. An O-ring and a lid placed on top of the plate secures it in place. A hole in the lid allows for the HOPG surface to react with the reactants in the electrolyte. This design was finalized within a few weeks of the submission of this thesis so only a single preliminary hydrogen evolution reaction (HER) measurement has been performed. Figure 6.11 shows a CV obtained using a HOPG plate with an approximate N-defect density of 1% and a Pt_1 coverage of 0.2%. The CV was measured in H_2 saturated 0.1 M $HClO_4$ with an Ir wire counter electrode. Since background measurements of a clean HOPG and NH_3 sputtered HOPG are yet to be performed, the CV cannot be used to gauge the HER activity of the Pt single atoms. Instead it serves as evidence that the RDE design can produce HER CVs using the HOPG plates.

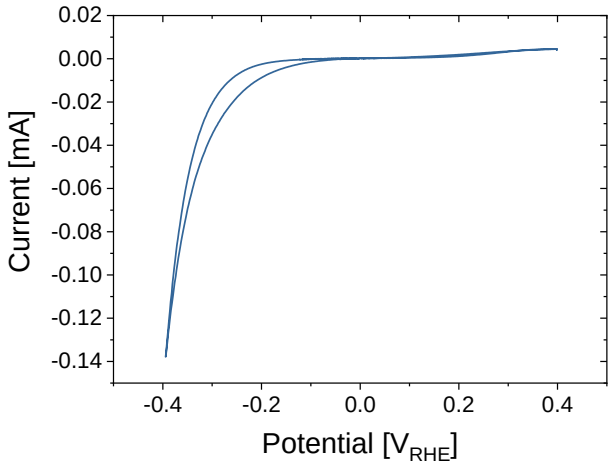

Figure 6.11: CVs measured in H_2 saturated 0.5 M H_2SO_4, with a HOPG plate with 1% N-defects and 0.2% Pt_1, mounted in the new RDE tip design.

6.5 Discussion

As the development of this model system is on-going there are many points that still need to be developed. First the use of these graphene grids is not ideal due to the amount of amorphous carbon contamination on the graphene. We tried to make our own grids with a clean graphene transfer process and also with graphene oxide flakes without success. However, if STEM characterization is to be complimentary to STM characterization, clean graphene grids are necessary.

From the fit of the N 1s peak and the STM images of N-defects it is evident that NH_3 sputtering can introduce N-defects similar to those previously reported N_2^+ sputtering [199]. Kondo and co-workers sputtered a HOPG surface with 200 eV N_2^+ and observed 32.6% pyridinic N, 17.4% pyrrolic N, 40.1% graphitic N and 9.8% oxide N. This is signficantly more graphitic-N and less pyrrolic/pyridinic-N compared to the fit in Figure 6.2, which can be explained by the structure of the graphitic-N sites. The 1:1 substitution of a N atom for a C atom in a graphitic-N defect is less likely at higher ion energies due to sputtering of the surface. Therefore the lower ion energy of 150 eV is expected to produce a defect distribution similar to the results from Kondo et al. [199]. Furthermore Kondo et al. observe an increase in graphitic-N after annealing at 900 K due to reconstruction of the graphite surface. This supports the observations in Figure 6.9, that the annealing temperature may change the domes of NH_3 into N-defect in the surface. Considering the effect of a lower ion energy and the annealing procedure, it is likely that the NH_3 sputtering for 20 s with 150 eV NH_3 and annealing at 500/700 °C mostly creates pyridinic-N and graphitic-N. This would explain the observations in the STM images, where

these two defect types are prevalent.

The pyridinic-N, pyrrolic-N and graphitic-N were reported in literature in SACs that were anchored with porphyrin sites and lower N-coordination geometries [167, 171, 172]. Thus the presence of these defects in the HOPG plates indicates that single atom dispersion should be possible with N-defects created from NH_3 sputtering. The differences between the 0.13% N-content from 20 s sputtering and the 18% N-content from 10 min sputtering, indicate that the N-defect density can be tuned. Samples are currently being made for studying the exact degree of tunability in the N-defect density. The variation of defect density may allow for studying the effect of different anchoring geometries on the reactivity of a single metal atom, which could aid in the development of new SACs for electrochemical reactions [172, 173]. Additionally, given the N-defect density from 20 s of NH_3 sputtering, the defects are well separated. However, for electrochemical measurements the density must be significantly increased, possibly to a degree similar to the 10 min NH_3 sputtering. At sufficiently high N-defect density, it is possible that the density may affect the defect type. Specifically, as the N-density is increased, the coordination of single atoms to porphyrin sites will become increasingly likely since multiple N-defects will be in proximity of one another. Therefore the influence of N-defect density on the defect type should be studied.

The 0.13% of N-defects in the graphene surface on Figure 6.7a is substantially less than the 1% coverage of Pt_1 that was deposited on the HOPG surface in Figure 6.9. This increases the probability of Pt agglomeration in the samples prepared for STM and should be reduced in the future. However, no agglomerations of Pt were observed in the STM imaging, instead such observations were made on the STEM image in Figure 6.7b. Unfortunately, the presence of amorphous carbon on the graphene grids excludes a direct comparison of the two systems and is likely to have caused the atomic dispersion of Pt_1 in Figure 6.6a. The ISS spectra before and after annealing in Figure 6.10a confirm that the Pt atoms should be dispersed on the N defected surface, but their presence is not easily detectable. Therefore the comparison of STM simulations and images such as Figure 6.10b will be necessary in determining if the N-defects produced by NH_3 sputtering can anchor a single atom or cluster of atoms. The presence of atomically dispersed Pt_1 in Figures 6.9 and 6.10b is therefore still undocumented and requires further characterization and the behaviour of the deposited clusters also remains to be examined. Given the 4.5 and 6 eV/atom bias necessary for depositing Pt_2 and Pt_3 it is possible that the clusters split into smaller entities.

6.6 Conclusion

While this is still a development project, that is in its early stages, there are some available conclusions. First of all, we selected a model system that fulfills most of the requirements.

- The graphite based models system has a structure that can be characterized with microscopy and spectroscopy techniques. The uniformity of active sites remains to be solved given the presence of different N-defects.
- The density of anchoring N defects has been shown to be tunable within the range relevant for the model system.
- The Nanobeam cluster source was shown to be able to produce uniformly dispersed single atoms, suggesting that larger clusters also can be produced in a similar fashion without any contaminations. Additionally, the cluster source can easily change the metal used to produce the single atoms.
- The sample geometry can be used for electrochemical RDE measurements.

However, from the preliminary results there are still open questions. The presence of N-anchored single atoms and clusters remains to be shown with a combination of microscopy and simulation. Furthermore, the role of different types of N-defects in anchoring of the single atoms and clusters should be investigated, to enable tuning of the sputtering process. Finally, the stability and activity of these anchored species in electrochemical reactions must be shown to validate the model system.

6.6.1 Outlook

Since there are many things in the pipeline for this project I will briefly mention some of the work that I believe could give significant contributions to the existing knowledge on single atom and clusters for catalysis. First off, XPS measurements of the N 1s peak on HOPG sputtered with the milder sputtering conditions can confirm the types of defects produced from the process. This may require going to a larger X-ray facility such as the small synchrotron in Århus.

Next, I think that several variations of sputtering, depositing and annealing should be tested, specifically the order in which they are performed. The effect of sputtering and annealing before/after deposition could provide interesting results on the formation of anchored species. Additionally, the annealing temperature should be examined since reports in literature have adopted a higher annealing temperature [166].

To further understand the trends in the reactivity and selectivity of single atoms and clusters, I believe TPD measurements can be a valuable tool. The TPD chamber on the Omicron system has been under development during this work and I look forward to seeing how it can contribute to this field.

Finally, perhaps the most exciting future work is the testing of these systems for electrochemical reactions, assuming that the atoms and clusters can be anchored. Given the promising results already reported in literature, I hope this system can provide novel insight into the mechanisms behind the novel activity and selectivity.

Chapter 7

Conclusion and Outlook

The purpose of this thesis was to describe the development of novel model systems for fundamental catalysis research using the Nanobeam cluster source. The research efforts were focused on four different catalytic systems as summarized below.

In Chapter 3 the Nanobeam cluster source was used to make a model system consisting of mass-selected Pt nanoparticles with a well-defined coverage. This allowed for simulations of the edge-to-edge interparticle distance for these systems. Thus, SFC-ICP-MS measurements of the Pt dissolution under AST protocols in ORR conditions, could be compared to identical measurements on an industrially relevant catalyst. The study shows that the dissolution rate and total Pt dissolution are proportional to the interparticle distance. The proportionality is attributed to three effects; a shift in the Nernst potential for dissolution, Pt redeposition and a decreasing electronic double layer overlap for larger interparticle distances. Furthermore, the model system was used to determine that the lower potential limit of the AST protocol can cause a misleading particle size effect.

In Chapter 4 mass-selected 370k amu Pt nanoparticles were deposited on glassy carbon discs with well-defined loadings from 13-5000 ng/cm^2, to create a "benchmark" system for HER. The Pt "benchmark" system shows that increasing the Pt loading on the working electrode will lead to a lower $\eta_{10\mathrm{mA/cm^2}}$. The HER activity was reported in $\eta_{10\mathrm{mA/cm^2}}$, mass activity and turnover frequency to enable comparisons to studies on earth-abundant HER catalysts. Ultimately, the results highlight the importance of reporting catalyst loadings and performing scientific comparisons based on mass activity or TOF, when claiming platinum-like HER activity.

Chapter 5 presents the preliminary results on increasing the CO oxidation stability of Au nanoparticles through alloying with Ti. Mass-selected AuTi nanoparticles from 2.5 nm to 5.5 nm were deposited on SiO_x and TiO_x supports in the microreac-

tors for thermochemical testing. The CO oxidation measurements displayed issues with reproducing the activity of the AuTi particles. However, the preliminary results show that AuTi nanoparticles are active for CO oxidation, with 2.5 nm AuTi particles on TiO_x support displaying significantly higher CO oxidation activity than the well-known Au nanoparticles on TiO_x.

Finally, Chapter 6 motivates and presents the development of a highly ordered pyrolitic graphite (HOPG) based model system, for electrochemical catalysis with single atoms and small clusters. Preliminary results show that NH_3 sputtering can be used to create pyridinic, pyrollic, oxide and graphitic nitrogen defects in the HOPG surface, which are known to anchor single atoms. Evidence of anchored Pt single atoms is not yet available, but the NH_3 sputtered HOPG support with 0.2% Pt_1 produces HER cyclic voltammograms. Thus the model system appears promising for investigating the binding energies and coordination effects of single atoms and cluster for electrochemical catalysis.

In conclusion, I would like to note that the development of these 4 model systems would not be possible without a mass-selected cluster source. as it provides the model systems' strengths. Namely the narrow size distribution and well-defined loadings/coverages dispersed on a flat geometry, which allow detailed characterization and close comparison to theoretical simulations as in Chapters 3, 4 and 6. However, these strengths also come with the disadvantage of a low particle deposition rate and limited support geometries. Thus widespread application of the knowledge obtained from studying these model systems, will always require reciprocal chemical synthesis procedures.

Outlook

Before closing, I would like to share my thoughts on how mass-selected model systems can play a role in future catalysis research. First of all, key to successfully applying model systems in catalysis will always be the combination of a well-defined system with thorough chemical and structural characterization. In the past, the model systems at SurfCat have been focused on size selected studies of nanoparticles and especially binary nanoparticles such as NiFe, PtY, and now AuTi. With the development of multiple magnetron sources I believe that many new binary and ternary alloys, that are not easily synthesized by wet chemistry, can prove promising for catalysis, given the different binding sites in close proximity. However, as chemical synthesis procedures develop, I think the strength of mass-selected model systems is best applied to the cluster size range with a countable number of atoms. As discussed throughout the thesis, several groups have already applied model systems to catalysis with small clusters, but given the small number of groups working on this, there is still a large range of reactions and catalysts to study. This is especially valid for electrochemical reactions relevant for sustainable energy technologies such as HER, ORR and OER, where very little has been reported.

Appendices

Appendix A

ETEM studies of AuTi for CO Oxidation

In an attempt to check the stability of the 2.5 nm AuTi nanoparticles, I performed ETEM measurements using the DENS Wildfire TEM chips. The grids have a SiN membrane which can be heated to 1000 °C in the ETEM. I deposited 3% coverage of 2.5 nm AuTi nanoparticles on the grids using the Nanobeam cluster source, with conditions similar to the ones described in Chapter 5. Figure A.1a shows the 2.5 nm AuTi nanoparticles at 80 °C in vacuum. The particles display a dark core with a lighter shell, identical to the structure observed in STEM. Figure A.1b shows another area of the SiN membrane with AuTi particles in 3 mbar CO_2 and 2 mbar O_2 at 400 °C. At the time of acquiring the image, the particles had been exposed to these conditions for more than 1 hour. The particles have not grown significantly and still display the same core-shell structure. This indicates that the AuTi nanoparticles are stable in a 3 mbar CO_2, 2 mbar O_2 atmosphere at 400 °C. Images of higher magnification were not acquired to avoid beam induced effects from the elevated electron dose rates [$e^-/(Å^2s)$]. Additionally, these images are acquired from areas that were not illuminated by the electron beam prior to imaging, thus reducing the likelihood of beam induced effects.

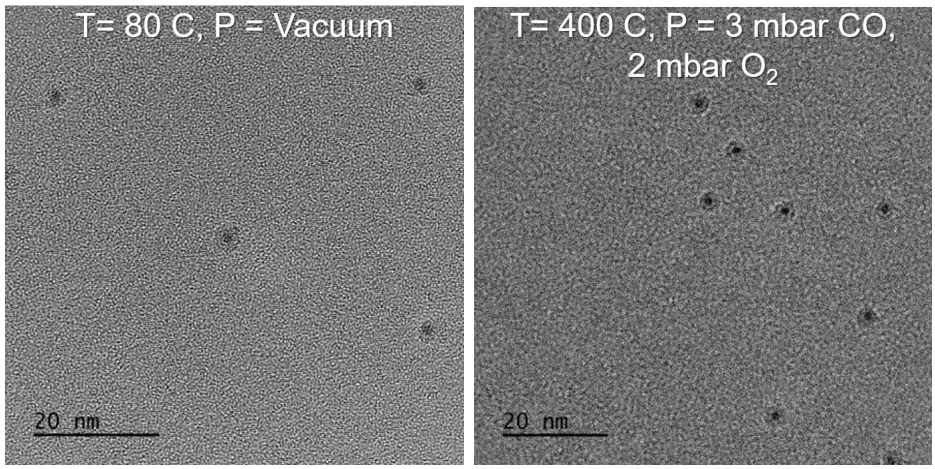

(a) **(b)**

Figure A.1: ETEM images of 2.5 nm AuTi nanoparticles at two different temperatures and pressures. The images were acquired with an electron dose rate of 100 $e^-/(Å^2 s)$.

Appendix B

Appended Papers

Paper I: The Dissolution Dilemma for Low Pt Loading Polymer Electrolyte Membrane Fuel Cells
Daniel J. S. Sandbeck*, **Niklas Mørch Secher***, Masanori Inaba, Jonathan Quinson, Jakob Ejler Sørensen, Jakob Kibsgaard, Alessandro Zana, Francesco Bizzotto, Florian D. Speck, Alexandra Dworzak, Carsten Dosche, Mehtap Oezaslan, Ib Chorkendorff, Matthias Arenz, Serhiy Cherevko
Subtmitted to Advanced Energy Materials
*These authors contributed equally.

Paper II: The Particle Size Effect on Platinum Dissolution: Considerations for Accelerated Stability Testing of Fuel Cell Catalysts
Daniel J. S. Sandbeck*, **Niklas Mørch Secher***, Florian D. Speck, Jakob Ejler Sørensen, Jakob Kibsgaard, Ib Chorkendorff, Serhiy Cherevko
In review at ACS Catalysis
*These authors contributed equally.

The Dissolution Dilemma for low Pt Loading Polymer Electrolyte Membrane Fuel Cells

Daniel J. S. Sandbeck,[a,b,♯,*] Niklas Mørch Secher,[c,♯] Masanori Inaba,[d,e] Jonathan Quinson,[d] Jakob Ejler Sørensen,[c] Jakob Kibsgaard,[c] Alessandro Zana,[f] Francesco Bizzotto,[f] Florian D. Speck,[a,b] Alexandra Dworzak,[g,h] Carsten Dosche,[g,h] Mehtap Oezaslan,[g,h] Ib Chorkendorff,[c] Matthias Arenz,[d,f] Serhiy Cherevko[a,*]

[a]Helmholtz-Institute Erlangen-Nürnberg for Renewable Energy (IEK-11), Forschungszentrum Jülich GmbH, 91058 Erlangen, Germany

[b]Department of Chemical and Biological Engineering, Friedrich-Alexander-Universität Erlangen-Nürnberg, 91058 Erlangen, Germany

[c]Department of Physics, Technical University of Denmark, 2800 Lyngby, Denmark

[d]Department of Chemistry, University of Copenhagen, Universitetsparken 5, DK-2100 Copenhagen Ø, Denmark

[e]Toyota Central R&D Labs, Inc., Nagakute, Aichi 480-1192, Japan

[f]Department of Chemistry and Biochemistry, University of Bern, CH-3012 Bern, Switzerland

[g]Department of Chemistry, Carl von Ossietzky University of Oldenburg, 26111 Oldenburg, Germany

[h]Institute of Technical Chemistry, Technical University of Braunschweig, 38106 Braunschweig, Germany

[♯]These authors contributed equally to this work

E-mail: d.sandbeck@fz-juelich.de

E-mail: s.cherevko@fz-juelich.de

Abstract

High cost and limited lifetime remain to be key challenges for widespread commercialization of polymer electrolyte membrane fuel cell (PEMFC) electric vehicles. Reduced Pt loadings can bring down the vehicle costs; however, the impact of loading on catalyst layer degradation remains unclear. The limited research on Pt loading and catalyst degradation largely stems from synthetic difficulties and the lack of in situ analytical techniques. This study circumvents these challenges by synthesizing Pt/C model catalyst systems via two precise routes: (a) magnetron-sputtered, mass-selected, Pt nanoclusters on a two-dimensional (2D) support and (b) three-dimensional (3D) Pt/Vulcan synthesized via the "toolbox" approach. For both the 2D and 3D materials the loading (and consequently the interparticle distance) were systematically varied. A set of advanced characterization techniques was used to investigate the loading dependent degradation processes of the 2D and 3D structured materials. Pt dissolution was monitored using on-line inductively coupled plasma mass spectrometry (on-line-ICP-MS), while different X-ray spectroscopy techniques were applied to establish the oxidation states of Pt in correlation with metal loading. Clear dissolution trends emerge which can be explained by three fundamental loading dependent mechanisms: (1) shifts in the Nernst dissolution potential, (2) redeposition, and (3) the oxidation states of Pt. Based on these results, we identify limitations and challenges on the pathway to lower loadings, which should be considered by researchers and engineers in fuel cell development and related fields.

1. Introduction

For years' polymer electrolyte membrane fuel cell (PEMFC) electrocatalysis research has been aimed at increasing catalyst activity towards the sluggish oxygen reduction reaction (ORR), in an effort to decrease the total Pt loading necessary in the cathode catalyst layer. By decreasing Pt loading the total cost[1] and amount of Pt in circulation can be reduced, thereby increasing manufacturing production volumes of fuel cell electric vehicles.[2]

Several strategies have been suggested to increase catalyst activity, with major research efforts focused on Pt alloys and shape-controlled Pt nanoparticles.[3] Although such advanced materials show promising ORR activity, less can be said regarding their stability. Furthermore, on the pathway to lower Pt loadings, it is of immediate interest to understand the degradation behavior of current state-of-the-art materials.[4]

Decreased Pt loading achieved via thin catalyst layers is known to severely compromise performance at high current densities in membrane electrode assemblies (MEAs).[1-2] Such loading dependent performance has been attributed to flooding and a local O_2 resistance related to changing Pt substrate-ionomer interactions when going from thick to thin ionomer films. In contrast, the mechanisms behind the observed increase in irreversible degradation can only be speculated without dedicated investigations.

Under well-defined half-cell conditions, which become necessary for elucidating fundamental phenomena undetectable in complex systems, studying the impact of catalyst layer thickness on the primary degradation mechanism of Pt dissolution revealed crucial phenomena.[5] On-line dissolution measurements with a scanning flow cell coupled to an inductively coupled

plasma mass spectrometer (SFC-ICP-MS) showed that electrochemical specific dissolution normalized by electrochemically active surface area (ECSA) increased with decreasing catalyst layer thickness. While the exact mechanism remains unknown, this observed dissolution trend was tentatively attributed to a shift in the Nernst potential for dissolution, which was greater for the increased diffusional path links of thicker catalyst layers. Due to these unambiguous performance and degradation issues, lower Pt content via catalyst layer thickness will be limited to a yet to be defined length without further materials improvements.

Considering the perceived limitations of thin catalyst layers, a new contrasting approach to lower Pt loading must be investigated. By lowering the Pt density within the catalyst layer, i.e. the wt. % Pt, the Pt content can be varied independent of thickness. Similar to the low Pt content of thin catalyst layers, low Pt density has been reported to decrease ORR activity.[6] However, in comparison to catalyst layer thickness, the dependence of Pt density on degradation remains largely unexplored.[6b, c, 7] Therefore, in this work the SFC-ICP-MS technique was employed to elucidate the effect of loading on dissolution with constant catalyst layer thickness. Three-dimensional (3D) Pt/Vulcan materials and two-dimensional (2D) model magnetron-sputtered mass-selected systems of varied loadings were investigated. For the 3D Pt/C materials, exclusive control of material properties such as particle size and loading was achieved with a two-step surfactant-free polyol synthetic technique, termed the "toolbox" approach.[6a, b, 8] Moving to the 2D model systems, particle size and distribution were precisely tuned using a magnetron-based cluster source where Pt clusters were deposited on a planar glassy carbon substrate.[6d] By studying model 2D systems, further analytical confirmation becomes possible which ensures firm conclusions on the complex, applied 3D systems. For direct comparison, the common parameter of the edge-to-edge interparticle distance (ipd) is used, which was recently shown to be crucial in the degradation of Pd heterogeneous catalysts[9] and now also to electrocatalyst degradation via Pt dissolution.

2. Experimental

Mass-selected (2D) sample preparation:

The Pt nanoparticles were prepared by noble-gas aggregation of a magnetron sputtered Pt target (99.99%, AJA International Inc., USA) followed by a time-of-flight mass filter allowing for fine control of particle sizes as previously described.[10] For these samples, the nanoparticle source (Birmingham Instruments Ltd. 2011) was optimized for high deposition rates, therefore the mass filter was set to a resolution of $m/\Delta m=20$, which results in a particle size of 6 nm and an uncertainty of 0.1 nm. Subsequently, the charged particles were soft-landed on a planar glassy carbon substrate (10 mm x 10 mm x 3 mm, SIGRADUR® G, HTW GmbH) under ultra-high vacuum (UHV) conditions. The glassy carbon substrate was sputtered with 1 keV Ar^+ for 10 minutes before deposition to remove adventitious carbon from the surface, ensuring the particles land on the glassy carbon. Since the vast majority of particles exiting the mass filter are singly charged, the projected coverage of the nanoparticles was controlled by monitoring the current on the substrate during deposition. Furthermore, to ensure a homogeneous coverage of 2D particles across the entire sample geometry, the substrate was rastered in front of the particle beam during the deposition.

For the 2D materials the coverage is calculated as the projected coverage of the nanoparticles and reported in % of a monolayer.

Pt/Vulcan (3D) sample preparation:

Pt/Vulcan catalyst samples were synthesized via the toolbox approach as reported previously.[8b] In short, the synthesis consists of two main steps: the preparation of a suspension of colloidal Pt nanoparticles (NPs) via an alkaline ethylene glycol (EG) route and a subsequent immobilization of the NPs onto the carbon support. A colloidal suspension of Pt NPs (ca. 2 nm in diameter) was synthesized by mixing 4 mL of 0.4 M NaOH solution in EG with 4 mL of a solution of 40 mM $H_2PtCl_6 \cdot 6H_2O$ in EG in a microwave reaction vessel. The mixture was heated for 3 min at 160 °C with a microwave reactor (CEM Discover SP, 100 W heating power). In order to support the Pt NPs onto a carbon support, 30 mL of 1M HCl solution was added to 7.3 mL of the colloidal Pt NPs suspension for precipitation. The mixture was centrifuged at 2400 relative centrifugal force (4000 rotations per minute (rpm), Sigma 2-5) for 5 minutes and the supernatant solvent discarded. This washing/centrifugation with 1M HCl was repeated twice. Then the Pt NPs were re-dispersed in 7 mL of acetone, and 27.5 mg of carbon black (Vulcan XC72R) was added to the suspension. By sonicating the mixture in an ultrasonic bath (Ultrasonic cleaner, VWR) for 1 hour, the acetone was evaporated, and a dried powder of Pt NPs supported on carbon (Pt/Vulcan, 50 wt. % in nominal Pt loading) was obtained. The dried powder was re-dispersed in water and sonicated for 10 min. The Pt/Vulcan catalyst powder was filtered and washed with 200 mL of DI water, and then dried at 100 °C in air. Pt/Vulcan catalysts with different Pt loadings were prepared by changing the amount of the carbon support mixed with the Pt NPs in the immobilization step.

The Pt loading was determined by digestion of aqua regia and calibrated UV-Vis measurements, as described previously.[11] The average interparticle distances were calculated based on the previously used equation shown below, where A is the support (BET) surface area, N is the number of nanoparticles and d(NP) is the particle diameter.[6a, b, d, 8c] It is important to recognize that this formula overestimates the interparticle distances (**Figure 1d** and **Figure S3**) due to the assumption of equally spaced particles, while more accurate experimental determination remains to be developed (to be discussed further in the following sections).

$$(1)\quad ipd = \sqrt{\frac{A}{N}} - d(NP)$$

Catalyst Inks & Dropcasting:

Catalyst inks were prepared based on the work of Inaba et al.,[12] with slight modifications in order to obtain dropcast catalyst spots compatible with the SFC-ICP-MS technique. Such modifications are necessary when going from PTFE shrouded RDE tips to glassy carbon plates as working electrodes (WEs), required for SFC analysis. The solution used for inks was 1 mM KOH with 25 % isopropanol (IPA), prepared from ultrapure water (18.2 MΩ·cm, Milli-Q®, Merck), KOH pellets (EMSURE®, Merck) and IPA (SupraSolv®, Merck). The Pt/Vulcan catalyst material was weighed and an appropriate amount of 1 mM KOH with 25 % isopropanol was added (ca. 2.5-

3.5 mL) in order to obtain 10 µg carbon per cm^2 in the final dropcasting step (in order to keep the catalyst layer thickness constant). The ink was subsequently horn-sonicated (SFX 150, Branson) for two minutes at 35 % amplitude, in intervals of 4 s on, 2 s off, with ice cooling. The pH was then measured (FiveEasy Plus FP20, InLab® Nano, Mettler-Toledo), and the pH value was adjusted to 10-11 using 1 M KOH. The ink was then additionally sonicated for 10 mins with the above conditions. Next a 0.2 mL aliquot of the ink was diluted by half with ultrapure water and sonicated for 4 s, in order to obtain a 12.5 % IPA concentration compatible with the following dropcasting procedure (higher alcohol content caused the spots to spread out, drying with too large surface areas to fit within the SFC WE). For reference, a commercial TKK catalyst was also studied with similar properties, having 2.2 nm average particle diameter and 38.0 wt. % loading (TEC10V40E).

Glassy carbon (GC) plates sized 50 mm x 50 mm x 3 mm (SIGRADUR® G, HTW GmbH) were vigorously polished with 0.05 µm Al_2O_3 suspension (Struers) on woven wool cloth (MD-Mol, Struers), rinsed with ultrapure water and again polished very lightly with slightly diluted suspension until ultrapure water easily beaded off the GC surface when rinsing, then dried overnight in air. Freshly prepared ink was then pipetted/dropcast in arrays onto the glassy carbon plates in 0.2 µL drops ca. 6 mm apart, and covered with a lid to avoid air currents while drying. Dried spots were ca. 0.011 cm^2 in area, and were monitored via laser microscopy and profilometry (VK-X200, KEYENCE) for consistent diameter and surface homogeneity. Only the most homogenous spots with diameters corresponding most closely to the desired area of 0.011 cm^2 were chosen for electrochemical dissolution measurements, which typically consisted of choosing 9-12 out of 30-60 spots.

SFC-ICP-MS Measurements:

Transient electrochemical dissolution of ^{195}Pt was monitored on the previously described SFC-ICP-MS setup.[13] A saturated Ag/AgCl and graphite rod were used as reference and counter electrodes, respectively. The working electrode contact area was ca. 0.035 cm^2, which fully enclosed the dropcast spots of catalyst material. The 0.1 M $HClO_4$ electrolyte was freshly prepared from 70 % $HClO_4$ (Suprapur®, Merck) and ultrapure water (18.2 MΩ·cm, Milli-Q®, Merck) and was saturated with argon via continuous purging immediately before introduction to the cell. An electrolyte flow rate of 190-235 $\mu L \cdot min^{-1}$ was employed, which varied depending on the age of the ICP-MS pump tubing. Dissolution was monitored with the NexION 300 (Perkin Elmer), which was calibrated daily for ^{195}Pt signal from dilution of a standard ICP-MS solution (Certipur®, Merck). As an internal standard 10 $\mu g \cdot L^{-1}$ ^{187}Re was used for ^{195}Pt. Total quantities of dissolution were obtained via integration of the ICP-MS signal with the measured flow rate. Experimental potential was controlled with the Reference 600™ potentiostat (Gamry). All potentials are reported against the reversible hydrogen electrode (RHE) and all experiments were performed at room temperature.

TEM:

For transmission electron microscopy (TEM), the supported nanoparticles on carbon (Pt/Vulcan, 3D materials) were dispersed in ethanol and the solution dropped on a TEM Cu grid

with holey carbon film (Quantifoil). The samples were imaged with a Jeol 2100 operated at 200 kV. At least four randomly selected areas of the grid were imaged at 4 different magnifications. Nanoparticle size was evaluated by measuring manually the diameter of 50 to 145 nanoparticles with the ImageJ software.

STEM:

For scanning transmission electron microscopy (STEM) the mass-selected nanoparticles (2D materials) were deposited on a Cu TEM grid with lacey carbon film (SPI Supplies®) using the nanoparticle source. The microscope was a FEI Titan Analytical 80-300ST TEM with a pre-objective lens spherical aberration corrector (CESCOR from CEOS Company) operated at 300 kV in STEM mode using the high angle annular dark field detector (HAADF) with a maximum resolution of 0.08 nm. Nanoparticle sizes were evaluated from 12 different areas using a thresholding technique in ImageJ (1.51j8) to find the area of each of the 590 imaged particles. Subsequently the particle diameter was found by assuming spherical particles.

SEM:

Scanning electron microscopy (SEM) images were acquired on a FEI Quanta 200 ESEM FEG with an acceleration voltage of 30 kV in high vacuum using an Everhart-Thornley secondary electron detector resulting in a maximum resolution of 2 nm. Image treatment was done in ImageJ (1.51j8).

XPS:

X–ray photoelectron spectra (XPS) were measured on a PHI Quantera II scanning X–ray microprobe for the mass-selected magnetron-sputtered 2D materials. Spectra were acquired using Al–Kα irradiation ($h\nu$ = 1486.6 eV) of a 100 μm diameter area at 25 W and 15 kV. Survey scans at a step size of 1 eV and 280 eV pass energy were collected for 200 ms dwell time per step. Data were analyzed in CasaXPS (2.3.18PR1.0), using instrument specific relative sensitivity factors, Shirley type backgrounds, and a binding energy scale calibrated to the graphitic carbon peak at 284.5 eV.

XPS for the Pt/Vulcan measurements was performed using an ESCALAB 250 Xi instrument (Thermo Fisher, East Grinsted, UK) with monochromatized Al Kα ($h\nu$ = 1486.6 eV) radiation. An in-lens electron source was used for charge compensation. Survey spectra were measured with a pass energy of 100 eV, 10 ms dwell time and 1 eV step width. High resolution spectra were measured with a pass energy of 10 eV, 50 ms dwell time and 0.02 eV steps. Spectra of the reference substances were referenced to remaining adventitious carbon at 284.8 eV. Spectra of carbon supported materials were referenced to graphitic carbon at 284.3 eV. Peak fitting was performed with the XPS Peak41 software using a Gaussian Lorential (G/L) mixed function after a Shirley background subtraction.

EXAFS:

Extended X-ray absorption fine structure spectroscopy (EXAFS) was carried out at the SuperXAS beamline of the Swiss Light Source (SLS), Switzerland (beam current of 400 mA; energy of storage ring of 2.4 GeV) and B18 beamline of the Diamond Light Source, UK (beam current of 300 mA; energy of storage ring of 3 GeV). Solid pellets were prepared by mixing of Pt/Vulcan and cellulose as binder. All Pt LIII edge EXAFS spectra were recorded in transmission mode. The IFEFFIT software package was applied to align, average, correct and normalize the raw data.[14] The extracted data were Fourier transformed from the k-space, where k is the photoelectron wavenumber, to the R space and fitted by using FEFF6 theory. Reference EXAFS spectrum of a Pt foil was taken to establish the amplitude reduction factor (S02).

3. Results

By studying well-defined model 2D (mass-selected, magnetron sputtered) in parallel to the applied 3D (Pt/Vulcan) materials, the combined simplicity of the former and complexity of the latter reaffirm the conclusions to be discussed. The model 2D materials eliminate possible support effects, contaminations from wet-chemical syntheses and allow precise calculation of interparticle distance,[5b, 8b, 12b, 15] while the 3D Pt/Vulcan materials provide a realistic applied material. The critical parameters of particle size and interparticle distance for both the 2D and 3D materials were analyzed and are shown in **Figure 1**. SEM images of the 1, 2 and 5 % coverages for the 2D materials are displayed in the top row of **Figure 1a-c**. At higher coverages, the interparticle distances become difficult to estimate from the SEM images due to poor resolution and increasing probability of particle overlap; therefore, the three lowest coverages are used to estimate values of interparticle distance from the SEM images and are plotted in **Figure 1d**. To obtain interparticle distances at higher coverages, it is possible to use calculations assuming a homogenous (evenly spaced) distribution. However, it is seen in **Figure 1d** (magnified in **Figure S1**) that this overestimates interparticle distances at low coverages. Therefore, the interparticle distances were simulated by generating random particle positions with the number of particles in a given area determined by coverage (detailed in supplementary information), which fit well with the measured SEM values and are used in the following discussion. To ensure a narrow size distribution as a result from the synthesis, Pt particles were deposited on a Cu TEM grid and analyzed via STEM. The resulting particle size distribution is displayed in **Figure 1e** (full image sets are found in **Figure S4**). Two narrow distributions were obtained, the single mass and double mass particles. Due to the low number of double mass particles these can be neglected. A mean diameter of 6.5 ± 0.4 nm was obtained. The deviation from 6 to 6.5 nm is due to the error of the assumption of spherical particles when calculating particle size from mass. The particles are not perfect spheres as is evident from **Figure S4b**. The use of rather large particle sizes here enabled the estimation of interparticle distances at low coverages confirming the accuracy of the simulation and enabling it predict values at higher coverages, which becomes nearly impossible for smaller particle sizes due to the limited resolution of SEM analysis.

Analysis of the 3D Pt/Vulcan materials was carried out using TEM, and is analogously displayed with increasing loading in the bottom row of **Figure 1f-h** (a full set of images is found in **Figure S5**). Highly homogeneous particle distributions and increasing loading of NPs are clearly observed. In contrast to the 2D materials, estimation of the interparticle distance becomes

difficult from a 2D image of a 3D material,[6b, 8c] highlighting the increased complexity of moving from model to applied catalyst systems. Therefore, for the 3D systems, the interparticle distance was calculated using Equation (1) which assumes homogeneously spaced particles and is shown in **Figure 1i** (magnified in **Figure S3**) for all Pt/Vulcan materials. However, it should be noted that for the 2D materials this treatment overestimates the distances at low coverages, as similarly reported for Pt/Vulcan previously.[8c] The particle size distribution of each material was measured and a representative histogram is displayed in **Figure 1j** (a full set of data is found in **Figure S6**). The particle sizes were found to be identical within error (1.9 ± 0.5 nm average), as to be expected with the two-step synthetic approach which yields high control over particle size and loading.

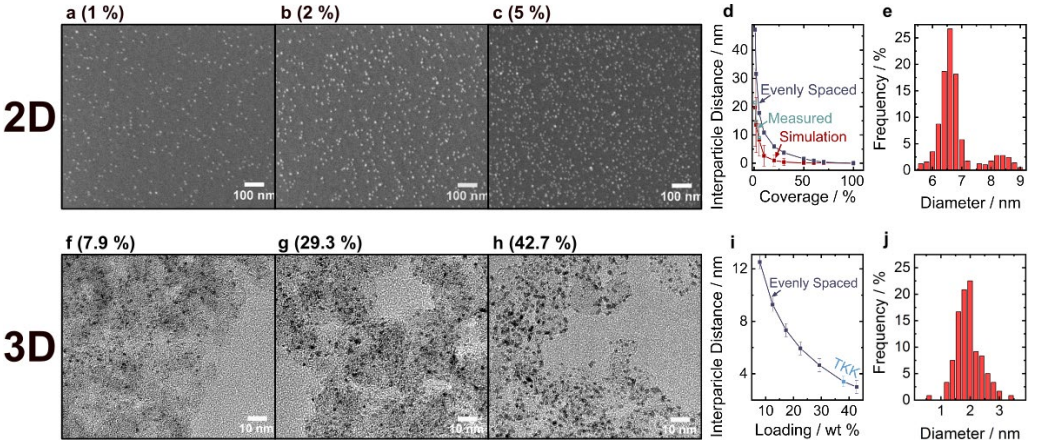

Fig 1. (a-c) Selected SEM images of the 2D mass-selected materials of 1, 2 and 5 % coverage. (d) Interparticle distances measured from the SEM images, calculated assuming homogeneous spacing and from simulations. (e) Particle size distribution obtained from STEM. (f-h) TEM images of the 3D Pt/Vulcan materials of 7.9, 29.3 and 42.7 wt. % Pt. (i) Interparticle distance calculated assuming a homogenous distribution. (j) Particle size distribution measured for the 29.3 wt. % Pt/Vulcan. Note that the percent values in the top and bottom rows represent Pt coverage and Pt to carbon mass ratio, respectively.

Aside from the physical properties on the nanoscale of the material, macroscopic properties are critical in fundamental electrochemical studies. The 2D materials are sputtered in a raster pattern (**Figure S7**) over a large area of glassy carbon, relative to the contact area of the SFC comprising the working electrode. Therefore, the Pt coverage must be highly homogeneous to ensure that any area can be contacted and measured electrochemically. By measuring an array of XPS spectra and quantifying the atomic concentration of Pt across each sample (**Figure S8 and Figure S9**) the homogeneity of each sample was assured after synthesis. For the 70 % coverage sample, a relative standard deviation of only 3.4 % was obtained, demonstrating the effectiveness of the raster technique. In addition to ensuring coverage homogeneity, the XPS spectra (**Figure S8**) indicate a clean surface with no contaminations while the atomic concentration of Pt shows a linear increase with coverage (**Figure S10**), indicating that significant particle overlap is only taking place at coverages > 50 %.

In contrast to the 2D materials sputtered over a large piece of glassy carbon, the 3D Pt/Vulcan materials are dropcast as spots onto glassy carbon, and completely enclosed by the SFC contact area. The amount of Pt on the working electrode will be determined simply by the volume of ink dropcast; however, constant and uniform catalyst layer thickness becomes a prerequisite to separate the previously reported effects of varying thickness from Pt density (i.e. wt. % loading). Therefore, profilometry was employed as a screening tool. A constant average thickness/height of 0.4 µm was found for all samples as shown in **Figure S11**. Microscopy and profilometry (**Figure S12** and **Figure S13**) show homogenous catalyst layer surfaces with no "coffee ring"[8c, 11-12, 16] effect and only slight agglomeration in the middle of the spots. However, the commercial Pt/Vulcan (TKK) catalyst has a significant amount of agglomeration and some degree of the coffee ring effect, causing a bumpy surface. The differing dropcasting results could possibly be due to varying properties of the Vulcan support, such as surface area and/or functionalization degree. It is well known that small variations of parameters can yield vastly different dropcasting results.[8c, 11-12, 16a, c, d, 17]

To measure the electrochemical dissolution of the 2D and 3D systems the samples were subjected to a slow cyclic voltammogram (CV, 0.05-1.5 V_{RHE}, 10 $mV \cdot s^{-1}$) followed by aggressive accelerated degradation test (ADT) protocol (1000 cycles of 0.6-1.5 V, 500 $mV \cdot s^{-1}$) and finally another slow CV, as seen in **Figure 2a**. By employing these two specific scan rates and potential windows, different aspects of dissolution are elucidated. The potential window used here has been demonstrated to cause significant Pt dissolution with rather minimal carbon corrosion.[18] In comparison, the typically used potential windows in accelerated degradation tests in the range of 0.6-1.0 V_{RHE} and 1.0-1.5 V_{RHE} (used to simulate load and start/stop conditions, respectively), will not cause significant Pt dissolution in such a half-cell experiment designed for online detection. The impact of potential window will additionally be addressed in an upcoming manuscript.

The mass-normalized dissolution rate profiles for the 3D and 2D systems during the ADT are shown in **Figure 2b** and **Figure 2c**, which caused extensive Pt dissolution from 15-65 % loss for the 2D and 3D systems (**Figure S14**). No particle detachment is observed in the ICP-MS signal (which would cause excessively large spikes), even in the absence of ionomer, indicating strong binding of the nanoparticles to oxygenated support sites, as observed previously for the Pt/Vulcan toolbox synthesis method.[8b] Dissolution clearly decreases with decreasing interparticle distance (increasing loading), but here the distinct shapes of the profiles are strikingly different. For the 3D systems, the rate drastically decreases in the initial stages of the ADT, which is far more pronounced for large interparticle distances. At the end of the ADT, an additional cathodic dissolution peak is observed only at large interparticle distances when a reductive potential of 0.05 V_{RHE} was applied (**Figure 2b, inset**). This is most pronounced for the 12.5 nm interparticle distance and is only observed for the three largest interparticle distances of the 3D systems. Such behavior is absent from the rather linear decline in dissolution rate of the 2D system, which has larger 6.8 nm particles in comparison to 1.9 nm for Pt/Vulcan.

It appears that for large interparticle distances, the Pt nanoparticles become (partially) passivated by formed PtO_x, i.e. the lower potential limit (LPL) of 0.6 V_{RHE} is too positive to fully reduce this formed layer on the time scale of the ADT cycling. This is further illustrated in the mass-normalized charge during the reductive hold following the ADT in **Figure 2d** (error from $n \geq 3$ where raw data treatment is shown in **Figure S15** and **Figure S16**). The mass-normalized charge is used to take into account variations of Pt mass on the WE. The larger interparticle

distances contain more PtO_x at the end of the ADT and thus more charge is passed to the nanoparticles, which leads to a higher accumulated charge measured during the reductive hold. This is further pronounced by the Gibbs-Thomson effect[19] for the 3D system of smaller particle size, causing the additional cathodic peak at the end of the ADT.

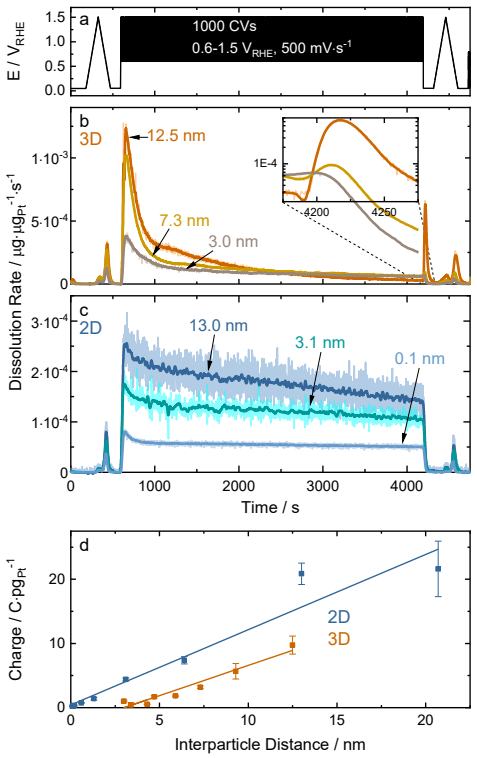

Fig. 2. (a) Full ADT protocol of CVs from 0.6-1.5 V_{RHE}, 500 $mV \cdot s^{-1}$ for 1000 cycles. (b) Resultant dissolution rate profiles for the 3D Pt/Vulcan and (c) 2D magnetron-sputtered systems for three interparticle distances. (d) The mass-normalized charge during the 0.05 V_{RHE} reductive hold immediately following the ADT cycling ($n \geq 3$).

The intercept of the mass-specific reduction charge (**Figure 2d**) is shifted for the 3D materials. Calculation of interparticle distances for the 3D materials assumed homogeneously distributed, evenly spaced particles, due to lack of accurate experimental techniques. For the 2D materials this was shown by SEM and simulations to overestimate interparticle distances (**Figure 1d**), while for Pt/Vulcan it has been suggested that inaccessible pores cause an overestimation of surface area (and thus interparticle distance), which explains the observed shift of the intercept away from the origin. This result highlights the importance of comparing well-defined model systems to applied materials on the quest to understand electrocatalytic materials and their degradation.

To further explore the phenomena of particle passivation, which may be compounded by particle size shrinking during the ADT (due to dissolution), an "extended" ADT to 2,500 cycles was applied to the 20.7 nm interparticle distance (1 % coverage) 2D sample. As shown in **Figure S17**, ~ 80 % of the initial material was lost as the dissolution rate decreases to near baseline values, indicating highly passivated Pt particles. In comparison ~ 60 % Pt loss was observed in **Figure S14** for 1000 cycles for the same material. After 2,500 cycles the potential was held again at 0.05 V_{RHE} and a large spike in the dissolution rate was observed, due to the reduction of oxide-passivated Pt particles. The reduction charge after 2,500 cycles of ADT was found to be identical to after 1,000 cycles, which follows that the dissolution rate is approaching low values and the particles are approaching full passivation by this point of the experiment.

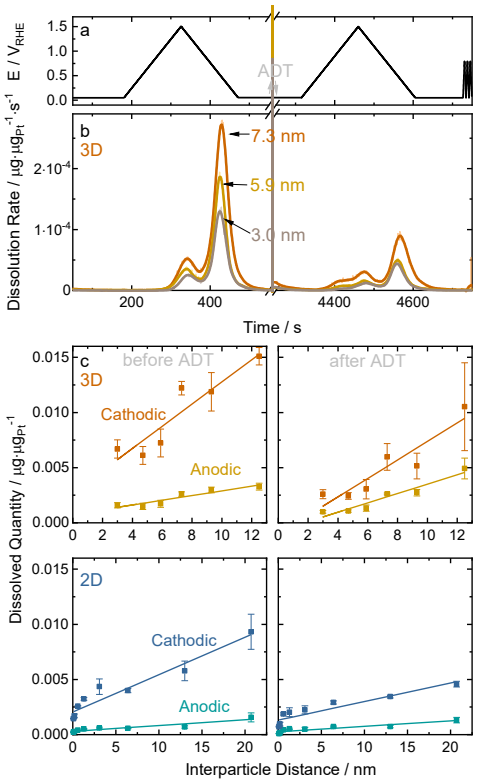

Fig. 3. (a) Two 10 $mV \cdot s^{-1}$ CVs from 0.05-1.5 V_{RHE} prior and following a harsh ADT protocol from 0.6-1.5 V_{RHE}, 500 $mV \cdot s^{-1}$ for 1000 cycles. (b) Resultant dissolution rate profiles normalized to total Pt mass on the working electrode for varying interparticle distance. (c) Quantified anodic and cathodic dissolution before and after the ADT also normalized to mass for the 3D Pt/Vulcan (top) and 2D magnetron-sputtered (bottom) materials ($n \geq 3$).

The slower CVs preceding and following the ADT have a larger potential window with a more negative lower potential limit (LPL) of 0.05 V_{RHE}, in comparison to 0.6 V_{RHE} during the ADT. Therefore, the formed oxide layers should be fully reduced during the cathodic scan and

eliminate formed passivating layers skewing results, thus the intrinsic interparticle distance effect on dissolution can be observed. **Figure 3b** shows the electrochemical mass-normalized dissolution rate profiles for the 3D systems during the two slow CVs before and after the ADT. The separate anodic and cathodic dissolution processes are visible at this relatively slow scan rate and dissolution is clearly diminished after the ADT (expected after significant Pt loss). Some degree of tailing is seen, as compared to slower 2 $mV \cdot s^{-1}$ scans.[5a] Most importantly, a trend is observed for both 2D and 3D systems in which dissolution decreases with decreasing interparticle distance, exemplified in the dissolved quantities for the anodic and cathodic peaks in **Figure 3c**. A similar observation for varying catalyst layer thickness and constant interparticle distance was earlier attributed to a diffusional effect causing a shift in the Nernst potential for dissolution.[5b] An additional observation is seen in the anodic dissolution peak after the ADT (only for Pt/Vulcan materials), where a shoulder appears with an onset ≤ 0.5 V_{RHE}. Dissolution during the ADT will cause the shrinking of some particles to sizes below 1 nm which are possibly susceptible to dissolution at such low potentials;[5a, 20] however, further investigations are required to fully understand these observations.

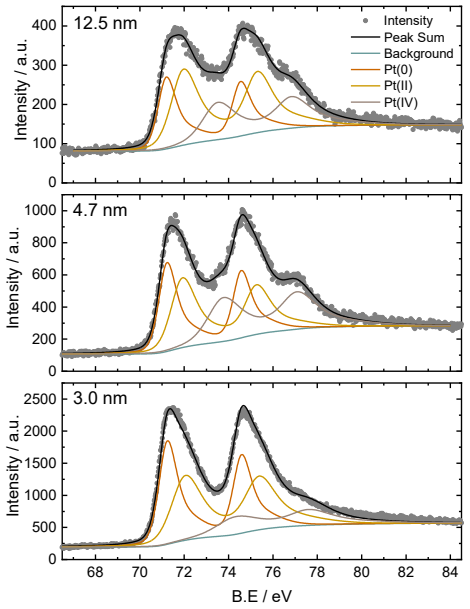

Fig. 4. Ex-situ Pt 4f XPS spectra of the 12.5, 4.7 and 3.0 nm interparticle distance samples, showing the measured intensity and fitted spectra.

Ex-situ XPS, XANES and EXAFS characterization techniques were used to further corroborate the above observations of increasing nanoparticle oxidation at larger interparticle distances for the 3D Pt/Vulcan materials. Considering that the 2D mass-selected materials are limited to flat surfaces for accurate interparticle distance control and that the 3D Pt/Vulcan materials with smaller particle sizes showed a much more drastic passivation effect on the Pt dissolution above, only the 3D applied systems were characterized further. By analyzing the Pt 4f XPS peak positions and areas it is possible to ascertain the relative amount of Pt surface oxidation.

The fitted XPS spectra of 3.0, 4.7 and 12.5 nm interparticle distance Pt/Vulcan materials are shown in **Figure 4** and as interparticle distance increases, the relative amounts of Pt(0) decreases and the Pt 4f peak shifts to higher binding energies (**Table S2**), indicating increased oxidation state of the Pt species.

With EXAFS and XANES characterization, inferences regarding the nearest neighbor coordination and the density of unoccupied states may be made, providing further information on the surface oxidation of the Pt NPs. The FT-transformed magnitudes of the k^2-weighted EXAFS data and the corresponding fits for Pt/Vulcan materials with different interparticle distances are shown in **Figure 5a**. For analysis, the nearest neighbor Pt-O and Pt-Pt contributions to the EXAFS data were determined and summarized in **Table S3**. The total coordination number of Pt (sum of the partial coordination numbers (N(Pt-Pt) and N(Pt-O)) are similar irrespective of the interparticle distance, indicating that the particle size of the Pt NPs are in the same range. More interestingly, the contribution of Pt-O increases with increasing interparticle distance. Despite similar total coordination numbers, the partial coordination number of Pt-O increases from 2.4 ± 0.9 to 3.1 ± 1.6 for 3.0 and 12.5 nm interparticle distance, respectively. Evidently, the oxophilic properties of these Pt NPs are enhanced with increasing interparticle distance. The changes in the oxidation state of Pt NPs coincide with changes in the white line intensity from the Pt L_{III} edge XANES data (**Figure 5b**), which corresponds closely to the density of unoccupied states and thus affinity to PtOH formation.

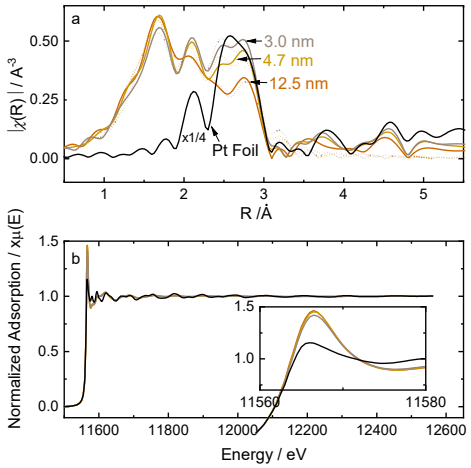

Fig. 5. (a) FT-transformed magnitudes of the k^2-weighted EXAFS spectra and fits (dotted) and (b) Pt L_{III} XANES spectra of the 12.5, 4.7 and 3.0 nm interparticle distance samples and Pt foil as reference.

4. Discussion

The trends of decreasing dissolution rate and quantities with decreasing interparticle distance can be explained by three fundamental mechanisms, which are also visually illustrated in **Figure 6** for the 2D (mass-selected) materials:

1) As interparticle distance decreases, local Pt^{n+} ion concentrations will more quickly build up in the vicinity of the Pt nanoparticles, causing a shift in the Nernst equilibrium potential for electrochemical dissolution.[5b]
2) As interparticle distance decreases, the probability for Pt^{n+} ion redeposition on adjacent Pt particles or particles within the diffusion path from inside the electrode pores to the bulk electrolyte during cathodic potentials will increase.
3) As interparticle distance decreases, the Pt NPs begin to impact each other's oxophilicity. In acidic electrolyte there is increasing overlap between the Pt nanoparticles' electrochemical double layer (EDL), which shifts the oxidation potential of the particles to more positive potentials. Therefore, the Pt nanoparticles become less oxidized during the electrochemical protocol,[6, 21] which results in decreased dissolution. As evidenced by ex-situ XPS and XANES/EXAFS, there is also an impact on the electronic configuration of the NPs, which move from one of isolated NPs towards one of NP ensembles with screened coulomb interaction and more metallic film like properties.[22] According to the shift in the oxygen reduction potential from CVs (**Figure S18**)[6, 21] and the diminished d-band vacancy from XANES at low interparticle distances, there are changes in the affinity of Pt nanoparticles for oxidation. Consequently, and similar to the impact of double layer overlap, the Pt nanoparticles with lower interparticle distance will become less oxidized during the electrochemical protocol which results in decreased dissolution.

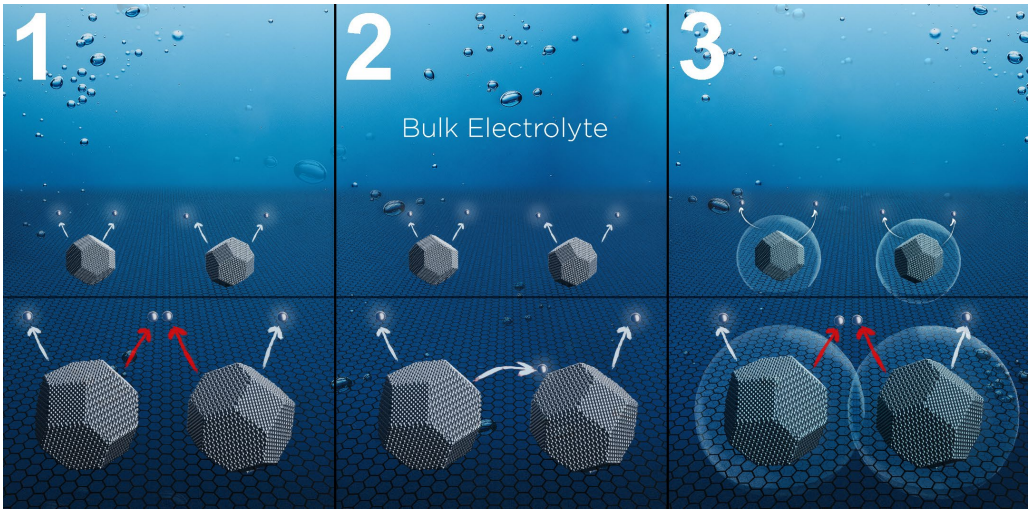

Fig. 6. Schematic representation of mechanisms (1-3) on a planar carbon surfaces below a liquid electrolyte for (foreground) small interparticle distance and (background) large interparticle distance. White arrows show dissolved Pt atoms while red arrows indicate inhibited dissolution.

Although all suggested mechanisms (1-3) must contribute to the trends in mass-specific dissolution shown in **Figure 2** and **Figure 3**, they cannot be the only factors at play. If the dissolution trend were entirely a consequence of mechanism (1) and (2), a directly proportional change in dissolution with coverage or loading should be expected. Mechanism (3) would also contribute to a more drastic decrease in specific dissolution when combined with (1) and (2); however, the dissolution decreases more gradually than can be accounted for by these mechanisms alone. It appears that dissolution is also being controlled kinetically due to low-coordinated defect sites (i.e. edges, corners, adislands and adatoms) present on the nanoparticles surface.[23]

While mechanisms (1-2) are arguably intuitive and have shown to play a role in dissolution on varied diffusion path lengths (catalyst layer thicknesses) at constant interparticle distance, mechanisms (3) has a very interesting effect on electrochemical dissolution. During the 0.6-1.5 V_{RHE} ADT (**Figure 2**), for both the 2D and 3D systems the Pt particles become (partially) passivated by PtO_x, which clearly depends on the interparticle distance. From the shape of the 3D dissolution rate profile, the sharp initial decrease indicates such passivation is pronounced at large interparticle distances, further evidenced by the cathodic dissolution peak during the subsequent reductive hold. Small interparticle distances diminish this effect and the particles are more easily reduced (become less passivated during the ADT). Similarly, mechanism (3) has previously been attributed to observed increases in ORR activity with decreasing interparticle distance for 2D and 3D systems, as poisoning oxygenated species can block active catalytic sites.[6] Inhibited oxide formation also explains the observed shift in the Pt CV reduction peak (**Figure S18**).[6, 21]

The XPS and XANES data demonstrate that the shift in the Pt CV reduction peak is at least partially due to mechanism (3), i.e. a change in electronic configuration of Pt with decreasing interparticle distance. As interparticle distance increases, the relative amounts of Pt(0) decrease and Pt(II) and Pt(IV) increase, and consequently the Pt 4f peak shifts to higher binding energies in the XPS spectra. From the EXAFS experiments an increase in Pt-O coordination is seen, while XANES results clearly show a decreased d-band vacancy at small interparticle distances, resulting in less affinity to PtOH formation. This suggests that the interface between the particles is influenced by coupling / dipole-dipole interactions between the particles. Similar effects have been observed previously in the electronic structure of ensembles of metallic and semiconducting NPs,[22a-c] but so far have not been related to catalytic reactions. Coupling in closely-spaced NP systems has been shown to modify electronic structures and transport properties. In isolated sub-10 nm NPs the electronic structure can be described by isolated wavefunctions, but when brought in close proximity the wave functions can couple, forming bands transition from insulator to conductor with decreasing interparticle distance.[22] Although the individual contributions of the double layer and electronic structure of mechanism (3) on observed dissolution trends may only be speculated at this time, it is highly evident that smaller interparticle distances cause profound interactions which significantly impact oxidation, reduction and dissolution.

With larger particles size of 6.8 nm compared to 1.9 nm, the Gibbs-Thomson equation dictates a more positive oxidation potential for larger particles,[19a-c] and this system is less easily passivated than the 3D system. This explains the distinctly different shapes of the dissolution rate profiles during the ADT: the 2D systems fit a more linear trend. However, the recorded mass-specific reduction charge at 0.05 V_{RHE} after the ADT follows a similar slope to the 3D system of smaller particle size. As particles shrink during the ADT, they will become more easily passivated

due to mechanism (3). This is further corroborated by the extended ADT to 2500 cycles (**Figure S17**), where the dissolution rate ceases as shrinking particles become heavily passivated, and the reduction charge after 1000 or 2500 cycles becomes identical.

The study presented here investigated fundamental aspects of PEMFC catalyst degradation, while some important aspects of applied systems should be considered. In real PEMFC devices, the effect of ionomer and interaction with Pt influences performance and degradation.[1-2] However, in situ/online dissolution studies as conducted here are currently infeasible on a full cell level, and a bottom-up approach gives us valuable insights that can predict PEMFC degradation. For instance, Pt dissolution in full cell MEAs is known to be most pronounced close to the membrane, resulting in a Pt "depletion band", where a significant portion of the Pt is redeposited within the membrane itself.[24] This is not unexpected, as dissolved Pt^{n+} atoms require a conductive medium (ionomer/membrane), and effectively increased degrees of freedom close to the membrane allow increased Pt^{n+} diffusion. Therefore, decreasing Pt interparticle distance (Pt density) near the membrane should alleviate the depletion band effect, as was found by Yu et al.[24]

Current applied PEMFC electocatalysts take advantage of the high activity of Pt-transition metal alloys in vehicles such as the Toyota Mirai.[25] The dissolution of the alloying metal will also contribute to degradation, via loss of activity enhancement.[26] Dissolution of the alloying metal can cause an increased particle surface area and enhance dissolution of Pt, while Pt dissolution itself can expose additional alloy towards further dissolution.[27] Therefore, increased Pt dissolution remains detrimental to alloyed systems. However, the composition, nature of the alloying metal, initial leeching procedure and applied potential protocol (i.e. accelerated durability test) all drastically impact the dissolution of both metals. Here, the single, fundamental parameter of interparticle distance for pure Pt nanoparticles was varied independently of others, while additional studies will be required to definitively determine the impacts of additional variables in increasingly complex catalytic systems.

In addition to the complexity of alloyed systems, the complete degradation of PEMFC catalysts is convoluted. The additional degradation mechanisms of carbon corrosion, Ostwald ripening, coalescence and particle detachment are all intricately intertwined with Pt dissolution.[19a] Following the discoveries presented here on the impact of interparticle distance on Pt dissolution, future studies should investigate the impact on the other detrimental degradation mechanisms.

Nevertheless, the observations on both 2D model systems and 3D porous Pt/Vulcan materials clearly demonstrate a dissolution dependence on interparticle distance, governed by three different mechanisms. Mechanism (3) contributes to this dependence by altering the redox behavior of the nanoparticles, which can be further compounded by the Gibbs-Thomson (particle-size) effect as nanoparticles shrink from electrochemical dissolution. Therefore, in conventional half-cell ADT experiments, potential limits should be chosen carefully with regards to the large variety of loadings and particle sizes in experimental and commercially available electrocatalytic materials.

It is also important for future engineers to take such considerations into account when designing PEMFC stacks in order to optimize performance and lifetime. Very high loadings can lead to nanoparticle agglomeration and lower Pt utilization, while very low loadings may cause increased mass transport, both lowering performance. As Pt dissolution decreases with increased loading, the clear goal would be to synthesize Pt/C materials with as high loadings as possible without substantial agglomeration effects. In the quest for increasingly active ORR electrocatalysts

to reduce required Pt quantities in PEMFCs, from this perspective lower loadings should come in the form of thin catalyst layers made from high wt. % Pt/C materials. However, thin catalyst layers may present their own performance and degradation issues.[1-2, 28] Furthermore, the effect of interparticle distance on Pt dissolution and catalyst layer degradation in full cell MEAs still remains to be explored.

5. Conclusion

A clear coverage/loading effect on transient Pt electrochemical dissolution has been observed for model 2D mass-selected systems and applied 3D porous Pt/C materials. With increased coverage/loading mass-specific electrochemical dissolution significantly decreases and stability increases. These observations can be attributed to three mechanisms: (1) increased local Pt^{n+} ion concentrations causing a shift in the Nernst equilibrium potential for dissolution, (2) increased probability for Pt^{n+} ion redeposition, (3) increasing overlap between the nanoparticles electric double layer and coupling / with pronounced dipole-dipole interactions between neighboring nanoparticles. Further ex-situ characterization has provided evidence of (3) where Pt oxidation decreases in XPS spectra, and EXAFS unveils decreasing Pt coordination to oxygen with increasing loading. The consequential passivation effect during accelerated degradation testing is seen to be pronounced for large interparticle distances due to (3), which is diminished for larger particle sizes, emphasizing the importance of potential limits in accelerated degradation test experiments with varied loading or particle size.

Conflicts of interest

There are no conflicts of interest to declare.

Acknowledgements

This work was funded by the Villum Foundation V-SUSTAIN grant 9455 to the Villum Center for the Science of Sustainable Fuels and Chemicals and the Swiss National Science Foundation (SNSF) via the project No. 200021_184742. The Escalab 250 Xi XPS facility has been co-funded by the Deutsche Forschungsgemeinschaft (INST 184/144-1 FUGG). Bundesministerium für Bildung und Forschung (BMBF, FKZ 03SF0539) are gratefully acknowledged. The SLS is acknowledged for the provision of beamtime at the SuperXAS beamline (project ID 20161303). Diamond Light Source, Hartwell, UK is thanked - in particular Dr Giannantonio Cibin and Ann-Kathrin Geiger - for access to synchrotron beamline B18 (proposal SP12746). We thank Dr L. Theil Kuhn and Dr. S. B. Simonsen, Technical University of Denmark for access to TEM facilities.

References

1. A. Kongkanand and M. F. Mathias, *J. Phys. Chem. Lett.*, 2016, **7**, 1127-1137.

2. P. Gazdzicki, J. Mitzel, A. M. Dreizler, M. Schulze and K. A. Friedrich, *Fuel Cells*, 2018, **18**, 270-278.
3. (a) V. R. Stamenkovic, B. Fowler, B. S. Mun, G. Wang, P. N. Ross, C. A. Lucas and N. M. Marković, *Science*, 2007, **315**, 493-497; (b) P. Hernandez-Fernandez, F. Masini, D. N. McCarthy, C. E. Strebel, D. Friebel, D. Deiana, P. Malacrida, A. Nierhoff, A. Bodin, A. M. Wise, J. H. Nielsen, T. W. Hansen, A. Nilsson, I. E. Stephens and I. Chorkendorff, *Nat. Chem.*, 2014, **6**, 732-738; (c) M. Escudero-Escribano, P. Malacrida, M. H. Hansen, U. G. Vej-Hansen, A. Velázquez-Palenzuela, V. Tripkovic, J. Schiøtz, J. Rossmeisl, I. E. L. Stephens and I. Chorkendorff, *Science*, 2016, **352**, 73-76; (d) D. Li, C. Wang, D. S. Strmcnik, D. V. Tripkovic, X. Sun, Y. Kang, M. Chi, J. D. Snyder, D. van der Vliet, Y. Tsai, V. R. Stamenkovic, S. Sun and N. M. Markovic, *Energy. Environ. Sci.*, 2014, **7**, 4061-4069; (e) M. Oezaslan, F. Hasché and P. Strasser, *J. Phys. Chem. Lett.*, 2013, **4**, 3273-3291; (f) I. A. Safo, C. Dosche and M. Oezaslan, *ChemPhysChem*, 2019, **20**, 15; (g) S. Chen, H. A. Gasteiger, K. Hayakawa, T. Tada and Y. Shao-Horn, *J. Electrochem. Soc.*, 2010, **157**; (h) C. E. Carlton, S. Chen, P. J. Ferreira, L. F. Allard and Y. Shao-Horn, *J. Phys. Chem. Lett.*, 2012, **3**, 161-166.
4. S. Cherevko, *Current Opinion in Electrochemistry*, 2018, **8**, 118-125.
5. (a) S. Cherevko, N. Kulyk and K. J. J. Mayrhofer, *Nano Energy*, 2016, **29**, 275-298; (b) G. P. Keeley, S. Cherevko and K. J. Mayrhofer, *ChemElectroChem*, 2016, **3**, 51-54.
6. (a) J. Speder, I. Spanos, A. Zana, J. J. K. Kirkensgaard, K. Mortensen, L. Altmann, M. Bäumer and M. Arenz, *Surf. Sci.*, 2015, **631**, 278-284; (b) J. Speder, L. Altmann, M. Bäumer, J. J. K. Kirkensgaard, K. Mortensen and M. Arenz, *RSC Advances*, 2014, **4**; (c) E. Fabbri, S. Taylor, A. Rabis, P. Levecque, O. Conrad, R. Kötz and T. J. Schmidt, *ChemCatChem*, 2014, **6**, 1410-1418; (d) M. Nesselberger, M. Roefzaad, R. F. Hamou, P. U. Biedermann, F. F. Schweinberger, S. Kunz, K. Schloegl, G. K. Wiberg, S. Ashton, U. Heiz, K. J. Mayrhofer and M. Arenz, *Nat. Mater.*, 2013, **12**, 919-924.
7. (a) M. Inaba, PhD PhD Thesis, Unversity of Copenhagen, 2018; (b) S. Taylor, E. Fabbri, P. Levecque, T. J. Schmidt and O. Conrad, *Electrocatalysis*, 2016, **7**, 287-296.
8. (a) J. Quinson, M. Inaba, S. Neumann, A. A. Swane, J. Bucher, S. B. Simonsen, L. Theil Kuhn, J. J. K. Kirkensgaard, K. M. Ø. Jensen, M. Oezaslan, S. Kunz and M. Arenz, *ACS Catal.*, 2018, **8**, 6627-6635; (b) J. Speder, L. Altmann, M. Roefzaad, M. Baumer, J. J. Kirkensgaard, K. Mortensen and M. Arenz, *Phys. Chem. Chem. Phys.*, 2013, **15**, 3602-3608; (c) S. Proch, K. Kodama, M. Inaba, K. Oishi, N. Takahashi and Y. Morimoto, *Electrocatalysis*, 2016, **7**, 249-261; (d) J. Speder, A. Zana, I. Spanos, J. J. K. Kirkensgaard, K. Mortensen and M. Arenz, *Electrochem. Commun.*, 2013, **34**, 153-156; (e) J. Speder, A. Zana, I. Spanos, J. J. K. Kirkensgaard, K. Mortensen, M. Hanzlik and M. Arenz, *J. Power Sources*, 2014, **261**, 14-22.
9. E. D. Goodman, A. C. Johnston-Peck, E. M. Dietze, C. J. Wrasman, A. S. Hoffman, F. Abild-Pedersen, S. R. Bare, P. N. Plessow and M. Cargnello, *Nat. Catal.*, 2019, **2**, 748-755.
10. C. Roy, B. Sebok, S. B. Scott, E. M. Fiordaliso, J. E. Sørensen, A. Bodin, D. B. Trimarco, C. D. Damsgaard, P. C. K. Vesborg, O. Hansen, I. E. L. Stephens, J. Kibsgaard and I. Chorkendorff, *Nat. Catal.*, 2018, **1**, 820-829.
11. M. Inaba, J. Quinson, J. R. Bucher and M. Arenz, *J. Vis. Exp.*, 2018, **133**.
12. (a) M. Inaba, J. Quinson and M. Arenz, *J. Power Sources*, 2017, **353**, 19-27; (b) J. Quinson, M. Inaba, S. Neumann, A. A. Swane, J. Bucher, S. B. Simonsen, L. T. Kuhn, J. J. K. Kirkensgaard, K. M. O. Jensen, M. Oezaslan, S. Kunz and M. Arenz, *ACS Catal.*, 2018, **8**, 6627-6635.
13. (a) A. K. Schuppert, A. A. Topalov, I. Katsounaros, S. O. Klemm and K. J. J. Mayrhofer, *J. Electrochem. Soc.*, 2012, **159**, F670-F675; (b) S. Cherevko, A. A. Topalov, A. R. Zeradjanin, G. P. Keeley and K. J. J. Mayrhofer, *Electrocatalysis*, 2014, **5**, 235-240.
14. M. Newville, *J. Synchrotron. Radiat.*, 2001, **8**, 322-324.
15. G. S. Harzer, A. Orfanidi, H. El-Sayed, P. Madkikar and H. A. Gasteiger, *J. Electrochem. Soc.*, 2018, **165**, F770-F779.

16. (a) Y. Garsany, O. A. Baturina, K. E. Swider-Lyons and S. S. Kocha, *Anal. Chem.*, 2010, **82**, 6321-6328; (b) Y. Garsany, I. L. Singer and K. E. Swider-Lyons, *J. Electroanal. Chem.*, 2011, **662**, 396-406; (c) Y. Garsany, J. Ge, J. St-Pierre, R. Rocheleau and K. E. Swider-Lyons, *J. Electrochem. Soc.*, 2014, **161**, F628-F640; (d) K. Shinozaki, J. W. Zack, S. Pylypenko, B. S. Pivovar and S. S. Kocha, *J. Electrochem. Soc.*, 2015, **162**, F1384-F1396; (e) K. Ke, K. Hiroshima, Y. Kamitaka, T. Hatanaka and Y. Morimoto, *Electrochim. Acta*, 2012, **72**, 120-128.
17. R. Sharma and S. M. Andersen, *ACS Appl. Mater. Interfaces*, 2018, **10**, 38125-38133.
18. E. Pizzutilo, S. Geiger, J. P. Grote, A. Mingers, K. J. J. Mayrhofer, M. Arenz and S. Cherevko, *J. Electrochem. Soc.*, 2016, **163**, F1510-F1514.
19. (a) J. C. Meier, C. Galeano, I. Katsounaros, J. Witte, H. J. Bongard, A. A. Topalov, C. Baldizzone, S. Mezzavilla, F. Schuth and K. J. J. Mayrhofer, *Beilstein J. Nanotechnol.*, 2014, **5**, 44-67; (b) W. J. Plieth, *J. Phys. Chem.*, 1982, **86**, 3166-3170; (c) K. J. Mayrhofer, B. B. Blizanac, M. Arenz, V. R. Stamenkovic, P. N. Ross and N. M. Markovic, *J. Phys. Chem. B*, 2005, **109**, 14433-14440; (d) K. Yu, D. J. Groom, X. Wang, Z. Yang, M. Gummalla, S. C. Ball, D. J. Myers and P. J. Ferreira, *Chemistry of Materials*, 2014, **26**, 5540-5548.
20. (a) L. Tang, B. Han, K. Persson, C. Friesen, T. He, K. Sieradzki and G. Ceder, *J. Am. Chem. Soc.*, 2010, **132**, 596-600; (b) L. Tang, X. Li, R. C. Cammarata, C. Friesen and K. Sieradzki, *J. Am. Chem. Soc.*, 2010, **132**, 11722-11726.
21. J. Huang, J. Zhang and M. H. Eikerling, *J. Phys. Chem. C*, 2017, **121**, 4806-4815.
22. (a) C. B. Murray, C. R. Kagan and M. G. Bawendi, *Annu. Rev. Mater. Sci.*, 2000, **30**, 545-610; (b) H. Liu, B. S. Mun, G. Thornton, S. R. Isaacs, Y.-S. Shon, D. F. Ogletree and M. Salmeron, *Phys. Rev. B*, 2005, **72**; (c) J. Liao, S. Blok, S. J. van der Molen, S. Diefenbach, A. W. Holleitner, C. Schonenberger, A. Vladyka and M. Calame, *Chem. Soc. Rev.*, 2015, **44**, 999-1014; (d) D. V. Talapin, J. S. Lee, M. V. Kovalenko and E. V. Shevchenko, *Chem. Rev.*, 2010, **110**, 389-458.
23. J. Ustarroz, I. M. Ornelas, G. Zhang, D. Perry, M. Kang, C. L. Bentley, M. Walker and P. R. Unwin, *ACS Catal.*, 2018, **8**, 6775-6790.
24. H. Yu, A. Baricci, A. Casalegno, L. Guetaz, L. Bonville and R. Maric, *Electrochim. Acta*, 2017, **247**, 1169-1179.
25. R. L. Borup, R. Mukundan, K. More, K. C. Neyerlin, A. Z. Weber, D. Myers and R. Ahluwalia, Seatle, Washington, USA, 2018.
26. (a) I. Spanos, K. Divanis, J. J. Kirkensgaard, S. Jelavic and M. Arenz, *Phys. Chem. Chem. Phys.*, 2015, **17**, 28044-28053; (b) V. Beermann, M. E. Holtz, E. Padgett, J. F. de Araujo, D. A. Muller and P. Strasser, *Energy Environ. Sci.*, 2019, **12**, 2476-2485; (c) Q. Jia, Z. Zhao, L. Cao, J. Li, S. Ghoshal, V. Davies, E. Stavitski, K. Attenkofer, Z. Liu, M. Li, X. Duan, S. Mukerjee, T. Mueller and Y. Huang, *Nano Lett.*, 2018, **18**, 798-804.
27. (a) P. Jovanovič, V. S. Šelih, M. Šala, S. B. Hočevar, A. Pavlišič, M. Gatalo, M. Bele, F. Ruiz-Zepeda, M. Čekada, N. Hodnik and M. Gaberšček, *J. Power Sources*, 2016, **327**, 675-680; (b) M. Gatalo, P. Jovanovič, U. Petek, M. Šala, V. S. Šelih, F. Ruiz-Zepeda, M. Bele, N. Hodnik and M. Gaberšček, *ACS Appl. Energy Mater.*, 2019, **2**, 3131-3141; (c) R. K. Ahluwalia, D. D. Papadias, N. N. Kariuki, J.-K. Peng, X. Wang, Y. Tsai, D. G. Graczyk and D. J. Myers, *J. Electrochem. Soc.*, 2018, **165**, F3024-F3035; (d) C. Baldizzone, L. Gan, N. Hodnik, G. P. Keeley, A. Kostka, M. Heggen, P. Strasser and K. J. J. Mayrhofer, *ACS Catal.*, 2015, **5**, 5000-5007.
28. (a) M. K. Debe, A. K. Schmoeckel, S. M. Hendricks, G. D. Vernstrom, G. M. Haugen and R. T. Atanasoki, *ECS Transactions*, 2006, **1**, 16; (b) A. J. Steinbach, K. Noda and M. K. Debe, *ECS Transactions*, 2006, **1**, 19; (c) M. K. Debe, A. K. Schmoeckel, G. D. Vernstrom and R. Atanasoski, *J. Power Sources*, 2006, **161**, 1002-1011; (d) A. Bonakdarpour, K. Stevens, G. D. Vernstrom, R. Atanasoski, A. K. Schmoeckel, M. K. Debe and J. R. Dahn, *Electrochim. Acta*, 2007, **53**, 688-694; (e) P. K. Sinha, W. Gu, A. Kongkanand and E. Thompson, *J. Electrochem. Soc.*, 2011, **158**; (f) A. Kongkanand, M. Dioguardi, C. Ji and E. L. Thompson, *J. Electrochem. Soc.*, 2012, **159**, F405-F411;

(g) A. Kongkanand, J. Zhang, Z. Liu, Y.-H. Lai, P. Sinha, E. L. Thompson and R. Makharia, *J. Electrochem. Soc.*, 2014, **161**, F744-F753; (h) A. J. Steinbach, C. Duru, A. T. Haug, A. E. Hester, M. Kuznia, K. A. Lewinski, S. M. Luopa, J. T. Petrin, G. M. Thoma, A. J. Kropf, D. J. Myers, D. Yang, D. A. Cullen, J. Greeley and Z. Zeng, *ECS Transactions*, 2017, **80**, 659-676.

The Particle Size Effect on Platinum Dissolution: Considerations for Accelerated Stability Testing of Fuel Cell Catalysts

Daniel J. S. Sandbeck,[a,b,ǂ,*] Niklas Mørch Secher,[c,ǂ] Florian D. Speck,[a,b] Jakob Ejler Sørensen,[c] Jakob Kibsgaard,[c] Ib Chorkendorff,[c] Serhiy Cherevko[a,*]

[a]Helmholtz-Institute Erlangen-Nürnberg for Renewable Energy (IEK-11), Forschungszentrum Jülich GmbH, 91058 Erlangen, Germany

[b]Department of Chemical and Biological Engineering, Friedrich-Alexander-Universität Erlangen-Nürnberg, 91058 Erlangen, Germany

[c]Department of Physics, Technical University of Denmark, 2800 Lyngby, Denmark

[ǂ] These authors contributed equally

E-mail: d.sandbeck@fz-juelich.de

E-mail: s.cherevko@fz-juelich.de

Abstract

Polymer electrolyte membrane fuel cells (PEMFCs) are highly attractive for use in electric vehicles. In PEMFCs, small particle sizes of the Pt catalyst are required to increase Pt utilization, which lower costs and also increases Pt dispersion, which itself minimizes O_2 mass transport losses. Reducing particle size improves both the utilization and dispersion; however, stability of small particle sizes is an issue. Pt dissolution, as one of the major degradation mechanisms of PEMFC catalyst layers, is predicted to depend on particle size. Particle size cannot be independently varied from loading in commercial Pt/C materials that have been used in numerous studies employing accelerated stability tests (ASTs). Therefore, in the study presented here Pt particle diameter was varied from 2-10 nm by depositing mass-selected nanoparticles on a flat glassy carbon substrate using magnetron sputtering. This allows exclusive control over particle density (interparticle distance) and particle size, which becomes difficult even with advanced synthetic techniques for applied Pt/C materials. Additionally, effects of the 3D porous support are eliminated. These model systems were subjected to an aggressive AST in order to cause significant Pt dissolution, which was monitored online using the scanning flow cell coupled to an inductively coupled plasma mass spectrometer (SFC-ICP-MS). The results uncover a previously overlooked phenomenon: two competing trends in dissolution from (1) particle passivation caused by particle size dependent shifts on oxophilicity and (2) electrochemically active surface area (ECSA). Therefore, crucial impacts of particle size on degradation may be overlooked in a variety of electrochemical studies which compare catalytic materials. Finally, suggestions are given for improved ASTs for dissolution, which provide insights into the intrinsic stability of Pt nanoparticles towards dissolution.

Keywords: Pt Dissolution, Particle Size Effect, AST, ADT, PEMFC

Introduction

Due to increasing interest in alternative transportation technologies, electric vehicles have gained considerable attention in recent years. Battery electric vehicles have been prominently covered in media with the advent of Tesla Inc. and other manufacturers. If electricity is generated from renewable sources, battery electric vehicles present a promising green technology to help reduce CO_2 and other toxic emissions, alleviating air pollution and climate change concerns. However, there is still room for improvement of such electrochemical technologies as they are to some extend limited in driving range, charging time, and there exist concerns regarding lithium resources.[1] Regardless, developing a singular economy dependent on a narrow range of technology and resources is a precarious endeavor and increased economic stability will benefit from complimentary industries.[1d, e]

Polymer electrolyte fuel cell (PEMFC) electric vehicles alleviate several shortcomings of battery electric vehicles, such as driving range and charging time,[2] and have already entered consumer production by several automakers.[3] However, this technology also comes with its own set of challenges such as high costs and limited lifetime, which remain as key challenges on the road to widespread market penetration. A majority of the cost comes from the use of Pt as an electrocatalyst for the sluggish oxygen reduction reaction (ORR) in the catalyst layer.[4] In order to minimize required quantities, Pt is dispersed in the form of nanoparticles on a carbon support (Pt/C) to maximize the available surface area relative to mass, i.e., Pt utilization. Furthermore, small particle sizes, yielding high Pt utilization and dispersion, are required to minimize local O_2 mass transport loses necessary for high power performance.[5] Therefore, considerable research efforts have focused on developing highly active and highly dispersed nanoparticulate catalysts,[6] with the end goal of reducing the required quantities of Pt via decreased metal loading.[5a, 7] By minimizing the Pt particle size and maximizing dispersion, (*ideally*) higher ORR currents relative to Pt mass (i.e., mass-specific activity) can be achieved, reducing required Pt quantities.

Unfortunately, elucidation of the particle size on activity has been met with discrepancies. Several studies have shown a maximum in mass-specific activity ($mA \cdot mg_{Pt}^{-1}$) in the range 2-5 nm, which has been attributed to the adsorption strength of oxygenated species on terraces reaching a minimum at a particular particle size.[8] However, some studies have reported a continuous decrease in mass activity with increasing particle size.[6e, 9] It is possible that the lack of observed maxima was hindered by experimental error, limited variation of particle sizes within the studied materials and wide particle size distributions within single samples.

Additionally, disparities exist between studies on area-specific activity (i.e. $mA \cdot cm_{Pt}^{-2}$). By normalizing to the real, i.e. electrochemically active surface area (ECSA), intrinsic activity of catalytic surfaces may be understood. Many studies converge on the conclusion of increasing area-specific activity with increasing particle size approaching that of bulk Pt,[6e, 8a, c, 9b, 10] although some reports have not seen a change within experimental error, depending on the conditions.[9c, 11] The observed trend has been attributed to decreasing oxophilicity of Pt nanoparticles with size, which diminishes the adsorption of poisoning oxygenated species for the ORR.[10] Although the area-specific activity appears to be diminished as particle sizes are reduced, mass activity remains to be the critical parameter dictated by costs. Furthermore, small particle sizes and high dispersion are required to meet high power performance targets.[5] However, stability may become an issue in implementing very small particle sizes.

Recently, in addition to activity, a surge in publications which includes catalyst stability reflects the recognition of this vital issue.[12] Platinum dissolution and carbon corrosion have been recognized as the primary degradation mechanisms of the catalyst layer, which are closely related to the secondary degradation mechanisms of Ostwald ripening, agglomeration and particle detachment.[13] To study degradation, experiments typically measure ORR activity before and after an accelerated stability/stress test (AST), otherwise known as accelerated degradation test (ADT) or accelerated degradation protocol (ADP). Various tests/protocols have been adapted, but in general, most studies use potential ranges from 0.6-1.0 (or 0.6-0.95) V_{RHE} and 1.0-1.5 V_{RHE}, in an effort to exclusively study Pt dissolution and carbon corrosion, respectively (these ranges are intended to represent the load and start/stop conditions of a PEMFC, respectively).[5a, 6e, f, h, 8c, 9c, 11, 14]

In recent years our research group and others have uncovered fundamental aspects of transient electrochemical Pt dissolution and a very brief summary should be given here, while interested readers may be referred to comprehensive reviews.[15] During relatively slow scan rates during a cyclic voltammogram (CV) a so-called anodic dissolution peak is seen at an onset of ca. 1.0 V_{RHE} during the positive-going, anodic potential scan.[15-16] This dissolution coincides with the place-exchange mechanism during Pt oxidation, and as an oxide layer forms the dissolution rate decreases as the Pt surface becomes passivated. In the negative-going, cathodic potential scan, a much larger so-called cathodic dissolution peak is seen as the formed oxide is reduced. The extent and onset of cathodic dissolution depends on the amount of oxide which was formed; however, significant dissolution does not take place without reaching potentials below approximately 1.0 V_{RHE}.

From this it is clear that minimal dissolution will take place during typically used ASTs which do not transverse 1.0 V_{RHE}, and furthermore, realistic spikes in potential during start/stop of a PEMFC will go from potentials < 1.0 V_{RHE} to even higher than 1.5 V_{RHE}. Hence, Pizzutilo et al. exclusively investigated the impact of AST potential limits using in situ Pt dissolution and carbon corrosion (CO_2) experiments.[17] The central outcome of the study was the suggested use of a "combined cycle" AST spanning 0.6-1.5 V_{RHE}, as the results showed this to cause substantial Pt dissolution with relatively minimal carbon corrosion. Therefore, this AST could aid in understanding the degradation behavior of PEMFC catalysts.

Stability investigations focused on particle size effects remain to establish firm conclusions, as ambiguities exist in analogy to the discussed activity studies. Many studies have indeed shown a decreasing stability with decreasing particle size via losses in ECSA and area-specific activity.[6e, 8c, 9c] On the contrary, some studies have reported no particle size dependence by studying materials of varying size but with narrow particle size distributions within each material, and rather suggest that large particle size distributions promote degradation via Ostwald ripening.[11, 14a] However, in the studies which found small sizes to be the least stable, the smallest particle sizes had the narrowest particle size distributions, a consequence of the commonly used procedures of annealing heat treatments to increase the particle size of Pt/C materials. Furthermore, Ahluwalia et al. observed that the particle size effect on Pt dissolution can depend on the applied potential protocol with ex-situ ICP-MS dissolution experiments.[14b]

These uncertainties in particle size effects described above highlight the need for well-defined systems in fundamental investigations. To vary particle size via typically used impregnation and precipitation synthetic techniques of commercial materials, a subsequent

annealing procedure is used, which results in wide size distributions, increased interparticle distances and can alter the carbon support.[8a, 11, 14a, b, 18] Some chemical approaches yield exclusive control over particle size and loading, with much narrower size distributions; however, the surfactants used in synthesis can be difficult to remove from the products. Furthermore, the type of support used will influence interparticle distance and diffusional paths of dissolved Pt species.

Therefore, there is an immediate need for well-defined systems to reach firm conclusions on particle size effects. The use of a magnetron gas aggregation source allows the precise control over particle size and coverage (interparticle distance) by depositing mass-selected nanoparticles on a relatively-flat substrate.[19] Also alloy clusters have been investigated using this method, but they show optimal mass activity at much larger sizes than pure Pt.[20] This method eliminates the possibility of organic contaminations, impacts of a 3D porous support on Pt dissolution[21] and also results in a narrow size distribution. Furthermore, precise control over interparticle distance excludes possible effects which have recently shown to drastically alter dissolution/degradation,[22] and will be addressed further in a parallel investigation.

Here in this study magnetron-sputtered mass-selected materials were synthesized with varying particle sizes (i.e. masses) of 2, 3, 4, 6, 7, 8 and 10 nm diameters (identical diameter within a given sample) with similar interparticle distances of around 6 nm (1-9 % coverages). Using a large sample set reduces the possibility of missing trends and the reasonably large interparticle distance should minimize possible interparticle distance effects (addressed in a parallel study). To investigate degradation, online electrochemical dissolution of Pt was monitored using the scanning flow cell coupled to an inductively coupled plasma mass spectrometer (SFC-ICP-MS). An AST was chosen that was previously suggested to cause minimal carbon corrosion with enhanced transient Pt dissolution. Trends in Pt dissolution rates and dissolved quantities are observed which depend on the applied potential protocol, and a Volcano effect emerges as a consequence of two competing phenomena. These critical conclusions highlight overlooked mechanisms which should be given careful consideration by researchers when designing stability studies.

1. Experimental

Mass-selected sample preparation:

The Pt nanoparticles were prepared using magnetron sputtering of a Pt target (99.99%, AJA International Inc., USA) and subsequent noble-gas aggregation in a liquid nitrogen cooled aggregation zone. This was followed by a time-of-flight mass filtering which allows for fine control of particle sizes as previously described.[19b] The nanoparticle source (Birmingham Instruments Ltd. 2011) was operated at a mass filter resolution of $m/\Delta m=20$ for high deposition rates which for 6 nm particles results in an uncertainty in size of 0.1 nm. Following the filtering the charged particles were soft-landed (0.001-0.15 eV/atom) on a planar glassy carbon substrate (10 x 10 x 3 mm, SIGRADUR® G, HTW GmbH) under ultra-high vacuum conditions. The glassy carbon substrate was sputtered for 10 minutes with 1 keV Ar^+ to clean the surface of adventitious carbon and increase the stability of the nanoparticles against sintering. Since most particles exiting the mass filter are singly charged, the coverage of nanoparticles on the sample was controlled by monitoring the neutralization current on the sample. Coverage was calculated by comparing the total projected area of the nanoparticles to the deposition area and is reported in % of a monolayer

of particles. To ensure a homogeneous coverage across the entire sample area the supports were rastered in front of the beam during deposition. Particles of 7 different sizes were prepared with similar interparticle distances resulting in different coverages determined by simulation of interparticle distances[3].[23] The mean interparticle distance was kept constant to eliminate the recently reported effects of interparticle distance on Pd degradation,[22] and is exclusively addressed in a parallel investigation on platinum dissolution under AST protocols. Due to the random nature of particle depositions, there is an inherent normal distribution in the interparticle distances for all the particles in a sample (see interparticle distance distributions in **Figure S1**). The mean interparticle distance is therefore a variable that represents these distributions and can be used to distinguish between different distributions. The samples were deposited with mean interparticle distances between 6.1 and 6.5 nm with the standard deviation of the distributions ranging from 4.4 to 6.8 nm. Since the particles are filtered based on mass and not size, equivalent particle diameters were calculated using the density of Pt and assuming spherical particles. The different sample parameters are summarized in **Table S1.**

Scanning Transmission Electron Microscopy:

Scanning Transmission Electron Microscopy (STEM) images were acquired on a FEI Titan Analytical 80-300ST TEM with a pre-objective lens spherical aberration corrector (CESCOR form CEOS Company) operated at 300 kV in STEM mode using a high angle annular dark field detector with a maximum resolution of 0.08 nm. For STEM imaging the mass-selected particles were deposited on a Cu TEM grids with lacey carbon film (SPI Supplies®) at suitable coverages for image analysis ensuring a low number of overlapping particles (See **Figure S3)**. All images used for image analysis were acquired with a pixel size of approx. 0.1 nm and more than 100 particles were measured for each sample. Size analysis was performed with ImageJ (1.51j8) by using the Threshold and Analyze Particles functions to find the projected area of each individual particle. The particle diameters were calculated from the projected particle areas assuming circular particle projections due to the number of different particle shapes. Any overlapping particles were ignored in the analysis.

X-ray Photoelectron Spectroscopy:

X–ray photoelectron spectra (XPS) were measured on a PHI Quantera II scanning X–ray microprobe using Al–Kα irradiation ($h\nu$ = 1486.6 eV) of a 100 μm diameter area at 25 W and 15 kV. Survey scans at a step size of 1 eV and 280 eV pass energy were collected for 200 ms dwell time per step. Data were analyzed in CasaXPS (2.3.18PR1.0), using instrument specific relative sensitivity factors, Shirley type backgrounds, and a binding energy scale calibrated to the graphitic carbon peak at 284.5 eV.

Online Electrochemical Dissolution (SFC-ICP-MS):

Potential control was supplied by a Gamry Reference 600™ potentiostat/galvanostat. The working electrode (WE) was created by making contact with the mass-selected nanoparticles on the glassy carbon substrate. The contact area inside the SFC silicon ring was 0.011 cm^2 and contact

was maintained with a force sensor (KD45, ME-Meßsysteme) at 400 mN. A graphite rod (Pentel Hi-polymer® HB) in the SFC electrolyte inlet was used as a counter electrode (CE) with a double junction Ag/AgCl (3 M, Metrohm) reference electrode (RE).

Dissolution of Pt was measured online with the scanning flow cell coupled to an inductively coupled plasma mass spectrometer (SFC-ICP-MS) (NexION 300X, Perkin Elmer), with detection of ^{195}Pt, as described previously.[24] For an internal standard ^{187}Re was used with a concentration of 10 $\mu g \cdot L^{-1}$. The internal standard in all cases was constantly fed into the ICP-MS, and connected to the SFC outlet via a Y-connector. The ICP-MS dwell time per AMU was set to 50 ms, with 5 sweeps/reading. The Pt ICP-MS signal was calibrated daily from solution of 0.5, 1 and 5 $\mu g \cdot L^{-1}$ in 0.1 M $HClO_4$ prepared from 70 % $HClO_4$ (Suprapur®, Merck), ultrapure water (18.2 MΩ·cm, Milli-Q®, Merck) and ICP-MS calibration standards (Certipur®, Merck). The dissolution rate was calculated from regularly measured flow rates of ca. 200 $\mu L \cdot min^{-1}$, and the dissolution rate profiles were correlated to potential considering the delay time between the SFC and the ICP-MS of 25 s. The total quantities of dissolution were obtained by integration of the ^{195}Pt dissolution signal with the flow rate. The 0.1 M $HClO_4$ electrolyte was continuously purged with Ar immediately before introduction into the cell.

1. Results

Initial XPS characterization showed that there were no contaminants present on the surface with only Pt, O, Ar and C peaks present in the spectra, as seen in the representative spectra in **Figure S2.** The STEM imaging and subsequent particle size analysis showed narrow particle size distributions with two distributions for each size, the single charged and double charged double mass particles (**Figure 1**). Due to the low number of double charged particles, these are negligible and only the mean and standard deviation for the single charged particles are shown. These particles have sizes similar to the equivalent particle diameter calculated in **Table S1**. The discrepancy between the equivalent particle diameter and measured particle sizes comes from the non-spherical structure of the particles, which are instead a variety of shapes (**Figure 1 inset)**. The standard deviation is limited by the STEM pixel size for the 2, 3, 4 and 6 nm samples, but increases with particle size due to the variation in the projected area for different particle shapes. This is a consequence of the 2D projection generated from a 3D structure in STEM. It should be noted, that the particles with an equivalent particle diameter of 10 nm appear to be significantly larger due to their shapes, which are noticeably different from the smaller particles; however, it does not appear to lead to significant differences in dissolution rates. (**Figure 2 and S3).**

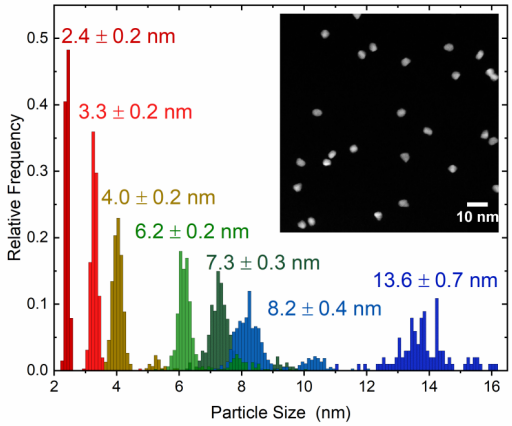

Figure 1. Size distribution of different particle sizes labeled with the average size and standard deviation. The inset shows a representative image of the 4 nm particles.

An AST protocol that was previously shown to cause extensive Pt dissolution with minimal carbon corrosion was chosen for this study.[17] The electrochemical conditions of the AST are shown in **Figure 2a**, which is also preceded and followed by relatively slower CVs which allow the deconvolution of the separate anodic and cathodic dissolution processes (to be discussed later).[15b, 16a-c, 21, 24b] The resulting mass-specific (normalized to total Pt mass on the WE) smoothed dissolution rate profiles are displayed in **Figure 2b** (**Figure S4** and **Figure S5** alternatively show raw data and rates normalized to geometrical surface area, respectively). Slightly higher noise in the signal for smaller particles results from the mass normalization since smaller particle sizes result in lower loadings in order to maintain a similar interparticle distance (1.2% vs. 8.6% coverage for 2 nm and 10 nm particles, respectively) **Table S1**. For the smallest (2 nm) particles, the dissolution rate in the initial stages of the AST drastically peaks due to higher surface area relative to mass (ECSA), followed by a very sharp deceleration of the rate to baseline values. A smaller initial peak is seen for the 3 nm material. A smaller initial peak is seen for the 3 nm material The deceleration of rate also becomes less drastic for the 3 nm system. Moving to the 4 nm particle size, the peak is even less pronounced and even slower deceleration in rate is observed. The larger particle sizes ≥ 6 nm behave similarly to one another, where no initial peak in the dissolution rate is seen and the dissolution rates only gradually decrease (from loss of Pt material) and remain far above baseline until the end of the AST. For these larger particles (≥ 6 nm), the mass-specific dissolution rate very clearly decreases with increasing particle size (**Figure 2b^{I} inset**).

After the AST a reductive potential of 0.05 V_{RHE} is immediately applied. Subsequently, an additional cathodic dissolution peak caused by reduction of formed PtO_x is seen for the three smallest particle sizes of 2, 3 and 4 nm (**Figure 2b^{II}**). The peak height during this reductive hold decreases with increasing particle size.

The mass-specific dissolution rate profiles appear highly distinct for the different particle sizes, and a plausible explanation is given in the following. It appears that the lower potential limit

(LPL) of 0.6 V_{RHE} is too positive to fully reduce the formed PtO_x on the timescale of the AST for small particle sizes. This causes a dissolution inhibiting passivation of the Pt nanoparticles that increases with decreasing particle size, and in turn causes the drastic deceleration of initial dissolution rate, i.e. a stable layer of PtO_x prevents further dissolution. This may be expected, due to the known increase in oxophilicity with decreasing particle size.[10] Furthermore, this is evidenced in the additional cathodic peak during the reductive hold at 0.05 V_{RHE} following the ADT, which indicates increasing oxidation/passivation going from 4, 3 to 2 nm particle sizes.

The particle size effect on passivation becomes clearly evident in **Figure 2c**, where the total quantity of Pt dissolved during the AST is shown as percentage of Pt mass lost. A "volcano" type effect appears, where there is a tradeoff between decreased dissolution due to passivation of smaller particles, and decreased dissolution due to increasing particle size. As particle size increases, less mass-specific dissolution is inherently expected due to decreasing ECSA (i.e. less surface area relative to total Pt mass).[6e, 8a, c, 9b, c, 11, 14a] Based on the total quantities dissolved (**Figure 2c)** and the dissolution rate profiles (**Figure 2b**), it appears the 2 nm size is highly oxophilic and quickly passivating, while for the 3 and 4 nm particle sizes the passivation and ECSA effects are mixed, and for ≥ 6 nm sizes have negligible passivation during the AST. It should be made clear, that such "volcano" behaviour is highly dependent on the applied AST: potential limits, scan rate and number of cycles. For instance, slower scan rates and lower potential limits may allow further reduction of formed passivating PtO_x, while a sufficient number of cycles may negate initial transient effects (**Figure 2b** and **b**^{I}).

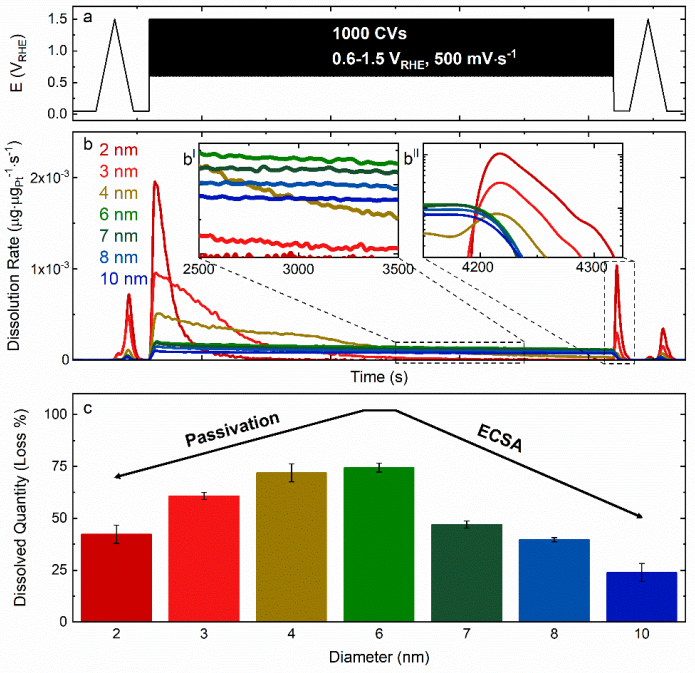

Figure 2. (a) Applied AST of CVs from 0.6-1.5 V_{RHE} at 500 mV·s^{-1} for 1000 cycles preceded and followed by a CV from 0.05-1.5 V_{RHE} at 10 mV·s^{-1}. (b) Corresponding mass-normalized

dissolution rate of the samples of varied particle size with $b^{|}$ and $b^{||}$ insets showing midway dissolution and cathodic peak during reductive hold following the AST. (c) Quantified dissolution during the AST total Pt loss % (mass-normalized).

To further corroborate the attribution of the dissolution trends to Pt passivation, **Figure 3** shows the electrical charges during the course of the AST, which comes from oxidation and reduction of the Pt nanoparticles. It is important to note that dissolution currents contribute negligibly (e.g. 0.1-0.5 %) to the measured electrical currents, and by cycling from 0.6-1.5 V_{RHE} the majority of measured charge should originate from oxidation and reduction of Pt (carbon quickly passivates at such cycling conditions).[17] By normalizing to the measured charge from the first cycle, the trends appear to closely mirror those of the dissolution rate profile. In the first 10 cycles there is a drastic drop in charge, possibly due to the oxidation of minor contaminants that were initially present on the surfaces. With decreasing particle size, increased passivation is visible by a loss in oxidation and reduction charges (indicating the particles are not being fully oxidized and reduced in the later cycles). For the 2 nm particles, the charges drop drastically and remain constant after 100 cycles, indicating a large degree of passivation quickly takes place. The charges drop more gradually for the 3 and 4 nm particles but eventually reach a similar level to the 2 nm particles, in analogy to the dissolution rate profile. It is possible that as significant dissolution takes place (ca. 75 % loss for 3 and 4 nm, **Figure 2c**) some particle sizes are shrinking with a lowering of their oxidation potential. The 6 and 7 nm particles retain a much higher charge which only slightly decreases during the AST. For particle sizes of 8 and 10 nm, the charge remains approximately constant between 10-1000 cycles. With such large particles sizes and relatively less dissolution (ca. 50-25 % loss, **Figure 2c**) the large particles are not passivated and minimal shrinking from dissolution should be expected.

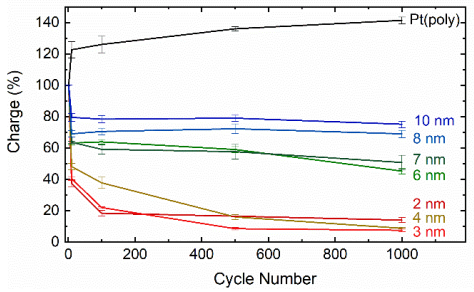

Figure 3. Total charge during a CV normalized to the first CV cycle for the 1st, 10th, 100th, 500th and 1000th cycle for the ADT from 0.6-1.5 V_{RHE}, at 500 $mV \cdot s^{-1}$ for 1000 cycles.

It is clear that particle size has a severe impact on the oxidation and reduction of Pt, which causes transient platinum dissolution. This is typically seen in the shift of the oxidation and reduction peaks of CVs to more positive potentials for large particles,[6e, 8d, 9c, 10, 25] while unfortunately the low loadings and low currents from the flat (2D) model systems inhibit such detection.[23, 26] Increased loadings become possible with the use of 3D, porous Pt support on carbon, and these applied materials will be addressed in a parallel study.

The relatively slower CVs preceding and following the AST span a much larger potential window (**Figure 4a**), with a much more negative LPL of 0.05 V_{RHE} and slower scan rate of 10 $mV \cdot s^{-1}$ which will fully reduce formed oxides in the cathodic scan. The mass-normalized dissolution rates and total dissolved quantities shown in **Figure 4b** and **Figure 4c** (normalized to geometrical WE surface area in **Figure S6**) show a clear decrease with increasing particle size, which may be attributed to decreasing ECSA, as mentioned above.[6e, 8a, c, 9b, c, 11, 14a] Unfortunately, estimating ECSA through the conventional hydrogen underpotential deposition area of the CV becomes difficult due to the low loadings used in an effort to eliminate possible interparticle distance effects,[9a, 18a-c, 18e, 23, 27] which will be addressed on applied Pt/C materials.

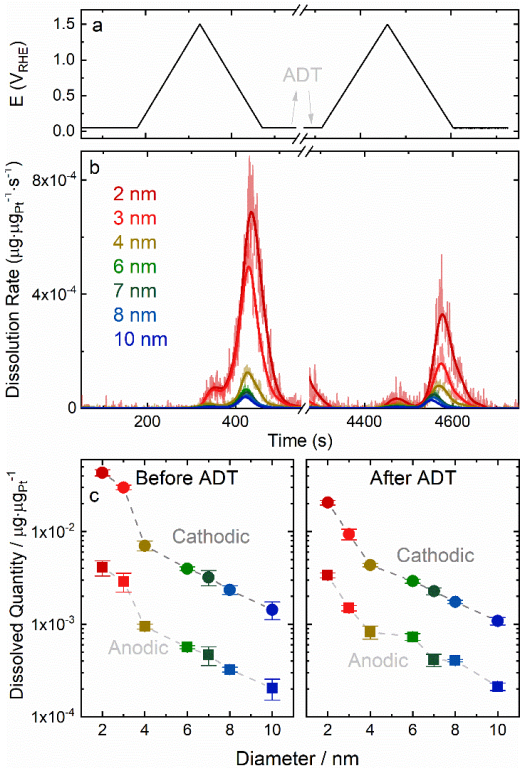

Figure 4. (a) CVs preceding and following the AST from 0.05-1.5 V_{RHE}. (b) Corresponding mass-normalized dissolution rate of the samples of varied particle size. (c) Total mass-normalized dissolved quantities from the anodic (■) and cathodic (●) dissolution peaks.

2. Discussion

Using well-defined 2D model systems with particle diameters from 2-10 nm and similar interparticle distance distributions, particle size has been shown to have a severe impact on the oxidation, reduction and subsequent dissolution of Pt nanoparticles. Considering recent

developments on the impact of interparticle distance on stability,[22] this has been recognized as the critical parameter rather than loading as is also further investigated in an upcoming dedicated publication. In recent years it has become well-established that significant Pt dissolution is caused by the oxidation and reduction of Pt, governed by the place-exchange mechanism.[15b, 16c, 28] When applying CVs in a large potential range causing significant Pt oxidation and reduction (**Figure 4**), a clear trend of decreasing mass-specific dissolution with increasing particle size was observed. This was simply rationalized by decreasing surface area relative to total Pt mass, i.e. ECSA.[6e, 8a, c, 9b, c, 11, 14a] Therefore, from an engineering standpoint, larger Pt particles are more stable towards dissolution, in agreement with many activity based studies.[6e, 8c, 9c, 14f]

Intriguingly, a rather unexpected "volcano" type trend in dissolved Pt quantities was observed which depends on particle size in the potential range of the applied AST (**Figure 2**). Decreasing particle sizes causes a negative potential shift, causing particle passivation and quickly inhibiting dissolution rates in the initial stages of the AST (further exemplified by loss of charge in **Figure 3**). As particle sizes increase from 2-6 nm this effect is diminished and dissolved quantities of Pt increase. At larger particle sizes (≥ 6 nm) dissolved quantities of Pt again decrease; however, this is due to the above mentioned decreasing ECSA with increasing particle size. At these larger particle sizes a positive shift in oxidation potential prevents significant passivation.

This situation becomes more complex when moving to more commonly employed AST experiments. In 2011 the Fuel Cell Commercialization Conference of Japan (FCCJ) proposed two types of ASTs with different potential windows in order to simulate the operational load and the start/stop conditions of PEMFCs.[29] Square wave cycling from 0.6-1.0 V_{RHE} for the load and triangular wave cycling from 1.0-1.5 V_{RHE} for the start/stop was suggested. A triangular wave form from 0.6-1.0 V_{RHE} had also been adopted by the US DOE by as early as 2010, while in 2013 their suggested protocols also included a 1.0-1.5 V_{RHE} test for start/stop conditions (identical to above FCCJ).[14g, 30] The load cycle ASTs are thought to largely induce Pt dissolution/degradation while the start/stop ASTs induce carbon corrosion, i.e. these two types of tests should ideally separate the two primary degradation mechanisms of PEMFC catalyst layers.[13] Furthermore, without any type of standardized testing, comparisons across different laboratories would be infeasible, and to a large extent many scientific groups have adopted the use of ASTs within these potential limits (although with small variations in potential limits and scan rates).[5a, 6e, f, h, 8c, 9c, 11, 14] However, it is known that the potential profile (square wave vs. triangular wave) impacts degradation and Pt dissolution,[14f, 16c, 31] while even slight variations to potential limits which transverse 1.0 V_{RHE} will drastically impact Pt dissolution.[16a, c]

In recent years it has been shown that significant transient electrochemical dissolution of Pt coincides with Pt oxidation and reduction when crossing a threshold of ca. 1.0 V_{RHE}.[16a, c] When cycling below 1.0 V_{RHE} Pt will not be significantly oxidized, and when cycling above 1.0 V_{RHE} Pt will not be significantly reduced. Therefore, it is clear that neither type of potential window suggested above will cause substantial Pt dissolution. However, many AST studies span a much larger timescale than presented here, easily possible in typical bulk-cell experiments, and over many thousands of cycles low rates of Pt dissolution may amount to significant degradation which depends on particle size due to shifts in oxidation, reduction and dissolution potentials. Several degradation studies on particle size effects have been conducted within a load cycle potential range similar to those described above, (although with slight variations in potential limits and scan rates).[6e, 8c, 9c, 11, 14a, f] Most results have shown a trend of increased degradation with decreasing

particle size based on losses in ECSA and activity,[6e, 8c, 9c, 14f] while some have shown no dependence.[11, 14a] Additionally, Ahluwalia et el. used ex-situ dissolution (ICP-MS) experiments and demonstrated a reversal in this trend to larger particles dissolving more (mass-specific dissolution) when changing their AST protocol from 0.6-1.0 V_{RHE} at 50 $mV \cdot s^{-1}$ to 0.5-1.15 V_{RHE} at 10 $mV \cdot s^{-1}$.[14b] This surprising result was attributed to size dependent kinetic/thermodynamic control of oxide formation.

Considering the limited degradation of the typically used load and start/stop ASTs, Pizzutilo et al. investigated the impact of a variety of potential windows on Pt/C degradation in an online SFC-ICP-MS dissolution study.[17] As expected,[16a-c, 32] no significant Pt dissolution was seen when cycling from 0.6-1.0 V_{RHE} or 1.0-1.5 V_{RHE}. The Pt dissolution rate signal then jumped over two orders of magnitude when cycling in a "combined cycle" from 0.6-1.5 V_{RHE} and one order of magnitude for 0.05-1.5 V_{RHE}. The lower rate for the latter (large potential window) can be explained by increased redeposition caused by the more negative potentials. From online SFC-OLEMS (scanning flow cell coupled to online electrochemical mass spectrometry) CO_2 measurements the larger potential window induced a much higher corrosion rate of the carbon support, attributed to reduction of oxygenated surface functional groups by reaching potentials below the thermodynamic potential for carbon oxidation (0.2 V_{RHE}). Therefore, the combined cycle which caused significant Pt dissolution with rather minimal carbon corrosion was suggested for use in degradation studies and adapted in this work.

Due to the significant dissolution observed during the combined cycle AST by Pizzutilo et al., it was assumed that the LPL of 0.6 V_{RHE} was sufficient to reduce their commercial (TKK) 3 nm Pt nanoparticles.[17] However, here it was shown that this size is in the range of particle passivation, i.e. 0.6 V_{RHE} is too positive to fully reduce this particle size. Therefore, a similar experiment on an identical sample of annealed TKK Pt/C with larger particle size of ca. 5 nm should yield increased mass-specific dissolution (assuming identical loading) and could be misinterpreted as an instrinsic particle size dependent property rather than the competition of two effects.

As the results here have shown, particle size drastically impacts degradation through Pt dissolution in ASTs depending on the potential limits. Therefore, the authors suggest caution in studies comparing different materials of varying particle size. For instance, if studying 2 and 8 nm particle sizes, the former may be protected by a passivating oxide layer while the latter has lower ECSA. In samples containing large size distributions different populations could degrade completely differently, skewing firm conclusions on the parameters of interest. Comparisons between samples with varied loading via catalyst layer thickness or particle density (i.e. interparticle distance) could also become compromised without exclusive control of particle size. Commercial catalysts synthesized using impregnation or precipitation methods typically increase particle size via heat/annealing treatments which change interparticle distance, alter the carbon support and also result in increased size distributions with the extent of the treatment (i.e. larger distributions for larger sizes).[8a, 11, 14a, b, 18] These important insights demonstrate the importance of studying well-defined model systems on the road to improved experimental techniques in PEMFC electrocatalytic research.

With the new data that has shed light on this critical issue of competing particle size effects of passivation and dissolution, we suggest an AST protocol in addition to the commonly used load and start/stop cycle potential ranges. Indeed, a more aggressive AST can aid in the understanding of the degradation of promising electrocatalytic materials, by causing significant Pt dissolution in

a short time frame.[6g] Applying a UPL of 1.5 V_{RHE} will cause significant Pt oxidation without extending into the oxygen evolution reaction (OER) range which causes Pt dissolution at ca. 1.7 V_{RHE}.[15b, 16b] By Using a LPL of 0.3 V_{RHE} formed oxides should be fully reduced while avoiding extensive Pt redeposition and carbon corrosion through reduction at low potentials.[17] Therefore, a Pt "dissolution AST" from 0.3-1.5 V_{RHE} at 500 $mV \cdot s^{-1}$ is suggested for a protocol to cause extensive Pt dissolution on a short time scale while also circumventing the particle size dependent passivation effect, providing a clear picture of the intrinsic stability. Alternatively, slower scan rates or square waveforms of applied potential can provide increased time lengths at oxidative and reductive potentials which may narrow the necessary potential window; however, such recommendations will require dedicated investigations.

3. Conclusion

Using magnetron sputtering, particle size was exclusively controlled over Pt particle density on a planar glassy carbon substrate with narrow size distributions and constant interparticle distance distributions. In the range studied with diameters from 2-10 nm, the applied AST revealed a volcano type trend in dissolution detected online, caused by competing effects: particle size dependent shifts in oxophilicity and ECSA. As particle size decreases the particles become more oxophilic, causing the formation of a dissolution inhibiting passivation layer of PtO_x. As particle size increases, ECSA decreases, similarly decreasing the amount of Pt dissolution. These effects have likely been overlooked in many investigations on the particle size effect on Pt stability. Furthermore, minimizing particle size is a critical issue in decreasing PEMFC costs by maximizing Pt utilization, and alleviating mass transport issues with high dispersion. Therefore, these competing trends on this primary degradation mechanism of PEMFC catalyst layers needs to be recognized when comparing the stability of materials of varying particle size, which may result in skewed interpretations during commonly employed ASTs. The subsequent suggestions for AST protocols should be helpful for researchers designing future studies on particle size effects.

4. References

1. (a) Gruber, P. W.; Medina, P. A.; Keoleian, G. A.; Kesler, S. E.; Everson, M. P.; Wallington, T. J., Global Lithium Availability. *J. Ind. Ecol.* **2011,** *15* (5), 760-775; (b) Kesler, S. E.; Gruber, P. W.; Medina, P. A.; Keoleian, G. A.; Everson, M. P.; Wallington, T. J., Global lithium resources: Relative importance of pegmatite, brine and other deposits. *Ore Geology Reviews* **2012,** *48*, 55-69; (c) Kavanagh, L.; Keohane, J.; Garcia Cabellos, G.; Lloyd, A.; Cleary, J., Global Lithium Sources—Industrial Use and Future in the Electric Vehicle Industry: A Review. *Resources* **2018,** *7* (3); (d) Harvey, L. D. D., Resource implications of alternative strategies for achieving zero greenhouse gas emissions from light-duty vehicles by 2060. *Appl. Energy* **2018,** *212*, 663-679; (e) Jasiński, D.; Meredith, J.; Kirwan, K., The life cycle impact for platinum group metals and lithium to 2070 via surplus cost potential. *Int. J. LCA* **2017,** *23* (4), 773-786.

2. (a) Wang, J.; Wang, H.; Fan, Y., Techno-Economic Challenges of Fuel Cell Commercialization. *Engineering* **2018,** *4* (3), 352-360; (b) Gröger, O.; Gasteiger, H. A.; Suchsland, J.-P., Review—Electromobility: Batteries or Fuel Cells? *J. Electrochem. Soc.* **2015,** *162* (14), A2605-A2622.
3. (a) Wang, G.; Yu, Y.; Liu, H.; Gong, C.; Wen, S.; Wang, X.; Tu, Z., Progress on design and development of polymer electrolyte membrane fuel cell systems for vehicle applications: A review. *Fuel Process. Technol.* **2018,** *179*, 203-228; (b) Curtin, S.; Gangi, J. *Fuel Cell Technologies Market Report 2016*; U.S. Department of Energy, Office of Energy Efficiency & Renewable Energy: 2016; (c) Yoshida, T.; Kojima, K., Toyota MIRAI Fuel Cell Vehicle and Progress Toward a Future Hydrogen Society. *Interface* **2015,** *24* (2), 45-49.
4. (a) Yang, Y. *PEM Fuel Cell System Manufacturing Cost Analysis for Automotive Applications*; Austin Power Engineering LLC: 2015; (b) de Frank Bruijn, A.; Janssen, G. J. M., PEM Fuel Cell Materials: Costs, Performance and Durability. In *Fuel Cells*, 2013; pp 249-303.
5. (a) Kongkanand, A.; Mathias, M. F., The Priority and Challenge of High-Power Performance of Low-Platinum Proton-Exchange Membrane Fuel Cells. *Journal of Physical Chemistry Letters* **2016,** *7* (7), 1127-37; (b) Kongkanand, A.; Subramanian, N. P.; Yu, Y.; Liu, Z.; Igarashi, H.; Muller, D. A., Achieving High-Power PEM Fuel Cell Performance with an Ultralow-Pt-Content Core–Shell Catalyst. *ACS Catal* **2016,** *6* (3), 1578-1583; (c) Owejan, J. P.; Owejan, J. E.; Gu, W., Impact of Platinum Loading and Catalyst Layer Structure on PEMFC Performance. *J. Electrochem. Soc.* **2013,** *160* (8), F824-F833; (d) Harzer, G. S.; Orfanidi, A.; El-Sayed, H.; Madkikar, P.; Gasteiger, H. A., Tailoring Catalyst Morphology towards High Performance for Low Pt Loaded PEMFC Cathodes. *J. Electrochem. Soc.* **2018,** *165* (10), F770-F779.
6. (a) Li, M.; Zhao, Z.; Cheng, T.; Fortunelli, A.; Chen, C. Y.; Yu, R.; Zhang, Q.; Gu, L.; Merinov, B. V.; Lin, Z.; Zhu, E.; Yu, T.; Jia, Q.; Guo, J.; Zhang, L.; Goddard, W. A., 3rd; Huang, Y.; Duan, X., Ultrafine jagged platinum nanowires enable ultrahigh mass activity for the oxygen reduction reaction. *Science* **2016,** *354* (6318), 1414-1419; (b) Bu, L.; Zhang, N.; Guo, S.; Zhang, X.; Li, J.; Yao, J.; Wu, T.; Lu, G.; Ma, J. Y.; Su, D.; Huang, X., Biaxially strained PtPb/Pt core/shell nanoplate boosts oxygen reduction catalysis. *Science* **2016,** *354* (6318), 1410-1414; (c) Stephens, I. E.; Rossmeisl, J.; Chorkendorff, I., Toward sustainable fuel cells. *Science* **2016,** *354* (6318), 1378-1379; (d) Chen, C.; Kang, Y.; Huo, Z.; Zhu, Z.; Huang, W.; Xin, H. L.; Snyder, J. D.; Li, D.; Herron, J. A.; Mavrikakis, M.; Chi, M.; More, K. L.; Li, Y.; Markovic, N. M.; Somorjai, G. A.; Yang, P.; Stamenkovic, V. R., Highly crystalline multimetallic nanoframes with three-dimensional electrocatalytic surfaces. *Science* **2014,** *343* (6177), 1339-43; (e) Li, D.; Wang, C.; Strmcnik, D. S.; Tripkovic, D. V.; Sun, X.; Kang, Y.; Chi, M.; Snyder, J. D.; van der Vliet, D.; Tsai, Y.; Stamenkovic, V. R.; Sun, S.; Markovic, N. M., Functional links between Pt single crystal morphology and nanoparticles with different size and shape: the oxygen reduction reaction case. *Energy. Environ. Sci.* **2014,** *7* (12), 4061-4069; (f) George, M.; Zhang, G. R.; Schmitt, N.; Brunnengraber, K.; Sandbeck, D. J. S.; Mayrhofer, K. J. J.; Cherevko, S.; Etzold, B. J. M., Effect of Ionic Liquid Modification on the ORR Performance and Degradation Mechanism of Trimetallic PtNiMo/C Catalysts. *ACS Catal* **2019,** *9* (9), 8682-8692; (g) Zhang, G. R.; Wolker, T.; Sandbeck, D. J. S.; Munoz, M.; Mayrhofer, K. J. J.; Cherevko, S.; Etzold, B. J. M., Tuning the Electrocatalytic Performance of Ionic Liquid Modified Pt Catalysts for the Oxygen Reduction Reaction via Cationic Chain Engineering. *ACS Catal.* **2018,** *8* (9), 8244-8254; (h) Lindahl, N.; Zamburlini, E.; Feng, L.; Grönbeck, H.; Escudero-Escribano, M.; Stephens, I. E. L.; Chorkendorff, I.; Langhammer, C.; Wickman, B., High Specific and Mass Activity for the Oxygen Reduction Reaction for Thin Film Catalysts of Sputtered Pt3Y. *Adv. Mater. Interfaces* **2017,** *4* (13).

7. Gazdzicki, P.; Mitzel, J.; Dreizler, A. M.; Schulze, M.; Friedrich, K. A., Impact of Platinum Loading on Performance and Degradation of Polymer Electrolyte Fuel Cell Electrodes Studied in a Rainbow Stack. *Fuel Cells* **2018,** *18* (3), 270-278.
8. (a) Shao, M.; Peles, A.; Shoemaker, K., Electrocatalysis on platinum nanoparticles: particle size effect on oxygen reduction reaction activity. *Nano Letters* **2011,** *11* (9), 3714-9; (b) Perez-Alonso, F. J.; McCarthy, D. N.; Nierhoff, A.; Hernandez-Fernandez, P.; Strebel, C.; Stephens, I. E.; Nielsen, J. H.; Chorkendorff, I., The effect of size on the oxygen electroreduction activity of mass-selected platinum nanoparticles. *Angew. Chem. Int. Ed. Engl.* **2012,** *51* (19), 4641-3; (c) Xu, Z.; Zhang, H.; Zhong, H.; Lu, Q.; Wang, Y.; Su, D., Effect of particle size on the activity and durability of the Pt/C electrocatalyst for proton exchange membrane fuel cells. *Appl. Catal. B. Environ.* **2012,** *111-112*, 264-270; (d) Gasteiger, H. A.; Kocha, S. S.; Sompalli, B.; Wagner, F. T., Activity benchmarks and requirements for Pt, Pt-alloy, and non-Pt oxygen reduction catalysts for PEMFCs. *Appl. Catal. B Environ.* **2005,** *56* (1-2), 9-35.
9. (a) Quinson, J.; Inaba, M.; Neumann, S.; Swane, A. A.; Bucher, J.; Simonsen, S. B.; Theil Kuhn, L.; Kirkensgaard, J. J. K.; Jensen, K. M. Ø.; Oezaslan, M.; Kunz, S.; Arenz, M., Investigating Particle Size Effects in Catalysis by Applying a Size-Controlled and Surfactant-Free Synthesis of Colloidal Nanoparticles in Alkaline Ethylene Glycol: Case Study of the Oxygen Reduction Reaction on Pt. *ACS Catal.* **2018,** *8* (7), 6627-6635; (b) Nesselberger, M.; Ashton, S.; Meier, J. C.; Katsounaros, I.; Mayrhofer, K. J.; Arenz, M., The particle size effect on the oxygen reduction reaction activity of Pt catalysts: influence of electrolyte and relation to single crystal models. *J. Am. Chem. Soc.* **2011,** *133* (43), 17428-33; (c) Sheng, W.; Chen, S.; Vescovo, E.; Shao-Horn, Y., Size Influence on the Oxygen Reduction Reaction Activity and Instability of Supported Pt Nanoparticles. *J. Electrochem. Soc.* **2011,** *159* (2), B96-B103.
10. Mayrhofer, K. J.; Blizanac, B. B.; Arenz, M.; Stamenkovic, V. R.; Ross, P. N.; Markovic, N. M., The impact of geometric and surface electronic properties of pt-catalysts on the particle size effect in electrocatalysis. *J. Phys. Chem. B* **2005,** *109* (30), 14433-40.
11. Yano, H.; Watanabe, M.; Iiyama, A.; Uchida, H., Particle-size effect of Pt cathode catalysts on durability in fuel cells. *Nano Energy* **2016,** *29*, 323-333.
12. Cherevko, S., Stability and dissolution of electrocatalysts: Building the bridge between model and "real world" systems. *Current Opinion in Electrochemistry* **2018,** *8*, 118-125.
13. Meier, J. C.; Galeano, C.; Katsounaros, I.; Witte, J.; Bongard, H. J.; Topalov, A. A.; Baldizzone, C.; Mezzavilla, S.; Schuth, F.; Mayrhofer, K. J. J., Design criteria for stable Pt/C fuel cell catalysts. *Bellstein Journal of Nanotechnology* **2014,** *5*, 44-67.
14. (a) Watanabe, M.; Yano, H.; Uchida, H.; Tryk, D. A., Achievement of distinctively high durability at nanosized Pt catalysts supported on carbon black for fuel cell cathodes. *J. Electroana.l Chem.* **2018,** *819*, 359-364; (b) Ahluwalia, R. K.; Arisetty, S.; Wang, X.; Wang, X.; Subbaraman, R.; Ball, S. C.; DeCrane, S.; Myers, D. J., Thermodynamics and Kinetics of Platinum Dissolution from Carbon-Supported Electrocatalysts in Aqueous Media under Potentiostatic and Potentiodynamic Conditions. *J. Electrochem. Soc.* **2013,** *160* (4), F447-F455; (c) Schmies, H.; Bergmann, A.; Drnec, J.; Wang, G.; Teschner, D.; Kühl, S.; Sandbeck, D. J. S.; Cherevko, S.; Gocyla, M.; Shviro, M.; Heggen, M.; Ramani, V.; Dunin-Borkowski, R. E.; Mayrhofer, K. J. J.; Strasser, P., Unravelling Degradation Pathways of Oxide-Supported Pt Fuel Cell Nanocatalysts under In Situ Operating Conditions. *Adv. Energy Mater.* **2018,** *8* (4); (d) Spanos, I.; Dideriksen, K.; Kirkensgaard, J. J.; Jelavic, S.; Arenz, M., Structural disordering of de-alloyed Pt bimetallic nanocatalysts: the effect on oxygen reduction reaction activity and stability. *Phys. Chem. Chem. Phys.* **2015,** *17* (42), 28044-53; (e) Fichtner, J.; Garlyyev, B.; Watzele, S.; El-Sayed, H. A.; Schwammlein, J. N.; Li, W. J.; Maillard, F. M.; Dubau, L.; Michalicka, J.; Macak, J. M.; Holleitner, A.; Bandarenka, A. S., Top-Down Synthesis of

Nanostructured Platinum-Lanthanide Alloy Oxygen Reduction Reaction Catalysts: Pt xPr/C as an Example. *ACS Applied Material Interfaces* **2019,** *11* (5), 5129-5135; (f) Yang, Z.; Ball, S.; Condit, D.; Gummalla, M., Systematic Study on the Impact of Pt Particle Size and Operating Conditions on PEMFC Cathode Catalyst Durability. *Journal of The Electrochemical Society* **2011,** *158* (11); (g) Yu, H.; Baricci, A.; Bisello, A.; Casalegno, A.; Guetaz, L.; Bonville, L.; Maric, R., Strategies to mitigate Pt dissolution in low Pt loading proton exchange membrane fuel cell: I. A gradient Pt particle size design. *Electrochim. Acta* **2017,** *247*, 1155-1168.

15. (a) Myers, D. J.; Wang, X.; Smith, M. C.; More, K. L., Potentiostatic and Potential Cycling Dissolution of Polycrystalline Platinum and Platinum Nano-Particle Fuel Cell Catalysts. *J. Electrochem. Soc.* **2018,** *165* (6), F3178-F3190; (b) Cherevko, S.; Kulyk, N.; Mayrhofer, K. J. J., Durability of platinum-based fuel cell electrocatalysts: Dissolution of bulk and nanoscale platinum. *Nano Energy* **2016,** *29*, 275-298.

16. (a) Topalov, A. A.; Katsounaros, I.; Auinger, M.; Cherevko, S.; Meier, J. C.; Klemm, S. O.; Mayrhofer, K. J. J., Dissolution of Platinum: Limits for the Deployment of Electrochemical Energy Conversion? *Angew. Chem. Int. Ed. Engl.* **2012,** *51* (50), 12613-5; (b) Cherevko, S.; Zeradjanin, A. R.; Keeley, G. P.; Mayrhofer, K. J. J., A Comparative Study on Gold and Platinum Dissolution in Acidic and Alkaline Media. *J. Electrochem. Soc.* **2014,** *161* (12), H822-H830; (c) Topalov, A. A.; Cherevko, S.; Zeradjanin, A. R.; Meier, J. C.; Katsounaros, I.; Mayrhofer, K. J. J., Towards a comprehensive understanding of platinum dissolution in acidic media. *Chem. Sci.* **2014,** *5* (2), 631-638; (d) Cherevko, S., Electrochemical Dissolution of Noble Metals. In *Encyclopedia of Interfacial Chemistry*, 2018; pp 68-75.

17. Pizzutilo, E.; Geiger, S.; Grote, J. P.; Mingers, A.; Mayrhofer, K. J. J.; Arenz, M.; Cherevko, S., On the Need of Improved Accelerated Degradation Protocols (ADPs): Examination of Platinum Dissolution and Carbon Corrosion in Half-Cell Tests. *J. Electrochem. Soc.* **2016,** *163* (14), F1510-F1514.

18. (a) Speder, J.; Altmann, L.; Bäumer, M.; Kirkensgaard, J. J. K.; Mortensen, K.; Arenz, M., The particle proximity effect: from model to high surface area fuel cell catalysts. *RSC Advances* **2014,** *4* (29); (b) Speder, J.; Zana, A.; Spanos, I.; Kirkensgaard, J. J. K.; Mortensen, K.; Hanzlik, M.; Arenz, M., Comparative degradation study of carbon supported proton exchange membrane fuel cell electrocatalysts – The influence of the platinum to carbon ratio on the degradation rate. *J. Power Sources* **2014,** *261*, 14-22; (c) Speder, J.; Spanos, I.; Zana, A.; Kirkensgaard, J. J. K.; Mortensen, K.; Altmann, L.; Bäumer, M.; Arenz, M., From single crystal model catalysts to systematic studies of supported nanoparticles. *Surf. Sci.* **2015,** *631*, 278-284; (d) Quinson, J.; Inaba, M.; Neumann, S.; Swane, A. A.; Bucher, J.; Simonsen, S. B.; Kuhn, L. T.; Kirkensgaard, J. J. K.; Jensen, K. M. O.; Oezaslan, M.; Kunz, S.; Arenz, M., Investigating Particle Size Effects in Catalysis by Applying a Size-Controlled and Surfactant-Free Synthesis of Colloidal Nanoparticles in Alkaline Ethylene Glycol: Case Study of the Oxygen Reduction Reaction on Pt. *ACS Catal.* **2018,** *8* (7), 6627-6635; (e) Proch, S.; Kodama, K.; Inaba, M.; Oishi, K.; Takahashi, N.; Morimoto, Y., The "Particle Proximity Effect" in Three Dimensions: a Case Study on Vulcan XC 72R. *Electrocatalysis* **2016,** *7* (3), 249-261.

19. (a) Kemppainen, E.; Bodin, A.; Sebok, B.; Pedersen, T.; Seger, B.; Mei, B.; Bae, D.; Vesborg, P. C. K.; Halme, J.; Hansen, O.; Lund, P. D.; Chorkendorff, I., Scalability and feasibility of photoelectrochemical H2evolution: the ultimate limit of Pt nanoparticle as an HER catalyst. *Energy & Environmental Science* **2015,** *8* (10), 2991-2999; (b) Roy, C.; Sebok, B.; Scott, S. B.; Fiordaliso, E. M.; Sørensen, J. E.; Bodin, A.; Trimarco, D. B.; Damsgaard, C. D.; Vesborg, P. C. K.; Hansen, O.; Stephens, I. E. L.; Kibsgaard, J.; Chorkendorff, I., Impact of nanoparticle size and lattice oxygen on water oxidation on NiFeOxHy. *Nat. Catal.* **2018,** *1* (11), 820-829.

20. (a) Hernandez-Fernandez, P.; Masini, F.; McCarthy, D. N.; Strebel, C. E.; Friebel, D.; Deiana, D.; Malacrida, P.; Nierhoff, A.; Bodin, A.; Wise, A. M.; Nielsen, J. H.; Hansen, T. W.; Nilsson, A.; Stephens, I. E.; Chorkendorff, I., Mass-selected nanoparticles of PtxY as model catalysts for oxygen electroreduction. *Nature Chemistry* **2014,** *6* (8), 732-8; (b) Velázquez-Palenzuela, A.; Masini, F.; Pedersen, A. F.; Escudero-Escribano, M.; Deiana, D.; Malacrida, P.; Hansen, T. W.; Friebel, D.; Nilsson, A.; Stephens, I. E. L.; Chorkendorff, I., The enhanced activity of mass-selected Pt Gd nanoparticles for oxygen electroreduction. *Journal of Catalysis* **2015,** *328*, 297-307.
21. Keeley, G. P.; Cherevko, S.; Mayrhofer, K. J., The Stability Challenge on the Pathway to Low and Ultra-Low Platinum Loading for Oxygen Reduction in Fuel Cells. *ChemElectroChem* **2016,** *3* (1), 51-54.
22. Goodman, E. D.; Johnston-Peck, A. C.; Dietze, E. M.; Wrasman, C. J.; Hoffman, A. S.; Abild-Pedersen, F.; Bare, S. R.; Plessow, P. N.; Cargnello, M., Catalyst deactivation via decomposition into single atoms and the role of metal loading. *Nat. Catal.* **2019,** *2* (9), 748-755.
23. Nesselberger, M.; Roefzaad, M.; Hamou, R. F.; Biedermann, P. U.; Schweinberger, F. F.; Kunz, S.; Schloegl, K.; Wiberg, G. K.; Ashton, S.; Heiz, U.; Mayrhofer, K. J.; Arenz, M., The effect of particle proximity on the oxygen reduction rate of size-selected platinum clusters. *Nat. Mater.* **2013,** *12* (10), 919-24.
24. (a) Schuppert, A. K.; Topalov, A. A.; Katsounaros, I.; Klemm, S. O.; Mayrhofer, K. J. J., A Scanning Flow Cell System for Fully Automated Screening of Electrocatalyst Materials. *J. Electrochem. Soc.* **2012,** *159* (11), F670-F675; (b) Cherevko, S.; Topalov, A. A.; Zeradjanin, A. R.; Keeley, G. P.; Mayrhofer, K. J. J., Temperature-Dependent Dissolution of Polycrystalline Platinum in Sulfuric Acid Electrolyte. *Electrocatalysis* **2014,** *5* (3), 235-240.
25. Fabbri, E.; Taylor, S.; Rabis, A.; Levecque, P.; Conrad, O.; Kötz, R.; Schmidt, T. J., The Effect of Platinum Nanoparticle Distribution on Oxygen Electroreduction Activity and Selectivity. *ChemCatChem* **2014,** *6*, 1410-1418.
26. Quinson, J.; Röefzaad, M.; Deiana, D.; Hansen, T. W.; Wagner, J. B.; Nesselberger, M.; Crampton, A. S.; Ridge, C. J.; Schweinberger, F. F.; Heiz, U.; Arenz, M., Electrochemical stability of subnanometer Pt clusters. *Electrochim. Acta* **2018,** *277*, 211-217.
27. (a) Speder, J.; Altmann, L.; Roefzaad, M.; Baumer, M.; Kirkensgaard, J. J.; Mortensen, K.; Arenz, M., Pt based PEMFC catalysts prepared from colloidal particle suspensions - a toolbox for model studies. *Phys. Chem. Chem. Phys.* **2013,** *15* (10), 3602-8; (b) Speder, J.; Zana, A.; Spanos, I.; Kirkensgaard, J. J. K.; Mortensen, K.; Arenz, M., On the influence of the Pt to carbon ratio on the degradation of high surface area carbon supported PEM fuel cell electrocatalysts. *Electrochem. Commun.* **2013,** *34*, 153-156.
28. (a) Eslamibidgoli, M. J.; Eikerling, M. H., Atomistic Mechanism of Pt Extraction at Oxidized Surfaces: Insights from DFT. *Electrocatalysis* **2016,** *7* (4), 345-354; (b) Fantauzzi, D.; Mueller, J. E.; Sabo, L.; van Duin, A. C. T.; Jacob, T., Surface Buckling and Subsurface Oxygen: Atomistic Insights into the Surface Oxidation of Pt(111). *ChemPhysChem* **2015,** *16* (13), 2797-2802; (c) Conway, B. E.; Jerkiewicz, G., Surface Orientation Dependence of Oxide Film Growth at Platinum Single-Crystals. *J. Electroanal. Chem.* **1992,** *339* (1-2), 123-146; (d) Drnec, J.; Ruge, M.; Reikowski, F.; Rahn, B.; Carlà, F.; Felici, R.; Stettner, J.; Magnussen, O. M.; Harrington, D. A., Initial stages of Pt(111) electrooxidation: dynamic and structural studies by surface X-ray diffraction. *Electrochim. Acta* **2017,** *224*, 220-227; (e) Conway, B. E., Electrochemical Oxide Film Formation at Noble-Metals as a Surface-Chemical Process. *Prog. Surf. Sci.* **1995,** *49* (4), 331-452.

29. Ohma, A.; Shinohara, K.; Iiyama, A.; Yoshida, T.; Daimaru, A., Membrane and catalyst performance targets for automotive fuel cells by FCCJ membrane, catalyst, MEA WG. *ECS Transactions* **2011,** *41* (1), 775-784.
30. (a) DOE, *U.S. DRIVE Fuel Cell Tech Team Cell Component Accelerated Stress Test and Polarization Curve Protocols for PEM Fuel Cells, https://www.energy.gov/eere/fuelcells/downloads/fuel-cell-tech-team-accelerated-stress-test-and-polarization-curve* **2013**; (b) DOE, *USCAR Fuel Cell Tech Team Cell Component Accelerated stress test protocols for PEM Fuel Cells* **2010**; (c) DOE, *DOE Cell Component Accelerated Stress Test Protocols for PEM Fuel Cells* **2007**; (d) Myers, D. J. *2010 Annual Progress Report - Polymer Electrolyte Fuel Cell Lifetime Limitations: The Role of Electrocatalysts Degradation*; US DOE: 2010, https://www.hydrogen.energy.gov/annual_progress10_fuelcells.html#h; (e) Borup, R.; Meyers, J.; Pivovar, B.; Kim, Y. S.; Mukundan, R.; Garland, N.; Myers, D.; Wilson, M.; Garzon, F.; Wood, D.; Zelenay, P.; More, K.; Stroh, K.; Zawodzinski, T.; Boncella, J.; McGrath, J. E.; Inaba, M.; Miyatake, K.; Hori, M.; Ota, K.; Ogumi, Z.; Miyata, S.; Nishikata, A.; Siroma, Z.; Uchimoto, Y.; Yasuda, K.; Kimijima, K.; Iwashita, N., Scientific Aspects of Polymer Electrolyte Fuel Cell Durability and Degradation. *Chem. Rev.* **2007,** *107* (10), 3904-51.
31. (a) Gilbert, J. A.; Kariuki, N. N.; Wang, X.; Kropf, A. J.; Yu, K.; Groom, D. J.; Ferreira, P. J.; Morgan, D.; Myers, D. J., Pt Catalyst Degradation in Aqueous and Fuel Cell Environments studied via In-Operando Anomalous Small-Angle X-ray Scattering. *Electrochim. Acta* **2015,** *173*, 223-234; (b) Uchimura, M.; Sugawara, S.; Suzuki, Y.; Zhang, J.; Kocha, S. S., Electrocatalyst Durability under Simulated Automotive Drive Cycles *ECS Trans.* **2008,** *16* (2), 9.
32. Cherevko, S.; Keeley, G. P.; Geiger, S.; Zeradjanin, A. R.; Hodnik, N.; Kulyk, N.; Mayrhofer, K. J. J., Dissolution of Platinum in the Operational Range of Fuel Cells. *ChemElectroChem* **2015,** *2* (10), 1471-1478.

Bibliography

[1] British Petroleum Company, "BP Statistical Review of World Energy Statistical Review of World," *The Editor BP Statistical Review of World Energy*, 2019.

[2] U. S. E. I. Administration, "Internation Energy Outlook 2019," *Choice Reviews Online*, vol. 44, no. 07, pp. 44–3624–44–3624, 2019.

[3] D. o. E. Population Division United Nations and S. Affairs, "World Population Prospects," tech. rep., United Nations, 2019.

[4] O. W. in Data, "Our World in Data," 2019.

[5] C. I. Jones, "Chapter 1 - The Facts of Economic Growth," in *Handbook of Macroeconomics* (J. B. Taylor and H. B. T. H. o. M. Uhlig, eds.), vol. 2, pp. 3–69, Elsevier, 2016.

[6] E. E. Agency, "Correlation of Energy Consumption and GDP per person," 2016.

[7] IPCC, "AR5 Synthesis Report: Climate Change 2014," tech. rep., United Nations, Cambridge, 2014.

[8] United Nations, "Summary of the Paris Agreement," *United Nations Framework Convention on Climate Change*, 2015.

[9] IAEA, "International Atomic Energy Agency Webpage," 2019.

[10] S. Gamesa, "Siemens Gamesa Webpage," 2019.

[11] Power-Technology, "The World's Biggest Solar Power Plants," 2020.

[12] Z. W. Seh, J. Kibsgaard, C. F. Dickens, I. Chorkendorff, J. K. Nørskov, and T. F. Jaramillo, "Combining theory and experiment in electrocatalysis: Insights into materials design," *Science*, vol. 355, no. 6321, 2017.

[13] R. Frydendal, "Improving performance of catalysts for water electrolysis," 2015.

[14] U. O. of Energy Efficiency and Renewable Energy, "Fuel Cell Types," 2020.

[15] L. Kavanagh, J. Keohane, G. G. Cabellos, A. Lloyd, and J. Cleary, "Global lithium sources-industrial use and future in the electric vehicle industry: A review," 2018.

[16] L. D. Harvey, "Resource implications of alternative strategies for achieving zero greenhouse gas emissions from light-duty vehicles by 2060," *Applied Energy*, 2018.

[17] D. Jasiński, J. Meredith, and K. Kirwan, "The life cycle impact for platinum group metals and lithium to 2070 via surplus cost potential," *International Journal of Life Cycle Assessment*, 2018.

[18] J. Wang, H. Wang, and Y. Fan, "Techno-Economic Challenges of Fuel Cell Commercialization," 2018.

[19] T. Yoshida and K. Kojima, "Toyota MIRAI fuel cell vehicle and progress toward a future hydrogen society," *Electrochemical Society Interface*, 2015.

[20] I. Chorkendorff and J. W. Niemantsverdriet, *Concepts of Modern Catalysis and Kinetics*. Wiley, oct 2003.

[21] H. Falsig, B. Hvolbæk, I. S. Kristensen, T. Jiang, T. Bligaard, C. H. Christensen, and J. K. Nørskov, "Trends in the catalytic CO oxidation activity of nanoparticles," *Angewandte Chemie - International Edition*, vol. 47, no. 26, pp. 4835–4839, 2008.

[22] A. Vojvodic and J. K. Nørskov, "New design paradigm for heterogeneous catalysts," *National Science Review*, 2015.

[23] V. R. Stamenkovic, B. Fowler, B. S. Mun, G. Wang, P. N. Ross, C. A. Lucas, and N. M. Markovic, "Improved oxygen reduction activity on Pt3Ni(111) via increased surface site availability," *Science*, 2007.

[24] P. L. Hansen, J. B. Wagner, S. Helveg, J. R. Rostrup-Nielsen, B. S. Clausen, and H. Topsøe, "Atom-resolved imaging of dynamic shape changes in supported copper nanocrystals," *Science*, 2002.

[25] M. P. Andersson, F. Abild-Pedersen, I. N. Remediakis, T. Bligaard, G. Jones, J. Engbæk, O. Lytken, S. Horch, J. H. Nielsen, J. Sehested, J. R. Rostrup-Nielsen, J. K. Nørskov, and I. Chorkendorff, "Structure sensitivity of the methanation reaction: H2-induced CO dissociation on nickel surfaces," *Journal of Catalysis*, vol. 255, pp. 6–19, apr 2008.

[26] B. Hammer and J. K. Norskov, "Why gold is the noblest of all the metals," *Nature*, vol. 376, no. 6537, pp. 238–240, 1995.

[27] M. Haruta, S. Tsubota, T. Kobayashi, H. Kageyama, M. Genet, and B. Delmon, "Low-Temperature Oxidation of CO over Gold Supported on TiO2, α-Fe2O3, and Co3O4," *Journal of Catalysis*, vol. 144, pp. 175–192, nov 1993.

[28] M. Haruta, "Size- and support-dependency in the catalysis of gold," *Catalysis Today*, vol. 36, pp. 153–166, apr 1997.

[29] P. Hernandez-Fernandez, F. Masini, D. N. McCarthy, C. E. Strebel, D. Friebel, D. Deiana, P. Malacrida, A. Nierhoff, A. Bodin, A. M. Wise, J. H. Nielsen, T. W. Hansen, A. Nilsson, I. E. L. Stephens, and I. Chorkendorff, "Mass-selected nanoparticles of PtxY as model catalysts for oxygen electroreduction," *Nature Chemistry*, vol. 6, pp. 732–738, aug 2014.

[30] L. Li, A. H. Larsen, N. A. Romero, V. A. Morozov, C. Glinsvad, F. Abild-Pedersen, J. Greeley, K. W. Jacobsen, and J. K. Nørskov, "Investigation of catalytic finite-size-effects of platinum metal clusters," *Journal of Physical Chemistry Letters*, vol. 4, no. 1, pp. 222–226, 2013.

[31] J. Kleis, J. Greeley, N. A. Romero, V. A. Morozov, H. Falsig, A. H. Larsen, J. Lu, J. J. Mortensen, M. Dułak, K. S. Thygesen, J. K. Nørskov, and K. W. Jacobsen, "Finite Size Effects in Chemical Bonding: From Small Clusters to Solids," *Catalysis Letters*, vol. 141, pp. 1067–1071, aug 2011.

[32] S. Abbet, A. Sanchez, U. Heiz, W.-D. Schneider, A. M. Ferrari, G. Pacchioni, and N. Rösch, "Acetylene Cyclotrimerization on Supported Size-Selected Pd n Clusters (1 n 30): One Atom Is Enough!," *Journal of the American Chemical Society*, vol. 122, pp. 3453–3457, apr 2000.

[33] A. Sanchez, S. Abbet, U. Heiz, W. D. Schneider, H. Häkkinen, R. N. Barnett, and U. Landman, "When Gold Is Not Noble: Nanoscale Gold Catalysts," *Journal of Physical Chemistry A*, vol. 103, no. 48, pp. 9573–9578, 1999.

[34] U. Landman, B. Yoon, C. Zhang, U. Heiz, and M. Arenz, "Factors in gold nanocatalysis: Oxidation of CO in the non-scalable size regime," *Topics in Catalysis*, vol. 44, no. 1-2, pp. 145–158, 2007.

[35] J. Kibsgaard and I. Chorkendorff, "Considerations for the scaling-up of water splitting catalysts," *Nature Energy*, vol. 4, no. 6, pp. 430–433, 2019.

[36] S. Yatsuya, T. Kamakura, K. Yamauchi, and K. Mihama, "A New Technique for the Formation of Ultrafine Particles by Sputtering," *Japanese Journal of Applied Physics*, vol. 25, pp. L42–L44, jan 1986.

[37] Y. Huttel, ed., *Gas-Phase Synthesis of Nanoparticles*. Weinheim, Germany: Wiley-VCH Verlag GmbH & Co. KGaA, jul 2017.

[38] H. Hahn and R. S. Averback, "The production of nanocrystalline powders by magnetron sputtering," *Journal of Applied Physics*, 1990.

[39] H. Haberland and M. Karrais, "Thin films from energetic cluster impact: A feasibility study," *Journal of Vacuum Science & Technology A: Vacuum, Surfaces, and Films*, vol. 10, no. 1992, pp. 3266–3271, 1992.

[40] S. Pratontep, S. J. Carroll, C. Xirouchaki, M. Streun, and R. E. Palmer, "Size-selected cluster beam source based on radio frequency magnetron plasma sputtering and gas condensation," *Review of Scientific Instruments*, 2005.

[41] B. von Issendorff and R. E. Palmer, "A new high transmission infinite range mass selector for cluster and nanoparticle beams," *Review of Scientific Instruments*, vol. 70, no. 12, p. 4497, 1999.

[42] K. Bromann, H. Brune, C. Félix, W. Harbich, R. Monot, J. Buttet, and K. Kern, "Hard and soft landing of mass selected Ag clusters on Pt(111)," *Surface Science*, vol. 377-379, pp. 1051–1055, 1997.

[43] K. Bromann, C. Félix, H. Brune, W. Harbich, R. Monot, J. Buttet, and K. Kern, "Controlled Deposition of Size-Selected Silver Nanoclusters," *Science*, vol. 274, pp. 956–958, nov 1996.

[44] U. Heiz and U. Landman, eds., *Nanocatalysis*. Nanoscience and Technology, Berlin, Heidelberg: Springer Berlin Heidelberg, 2007.

[45] C. D. Wagner and G. E. Muilenberg, *Handbook of X-ray Photoelectron Spectroscopy: A Reference Book of Standard Data for Use in X-ray Photoelectron Spectroscopy*. Perkin-Elmer, 1979.

[46] R. Hesse, P. Streubel, and R. Szargan, "Product or sum: comparative tests of Voigt, and product or sum of Gaussian and Lorentzian functions in the fitting of synthetic Voigt-based X-ray photoelectron spectra," *Surface and Interface Analysis*, vol. 39, pp. 381–391, may 2007.

[47] D. A. Shirley, "High-resolution x-ray photoemission spectrum of the valence bands of gold," *Physical Review B*, 1972.

[48] D. B. Williams and C. B. Carter, *Transmission Electron Microscopy*. Boston, MA: Springer US, second ed., 2009.

[49] C. f. E. N. Technical University of Denmark, "Center for Electron Nanoscopy Homepage," 2019.

[50] J. R. Jinschek and S. Helveg, "Image resolution and sensitivity in an environmental transmission electron microscope," *Micron*, 2012.

[51] D. Solutions, "DENS Solution Wildfire Chip."

[52] C. Kisielowski, L. W. Wang, P. Specht, H. A. Calderon, B. Barton, B. Jiang, J. H. Kang, and R. Cieslinski, "Real-time sub-Ångstrom imaging of reversible and irreversible conformations in rhodium catalysts and graphene," *Physical Review B - Condensed Matter and Materials Physics*, 2013.

[53] M. Ek, S. P. Jespersen, C. D. Damsgaard, and S. Helveg, "On the role of the gas environment, electron-dose-rate, and sample on the image resolution in transmission electron microscopy," *Advanced Structural and Chemical Imaging*, 2016.

[54] T. R. Henriksen, J. L. Olsen, P. Vesborg, I. Chorkendorff, and O. Hansen, "Highly sensitive silicon microreactor for catalyst testing," *Review of Scientific Instruments*, 2009.

[55] T. R. Henriksen, J. L. Olsen, P. Vesborg, I. Chorkendorff, and O. Hansen, "Highly sensitive silicon microreactor for catalyst testing," *Review of Scientific Instruments*, vol. 80, no. 12, 2009.

[56] P. C. Vesborg, J. L. Olsen, T. R. Henriksen, I. Chorkendorff, and O. Hansen, "Gas-phase photocatalysis in μ-reactors," *Chemical Engineering Journal*, 2010.

[57] T. Andersen, R. Jensen, M. K. Christensen, T. Pedersen, O. Hansen, and I. Chorkendorff, "High mass resolution time of flight mass spectrometer for measuring products in heterogeneous catalysis in highly sensitive microreactors," 2012.

[58] A. K. Schuppert, A. A. Topalov, I. Katsounaros, S. O. Klemm, and K. J. Mayrhofera, "A scanning flow cell system for fully automated screening of electrocatalyst materials," *Journal of the Electrochemical Society*, 2012.

[59] S. Cherevko, A. A. Topalov, A. R. Zeradjanin, G. P. Keeley, and K. J. Mayrhofer, "Temperature-Dependent Dissolution of Polycrystalline Platinum in Sulfuric Acid Electrolyte," *Electrocatalysis*, 2014.

[60] J. P. Grote, A. R. Zeradjanin, S. Cherevko, and K. J. Mayrhofer, "Coupling of a scanning flow cell with online electrochemical mass spectrometry for screening of reaction selectivity," *Review of Scientific Instruments*, 2014.

[61] M. Escudero-Escribano, P. Malacrida, M. H. Hansen, U. G. Vej-Hansen, A. Velázquez-Palenzuela, V. Tripkovic, J. Schiøtz, J. Rossmeisl, I. E. Stephens, and I. Chorkendorff, "Tuning the activity of Pt alloy electrocatalysts by means of the lanthanide contraction," *Science*, 2016.

[62] D. Li, C. Wang, D. S. Strmcnik, D. V. Tripkovic, X. Sun, Y. Kang, M. Chi, J. D. Snyder, D. Van Der Vliet, Y. Tsai, V. R. Stamenkovic, S. Sun, and N. M. Markovic, "Functional links between Pt single crystal morphology and nanoparticles with different size and shape: The oxygen reduction reaction case," *Energy and Environmental Science*, 2014.

[63] M. Oezaslan, F. Hasché, and P. Strasser, "Pt-based core-shell catalyst architectures for oxygen fuel cell electrodes," *Journal of Physical Chemistry Letters*, 2013.

[64] X. Huang, Z. Zhao, L. Cao, Y. Chen, E. Zhu, Z. Lin, M. Li, A. Yan, A. Zettl, Y. M. Wang, X. Duan, T. Mueller, and Y. Huang, "High-performance transition metal-doped Pt3Ni octahedra for oxygen reduction reaction," *Science*, 2015.

[65] C. He, S. Desai, G. Brown, and S. Bollepalli, "PEM fuel cell catalysts: Cost, performance, and durability," 2005.

[66] Y. Yang, "PEM fuel cell system manufacturing cost analysis for automotive applications," *Wellesley: Austin Power Engineering LLC*, 2015.

[67] A. Kongkanand and M. F. Mathias, "The Priority and Challenge of High-Power Performance of Low-Platinum Proton-Exchange Membrane Fuel Cells," 2016.

[68] P. Gazdzicki, J. Mitzel, A. M. Dreizler, M. Schulze, and K. A. Friedrich, "Impact of Platinum Loading on Performance and Degradation of Polymer Electrolyte Fuel Cell Electrodes Studied in a Rainbow Stack," *Fuel Cells*, 2018.

[69] C. Chen, Y. Kang, Z. Huo, Z. Zhu, W. Huang, H. L. Xin, J. D. Snyder, D. Li, J. A. Herron, M. Mavrikakis, M. Chi, K. L. More, Y. Li, N. M. Markovic, G. A. Somorjai, P. Yang, and V. R. Stamenkovic, "Highly crystalline multimetallic nanoframes with three-dimensional electrocatalytic surfaces," *Science*, 2014.

[70] S. Cherevko, "Stability and dissolution of electrocatalysts: Building the bridge between model and "real world" systems," 2018.

[71] J. C. Meier, C. Galeano, I. Katsounaros, J. Witte, H. J. Bongard, A. A. Topalov, C. Baldizzone, S. Mezzavilla, F. Schüth, and K. J. Mayrhofer, "Design criteria for stable Pt/C fuel cell catalysts," 2014.

[72] S. Cherevko, G. P. Keeley, S. Geiger, A. R. Zeradjanin, N. Hodnik, N. Kulyk, and K. J. Mayrhofer, "Dissolution of Platinum in the Operational Range of Fuel Cells," *ChemElectroChem*, 2015.

[73] G. P. Keeley, S. Cherevko, and K. J. Mayrhofer, "The Stability Challenge on the Pathway to Low and Ultra-Low Platinum Loading for Oxygen Reduction in Fuel Cells," *ChemElectroChem*, 2016.

[74] J. Speder, I. Spanos, A. Zana, J. J. Kirkensgaard, K. Mortensen, L. Altmann, M. Bäumer, and M. Arenz, "From single crystal model catalysts to systematic studies of supported nanoparticles," *Surface Science*, 2015.

[75] M. Nesselberger, M. Roefzaad, R. Fayçal Hamou, P. Ulrich Biedermann, F. F. Schweinberger, S. Kunz, K. Schloegl, G. K. H. Wiberg, S. Ashton, U. Heiz, K. J. J. Mayrhofer, and M. Arenz, "The effect of particle proximity on the oxygen reduction rate of size-selected platinum clusters," *Nature Materials*, vol. 12, pp. 919–924, oct 2013.

[76] J. Speder, L. Altmann, M. Bäumer, J. J. Kirkensgaard, K. Mortensen, and M. Arenz, "The particle proximity effect: From model to high surface area fuel cell catalysts," *RSC Advances*, 2014.

[77] E. Fabbri, S. Taylor, A. Rabis, P. Levecque, O. Conrad, R. Kötz, and T. J. Schmidt, "The effect of platinum nanoparticle distribution on oxygen electroreduction activity and selectivity," *ChemCatChem*, 2014.

[78] J. P. Owejan, J. E. Owejan, and W. Gu, "Impact of Platinum Loading and Catalyst Layer Structure on PEMFC Performance," *Journal of The Electrochemical Society*, 2013.

[79] H. A. Gasteiger, S. S. Kocha, B. Sompalli, and F. T. Wagner, "Activity benchmarks and requirements for Pt, Pt-alloy, and non-Pt oxygen reduction catalysts for PEMFCs," 2005.

[80] F. J. Perez-Alonso, D. N. McCarthy, A. Nierhoff, P. Hernandez-Fernandez, C. Strebel, I. E. Stephens, J. H. Nielsen, and I. Chorkendorff, "The effect of size on the oxygen electroreduction activity of mass-selected platinum nanoparticles," *Angewandte Chemie - International Edition*, 2012.

[81] M. Shao, A. Peles, and K. Shoemaker, "Electrocatalysis on platinum nanoparticles: Particle size effect on oxygen reduction reaction activity," *Nano Letters*, 2011.

[82] Z. Xu, H. Zhang, H. Zhong, Q. Lu, Y. Wang, and D. Su, "Effect of particle size on the activity and durability of the Pt/C electrocatalyst for proton exchange membrane fuel cells," *Applied Catalysis B: Environmental*, 2012.

[83] J. Quinson, M. Inaba, S. Neumann, A. A. Swane, J. Bucher, S. B. Simonsen, L. Theil Kuhn, J. J. Kirkensgaard, K. M. Jensen, M. Oezaslan, S. Kunz, and M. Arenz, "Investigating Particle Size Effects in Catalysis by Applying a Size-Controlled and Surfactant-Free Synthesis of Colloidal Nanoparticles in Alkaline Ethylene Glycol: Case Study of the Oxygen Reduction Reaction on Pt," *ACS Catalysis*, 2018.

[84] M. Nesselberger, S. Ashton, J. C. Meier, I. Katsounaros, K. J. Mayrhofer, and M. Arenz, "The particle size effect on the oxygen reduction reaction activity of Pt catalysts: Influence of electrolyte and relation to single crystal models," *Journal of the American Chemical Society*, 2011.

[85] W. Sheng, S. Chen, E. Vescovo, and Y. Shao-Horn, "Size influence on the oxygen reduction reaction activity and instability of supported Pt nanoparticles," *Journal of the Electrochemical Society*, 2012.

[86] H. Yano, M. Watanabe, A. Iiyama, and H. Uchida, "Particle-size effect of Pt cathode catalysts on durability in fuel cells," *Nano Energy*, 2016.

[87] M. Watanabe, H. Yano, H. Uchida, and D. A. Tryk, "Achievement of distinctively high durability at nanosized Pt catalysts supported on carbon black for fuel cell cathodes," *Journal of Electroanalytical Chemistry*, 2018.

[88] R. K. Ahluwalia, S. Arisetty, X. Wang, X. Wang, R. Subbaraman, S. C. Ball, S. DeCrane, and D. J. Myers, "Thermodynamics and kinetics of platinum dissolution from carbon-supported electrocatalysts in aqueous media under potentiostatic and potentiodynamic conditions," *Journal of the Electrochemical Society*, 2013.

[89] J. Speder, A. Zana, and M. Arenz, "The colloidal tool-box approach for fuel cell catalysts: Systematic study of perfluorosulfonate-ionomer impregnation and Pt loading," *Catalysis Today*, vol. 262, pp. 82–89, 2016.

[90] M. Inaba, J. Quinson, and M. Arenz, "pH matters: The influence of the catalyst ink on the oxygen reduction activity determined in thin film rotating disk electrode measurements," *Journal of Power Sources*, 2017.

[91] D. Sandbeck, N. Secher, M. Inaba, J. Quinson, J. Sørensen, J. Kibsgaard, A. Zana, F. Bizzotto, F. Speck, A. Dworzak, C. Dosche, and M. Oezaslan, "The Dissolution Dilemma for low Pt Loading Polymer Electrolyte Membrane Fuel Cells," *Submitted to Advanced Energy Materials*, 2020.

[92] D. Sandbeck, N. Secher, F. Speck, J. Sørensen, J. Kibsgaard, I. Chorkendorff, and S. Cherevko, "The Particle Size Effect on Platinum Dissolution: Considerations for Accelerated Stability Testing of Fuel Cell Catalysts," *In review at ACS Catalysis*, 2020.

[93] A. A. Topalov, S. Cherevko, A. R. Zeradjanin, J. C. Meier, I. Katsounaros, and K. J. Mayrhofer, "Towards a comprehensive understanding of platinum dissolution in acidic media," *Chemical Science*, 2014.

[94] S. Cherevko, A. R. Zeradjanin, G. P. Keeley, and K. J. Mayrhofer, "A comparative study on gold and platinum dissolution in acidic and alkaline media," *Journal of the Electrochemical Society*, 2014.

[95] A. A. Topalov, I. Katsounaros, M. Auinger, S. Cherevko, J. C. Meier, S. O. Klemm, and K. J. Mayrhofer, "Dissolution of platinum: Limits for the deployment of electrochemical energy conversion?," *Angewandte Chemie - International Edition*, 2012.

[96] S. Cherevko, N. Kulyk, and K. J. Mayrhofer, "Durability of platinum-based fuel cell electrocatalysts: Dissolution of bulk and nanoscale platinum," *Nano Energy*, 2016.

[97] D. J. Myers, X. Wang, M. C. Smith, and K. L. More, "Potentiostatic and potential cycling dissolution of polycrystalline platinum and platinum nanoparticle fuel cell catalysts," *Journal of the Electrochemical Society*, 2018.

[98] E. Pizzutilo, S. Geiger, J. P. Grote, A. Mingers, K. J. Mayrhofer, M. Arenz, and S. Cherevko, "On the need of improved Accelerated Degradation Protocols (ADPs): Examination of platinum dissolution and carbon corrosion in half-cell tests," *Journal of the Electrochemical Society*, 2016.

[99] K. J. Mayrhofer, B. B. Blizanac, M. Arenz, V. R. Stamenkovic, P. N. Ross, and N. M. Markovic, "The impact of geometric and surface electronic properties of Pt-catalysts on the particle size effect in electrocatalysis," *Journal of Physical Chemistry B*, 2005.

[100] J. Huang, A. Malek, J. Zhang, and M. H. Eikerling, "Non-monotonic Surface Charging Behavior of Platinum: A Paradigm Change," *Journal of Physical Chemistry C*, 2016.

[101] H. Yu, A. Baricci, A. Casalegno, L. Guetaz, L. Bonville, and R. Maric, "Strategies to mitigate Pt dissolution in low Pt loading proton exchange membrane fuel cell: II. A gradient Pt loading design," *Electrochimica Acta*, 2017.

[102] A. Cowley, "Platinum Metals Interrim Review 2013," *Platinum Metals Review*, vol. 57, jul 2013.

[103] I. Roger, M. A. Shipman, and M. D. Symes, "Earth-abundant catalysts for electrochemical and photoelectrochemical water splitting," *Nature Reviews Chemistry*, vol. 1, 2017.

[104] J. N. Tiwari, S. Sultan, C. W. Myung, T. Yoon, N. Li, M. Ha, A. M. Harzandi, H. J. Park, D. Y. Kim, S. S. Chandrasekaran, W. G. Lee, V. Vij, H. Kang, T. J. Shin, H. S. Shin, G. Lee, Z. Lee, and K. S. Kim, "Multicomponent electrocatalyst with ultralow Pt loading and high hydrogen evolution activity," *Nature Energy*, vol. 3, no. 9, pp. 773–782, 2018.

[105] P. C. Vesborg and T. F. Jaramillo, "Addressing the terawatt challenge: Scalability in the supply of chemical elements for renewable energy," *RSC Advances*, vol. 2, no. 21, pp. 7933–7947, 2012.

[106] K. A. Lewinski, D. van der Vliet, and S. M. Luopa, "NSTF advances for PEM electrolysis-the effect of alloying on activity of NSTF electrolyzer catalysts and performance of NSTF based PEM electrolyzers," *ECS Transactions*, vol. 69, no. 17, pp. 893–917, 2015.

[107] B. Hinnemann, P. G. Moses, J. Bonde, K. P. Jørgensen, J. H. Nielsen, S. Horch, I. Chorkendorff, and J. K. Nørskov, "Biomimetic hydrogen evolution: MoS2 nanoparticles as catalyst for hydrogen evolution," *Journal of the American Chemical Society*, vol. 127, no. 15, pp. 5308–5309, 2005.

[108] T. F. Jaramillo, K. P. Jørgensen, J. Bonde, J. H. Nielsen, S. Horch, and I. Chorkendorff, "Identification of active edge sites for electrochemical H2

evolution from MoS2 nanocatalysts.," *Science (New York, N.Y.)*, vol. 317, no. July, pp. 100–102, 2007.

[109] J. Kibsgaard, Z. Chen, B. N. Reinecke, and T. F. Jaramillo, "Engineering the surface structure of MoS2 to preferentially expose active edge sites for electrocatalysis," *Nature Materials*, vol. 11, pp. 963–969, nov 2012.

[110] Y.-F. Xu, M.-R. Gao, Y.-R. Zheng, J. Jiang, and S.-H. Yu, "Nickel/Nickel(II) Oxide Nanoparticles Anchored onto Cobalt(IV) Diselenide Nanobelts for the Electrochemical Production of Hydrogen," *Angewandte Chemie International Edition*, vol. 52, pp. 8546–8550, aug 2013.

[111] E. J. Popczun, J. R. McKone, C. G. Read, A. J. Biacchi, A. M. Wiltrout, N. S. Lewis, and R. E. Schaak, "Nanostructured nickel phosphide as an electrocatalyst for the hydrogen evolution reaction," *Journal of the American Chemical Society*, 2013.

[112] L. Fan, P. F. Liu, X. Yan, L. Gu, Z. Z. Yang, H. G. Yang, S. Qiu, and X. Yao, "Atomically isolated nickel species anchored on graphitized carbon for efficient hydrogen evolution electrocatalysis," *Nature Communications*, vol. 7, p. 10667, apr 2016.

[113] M. Ledendecker, J. S. Mondschein, O. Kasian, S. Geiger, D. Göhl, M. Schalenbach, A. Zeradjanin, S. Cherevko, R. E. Schaak, and K. Mayrhofer, "Stability and Activity of Non-Noble-Metal-Based Catalysts Toward the Hydrogen Evolution Reaction," *Angewandte Chemie - International Edition*, vol. 56, no. 33, pp. 9767–9771, 2017.

[114] A. J. Bard and L. R. Faulkner, *Electrochemical Methods: Fundamentals and Applications*. New York: John Wiley & Sons, Inc., second ed ed., 2001.

[115] E. Kemppainen, A. Bodin, B. Sebok, T. Pedersen, B. Seger, B. Mei, D. Bae, P. C. Vesborg, J. Halme, O. Hansen, P. D. Lund, and I. Chorkendorff, "Scalability and feasibility of photoelectrochemical H2 evolution: the ultimate limit of Pt nanoparticle as an HER catalyst," *Energy and Environmental Science*, vol. 8, no. 10, pp. 2991–2999, 2015.

[116] J. F. Callejas, J. M. McEnaney, C. G. Read, J. C. Crompton, A. J. Biacchi, E. J. Popczun, T. R. Gordon, N. S. Lewis, and R. E. Schaak, "Electrocatalytic and photocatalytic hydrogen production from acidic and neutral-pH aqueous solutions using iron phosphide nanoparticles," *ACS Nano*, vol. 8, no. 11, pp. 11101–11107, 2014.

[117] M. Tavakkoli, N. Holmberg, R. Kronberg, H. Jiang, J. Sainio, E. I. Kauppinen, T. Kallio, and K. Laasonen, "Electrochemical Activation of Single-Walled Carbon Nanotubes with Pseudo-Atomic-Scale Platinum for the Hydrogen Evolution Reaction," *ACS Catalysis*, vol. 7, no. 5, pp. 3121–3130, 2017.

[118] J. Kibsgaard, T. F. Jaramillo, and F. Besenbacher, "Building an appropriate active-site motif into a hydrogen-evolution catalyst with thiomolybdate [Mo3S13]2- clusters," *Nature Chemistry*, vol. 6, no. 3, pp. 248–253, 2014.

[119] W. Sheng, H. A. Gasteiger, and Y. Shao-Horn, "Hydrogen Oxidation and Evolution Reaction Kinetics on Platinum: Acid vs Alkaline Electrolytes," *Journal of The Electrochemical Society*, vol. 157, no. 11, p. B1529, 2010.

[120] C. M. Zalitis, A. R. Kucernak, J. Sharman, and E. Wright, "Design principles for platinum nanoparticles catalysing electrochemical hydrogen evolution and oxidation reactions: Edges are much more active than facets," *Journal of Materials Chemistry A*, vol. 5, no. 44, pp. 23328–23338, 2017.

[121] A. R. Kucernak and C. Zalitis, "General Models for the Electrochemical Hydrogen Oxidation and Hydrogen Evolution Reactions: Theoretical Derivation and Experimental Results under Near Mass-Transport Free Conditions," *The Journal of Physical Chemistry C*, vol. 120, pp. 10721–10745, may 2016.

[122] A. Beniya and S. Higashi, "Towards dense single-atom catalysts for future automotive applications," *Nature Catalysis*, vol. 2, no. 7, pp. 590–602, 2019.

[123] M. HARUTA, "Gold catalysts prepared by coprecipitation for low-temperature oxidation of hydrogen and of carbon monoxide," *Journal of Catalysis*, vol. 115, pp. 301–309, feb 1989.

[124] J. Kašpar, P. Fornasiero, and N. Hickey, "Automotive catalytic converters: current status and some perspectives," *Catalysis Today*, vol. 77, pp. 419–449, jan 2003.

[125] C. T. Campbell, "Nanoparticle Gold Catalysis," *Science*, vol. 306, pp. 234–235, 2004.

[126] ExxonMobil, "2017 Outlook for Energy: A View to 2040," *Outlook for Energy*, 2017.

[127] M. Valden, S. Pak, X. Lai, and D. W. Goodman, "Structure sensitivity of CO oxidation over model Au/TiO2 catalysts," *Catalysis Letters*, 1998.

[128] G. R. Bamwenda, S. Tsubota, T. Nakamura, and M. Haruta, "The influence of the preparation methods on the catalytic activity of platinum and gold supported on TiO 2 for CO oxidation," *Catalysis Letters*, vol. 44, pp. 83–87, 1997.

[129] M. G. Taylor, N. Austin, C. E. Gounaris, and G. Mpourmpakis, "Catalyst Design Based on Morphology- and Environment-Dependent Adsorption on Metal Nanoparticles," *ACS Catalysis*, vol. 5, no. 11, pp. 6296–6301, 2015.

[130] N. Lopez, "On the origin of the catalytic activity of gold nanoparticles for low-temperature CO oxidation," *Journal of Catalysis*, vol. 223, pp. 232–235, apr 2004.

[131] M. Valden, X. Lai, and D. W. Goodman, "Onset of catalytic activity of gold clusters on titania with the appearance of nonmetallic properties," *Science*, 1998.

[132] M. Chen and D. W. Goodman, "Catalytically active gold on ordered titania supports," *Chemical Society Reviews*, vol. 37, no. 9, pp. 1860–1870, 2008.

[133] S. J. Tauster, "Strong metal-support interactions," *Accounts of Chemical Research*, vol. 20, pp. 389–394, nov 1987.

[134] M. Chen and D. W. Goodman, "Catalytically Active Gold: From Nanoparticles to Ultrathin Films," *Accounts of Chemical Research*, vol. 39, pp. 739–746, oct 2006.

[135] J. Guzman and B. C. Gates, "Catalysis by Supported Gold: Correlation between Catalytic Activity for CO Oxidation and Oxidation States of Gold," *Journal of the American Chemical Society*, 2004.

[136] G. J. Hutchings, M. S. Hall, A. F. Carley, P. Landon, B. E. Solsona, C. J. Kiely, A. Herzing, M. Makkee, J. A. Moulijn, A. Overweg, J. C. Fierro-Gonzalez, J. Guzman, and B. C. Gates, "Role of gold cations in the oxidation of carbon monoxide catalyzed by iron oxide-supported gold," *Journal of Catalysis*, 2006.

[137] A. S. Wörz, U. Heiz, F. Cinquini, and G. Pacchioni, "Charging of Au atoms on TiO2 thin films from CO vibrational spectroscopy and DFT calculations," *Journal of Physical Chemistry B*, vol. 109, no. 39, pp. 18418–18426, 2005.

[138] U. Heiz, A. Sanchez, S. Abbet, and W. D. Schneider, "Tuning the oxidation of carbon monoxide using nanoassembled model catalysts," *Chemical Physics*, vol. 262, no. 1, pp. 189–200, 2000.

[139] B. Yoon, H. Häkkinen, U. Landman, A. S. Wörz, J. M. Antonietti, S. Abbet, K. Judai, and U. Heiz, "Charging effects on bonding and catalyzed oxidation of CO on Au8 clusters on MgO," *Science*, 2005.

[140] S. C. Parker and C. T. Campbell, "Reactivity and sintering kinetics of Au/TiO2(110) model catalysts: Particle size effects," *Topics in Catalysis*, 2007.

[141] M. S. Chen and D. W. Goodman, "The structure of catalytically active gold on titania," *Science*, 2004.

[142] H. Tang, Y. Su, B. Zhang, A. F. Lee, M. A. Isaacs, K. Wilson, L. Li, Y. Ren, J. Huang, M. Haruta, B. Qiao, X. Liu, C. Jin, D. Su, J. Wang, and T. Zhang, "Classical strong metal–support interactions between gold nanoparticles and titanium dioxide," *Science Advances*, vol. 3, no. 10, pp. 1–9, 2017.

[143] Y. Niu, P. Schlexer, B. Sebok, I. Chorkendorff, G. Pacchioni, and R. E. Palmer, "Reduced sintering of mass-selected Au clusters on SiO 2 by alloying with Ti: an aberration-corrected STEM and computational study," *Nanoscale*, vol. 10, no. 5, pp. 2363–2370, 2018.

[144] E. Svanidze, T. Besara, M. Fevsi Ozaydin, C. S. Tiwary, J. K. Wang, S. Radhakrishnan, S. Mani, Y. Xin, K. Han, H. Liang, T. Siegrist, P. M. Ajayan, and E. Morosan, "High hardness in the biocompatible intermetallic compound b-Ti3Au," *Science Advances*, vol. 2, no. 7, pp. 1–7, 2016.

[145] D. Llamosa Pérez, A. Espinosa, L. Martínez, E. Román, C. Ballesteros, A. Mayoral, M. García-Hernández, and Y. Huttel, "Thermal diffusion at nanoscale: From coau alloy nanoparticles to Co@Au core/shell structures," *Journal of Physical Chemistry C*, vol. 117, no. 6, pp. 3101–3108, 2013.

[146] L. Martínez, A. Mayoral, M. Espiñeira, E. Roman, F. J. Palomares, and Y. Huttel, "Core@shell, Au@TiOx nanoparticles by gas phase synthesis," *Nanoscale*, vol. 9, no. 19, pp. 6463–6470, 2017.

[147] D. Llamosa, M. Ruano, L. Martínez, A. Mayoral, E. Roman, M. García-Hernández, and Y. Huttel, "The ultimate step towards a tailored engineering of core@shell and core@shell@shell nanoparticles," *Nanoscale*, vol. 6, no. 22, pp. 13483–13486, 2014.

[148] J. F. Creemer, S. Helveg, G. H. Hoveling, S. Ullmann, A. M. Molenbroek, P. M. Sarro, and H. W. Zandbergen, "Atomic-scale electron microscopy at ambient pressure," *Ultramicroscopy*, vol. 108, no. 9, pp. 993–998, 2008.

[149] J. F. Creemer, F. Santagata, B. Morana, L. Mele, T. Alan, E. Iervolino, G. Pandraud, and P. M. Sarro, "An all-in-one nanoreactor for high-resolution microscopy on nanomaterials at high pressures," in *Proceedings of the IEEE International Conference on Micro Electro Mechanical Systems (MEMS)*, pp. 1103–1106, 2011.

[150] S. B. Vendelbo, C. F. Elkjær, H. Falsig, I. Puspitasari, P. Dona, L. Mele, B. Morana, B. J. Nelissen, R. van Rijn, J. F. Creemer, P. J. Kooyman, and S. Helveg, "Visualization of oscillatory behaviour of Pt nanoparticles catalysing CO oxidation," *Nature Materials*, vol. 13, no. 9, pp. 884–890, 2014.

[151] A. Boubnov, S. Dahl, E. Johnson, A. P. Molina, S. B. Simonsen, F. M. Cano, S. Helveg, L. J. Lemus-Yegres, and J. D. Grunwaldt, "Structure-activity relationships of Pt/Al 2O 3 catalysts for CO and NO oxidation at diesel exhaust conditions," *Applied Catalysis B: Environmental*, vol. 126, pp. 315–325, 2012.

[152] G. Wan, G. Zhang, and X. M. Lin, "Toward Efficient Carbon and Water Cycles: Emerging Opportunities with Single-Site Catalysts Made of 3d Transition Metals," *Advanced Materials*, vol. 1905548, pp. 1–19, 2019.

[153] Y. Chen, S. Ji, C. Chen, Q. Peng, D. Wang, and Y. Li, "Single-Atom Catalysts: Synthetic Strategies and Electrochemical Applications," *Joule*, vol. 2, pp. 1242–1264, jul 2018.

[154] S. Mitchell, E. Vorobyeva, and J. Pérez-Ramírez, "The Multifaceted Reactivity of Single-Atom Heterogeneous Catalysts," *Angewandte Chemie - International Edition*, vol. 57, no. 47, pp. 15316–15329, 2018.

[155] H. Zhang, G. Liu, L. Shi, and J. Ye, "Single-Atom Catalysts: Emerging Multifunctional Materials in Heterogeneous Catalysis," 2018.

[156] T. Maschmeyer, F. Rey, G. Sankar, and J. M. Thomas, "Heterogeneous catalysts obtained by grafting metallocene complexes onto mesoporous silica," *Nature*, 1995.

[157] Q. Fu, H. Saltsburg, and M. Flytzani-Stephanopoulos, "Active nonmetallic Au and Pt species on ceria-based water-gas shift catalysts," *Science*, 2003.

[158] X. Li, X. Yang, Y. Huang, T. Zhang, and B. Liu, "Supported Noble-Metal Single Atoms for Heterogeneous Catalysis," *Advanced Materials*, vol. 31, no. 50, pp. 1–19, 2019.

[159] L. Tang, X. Meng, D. Deng, and X. Bao, "Confinement Catalysis with 2D Materials for Energy Conversion," *Advanced Materials*, vol. 31, no. 50, pp. 1–16, 2019.

[160] E. Proietti, F. Jaouen, M. Lefèvre, N. Larouche, J. Tian, J. Herranz, and J. P. Dodelet, "Iron-based cathode catalyst with enhanced power density in polymer electrolyte membrane fuel cells," *Nature Communications*, vol. 2, no. 1, 2011.

[161] Y. J. Sa, D. J. Seo, J. Woo, J. T. Lim, J. Y. Cheon, S. Y. Yang, J. M. Lee, D. Kang, T. J. Shin, H. S. Shin, H. Y. Jeong, C. S. Kim, M. G. Kim, T. Y. Kim, and S. H. Joo, "A General Approach to Preferential Formation of Active Fe-Nx Sites in Fe-N/C Electrocatalysts for Efficient Oxygen Reduction Reaction," *Journal of the American Chemical Society*, 2016.

[162] B. You, N. Jiang, M. Sheng, W. S. Drisdell, J. Yano, and Y. Sun, "Bimetal-Organic Framework Self-Adjusted Synthesis of Support-Free Nonprecious Electrocatalysts for Efficient Oxygen Reduction," *ACS Catalysis*, vol. 5, no. 12, pp. 7068–7076, 2015.

[163] L. Jiao, G. Wan, R. Zhang, H. Zhou, S. H. Yu, and H. L. Jiang, "From Metal–Organic Frameworks to Single-Atom Fe Implanted N-doped Porous Carbons: Efficient Oxygen Reduction in Both Alkaline and Acidic Media," *Angewandte Chemie - International Edition*, vol. 57, no. 28, pp. 8525–8529, 2018.

[164] H. Fei, J. Dong, M. J. Arellano-Jiménez, G. Ye, N. Dong Kim, E. L. Samuel, Z. Peng, Z. Zhu, F. Qin, J. Bao, M. J. Yacaman, P. M. Ajayan, D. Chen, and J. M. Tour, "Atomic cobalt on nitrogen-doped graphene for hydrogen generation," *Nature Communications*, vol. 6, pp. 1–8, 2015.

[165] C. Zhang, J. Sha, H. Fei, M. Liu, S. Yazdi, J. Zhang, Q. Zhong, X. Zou, N. Zhao, H. Yu, Z. Jiang, E. Ringe, B. I. Yakobson, J. Dong, D. Chen, and J. M. Tour, "Single-Atomic Ruthenium Catalytic Sites on Nitrogen-Doped Graphene for Oxygen Reduction Reaction in Acidic Medium," *ACS Nano*, vol. 11, no. 7, pp. 6930–6941, 2017.

[166] H. Fei, J. Dong, Y. Feng, C. S. Allen, C. Wan, B. Volosskiy, M. Li, Z. Zhao, Y. Wang, H. Sun, P. An, W. Chen, Z. Guo, C. Lee, D. Chen, I. Shakir, M. Liu, T. Hu, Y. Li, A. I. Kirkland, X. Duan, and Y. Huang, "General synthesis and definitive structural identification of MN4C4 single-atom catalysts with tunable electrocatalytic activities," *Nature Catalysis*, vol. 1, pp. 63–72, jan 2018.

[167] A. Zitolo, V. Goellner, V. Armel, M. T. Sougrati, T. Mineva, L. Stievano, E. Fonda, and F. Jaouen, "Identification of catalytic sites for oxygen reduction in iron- and nitrogen-doped graphene materials," *Nature Materials*, vol. 14, no. 9, pp. 937–942, 2015.

[168] M. Nič, J. Jirát, B. Košata, A. Jenkins, and A. McNaught, eds., *IUPAC Compendium of Chemical Terminology*. Research Triagle Park, NC: IUPAC, jun 2009.

[169] H. T. Chung, D. A. Cullen, D. Higgins, B. T. Sneed, E. F. Holby, K. L. More, and P. Zelenay, "Direct atomic-level insight into the active sites of a high-performance PGM-free ORR catalyst," *Science*, vol. 357, pp. 479–484, aug 2017.

[170] Y. Li, W. Chen, J. Pei, C. He, J. Wan, H. Ren, Y. Zhu, Y. Wang, J. Dong, S. Tian, W.-C. Cheong, S. Lu, L. Zheng, X. Zheng, W. Yan, Z. Zhuang, C. Chen, Q. Peng, and D. Wang, "Rational Design of Single Mo Atoms Anchored on N-doped Carbon for Effective Hydrogen Evolution Reaction," *Angewandte Chemie International Edition*, pp. 1–6, 2017.

[171] C. Wenxing, P. Jiajing, H. Chun-Ting, W. Jiawei, R. Hanlin, W. Yu, D. Juncai, W. Konglin, C. Weng-Chon, M. Junjie, Z. Xusheng, Y. Wensheng, Z. Zhongbin, C. Chen, P. Qing, W. Dingsheng, and L. Yadong, "Single Tungsten Atoms Supported on MOF-Derived N-Doped Carbon for Robust Electrochemical Hydrogen Evolution," *Advanced Materials*, vol. 0, p. 1800396, jun 2018.

[172] X. Wang, Z. Chen, X. Zhao, T. Yao, W. Chen, R. You, C. Zhao, G. Wu, J. Wang, W. Huang, J. Yang, X. Hong, S. Wei, Y. Wu, and Y. Li, "Regulation of Coordination Number over Single Co Sites: Triggering the Effi-

cient Electroreduction of CO 2," *Angewandte Chemie International Edition*, vol. 57, pp. 1944–1948, feb 2018.

[173] Y. N. Gong, L. Jiao, Y. Qian, C. Y. Pan, L. Zheng, X. Cai, B. Liu, S. H. Yu, and H. L. Jiang, "Regulating the Coordination Environment of MOF-Templated Single-Atom Nickel Electrocatalysts for Boosting CO2 Reduction," *Angewandte Chemie - International Edition*, vol. 510006, pp. 2705–2709, 2020.

[174] E. C. Tyo and S. Vajda, "Catalysis by clusters with precise numbers of atoms," 2015.

[175] J. Wang, Z. Huang, W. Liu, C.-R. Chang, H. Tang, Z. Li, W. Chen, C. Jia, T. Yao, S. Wei, Y. Wu, and Y. Li, "Design of N-coordinated dual-metal sites: A stable and active Pt-free catalyst for acidic ORR," *Journal of the American Chemical Society*, p. jacs.7b10385, 2017.

[176] X. Han, X. Ling, D. Yu, D. Xie, L. Li, S. Peng, C. Zhong, N. Zhao, Y. Deng, and W. Hu, "Atomically Dispersed Binary Co-Ni Sites in Nitrogen-Doped Hollow Carbon Nanocubes for Reversible Oxygen Reduction and Evolution," *Advanced Materials*, vol. 31, no. 49, pp. 1–9, 2019.

[177] Y. Lei, F. Mehmood, S. Lee, J. Greeley, B. Lee, S. Seifert, R. E. Winansl, W. Elám, R. J. Meyer, P. C. Redfern, D. Teschner, R. Schlö'Gl, M. J. Pellin, L. A. Curtiss, and S. Vajda, "Increased silver activity for direct propylene epoxidation via subnanometer size effects," *Science*, 2010.

[178] S. Tian, Q. Fu, W. Chen, Q. Feng, Z. Chen, J. Zhang, W. C. Cheong, R. Yu, L. Gu, J. Dong, J. Luo, C. Chen, Q. Peng, C. Draxl, D. Wang, and Y. Li, "Carbon nitride supported Fe2 cluster catalysts with superior performance for alkene epoxidation," *Nature Communications*, 2018.

[179] Y. Zhao, K. R. Yang, Z. Wang, X. Yan, S. Cao, Y. Ye, Q. Dong, X. Zhang, J. E. Thorne, L. Jin, K. L. Materna, A. Trimpalis, H. Bai, S. C. Fakra, X. Zhong, P. Wang, X. Pan, J. Guo, M. Flytzani-Stephanopoulos, G. W. Brudvig, V. S. Batista, and D. Wang, "Stable iridium dinuclear heterogeneous catalysts supported on metal-oxide substrate for solar water oxidation," *Proceedings of the National Academy of Sciences of the United States of America*, 2018.

[180] S. Ji, Y. Chen, Q. Fu, Y. Chen, J. Dong, W. Chen, Z. Li, Y. Wang, L. Gu, W. He, C. Chen, Q. Peng, Y. Huang, X. Duan, D. Wang, C. Draxl, and Y. Li, "Confined Pyrolysis within Metal-Organic Frameworks to Form Uniform Ru3 Clusters for Efficient Oxidation of Alcohols," *Journal of the American Chemical Society*, 2017.

[181] D. M. Cox, W. Eberhardt, P. Fayet, Z. Fu, B. Kessler, R. D. Sherwood, D. Sondericker, and A. Kaldor, "Electronic structure of deposited monosized metal-clusters," *Zeitschrift für Physik D Atoms, Molecules and Clusters*, 1991.

[182] U. Heiz, F. Vanolli, A. Sanchez, and W.-D. Schneider, "Size-Dependent Molecular Dissociation on Mass-Selected, Supported Metal Clusters," *Journal of the American Chemical Society*, vol. 120, pp. 9668–9671, sep 1998.

[183] S. Abbet, K. Judai, L. Klinger, and U. Heiz, "Synthesis of monodispersed model catalysts using softlanding cluster deposition," *Pure and Applied Chemistry*, vol. 74, no. 9, pp. 1527–1535, 2002.

[184] W. E. Kaden, T. Wu, W. A. Kunkel, and S. L. Anderson, "Electronic Structure Controls Reactivity of Size-Selected Pd Clusters Adsorbed on TiO2 Surfaces," *Science*, vol. 326, pp. 826–829, nov 2009.

[185] C. Fan, T. Wu, W. E. Kaden, and S. L. Anderson, "Cluster size effects on hydrazine decomposition on Irn/Al2O3/NiAl(110)," *Surface Science*, vol. 600, pp. 461–467, jan 2006.

[186] S. Lee, C. Fan, T. Wu, and S. L. Anderson, "CO Oxidation on Au n /TiO 2 Catalysts Produced by Size-Selected Cluster Deposition," *Journal of the American Chemical Society*, vol. 126, pp. 5682–5683, may 2004.

[187] K. Judai, S. Abbet, A. S. Wörz, A. M. Ferrari, L. Giordano, G. Pacchioni, and U. Heiz, "Acetylene polymerization on supported transition metal clusters," *Journal of Molecular Catalysis A: Chemical*, vol. 199, pp. 103–113, may 2003.

[188] S. Gilb, M. Arenz, and U. Heiz, "The polymerization of acetylene on supported metal clusters," *Low Temperature Physics*, 2006.

[189] S. Vajda, M. J. Pellin, J. P. Greeley, C. L. Marshall, L. A. Curtiss, G. A. Ballentine, J. W. Elam, S. Catillon-Mucherie, P. C. Redfern, F. Mehmood, and P. Zapol, "Subnanometre platinum clusters as highly active and selective catalysts for the oxidative dehydrogenation of propane," *Nature Materials*, 2009.

[190] C. Liu, B. Yang, E. Tyo, S. Seifert, J. DeBartolo, B. von Issendorff, P. Zapol, S. Vajda, and L. A. Curtiss, "Carbon Dioxide Conversion to Methanol over Size-selected Cu 4 Clusters at Low Pressures," *Journal of the American Chemical Society*, vol. 137, no. 27, pp. 8676–8679, 2015.

[191] K. Jiang, S. Siahrostami, T. Zheng, Y. Hu, S. Hwang, E. Stavitski, Y. Peng, J. Dynes, M. Gangisetty, D. Su, K. Attenkofer, and H. Wang, "Isolated Ni single atoms in graphene nanosheets for high-performance CO 2 reduction," *Energy & Environmental Science*, pp. 8–14, 2018.

[192] J. Gu, C. S. Hsu, L. Bai, H. M. Chen, and X. Hu, "Atomically dispersed Fe3+ sites catalyze efficient CO2 electroreduction to CO," *Science*, vol. 364, no. 6445, pp. 1091–1094, 2019.

[193] S. Liu, H. B. Yang, S. F. Hung, J. Ding, W. Cai, L. Liu, J. Gao, X. Li, X. Ren, Z. Kuang, Y. Huang, T. Zhang, and B. Liu, "Elucidating the Electrocatalytic CO2 Reduction Reaction over a Model Single-Atom Nickel Catalyst," *Angewandte Chemie - International Edition*, vol. 59, no. 2, pp. 798–803, 2020.

[194] S. Yang, J. Kim, Y. J. Tak, A. Soon, and H. Lee, "Single-atom catalyst of platinum supported on titanium nitride for selective electrochemical reactions," *Angewandte Chemie - International Edition*, vol. 55, no. 6, pp. 2058–2062, 2016.

[195] H. Zhang, S. Hwang, M. Wang, Z. Feng, S. Karakalos, L. Luo, Z. Qiao, X. Xie, C. Wang, D. Su, Y. Shao, and G. Wu, "Single Atomic Iron Catalysts for Oxygen Reduction in Acidic Media: Particle Size Control and Thermal Activation," *Journal of the American Chemical Society*, vol. 139, pp. 14143–14149, oct 2017.

[196] Y. Ye, H. Li, F. Cai, C. Yan, R. Si, S. Miao, Y. Li, G. Wang, and X. Bao, "Two-Dimensional Mesoporous Carbon Doped with Fe-N Active Sites for Efficient Oxygen Reduction," *ACS Catalysis*, vol. 7, no. 11, pp. 7638–7646, 2017.

[197] E. Jung, H. Shin, B. H. Lee, V. Efremov, S. Lee, H. S. Lee, J. Kim, W. Hooch Antink, S. Park, K. S. Lee, S. P. Cho, J. S. Yoo, Y. E. Sung, and T. Hyeon, "Atomic-level tuning of Co–N–C catalyst for high-performance electrochemical H2O2 production," *Nature Materials*, 2020.

[198] A. H. Bodin, *Synthesis of Nanoparticle Model Systems for Sustainable Catalysis by Gas Aggregation*. PhD thesis, Technical University of Denmark, 2017.

[199] T. Kondo, S. Casolo, T. Suzuki, T. Shikano, M. Sakurai, Y. Harada, M. Saito, M. Oshima, M. I. Trioni, G. F. Tantardini, and J. Nakamura, "Atomic-scale characterization of nitrogen-doped graphite: Effects of dopant nitrogen on the local electronic structure of the surrounding carbon atoms," *Physical Review B - Condensed Matter and Materials Physics*, vol. 86, no. 3, pp. 1–6, 2012.

[200] D. Guo, R. Shibuya, C. Akiba, S. Saji, T. Kondo, and J. Nakamura, "Active sites of nitrogen-doped carbon materials for oxygen reduction reaction clarified using model catalysts," *Science*, vol. 351, pp. 361–365, jan 2016.

[201] R. Arrigo, M. Hävecker, S. Wrabetz, R. Blume, M. Lerch, J. McGregor, E. P. Parrott, J. A. Zeitler, L. F. Gladden, A. Knop-Gericke, R. Schlögl, and D. S. Su, "Tuning the acid/base properties of nanocarbons by functionalization via amination," *Journal of the American Chemical Society*, 2010.

[202] G. Zhang, A. G. Güell, P. M. Kirkman, R. A. Lazenby, T. S. Miller, and P. R. Unwin, "Versatile Polymer-Free Graphene Transfer Method and Applications," *ACS Applied Materials and Interfaces*, vol. 8, no. 12, pp. 8008–8016, 2016.

[203] J. Kibsgaard, J. V. Lauritsen, E. Lægsgaard, B. S. Clausen, H. Topsøe, and F. Besenbacher, "Cluster-support interactions and morphology of MoS2 nanoclusters in a graphite-supported hydrotreating model catalyst," *Journal of the American Chemical Society*, vol. 128, no. 42, pp. 13950–13958, 2006.